

**Design and Synthesis of Ferroelectric Metal-Ligand Architectures and
their Piezoelectric Energy Harvesting Studies**

A Thesis

Submitted in Partial Fulfillment of the Requirements

**For the Degree of
Doctor of Philosophy**

by

Neetu

ID: 20163465



Department of Chemistry

Indian Institute of Science Education and Research, Pune

March 2023

Dedicated to

My Family, Teachers and Friends.....




Prof. R. Boomi Shankar
Professor
Department of Chemistry,
IISER Pune

CERTIFICATE

Certified that the work incorporated in the thesis entitled “***Design and Synthesis of Ferroelectric Metal-Ligand Architectures and their Piezoelectric Energy Harvesting Studies***” submitted by **Ms. Neetu** was carried out by the candidate, under my supervision. The work presented here or any part of it has not been included in any other thesis submitted previously for the award of any degree or diploma from any other university or institution.

Date: 06th March 2023
Place: Pune


Dr. R. Boomi Shankar
(Research Supervisor)



DECLARATION

I declare that, this written submission represents my ideas in my own words and where other's ideas have been included; I have adequately cited and referenced the original sources. I also declare that I have adhered to all principles of academic honesty and integrity and have not misrepresented or fabricated or falsified any idea/data/fact/ source in my submission. I understand that violation of the above will be cause for disciplinary action by the Institute and can also evoke penal action from the sources which have thus not been properly cited or from whom proper permission has not been taken when needed.

Date: 06th March 2023

Place: Pune

A handwritten signature in blue ink, reading "Neetu", with a horizontal line underneath.

Ms. Neetu

ID: 20163465

Acknowledgements

An extensive and wavering six years journey of my PhD has come to an end. I want to express my gratitude towards those who supported and guided me professionally and personally.

My first and foremost sincere thanks go to my thesis supervisor Prof. Dr. R. Boomi Shankar, for his invaluable support, patience, excellent guidance and encouragement during the entire tenure of my doctoral research.

I am also indebted to Prof. K. N. Ganesh (Former Director) and the present Director Prof. Jayant B. Udgaonkar, IISER Pune, for providing world-class laboratories and a beautiful campus environment. I would also like to thank Dr. B. Praveenkumar (PZT Centre, ARDE-Pune, DRDO) and his students, Mrs. Priyangi Kulkarni, Mr. Prashant and Mr. Aniruddh, for providing the dielectric and piezoelectric data for all my samples. Their untimely helpful behaviour leads to the completion of the project on time.

I am grateful to the members of my Research Advisory Committee (RAC), Dr. Kadiravan Shanmuganathan (NCL-Pune) and Dr. Nirmalya Ballav (IISER-Pune) for providing their invaluable time and suggestions during the meetings and discussions which greatly upgrade the quality of my research work. I would also like to thank all the faculty members of the Department of Chemistry and mainly Prof. H. N. Gopi (Former) and Prof. Nirmalya Ballav (Present) Chair Chemistry, IISER-Pune providing the research facilities and various scientific activities in the department throughout the year. I also had great working experience with our collaborators starting from Dr. Maheswaran Shanmugam (IIT-Bombay), Dr. B. Praveenkumar (ARDE, DRDO), Dr. Satishchandra Ogale (IISER, Pune), Dr. Dinesh Kabra (IIT-Bombay) and his student Mr. Vijay, Prof. Thomas Anthopoulos (KAUST, Saudi Arabia), Dr. Jan K. Zaręba (Wroclaw, Poland) in a versatile projects which helped me in widening my knowledge in a different type of projects.

I am incredibly grateful to say thanks to all the IISER Pune technical staff for their endless support and for allowing me to access various instruments: Mrs. Archana (SCXRD), Mr. Ravinder (TGA, SCXRD), Mr. Parveen Nasa (SCXRD, PXRD), Mr. Nilesh Dumbre (SEM), Mr. Anil and Yathish (SEM), Mrs. Megha (AFM), Mr. Sandeep Kanade (HRMS), Mr. Mahesh Jadhav (TGA), Mr. Suresh Prajapati (MALDI-TOF), Mr. Prashant Kale, Mr. Santosh, Mr. Gopi, Mr. Ganesh Dimbar (IR), Mrs. Hemlata Phadke (DSC), Mrs. Amruta (DSC, TGA), Mrs. Bhagyashree (CHN Analysis). I am also thankful to the IT department for their help and

support. I would like to sincerely thank the entire administrative department of IISER Pune for their support, especially Col. (Retd.) G. Raja Sekhar (Registrar, IISER-Pune), Dr. V. S. Rao, Mr. Prabhash and Mr. Mayuresh. I also like to acknowledge the consistent support of Dean Doctoral Studies Office staff, especially Mrs. Dipali Dalvi and Mr. Tushar. I thank Dr. Umeshreddy Kacherki (Librarian) for support through library services.

It gives me immense pleasure to thank all the lab members. I thank the support and morale provided by my seniors, especially Dr. Anant Kumar Srivastava, Dr. Ashok Yadav, Dr. Mahesh Deshmukh, in the initial days of this journey. I am fortunate to share moments with Vijayakanth, Raja, Rishabh, Swati, Meghamala, Supriya, Cavya, Rishu, Nilotpal and Vikash whose friendly discussions and support led to my PhD completed in time. Also, I would like to thank many BSMS students, Atul, Sravan, Rani, Anindya, Anju, Hrithik and Ridham.

I feel blessed to have great friends by my side in IISER Pune. The four pillars are Mr. Chandan, Mr. Sanjit, Mr. Udaya and Mrs. Sandhya. I am always profoundly grateful for the time and support they have provided me in spite of their busy schedule and personal problems. They always encourage me to upstand my personal and professional difficulties.

Words cannot express my feeling and gratitude towards my parents, who are very supportive and aligned with my perspective towards my PhD journey. Mr. Radhey Shyam (my beloved father), Mr. Sita Ram (bade chacha ji), Mr. Ram Ratan (chote chacha ji), Mrs. Ayodhya Devi (my beloved mother), Mrs. Sarvesh (bdi chachi ji), Mrs. Chandra Kanta (choti chachi ji), I am the reflection of all of them. My brothers and sisters Mr. Deepak (Bhai), Mrs. Ritu (Bhabhi), Mr. Prateek, Mr. Manish, Mr. Satendra (Bhoja bhaiya), Ms. Dolly, Ms. Roopam, Ms. Lavanya they make me feel light and tension free. My little Shresth (bhatija) come as a ray of excitement in my life. Their unconditional emotional support, trust, encouragement and sacrifice made me what I am today. They are the biggest cheerleader for my every small achievement.

I cannot express enough thanks to the people involved in the whatsapp group named "The MAN" (Manish, Avni, and Neetu) (my M.Sc. batchmates). Thank you Avni and Manish for always triumphing my achievements and criticising my mistakes whenever it is required. Thank you for all the efforts you guys put in to keep me strong no matter what.

My sincere gratitude goes to all the friends from the 2016 and 2017 batch mates, including Subhajeet, Rashmi, Ruma, Jyoti, Puneeth, Debashish, Borris, Shabnum, Tariq, Debashree, Aslam, Sumanta, Jayshree, Minhaj, Manzoor. My other beloved friends from the Department, Debashis Mondal (Debu), for his unconditional support and Ankit Sharma (Sharma ji) for

always fixing my vision towards life. I always thank my childhood friend Anchal for always being with me.

I am also thankful for the mess (V-square), canteen (Shiv Sagar) and MDP Canteen for providing excellent food and beverage facilities. I always thank the housekeeping, gardening and security staff for keeping the campus clean, green and safe for peaceful living.

I thank IISER Pune and the Council of Scientific and Industrial Research (CSIR) for providing research scholarships for pursuing my PhD. I gratefully acknowledge the MTIC, MMM, Chemsymphoria conferences for allowing me to present my research work. My appreciation also extends to John Wiley and Sons, American Chemical Society (ACS), Royal Society of Chemistry (RSC), Elsevier Science Ltd., Springer etc., for accepting and publishing my research articles and their permission to reprint the materials under copyright.

I acknowledge all those people who directly or indirectly contributed to my PhD. Whether the help may be small or big, a word of motivation has cumulative effect to make up my character and achievements.

Finally, I thank the almighty God (Thakur Ji) for giving this wonderful life and people.

Neetu

Contents

Contents	i
Synopsis	iv
Abbreviations	ix
Rights and Permissions	x
List of Publications	xi
Chapter 1: Introduction	1-33
1.1. Introduction	1
1.2. Dielectric Materials	3
1.2.1 Dielectric Constant	5
1.2.2 Dielectric Loss	5
1.2.3 Dielectric Strength	6
1.2.4 Applications of Dielectric Materials	6
1.3. Classification of Dielectric Materials	6
1.4. Piezoelectricity	8
1.5. Pyroelectricity	9
1.6. Ferroelectricity	9
1.7. History of Ferroelectric materials and their Classification	11
1.8. Ferroelectricity in Metal-Ligand Coordination Complexes	12
1.9. Applications of ferroelectric materials	22
1.10. Piezo and Ferroelectric Properties for Mechanical Energy Harvesting Applications	24
1.11. Objective of the Thesis	29
1.12. References	30
Chapter 2: Ferroelectric Behavior of an Octahedral Metal-Ligand Cage and Its 2D- Connected Cage Framework	34-49
2.1. Introduction	35
2.2. Experimental Details	36
2.2.1 General Remarks	36
2.2.2 Syntheses	36
2.2.3 Crystallography	37
2.2.4 Ferroelectric and Dielectric Measurements	38
2.3 Results and Discussions	39
2.3.1 Synthesis and Crystal Structures	39
2.3.2 Ferroelectric and Dielectric Studies	42

Contents

2.3.3 Solvent Dependent Studies	45
2.4 Conclusion	47
2.5 References	47
Chapter 3: Visualization of Domain Structure and Piezoelectric Energy Harvesting in a Ferroelectric Metal-Ligand Cage	50-66
3.1. Introduction	51
3.2. Experimental Details	52
3.2.1 General Remarks	52
3.2.2 Syntheses	53
3.2.3 Crystallography	53
3.2.4 Non-linear Optical Measurements	54
3.2.5 Preparation of the Thin Film Crystallites of 1 and 2 for PFM Measurements	54
3.2.6 Piezoresponse Force Microscopy Characterization	54
3.2.7 Ferroelectric and Dielectric Measurements	55
3.2.8 Preparation of the 1-PDMS and 2-PDMS Composite Films and Testing of the Composite Devices	55
3.3 Results and Discussions	56
2.3.1 Synthesis, characterization and Crystal Structures	56
2.3.2 SHG, Ferroelectric, Dielectric and Piezoelectric Studies	57
2.3.3 Device Fabrication Process	
2.3.4 Mechanical Energy Harvesting Studies	62
3.4 Conclusion	64
3.3. References	
Chapter 4: A Ferroelectric Two-Dimensional Metal-Organic Coordination Polymer Showing Efficient Piezoelectric Energy Harvesting Properties	67-85
4.1 Introduction	68
4.2. Experimental Details	69
4.2.1 General Remarks	69
4.2.2 Syntheses	70
4.2.3 Ferroelectric and Dielectric Measurements	70
4.2.4 Crystallography	70
4.3 Results and Discussions	72
4.3.1 Synthesis, characterization and Crystal Structures	72
4.3.2 Piezoresponse Force Microscopy (PFM) Studies	77
4.3.3 Characterization of 2D MOF-Based Power Generator	79
4.4 Conclusion	83

Contents

4.5	References	83
Chapter 5: Flexible Piezoelectric Nanogenerators Based on One-Dimensional Neutral Coordination Network Composites		86-109
5.1	Introduction	87
5.2	Experimental Details	88
5.2.1	General Remarks	88
5.2.2	Syntheses	89
5.2.3	Crystallography	90
5.2.4	Ferroelectric, Dielectric and Piezoelectric Measurements	91
5.2.5	Second Harmonic Generation Study	91
5.2.6	Piezoresponse Force Microscopy Characterization	92
5.2.7	Computational Details	92
5.2.8	Preparation of the 1-TPU Composite Films and Testing of the Composite Devices	93
5.3	Results and Discussions	93
5.3.1	Synthesis, Characterization and Crystal Structures	93
5.3.2	SHG, Ferroelectric, Dielectric and Piezoelectric Studies	96
5.3.3	Fabrication and Characterization of the 1-TPU Composites	99
5.4	Conclusion	106
5.5	References	106
Chapter 6: Thesis Conclusion and Future Perspectives		110-112
Appendix		113-182

Synopsis

The thesis entitled "*Design and Synthesis of Ferroelectric Metal-Ligand Architectures and their Piezoelectric Energy Harvesting Studies*" focused on designing the intelligent pathways to obtain the non-centrosymmetric polar metal-organic cages and coordination polymers based on the amino phosphorous P(V) ligand motifs with a rigid and flexible backbone (N- or O-donor) (Figure 1), study their structure-function property, ferroelectric, piezoelectric, dielectric behaviour and utilize them for mechanical energy harvesting applications.

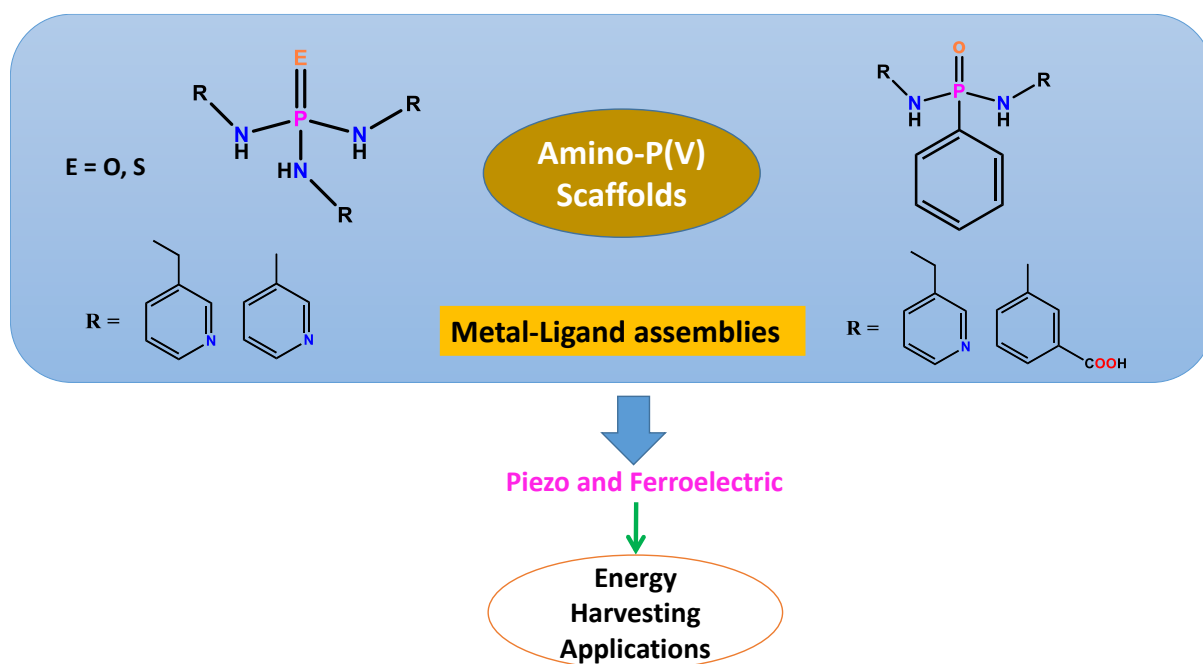


Figure 1: Outline of the Thesis.

Chapter 1: Introduction

Chapter 1 provides the basic idea relating to the materials' dielectric, piezoelectric, pyroelectric and ferroelectric properties. In particular, a thorough explanation of the ferroelectric characteristics, the polarisation mechanism, and the numerous uses of polar crystalline solids have been provided. Notably, a comprehensive survey on the various families of non-centrosymmetric polar metal-ligand architectures like perovskite systems, discrete supramolecular cages, one, two or three-dimensional coordination polymers and hybrid salts has been discussed in detail where supramolecular interaction with the polar solvent molecules, order-disorder arrangement of the backbone is responsible for the bistable polarization. The primary examples of the usage of piezoelectric and ferroelectric substances and their polymeric composite materials for mechanical energy harvesting applications are briefly illustrated in the later portion of this chapter. Also, it offers a summary of the current thesis.

Synopsis

Chapter 2: Ferroelectric Behavior of an Octahedral Metal-Ligand cage and its 2D-Connected Cage Framework

Supramolecular systems hold great potential as ferroelectric materials because they are easy to prepare and do not require toxic and environmentally damaging elements. However, directing the self-assembly process of a supramolecular array to yield polarizable solids is still challenging. Here, we describe induced ferroelectricity in a supramolecular framework of metal-organic cages that are supported by a flexible tripodal ligand (NHCH₂-(3-Py))₃PO (TPPA). Ferroelectric responses on the discrete cage [Cu₆(H₂O)₁₂(TPPA)₈](NO₃)₁₂·45H₂O (**1**) and its 2D-connected framework [{Cu₆Cl₄(H₂O)₆(TPPA)₈](NO₃)₈·60H₂O]_n (**2**) yielded well-resolved rectangular hysteresis loops at room temperature with remnant polarization values of 27.27 and 29.09 μC/cm², respectively. Thermal hysteresis measurements (THM) and capacitance-voltage (CV) plots further corroborate the ferroelectric behavior in these compounds. The polarization in them is due to the displacements of solvated molecules and nitrate ions in the pockets of these frameworks.

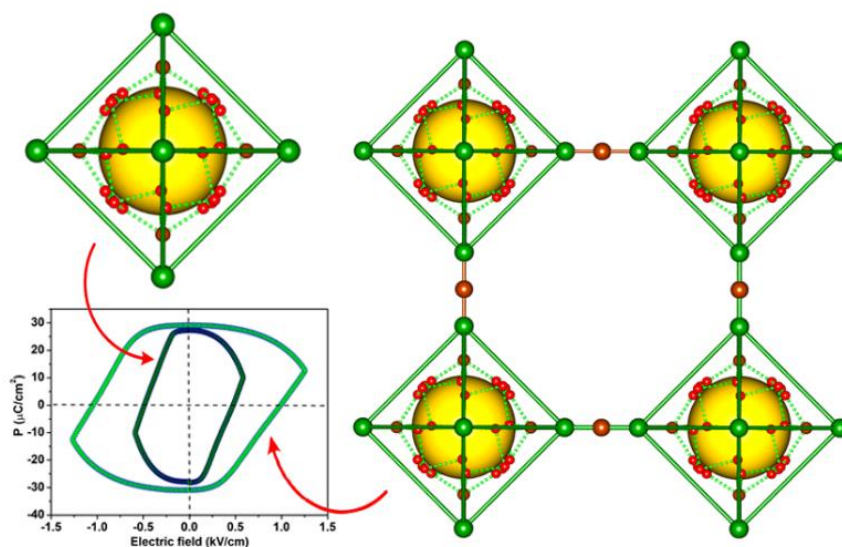


Figure 2: Discrete cage and its 2D connected cage framework templated by tripodal picolyl phosphoramidate ligand and their representative polarization vs. electric field (P-E) loop at room temperature

Chapter 3: Visualization of Domain Structure and Piezoelectric Energy Harvesting in a Ferroelectric Metal-Ligand Cage

The ferroelectric behaviour of an octahedral cage [[Ni₆(H₂O)₁₂(TPTA)₈](NO₃)₁₂·36H₂O] (**1**) exhibiting high remnant polarization of 25.31 μC/cm² is discovered. For the first time, clear

Synopsis

domain structures and the characteristic electromechanical responses are demonstrated using piezoresponsive force microscopy for a thin film of **1**. Owing to its mechanical energy conversion capability, polymer composites of **1** were employed as efficient piezoelectric nanogenerators.

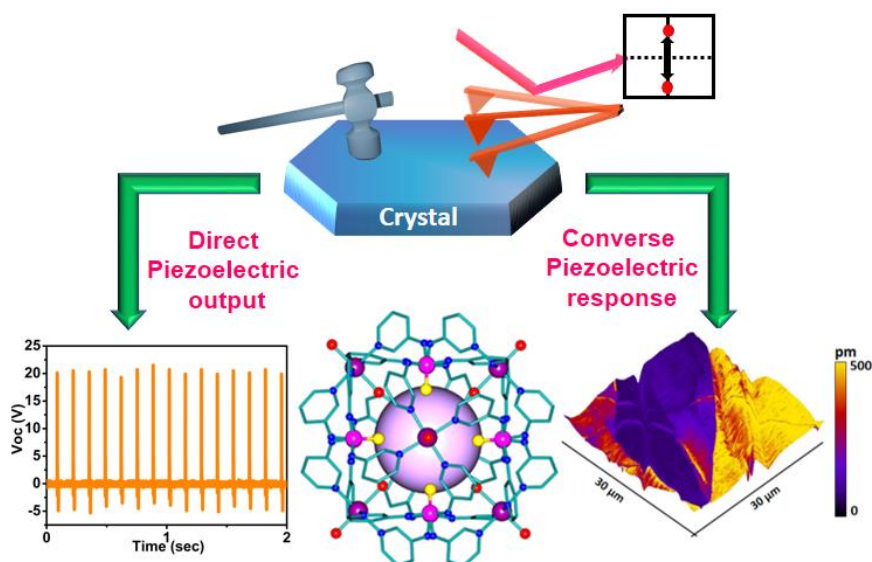


Figure 3: Single crystal X-ray structure of the discrete cage. The converse piezoelectric response obtained from the single-crystalline thin film of discrete cage from piezoresponsive force microscopy (PFM) measurements. The direct piezoelectric output obtained from the flexible composites made up of PDMS polymer of **1** from the home-built impact stimulator.

Chapter 4: Flexible Piezoelectric Nanogenerator of Two-Dimensional Metal-Organic Coordination Polymer that shows Efficient Electromechanical Coupling.

The non-centrosymmetric, polar two-dimensional coordination polymer (**1**) obtained from the flexible dipodal picolyl-based phosphoramidate ligand. The ferroelectric and piezoelectric behaviour was established by the piezoresponsive-force microscopy (PFM) experiments. The characteristic butterfly amplitude loop and rectangular phase hysteresis loop establish the firm ferroelectric and piezoelectric behaviour. The high longitudinal piezoelectric coefficient (d_{33}) value obtained was 82 pm/V which is unprecedented in the case of MOFs. Due to its inherent ferro- and piezoelectric properties, the flexible polymer composites of **1** in TPU were employed for mechanical energy harvesting studies. The high output value of 25.05 V and power density of 48.69 $\mu\text{W}/\text{cm}^2$ was obtained from the 10 wt% (**1**-TPU) champion device.

Synopsis

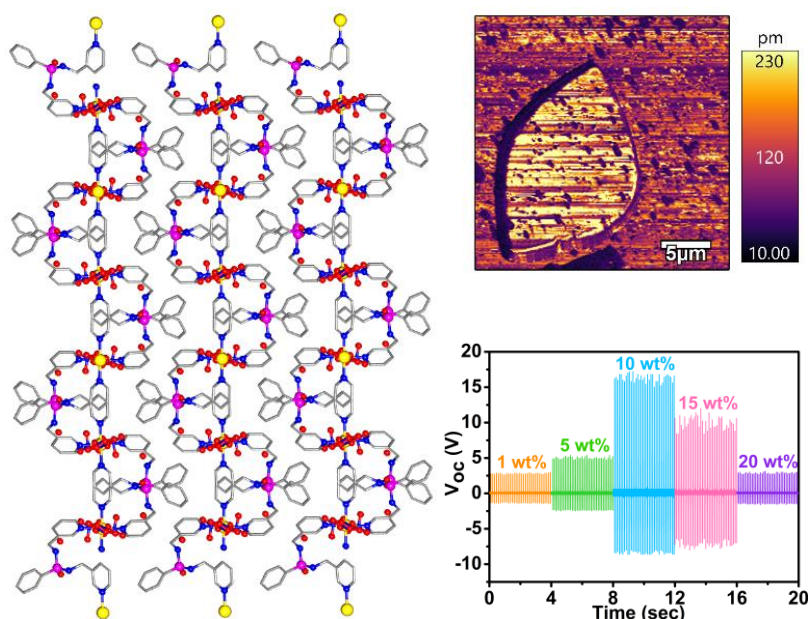


Figure 4: The polar two-dimensional coordination polymer; its direct and converse electromechanical performance.

Chapter 5: Flexible Piezoelectric Nanogenerators Based on One-Dimensional Neutral Coordination Network Composites.

Metal-organic coordination polymers are modular systems whose structures can be modified in numerous ways to introduce and influence non-linear optical and electrical properties. However, their full potential as piezoelectric nanogenerators for self-powered electronics is yet to be uncovered. Here, we report a Zn(II) based ferroelectric 1D-coordination network $\{[\text{Zn}(\text{L}^1)(\text{bpy})] \cdot (\text{H}_2\text{O})_{1.5}\}_\infty$ (**1**) derived from a flexible dicarboxylate ligand $[\text{PhPO}(\text{NH}(\text{C}_6\text{H}_4\text{COOH}))_2]$ (L^1H_2) and 2,2'-bipyridine as a co-ligand. The origin of polarization in **1**, despite its neutral structure, is due to the polyhedral distortions around the Zn(II) center as revealed by ab-initio calculations. The presence of polarizable domains was visualized by piezoresponse force microscopy (PFM) experiments. Also, from the PFM studies a sizable converse piezoelectric coefficient (d_{33}) value of 19.4 pm/V was noticed for **1**, which is unprecedentedly high for the class of neutral-network coordination polymers. Furthermore, flexible composite devices comprising thermoplastic polyurethane (TPU) polymer with different weight percentage (wt%) of **1** were prepared and examined for application as piezoelectric nanogenerators. Notably, the champion device of this series (poled 5 wt% **1**-TPU composite) exhibits a highest open-circuit voltage of 5.6 V and power density output of 14.6 $\mu\text{W}/\text{cm}^2$.

Synopsis

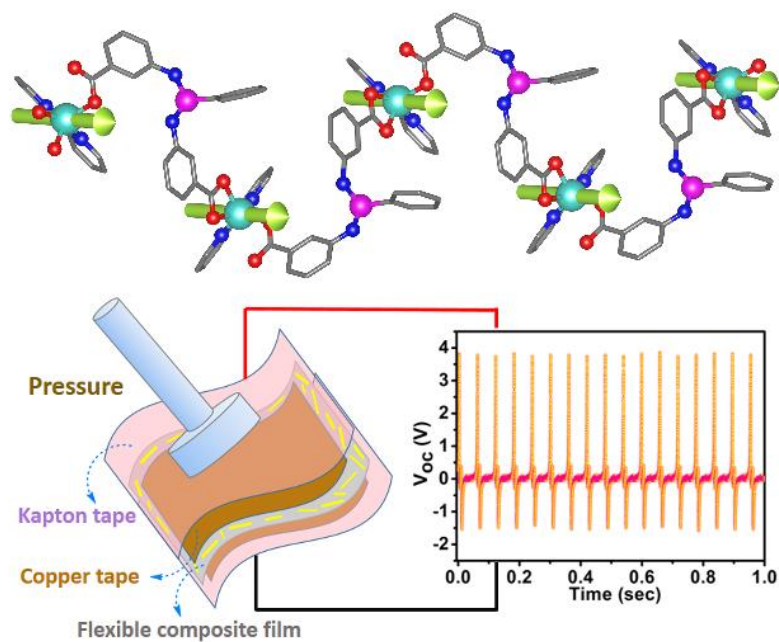


Figure 5: A one-dimensional neutral coordination polymer obtained from the dipodal carboxyl functionalised phosphoramidate ligand in which dipole moment is induced due to the distortion around the metal-centre and their polymer composite materials for mechanical energy harvesting studies.

Abbreviations

Anal.	Analysis
BTO	Barium Titanate
PZT	Lead Zirconate Titanate
TGS	Triglycine sulphate
PVDF	Polyvinylidene difluoride
RAM	Random Access Memory
Calcd.	Calculated
CCDC	Cambridge Crystallographic Data Centre
DFT	Density Functional Theory
DMF	N,N-Dimethyl Formamide
DMSO	Dimethyl sulphoxide
DSC	Differential Scanning Calorimetry
E_c	Coercive field
d_{33}	Longitudinal Piezoelectric coefficient
FET	Field-effect transistor
FT-IR	Fourier Transform Infrared Spectroscopy
MALDI-TOF	Matrix-Assisted Laser Desorption/Ionization – Time of Flight
KDP	Potassium dihydrogen phosphate
Hz	Hertz
MeOH	Methanol
MeCN	Acetonitrile
KBr	Potassium Bromide
mg	milligram
min	minutes
ml	milliliter
mmol	millimoles
MOF	Metal-Organic Framework
M.P.	Melting point
NMR	Nuclear Magnetic Resonance
RT	Room Temperature
Ph	Phenyl
P_s	Saturation Polarization
P_r	Remnant Polarization
PXRD	Powder X-ray Diffraction
VT-PXRD	Variable-temperature Powder X-ray Diffraction
SCXRD	Single-Crystal X-Ray Diffraction
NLO	Non-Linear Optical Property
T_c	Curie Temperature
TGA	Thermogravimetric Analysis
SEM	Scanning Electron Microscopy
PFM	Piezoresponse Force Microscopy
PFS	Piezoresponse Force Spectroscopy
PDMS	Polydimethyl Siloxane
TPU	Thermoplastic Polyurethane
TPPA	Tris(N-(3-picolyl))phosphoramidate
TPTA	Tris(3-aminopyridyl)thiophosphoramidate

Rights and Permissions

Chapter 2

Reprinted (adapted) with permission from “*Chem. Asian J.*, 2020, **15**, 3275-3280”.

Copyright © 2020, John Wiley and Sons.

Chapter 3

Reprinted (adapted) with permission from “*ACS Sustainable Chem. Eng.*, 2022, **10**, 9911-9920”.

Copyright © 2023, American Chemical Society.

Chapter 5

Reprinted (adapted) with permission from “*Chem. Commun.*, 2023, DOI: 10.1039/D3CC00098B”.

Copyright © 2023, Royal Society of Chemistry.

Publications

Contributions included in the thesis:

1. Ferroelectric Behavior of an Octahedral Metal-Ligand Cage and Its 2D-Connected Cage Framework
[Neetu Prajesh](#), Ashok Yadav, Rani Gourkhede, Balu Praveenkumar*, Alexander Steiner* and Ramamoorthy Boomishankar*
Chem. Asian J. **2020**, 15 (20), 3275-3280
2. Flexible Piezoelectric Nanogenerators Based on One-Dimensional Neutral Coordination Network Composites
[Neetu Prajesh](#), Vijay Bhan Sharma, Shatruhan Singh Rajput, Chandan Kumar Singh, Prashant Dixit, Balu Praveenkumar*, Jan K. Zareba*, Dinesh Kabra*, Satishchandra Ogale* and Ramamoorthy Boomishankar*
ACS Sustainable Chem. Eng. **2022**, 10, 9911-9920
3. Visualization of Domain Structure and Piezoelectric Energy Harvesting in a Ferroelectric Metal-Ligand Cage
[Neetu Prajesh](#), Dipti R. Naphade, Ashok Yadav, Vikash Kushwaha, Balu Praveenkumar*, Jan K. Zareba*, Thomas D. Anthopoulos* and Ramamoorthy Boomishankar*
Chem. Commun. **2023**, 59, 2919-2922
4. Flexible Piezoelectric Nanogenerator of Two-dimensional Metal-Organic Coordination Polymer showing Efficient Electromechanical Coupling
[Neetu Prajesh](#), Vikash Kushwaha, Vijay Bhan Sharma, Balu Praveenkumar*, Jan K. Zareba*, Dinesh Kabra* and Ramamoorthy Boomishankar*
(Manuscript under preparation)

Contributions not included in the thesis:

1. Chiral tetranuclear copper (ii) complexes: synthesis, optical and magnetic properties
Naushad Ahmed, Shalini Tripathi, Arup Sarkar, Kamal Uddin Ansari, Chinmoy Das, [Neetu Prajesh](#), Satoshi Horike, Ramamoorthy Boomishankar* and Maheswaran Shanmugam*
New J. Chem. **2020**, 44, 16845-16855
2. Growth of highly conducting MoS_{2-x}N_x thin films with enhanced 1T' phase by pulsed laser deposition and exploration of their nanogenerator application
Swati Parmar, [Neetu Prajesh](#), Minal Wable, Ram Janay Choudhary, Suresh Gosavi, Ramamoorthy Boomishankar* and Satishchandra Ogale*
iScience **2022**, 25, 103898
3. Synthesis and ferroelectric behaviour of an axially symmetric octahedral [Cu₆L₈]¹²⁺ cage
Rani Gourkhede†, [Neetu Prajesh](#)†, Rishabh Gupta and Ramamoorthy Boomishankar* († equal contribution)

Publications

J. Chem. Sci. **2022**, 134, 115

4. Photochemical Hydrogen Evolution from Water by a Tripodal Phosphoramidate Ligand Based Ni₆L₈ Discrete Octahedral Cage

[Neetu Prajesh](#), Vishwanath S. Mane, Avinash S. Kumbhar* and Ramamoorthy Boomishankar*

(Manuscript under preparation)

Chapter 1

Introduction

1.1 Introduction to Ferroelectric and Piezoelectric Metal-Ligand Architectures

Self-assembly is a powerful technique in the design of molecular and functional materials.¹ Metal-ligand self-assemblies have gained tremendous interest due to their easy synthesis, diverse structures, and their interesting physical and chemical properties.^{2,3} Formation of self-assembled metal-ligand motifs is achieved via the interaction of well-designed rigid and flexible organic linkers containing directional bonding sites (ligands) with an inorganic core (metal or metal-cluster centers). Moreover, these supramolecular ensembles take advantage of weak interactions (like covalent, hydrogen bonding, pi-pi interactions, etc.), resulting in the formation of discrete crystalline architectures like cages, 1D-chains (linear, helix), 2D coordination sheets/grids or 3D frameworks.^{4, 5} Due to their versatile architectures and functionalities, metal-ligand self-assemblies found applications in various domains such as catalysis,^{6, 7} storage and separation,⁸ host-guest chemistry,⁹⁻¹¹ and electrical/optical/magnetic devices.¹²⁻¹⁴ Over the years, materials exhibiting ferroelectricity, magnetism, magnetoelectricity, and piezoelectricity are of keen interest due to their utility in molecular electronics, non-linear optical devices, photovoltaics, and energy-harvesting applications.¹⁵⁻¹⁸ In recent times, ferroelectrics are getting prime importance because it is a subset of the piezoelectric and pyroelectric materials which can be utilised in technological applications.¹⁹⁻²⁵ Ferroelectric materials are an important class among all dielectrics, in which spontaneous polarisation can be reversed by the application of an external electric field.

The first ferroelectric compound is the hydrogen-bonded system, which is known as Rochelle salt (sodium potassium tartrate tetrahydrate; $\text{NaKC}_4\text{H}_4\text{O}_6 \cdot 4\text{H}_2\text{O}$). After that, various families like inorganic ceramic oxides, and organic, organic-inorganic hybrid materials were explored for their ferroelectric properties and further utilised in piezoelectric mechanical energy harvesting applications.^{12, 26, 27} The commercial market is dominated by inorganic ceramics, but they are intrinsically limited due to their requirement of high-temperature synthesis, longer processing time, tedious fabrication and poling procedures, toxic and heavy metal content, all of which complicate their use in wearable electronics.²⁸⁻³⁰ Although organic ferroelectrics like PVDF (polyvinyl difluoride) and its co-polymers provide flexibility and easy solution processability, it suffers from poor crystallinity, requirement of high-voltage poling to enhance electroactive β -phase and high-temperature annealing and poling. These short-comings triggered the research towards alternative materials with robust polarization and high device performance characteristics. In this context, the organic-inorganic hybrid materials with high

piezo-and ferroelectric properties are highly desirable for their potential to bridge the gap between organic and inorganic ferroelectrics.³¹⁻³³

This thesis describes the design, synthesis and characterisation of new metal-organic ferroelectric materials derived from dipodal and tripodal amino-P(V) phosphoramidate scaffolds. Subsequent discussion in this chapter provides an introduction to dielectrics and their subclasses piezoelectrics, pyroelectrics, and ferroelectrics, along with a brief discussion about the concepts and mechanisms behind them. It provides a key literature on new examples of metal-ligand hybrid materials showing ferroelectric materials and their further utilisation for piezoelectric energy harvesting applications.

1.2 Dielectric Materials

Dielectric materials are electrical insulators that are perturbed by the applied electric field. When a voltage is applied across the dielectric surface, the electric charges don't flow through the material, which means it does not conduct electricity as in the case of conductors. Instead, the randomly arranged bound electric charges slightly get shifted from their equilibrium positions and aligned in the opposite direction of an applied electric field. This induces electric dipoles in the material, which at once leads to the generation of dielectric polarization.³⁴

Polarisation includes the alignment of the existing dipoles or induced dipoles in the direction of the electric field. There are fundamentally four mechanisms of polarisation that controls the behaviour of an insulator material under the electric field as described below (Figure 1.1).^{34, 35}

- 1. Electronic Polarisation:** This polarisation is exhibited by all the materials, as evident by its name. It relates to the shifting of the electron cloud in an atom concerning the nucleus due to the external electric field. This creates a dipole moment within the atom. However, due to its small displacement, it leads to the induction of a small magnitude of electronic polarisation as compared to other mechanisms.^{34, 35}
- 2. Dipolar (or Orientational) Polarisation:** This type of polarisation is observed in materials having permanent dipole moments. Due to thermal motions, all the dipoles are randomly aligned or oriented in the material, and the net dipole moment tends to be zero. However, when exposed to the external electric field, the dipoles of the material start drifting or orienting towards the electric field and create a net electric polarization.^{34, 35}

3. **Ionic Polarisation:** As its name suggests, this type of polarisation occurs in ionic compounds like NaCl. In these compounds, ions are symmetrically arranged in such a manner that they nullify the overall dipole moment. In the presence of an electric field, the ions tend to displace from their positions which tends to create an overall dipole moment.^{34, 35}
4. **Space Charge (Interfacial) Polarisation:** This polarisation happens at the interfaces means the junction of the two dielectrics or the junction of the dielectric and electrode. When an electric field is applied, the free charge carriers at the grain boundaries tend to migrate to an appreciable distance through the dielectric, which becomes trapped and can't be discharged at the electrode.^{34, 35}

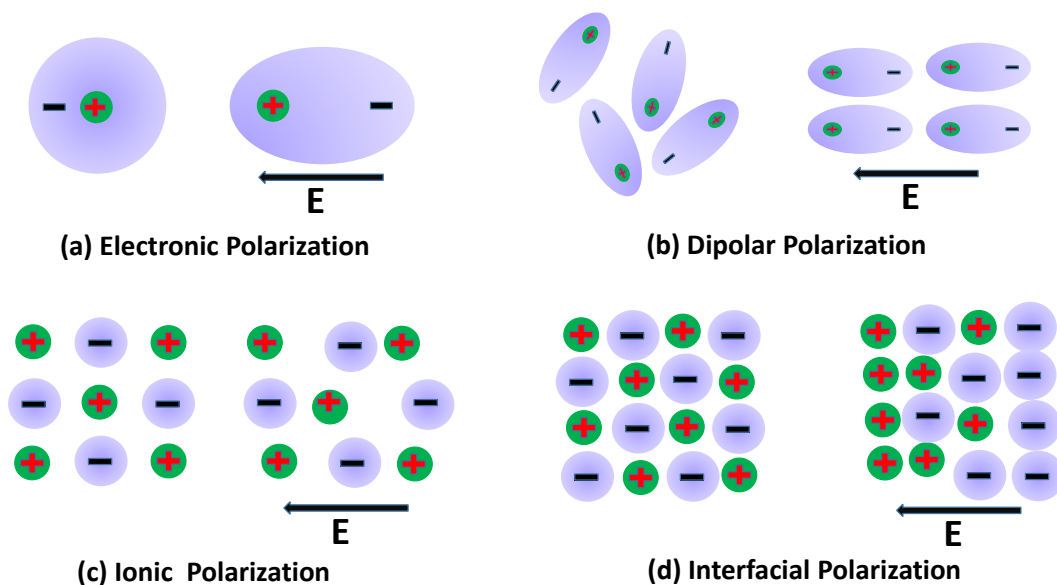


Figure 1.1 Schematic of various types of polarisation mechanisms in dielectrics.

All dielectric materials exhibit electronic polarisation. However, in most the cases more than one polarisation is present. For total polarisation, we can consider all other polarisation except interfacial polarisation because of the lack of a method for computing the charges present in interfacial polarisation.

$$\text{Total Polarization, } P = P_{\text{electronic}} + P_{\text{ionic}} + P_{\text{orientation}} \quad \dots\dots \text{Eq. 1.1}$$

These polarisations respond as a function of frequency as well as temperature as ions/atoms/molecules require time to move or orient, which turns out to be mass-dependent entities. The heavier entities take more time to displace than the lighter ones, a similar trend is witnessed for the polarisation mechanisms as going from electronic to ionic to dipolar. The

slowest polarisation mechanism, which occur under 10 Hz, is interfacial polarisation. The dipolar mechanism is faster than the interfacial and generally persists between $10^1 - 10^9$ Hz. The range of the ionic polarisation mechanism is even higher in between $10^9 - 10^{13}$ Hz. The electronic polarisation persists at higher frequencies ($10^9 - 10^{13}$ Hz) means it occurs very swiftly.

These polarisation mechanisms are also affected by the temperature. An increase in temperature contributes to increasing in the mobility of ions and charge carriers, which in turn increases the extent of polarisation in the case of ionic polarisation. The electronic polarisation comparably unresponsive to temperature, whereas a rise in temperature for dipolar polarisation leads to thermal agitation, which decreases or opposes the dipolar polarisation mechanism.

1.2.1 Relative Permittivity (ϵ')

The relative permittivity is a quantity that measures the capacity of a material to undergo polarisation on the application of an external electric field. It is referred to as dielectric permittivity (ϵ_r), which can also be defined as the ratio of the charge stored in an insulating material between two parallel metallic plates to the charge that can be stored when the vacuum is present in between the plates. Hence, it is also called as relative permittivity because it is measured relative to the free space (ϵ_0). Its formula is the ratio of the material's absolute permittivity (ϵ) to the permittivity of the vacuum. It is a unitless quantity.^{34, 36}

$$\epsilon_r = \epsilon / \epsilon_0 \quad \dots\dots \text{Eq. 1.2}$$

The relative permittivity can also be calculated as the ratio of the capacitance induced by the insulator (C_m) kept between two metallic plates to the capacitance of air between the same metallic plates (C_0).^{34, 36}

$$\epsilon_r = C_m / C_0 \quad \dots\dots \text{Eq. 1.3}$$

1.2.2 Dielectric Loss

Dielectric loss refers to the loss of electromagnetic energy in the form of heat while a dielectric material subjected to an external electric field. Dielectric loss is represented as loss tangent ($\tan \delta$) and it is a dimensionless quantity. The higher value of $\tan \delta$ corresponds to the high dielectric loss.

$$\tan \delta = \epsilon_r'' / \epsilon_r' \quad \dots\dots \text{Eq. 1.4}$$

Here, ϵ_r'' represents the loss factor while $\tan \delta$ represents the loss tangent.

The Dielectric loss majorly stems from conduction loss, electronic polarisation, atomic polarisation, ionic polarisation. Moreover, the dielectric losses are particularly high around the relaxation processes or at resonance frequencies of various polarisation mechanisms. It mainly depends upon the frequency and the nature of the dielectric material.^{34, 36}

1.2.3 Dielectric Strength

Dielectric strength is defined as the maximum potential that dielectric material can tolerate without electrical breakdown and become electrically conductive, and it is expressed as Volts per unit thickness. This value of dielectric strength puts a restriction on the electric field to be applied, which has to be less than the value of dielectric strength. The higher value of dielectric strength indicates the more insulating character of the material.^{34, 36}

1.2.4 Applications of Dielectric Materials

The dielectric materials with high permittivity are utilised in capacitors to store charge and enhance the performance of the semiconductor device, while low permittivity dielectric materials are used in microelectronic circuits. The good dielectric material is the one with high relative permittivity, low dielectric loss and high dielectric strength. Despite this, the materials exhibiting high dielectric loss found applications in heating thermosetting glues, drying fibrous materials, etc.^{34, 36}

1.3 Classification of Dielectric Materials

There are two types of dielectric materials, (a) linear (b) non-linear dielectrics.

Linear dielectrics – In the presence of an electric field, the dielectric materials tend to polarise and the relative permittivity increase linearly with the electric field. When an electric field is reduced to zero, the dielectric permittivity retraces its path and becomes zero (attains non-polarised state). Such materials are referred to as linear dielectrics.

Non-Linear dielectrics – These are the special class of dielectrics that possess large relative permittivity and show a non-linear relationship with an electric field. The extent of polarisation tends to increase with the electric field but does not retrace its path when the electric field becomes zero. This means non-zero polarisation or non-zero relative permittivity in the absence of an electric field. These special dielectrics display suitable physical phenomena such as

polarisation due to mechanical stress (piezoelectricity), temperature gradient (pyroelectricity), and reversal of polarisation under a sweeping electric field (ferroelectricity).

A critical and essential requirement for non-linear dielectric materials to exhibit these properties (piezo-, pyro-, or ferroelectricity) is crystallinity. Neumann gave the relationship between symmetry elements and physical properties of non-linear dielectric materials. There are 32 crystallographic point groups, out of which 11 of them belong to the centrosymmetric classes, which do not show any of these properties due to the presence of a center of inversion. Of the remaining 21 (except 432), 20 classes have no center of inversion, therefore, exhibits piezoelectricity in which mechanical stress induces polarisation. Out of these 20, the 10-point groups hold a unique polar axis and hence are called polar point groups. These point groups exhibit pyroelectricity (thermal energy change induces polarisation) as well as ferroelectricity (polarisation can be reversed by the application of an external electric field). The crystallographic classification and the relationship of these materials are schematically illustrated in Figure 1.2. As noted, ferroelectric materials are a subset of pyroelectric, which is a further subset of piezoelectric materials. So, all ferroelectric materials can show pyro- and piezoelectricity, but the reverse is not true.

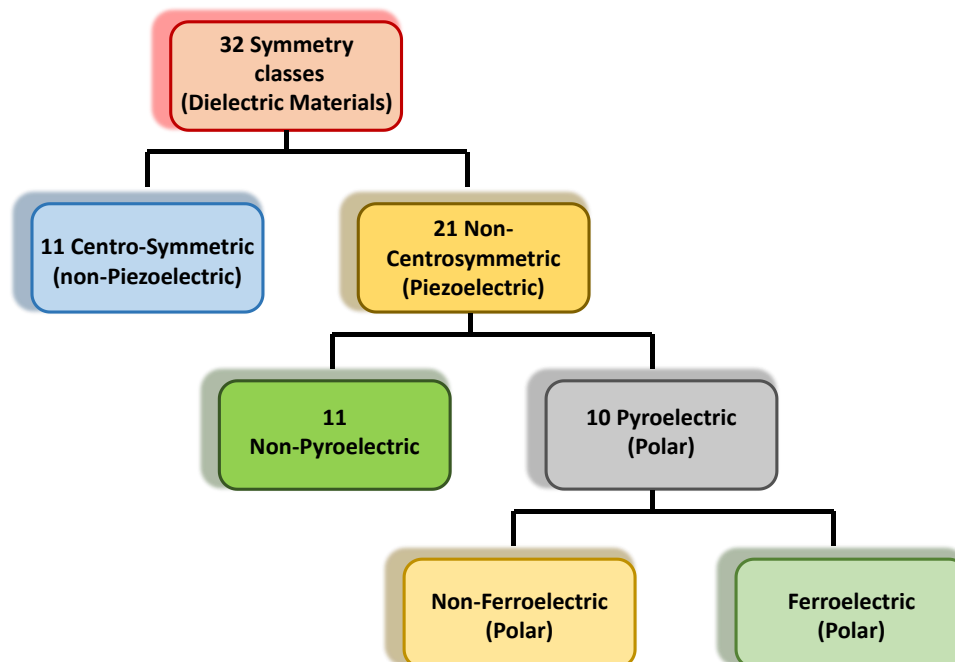


Figure 1.2 Classification of Dielectric materials.

1.4 Piezoelectricity

Piezoelectricity is defined as the charges that accumulate on the surface across the material when subjected to mechanical stress. This property is adopted by those materials which are crystalline in nature and lack inversion symmetry. When an asymmetric crystal is subjected to external stress, the voltage across the material is developed. It is called the Piezoelectric effect. It is discovered by the French brothers Jacques Curie and Pierre Curie in the year 1880. The word Piezoelectric is derived from the Greek word ‘Piezein’, which means to squeeze or press. One of the unique features of the piezoelectric material is the inverse piezoelectric effect which is the opposite of the direct effect. When a voltage is applied across the material, the material tends to vibrate or deform (Figure 1.3). Piezoelectric materials quantified by the piezoelectric coefficient or piezoelectric modulus, d , is the polarization generated per unit of mechanical stress. There are various piezoelectric coefficients such as d_{31} , d_{32} , and d_{33} .^{37, 38} The each subscript holds a different meaning. The first subscript stands for the applied electric field, and the second subscript denotes the direction of the mechanical effect. The magnitude of the direct piezoelectric effect, d_{33} , is expressed in the unit pC/N while for converse piezoelectric effect is represented in pm/V.

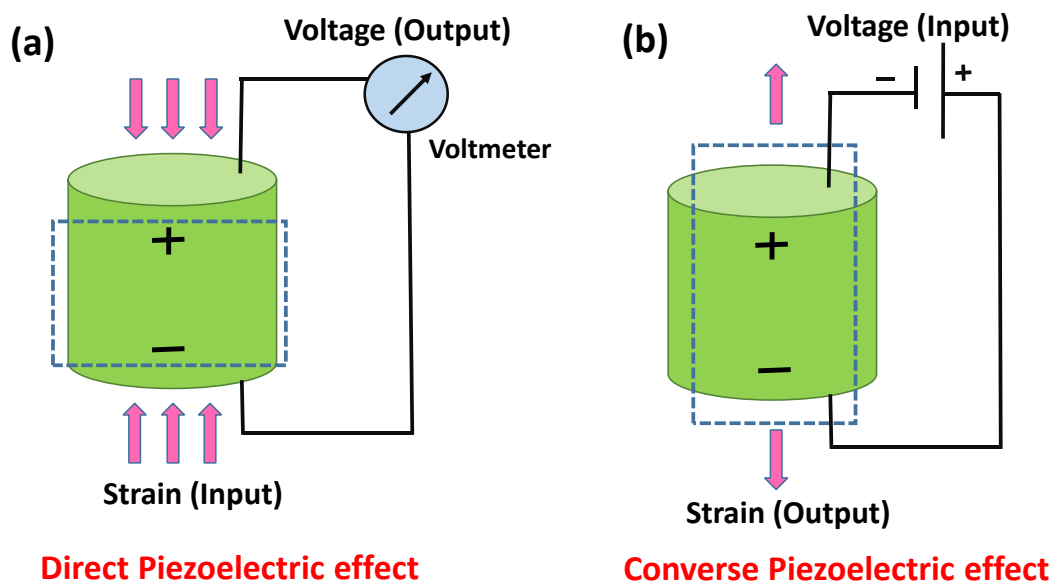


Figure 1.3 (a) Direct (b) Converse Piezoelectric effect

The Piezo-meter based on the Berlin-court method is generally employed to extract the direct piezoelectric coefficient, whilst the converse piezoelectric effect is measured by strain measurements and other surface probe methods such as PFM (Piezo-response force

microscopy). Piezoelectric materials are widely used for sensing, microphones, energy harvesting and as actuators and motors.^{38, 39}

1.5 Pyroelectricity

It is the ability to generate an electric potential across the material when it is heated or cooled. This special class of dielectrics belongs to those materials which adopt one of the ten polar point groups (i.e. spontaneously polarised). The spatial position of the atoms modifies slightly within the crystal lattice in response to the change in temperature. The pyroelectric effect found many applications in various fields, such as thermal and gas sensing devices, infrared sensors and detectors, and for pyroelectric power generation.³⁴

1.6 Ferroelectricity

Ferroelectrics are a special class of pyroelectrics in which the direction of spontaneous polarisation can be reversed or reoriented by the application of an external electric field. To be ferroelectric, a crystal requires the adoption of the space groups that are polar in nature. Thus, the ten polar point groups are C_1 , C_s , C_2 , C_{2v} , C_3 , C_{3v} , C_4 , C_{4v} , C_6 and C_{6v} .

Ferroelectric materials are characterised by the unique rectangular hysteresis loop (P-E), which reflects the dynamics of electric domains when an external electric field is applied (Figure 1.4). The hysteresis loop can be understood as follows. When one starts to apply an electric field, the domains start orientating in a particular direction and become saturated at point C, and this polarisation is known as saturation polarisation (P_s). When the field strength is reversed to zero, the polarisation does not follow the same path; rather, some domains remain aligned in a positive direction which leads to remnant polarisation (P_r). To nullify this remnant polarisation, some extra field in the negative direction is required, which is called a coercive field (E_c). Further, increment in the electric field in the negative direction, the polarisation completely reverses its direction, which is commonly referred to as switching and this way, it completes a rectangular loop.^{34, 40}

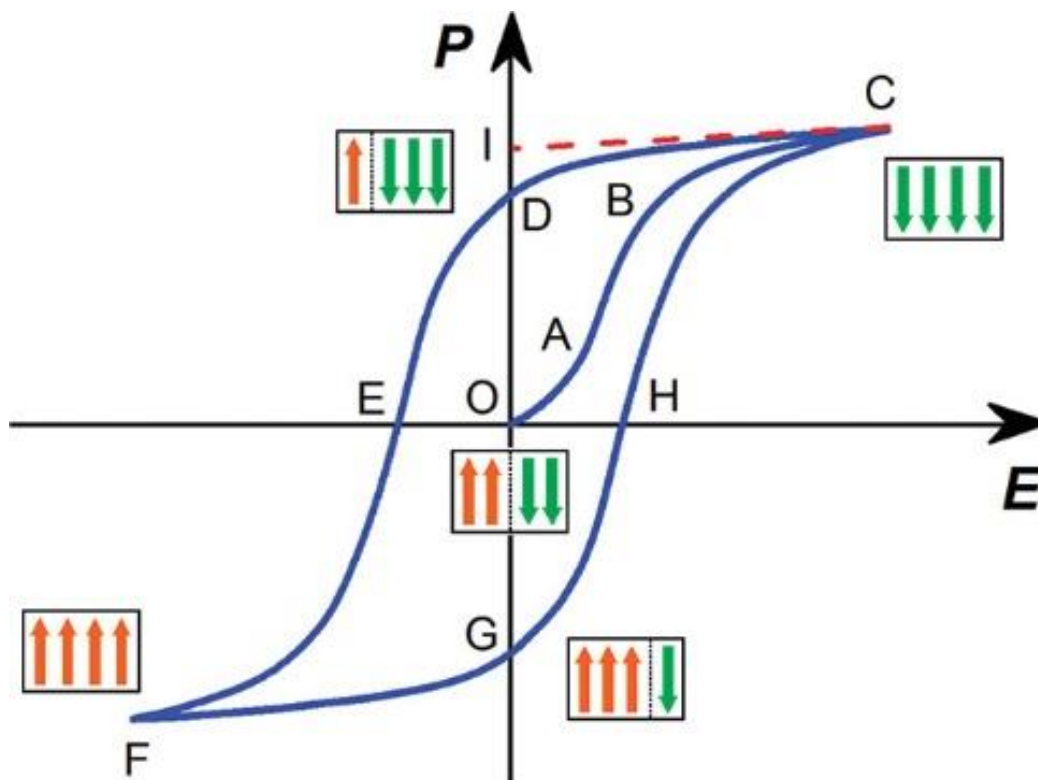


Figure 1.4 Typical Polarisation (P) vs Electric field (E) hysteresis loop. Adapted with permission from ref. 40. Copyright © 2012, American Chemical Society

Ferroelectricity does not happen at all temperatures. There is a transition happening from a high temperature, high symmetric paraelectric phase to a low temperature, low symmetric ferroelectric phase and this happens at a particular temperature which is called Curie temperature (T_c). There are two conventional mechanisms of phase change, including (1) displacive type and (2) order-disorder type (Figure 1.5). Many inorganic ceramics show a displacive type mechanism in which relative displacement of ions induces spontaneous polarisation, while an order-disorder type mechanism involves a reorientation of dipolar groups. For example, the NO_2^- ions of NaNO_2 re-aligns from the disordered positions to the ordered position inducing ferroelectricity.

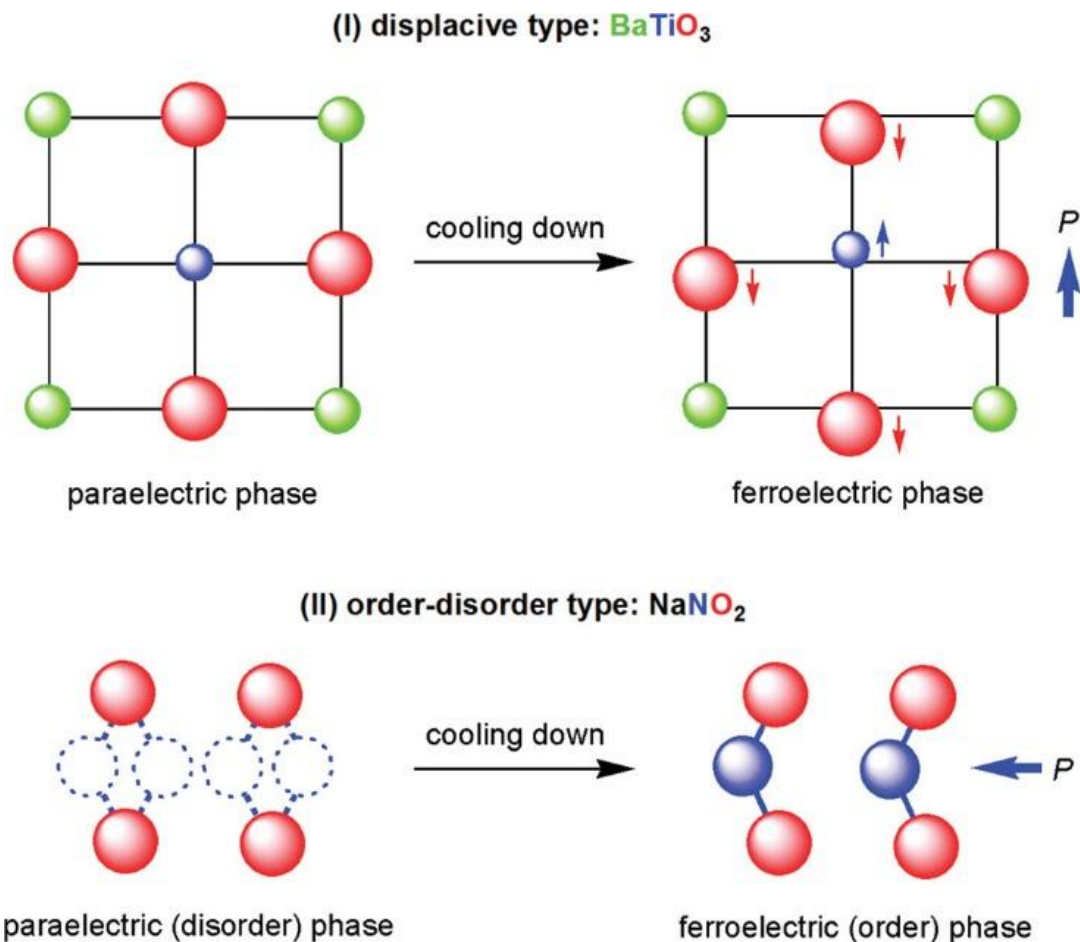


Figure 1.5 Mechanisms behind paraelectric to the ferroelectric phase transition. Adapted with permission from ref. 40. Copyright © 2012, American Chemical Society

The P-E hysteresis loop is an indispensable proof for the characterization of a ferroelectric material. Recently, microscopic techniques such as Piezoresponse force microscopy is employed to visualize the polarization domains and the amplitude and phase response of the polar domains. Ferroelectric phase transitions can be characterised by employing various techniques such as temperature-dependent single-crystal X-ray diffraction or powder X-ray diffraction, temperature-dependent Second-Harmonic Generation (SHG), Differential Scanning Calorimetry (DSC) techniques, etc.⁴⁰

1.7 History of Ferroelectric Materials and Their Classification

Ferroelectricity was discovered by Valasek in the year 1920, who gave its name as an analogy of ferromagnetism.²⁶ After fifteen years, the first example of hydrogen-bonded ferroelectric KH_2PO_4 (KDP) was discovered by Busch and Scherrer.⁴¹ In the early 1940s, the first non-

hydrogen bonded ferroelectric system barium titanate (BaTiO_3 , BTO) was discovered. Following that, many other oxide compounds such as lead zirconate titanate ($\text{Pb}(\text{ZrTi})\text{O}_3$; PZT), KNbO_3 , and LiNbO_3 , etc., were discovered, and they accelerated the research towards the application of ferroelectrics in various devices.⁴² Owing to the widespread possibility of chemical compositions and crystal structures, researchers have explored ferroelectricity in several compound classes ranging from ceramic oxides, polymers, liquid crystals to organic-inorganic hybrids.⁴³

The most commercially predominant ferroelectric materials are ceramics or inorganic oxides owing to their large polarisation values, fatigue-free, large relative permittivity values, higher T_c values, etc. However, they are intrinsically limited due to the high-temperature synthesis, rigidity, environmentally hazardous toxic and heavy metals, high voltage poling, etc., which prompted the search for alternative materials. The polymers like PVDF and its co-polymers are being commercially utilised for many applications like piezoelectrics, pyroelectrics, and ferroelectrics.⁴⁴ But its low crystallinity and large coercive field required for the reorientation of dipoles limits their use.^{27, 45} In this regard, the discovery of ferroelectricity in small molecules and self-assembled supramolecules (such as non-centrosymmetric crystals of molecular/polymeric organic or organic-inorganic hybrids) have shown enormous potential as an alternate choice of materials.^{27, 40}

Among all of them, metal-ligand coordination complexes have been the focus of interest as organic-inorganic hybrid ferroelectric materials due to their structural tunability, compositional variability, environment-friendliness due to the presence of 3d-metal ions, ease of synthesis, low cost, and noteworthy ferroelectric properties. Also, the covalent and non-covalent interactions facilitate the arrangement of the polar atoms into ordered assemblies. The non-covalent interactions create asymmetry in the electron density of the interacting molecules and hence assist in generating the desired polar dipoles. Thus, the introduction of secondary forces, such as hydrogen bonds, charge transfer, and molecular rotation, in lattice structures could assist in generating ferroelectric assemblies.

1.8 Ferroelectricity in Metal-Ligand Coordination Complexes

The metal-organic ferroelectric serves as a hybrid class of materials that bridges the gap between inorganic and organic ferroelectric materials. There are several advantages of metal-organic materials, such as structural tunability, compositional variability, and flexibility due to the presence of both inorganic and organic counterparts (metal ions, linkers/ligands, solvent, counteranions). As a result, a vast array of metal-organic compounds that can display

ferroelectricity are feasible, including coordination complexes, host-guest assemblies, ionic metal-organic salts, etc. The first ferroelectric material is a metal-organic salt (Rochelle salt) containing tartrate as anions and K^+ and Na^+ ions as cations.²⁶ Subsequently, researchers explored ferroelectricity in Rochelle salt analogues with other cations such as NH_4^+ , Li^+ , and Tl^+ in place of K^+ and Na^+ ions.

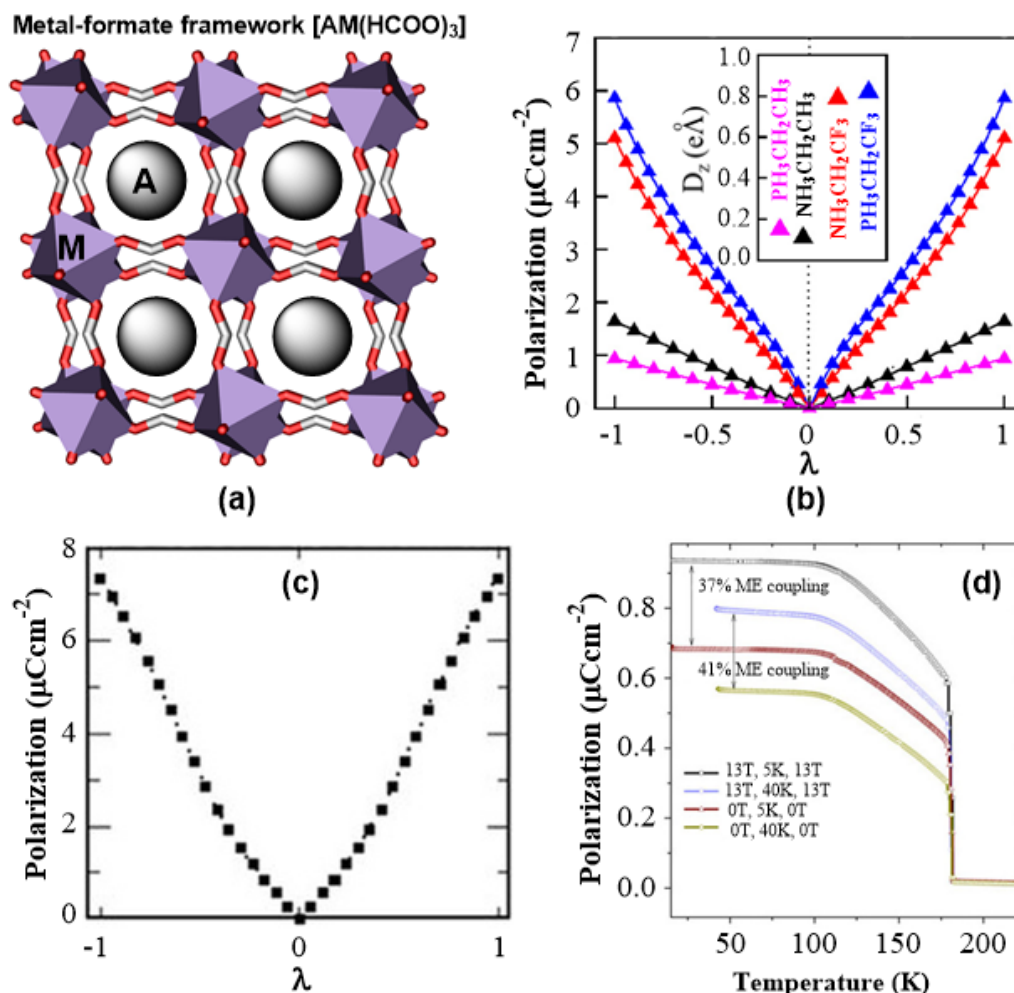


Figure 1.6 (a) A general representation of the crystal structures for the metal-formate framework and their organic guest cations (A). (b) Variation in the ferroelectric polarisation as a function of polar distortions ($\lambda=0$ corresponds to centric and $\lambda=\pm 1$ corresponds to polar configurations) for the Mn-formate frameworks with different organic cations. (c) Variation in polarisation as a function of polar distortions and (d) magneto-electric (ME) coupling observed for the $[(CH_3)_2NH_2]Mn(HCOO)_3$ framework. Adapted with permission from ref. 49. Copyright © 2013, American Chemical Society

Following this, various families of compounds such as metal-organic sulfates, metal-amino acid systems, organo-halogenometallates, metal-formates, and metal-carboxylates have been studied for their potential ferroelectric properties.⁴⁰ These metal-organic assemblies are often similar in structure to ferroelectric ceramics. For example, metal formates exhibit the ABX_3 perovskite type three-dimensional lattice composed of infinite metal-formate chains, which serve as X-sites, divalent transition metal-ions as B-sites, and organoammonium ions as interstitial guests, which serve as A-sites.^{40, 46-48} Similar to ceramic materials, the polarisation in metal-organic systems originates from the order-disorder or displacive type mechanism, which resulted from the host-guest interactions in the form of hydrogen bonding, π - π interactions, and dipolar interactions. Stroppa and co-workers suggested by theoretical calculations that engineering the A-site cations alter the ferroelectric polarisation in Mn-based perovskites (Figure 1.6a). The enhancement of ferroelectric polarisation by replacement of $[NR_4]^+$ units with cationic phosphorus moieties such as alkyl/aryl phosphonium cations ($[(PR'_xR_{4-x})^+]$) is predicted. The Mn-formate framework with a hypothetical A = $[PH_3(CH_2CF_3)]^+$ motif possesses the highest value of polarisation of $\sim 6 \mu\text{Ccm}^{-2}$ (Figure 1.6b).⁴⁹ Interestingly, the coexistence of ferromagnetism and ferroelectricity (multiferroicity) was observed in the Mn-formate framework having dimethylammonium (DMA) cation, $[(CH_3)_2NH_2]Mn(HCOO)_3$, which reveals the magnetic ordering and ferroelectricity at 4 and 180 K, respectively.⁵⁰ This multiferroic MOF shows order-disorder type structural phase transition at 180 K where the highest observed polarisation (of $\sim 1 \mu\text{Ccm}^{-2}$) is quite different from theoretically predicted polarisation values of $7.3 \mu\text{Ccm}^{-2}$ (Figure 1.6c). This discrepancy was explained by using the SHG imaging technique, which shows a possible inhomogeneity in the orientation of its ferroelectric domains. Further enhancement of polarisation and ordering in it was observed at 4 K by the application of external magnetic fields (Figure 1.6d).

Apart from these, several metal-organic frameworks (MOFs) have also been studied for their ferroelectric behaviour.⁵¹ Using (a) three-fold symmetric building blocks, (b) chiral linkers, (c) linkers with non-coordinating polar head groups, and (d) polar guests that interact with the host MOF through supramolecular interactions, the non-centrosymmetric arrangement can be accomplished in MOFs. Mak and co-workers have synthesised a homochiral metal-organic framework from Co(II) ions and (1,3-dicarboxy-5-benzyl)carboxymethylglycine and 1,3-bis(4-pyridyl)ethane linkers. It contains helical water columns in its packing structure.⁵² These

infinite water channels resulted in an ordered chain of polarisable molecules which led to solvation (on) and desolvation (off) assisted ferroelectric switching behaviour (Figure 1.7).

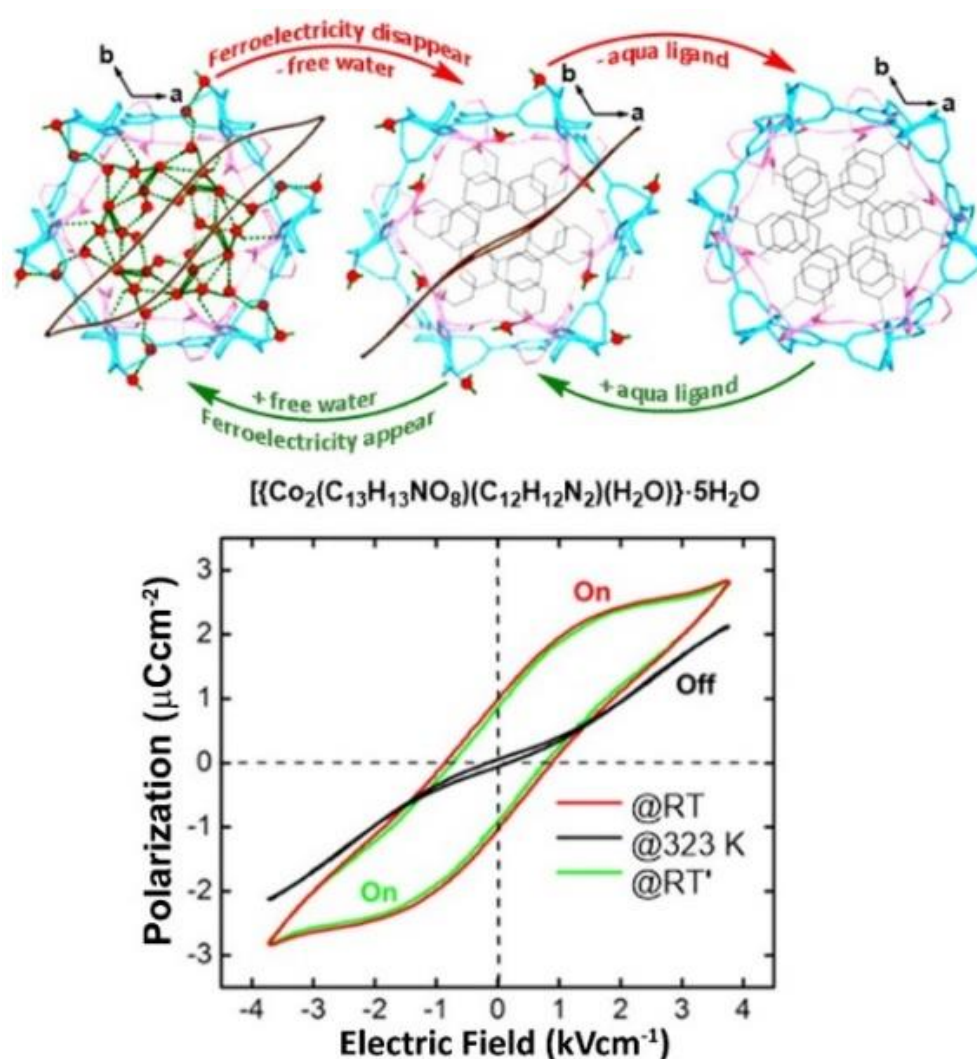


Figure 1.7 Solvent-dependent structural transformation and on-off switching of ferroelectric behaviour in a Co(II) based metal-organic framework. Adapted with permission from ref. 52. Copyright © 2013, American Chemical Society

Pardo and co-workers reported post-synthetic modification of a chiral metal-organic ferroelectric framework $\text{Ca}_6^{\text{II}}\{\text{Cu}_{24}^{\text{II}}[(\text{S,S})\text{-hismox}]_{12}(\text{OH}_2)_3\}\cdot 212\text{H}_2\text{O}$ (abbreviated as Ca-BioMOF) via a solid state single crystal to single crystal (SC to SC) process.⁵³ The Ca-BioMOF undergoes a cation (Ca^{2+}) exchange reaction with strong dipolar CH_3NH_3^+ (abbreviated as MA) cations to yield MA-BioMOF of formula $(\text{CH}_3\text{NH}_3)_{12}\{\text{Cu}_{24}^{\text{II}}[(\text{S,S})\text{-hismox}]_{12}(\text{OH}_2)_3\}\cdot 178\text{H}_2\text{O}$ (Fig. 1.8a-c). Both these MOFs are isomorphous and crystallise in the chiral polar space group $R3$. Hysteresis loop measurement of MA-BioMOF exhibits a below room temperature

ferroelectricity ($P_r = 1.06 \mu\text{C cm}^{-2}$) at 103 K (Fig. 1.8d). However, a double hysteresis loop has been obtained above its T_C (> 260 K), which supports the presence of an antiferroelectric nature before it reaches the paraelectric phase.⁵³

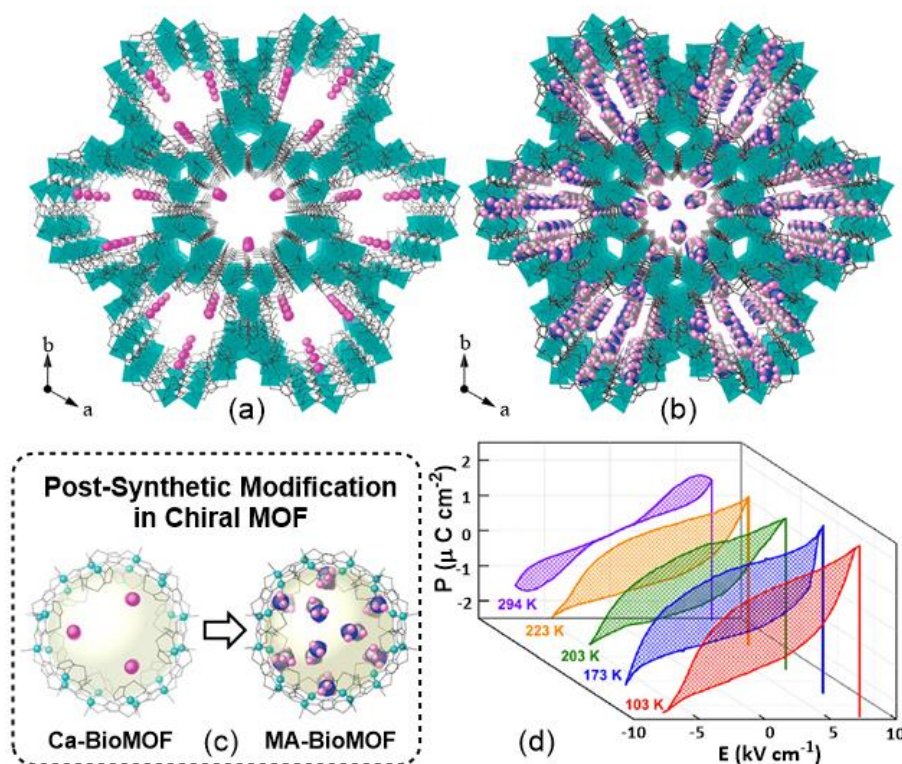


Figure 1.8 Perspective view of the crystal structures of (a) Ca-BioMOF and (b) MA-BioMOF along the c axis (Ca, purple; N, blue; C, gray; H, pink; Cu, cyan polyhedra). (c) View of their Cu₂₄ baskets showing the exchange of the Ca²⁺ cations with CH₃NH₃⁺ cations. (d) P-E loops of MA-BioMOF at different temperatures. Adapted with permission from ref. 53. Copyright © 2017, American Chemical Society

Ligands derived from pseudo- C_2 symmetric and C_3 symmetric platforms offer an attractive approach for the designing of metal-organic assemblies with ferroelectric properties. Thus, by utilising a series of isomeric flexible dipodal and tripodal amino-P(V) ligands, metal-organic assemblies with diverse structures in both centrosymmetric and non-centrosymmetric space groups have been obtained.⁵⁴⁻⁵⁷ Treatment of PhPO(NH³Py)₂ (³Py = 3-pyridyl) with Cu(II) ions gave a helical coordination polymer of formula $\{[\text{Cu}_2\text{L}_4(\text{H}_2\text{O})_2] \cdot (\text{ClO}_4)_4 \cdot 5(\text{H}_2\text{O}) \cdot (\text{CH}_3\text{OH})_\infty\}$ in presence of perchlorate ions (Fig. 1.9a). A controlled substitution of some of the perchlorates with nitrate ions retains the helical cationic structure as $[\text{Cu}_3\text{L}_6(\text{H}_2\text{O})_3] \cdot (\text{ClO}_4)_5 \cdot (\text{NO}_3) \cdot 11(\text{H}_2\text{O})_\infty$. Interestingly, the former helical assembly exhibits a

rectangular ferroelectric hysteresis loop with $P_r = 1.8 \mu\text{Ccm}^{-2}$, while the latter shows a distorted loop with a lower P_r value of $0.55 \mu\text{Ccm}^{-2}$ (Figure 1.9b). The lowering of the P_r value for the mixed anion-containing assembly was attributed to the variations in the long-range order caused by the doping of the nitrate ions into the packing structure of the perchlorate anions. This suggests that the presence of nitrate anion in the packing structure has an effect in altering the asymmetry of the system, which causes a change of polarisation. The corresponding 4-pyridyl (${}^4\text{Py}$) substituted ligand $\text{PhPO}(\text{NH}^4\text{Py})_2$ gave rise to a polar 2D-framework of formula $[\text{CuL}_2(\text{H}_2\text{O})_2] \cdot (\text{NO}_3)_2 \cdot 1.5(\text{H}_2\text{O}) \cdot (\text{CH}_3\text{OH})_\infty$ for the $\text{Cu}(\text{II})$ ions (Figure 1.9c,d). This 2D $[\text{CuL}_2]_n$ derived assembly exhibits a fatigue-free high polarisation value of $\sim 28 \mu\text{Ccm}^{-2}$ (0.1Hz) and $\sim 21 \mu\text{Ccm}^{-2}$ (1Hz) at room temperature, with the considerably low coercive field of 5.9 kVcm^{-1} (Figure 1.9e). Also, it exhibits a broad dielectric anomaly peak at 40°C , exhibiting desolvation-assisted relaxor behaviour (Figure 1.9f).

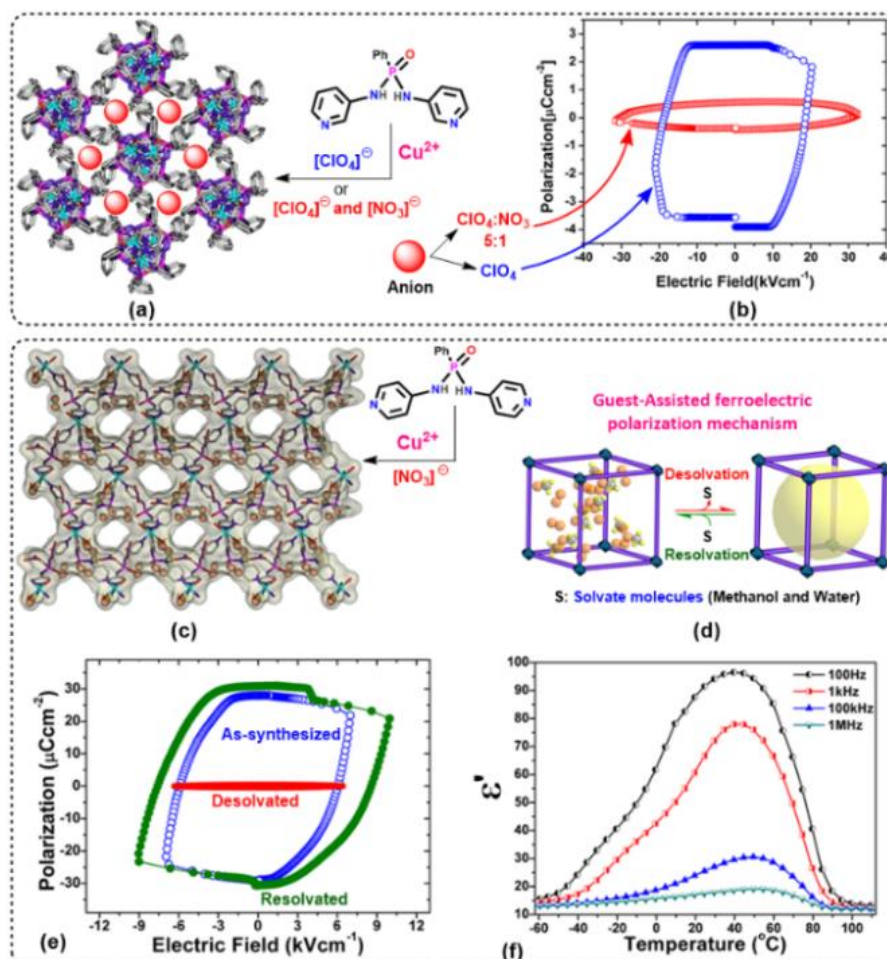


Figure 1.9 (a) Packing structure of the $[\text{CuL}_2]_n$ based 1D helical assemblies showing the location of anions in their trigonal channels. (b) Their corresponding P-E loops show anion-dependent ferroelectric behaviour. (c) Crystal structure of a $[\text{CuL}_2]_n$ based 2D-sheet structure,

obtained from an isomeric 4-pyridyl substituted ligand. (d) The schematic of its unit cell box in its solvated and desolvated phases. (e) Ferroelectric hysteresis loops of the as-synthesised, desolvated, and resolvated samples of the 2D- $[\text{CuL}_2]_n$ assembly and its temperature dependence of the real part of dielectric permittivity (ϵ'). Adapted with permission from ref. 55. Copyright © 2015, American Chemical Society Adapted with permission from ref. 56. Copyright © 2014, American Chemical Society.

Treatment of the ligand $\text{PhPO}(\text{NH}^3\text{Py})_2$ with the nitrate salts of first-row transition metal ions (M) such as Cu(II), Ni(II), and Co(II) ions leads to the formation of an interesting family of Metallo-cavitands of formula $[\text{M}_4\text{L}_8(\text{H}_2\text{O})_8] \cdot (\text{NO}_3)_8 \cdot x(\text{H}_2\text{O})$ (or simply M_4 cavitand) that can encapsulate hydrated alkali-metal guest cations (Figure 1.10a). For the Ni(II) and Co(II) ions, these tetrameric cavitands exhibit ferroelectric behaviour with guest-dependant variations in their polarisation attributes (Figure 1.10b). Both these cavitands were shown to encapsulate a series of hydrated alkali metal cations, such as $[\text{Li}(\text{H}_2\text{O})_5]^+$, $[\text{Na}(\text{H}_2\text{O})_5]^+$, $[\text{K}(\text{H}_2\text{O})_8]^+$, $[\text{Rb}(\text{H}_2\text{O})_9]^+$ and $[\text{Cs}(\text{H}_2\text{O})_{10}]^+$, having high hydration spheres (Fig. 1.10c-e). The dipole moment (ONIOM) calculations performed on the cavitand assembly shows that almost 60% of the polarisable dipoles in them originate from the intrinsic guest solvates. The P-E loop measurements gave notable polarisation values in the range of 27-30 μCcm^{-2} (Fig. 1.10f). Furthermore, all these host-guest systems show sizable variations as the cavitands with hard Li^+ ions exhibit the maximum (fatigue) tolerance, and the ones with higher polarisable Cs^+ ions show a reduction in P_r values up to 35%, after 10^5 switching cycles (Fig. 1.10g). The reduction of polarisation for the Cs^+ ion encapsulated systems at higher cycles can be attributed to its size and compact fitting within the cavitand structure.

BinXue and co-workers have prepared MIL-53(Cr) MOF with a polar linker by continuous flow chemistry.⁵⁸ The continuous flow approach can be employed to achieve the quick synthesis of MOFs without sacrificing product quality by optimising the critical reaction parameters.⁵⁹⁻⁶² MIL-53(Cr)-F structures consist of terephthalic acid ligands substituted by the polar atom fluorine (Figure 1.11a). The impact of the fluorine group on the MIL-53(Cr) structure was examined by using SHG microscopy. Figure 1.11b,c displays the optical pictures and SHG images of the MIL-53(Cr) and MIL-53(Cr)-F powders, respectively. It is evident that SHG is significantly produced by MIL-53(Cr)-F. MIL-53(Cr), in contrast, does not produce SHG. The MIL-53(Cr)-F's SHG signal denotes the presence of an acentric organisation.

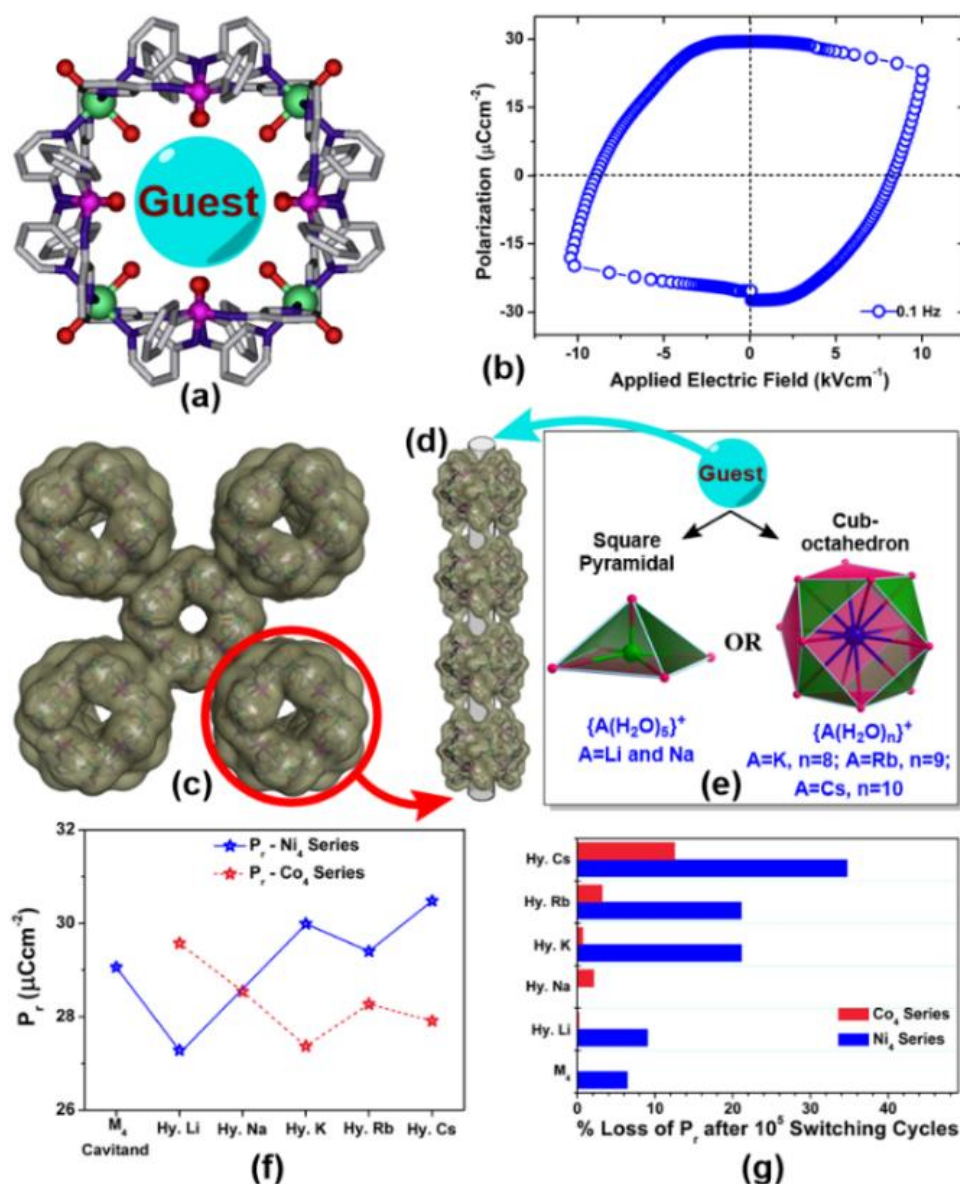


Figure 1.10 (a) The core structure of the M_4 -tetrameric cavitands ($M=Ni$ and Co) and the preferred location for guest encapsulation in them. (b) Ferroelectric hysteresis loop for the Ni_4 cavitand at room temperature. (c) The tetragonal packing structure in M_4 cavitand ($M=Ni$ and Co) and (d) view of a 1D-channels formed by the eclipsed stacking of the cavitands that runs parallel to the c -axis. (e) Idealised core structures of hydrated alkali metal guest cations along with their geometries and primary hydration spheres. Comparison of (f) the P_r values and (g) ferroelectric fatigue behaviour for all the guest-encapsulated Ni_4 and Co_4 cavitands (“Hy.” before the symbol of alkali metal refers to their hydrated form in the host-guest assembly). Adapted with permission from ref. 56. Copyright © 2017 The Royal Society of Chemistry

In addition, local ferroelectric hysteresis loops were extracted from the surface of the MIL-53(Cr)-F nanoparticles using piezoresponse force spectroscopy (PFS). In order to capture the MIL-53(Cr)-F piezoelectric responses, the amplitude butterfly loops were recorded with the DC in the off state. The amplitude-bias butterfly loop and phase hysteresis loop displays the existence of ferroelectricity and piezoelectric characteristics of the MIL(Cr)-53-F.

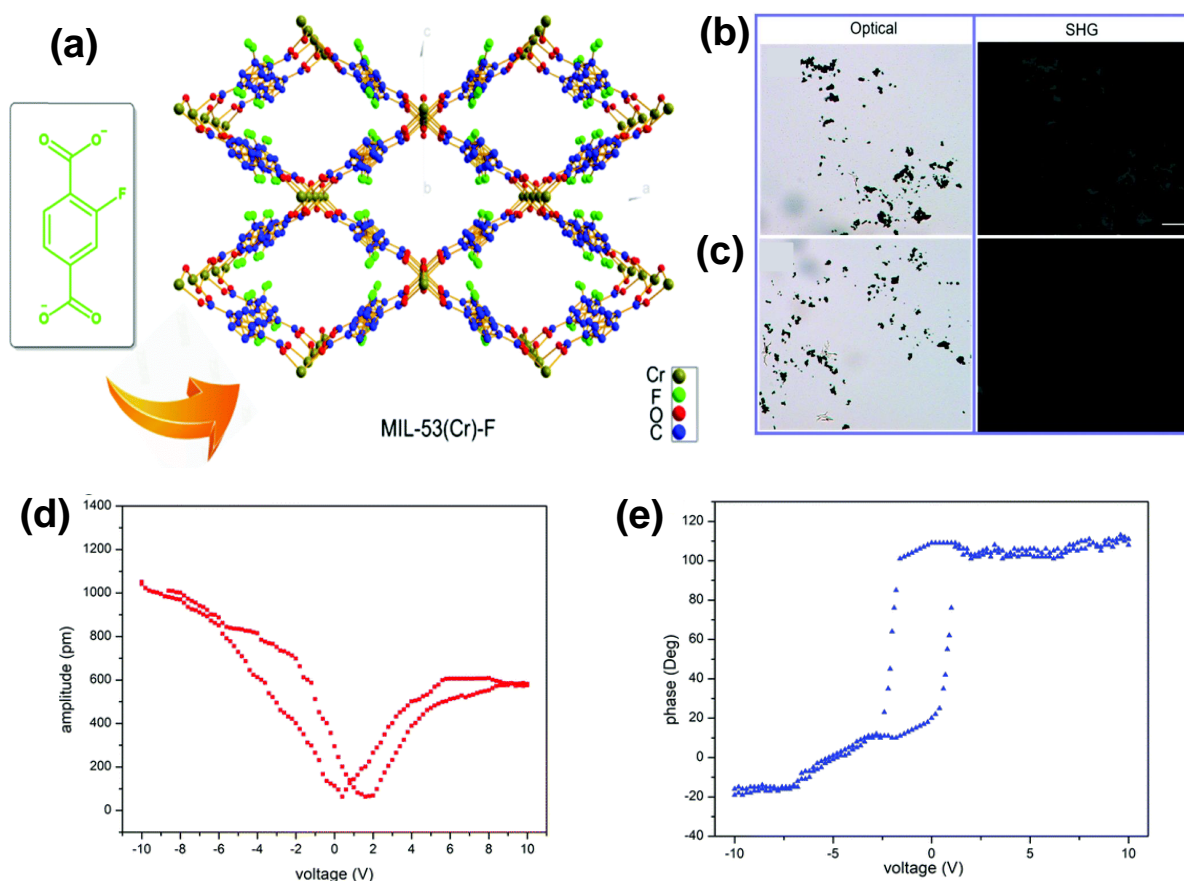


Figure 1.11 (a) MIL-53(Cr)-F MOF. Optical and SHG images of MIL-53(Cr)-F (b) and MIL-53(Cr) (c). Piezoresponse-force spectroscopy results of MIL(Cr)-53-F: (d) amplitude-bias ‘butterfly’ loop (e) phase-bias loop. Adapted with permission from ref. 58. Copyright © 2021 The Royal Society of Chemistry

Yi Zhang and co-workers confirmed the ferroelectricity in an amphidynamic 2D coordination polymer (15-crown-5) Cd_3Cl_6 (CCC).⁶³ Amphidynamic crystals are made of a combination of dynamic materials that exhibit conformational motions in certain directions and static elements that direct crystalline order. This coordination polymer is composed of inorganic stators and organic rotators (crown-ether); and exhibits van der Waal interactions between the layers (Figure 1.12a,b). Single-crystal analysis reveals that at the high-temperature phase (HTP)

exhibits centrosymmetric structure with space group $P2_1/n$ while at low-temperature phase (LTP) symmetry lowers and attains space group $P2_1$. At high temperatures, the rotation of 15-crown-5 is noted signifying a disordered position, while at low temperatures, it gets frozen at a fixed position (ordered phase) (Figure 1.12c,d). In addition to structural analysis, the SHG measurement reveals the signal appears up to $T_c = 320$ K, and further, its intensity decreases upon heating (Figure 1.12e). The characteristic rectangular P-E loop along with the peaks at the coercive field, which corresponds to the two stable polarisation states, confirms the ferroelectricity (Figure 1.12f). The two mechanisms involved here can be termed geometric ferroelectricity and sliding ferroelectricity. The geometric and sliding ferroelectric contribution was analysed by monitoring the ion positions from the single-crystal X-ray diffraction and DFT calculation. Geometric ferroelectricity involves the disorder-order transition of crown-ether when going from high temperature phase (HTP) to the low-temperature phase (LTP). The two apical chloride ions of the crown-ether are likewise marginally impacted by the polar crown-ether. For each distinct layer, a dipole can be produced by the crown ether in the LTP. The other ferroelectric origin, as shown by analysis of the HTP and LTP structures of CCC is due to the interlayer sliding present along the b-axis. The relative sliding distance in the ac plane is 0.30 \AA using the cadmium ions in crown-ethers as a distance indicator (0.62 \AA between the $\pm P$ ferroelectric states) (Figure 1.12g).

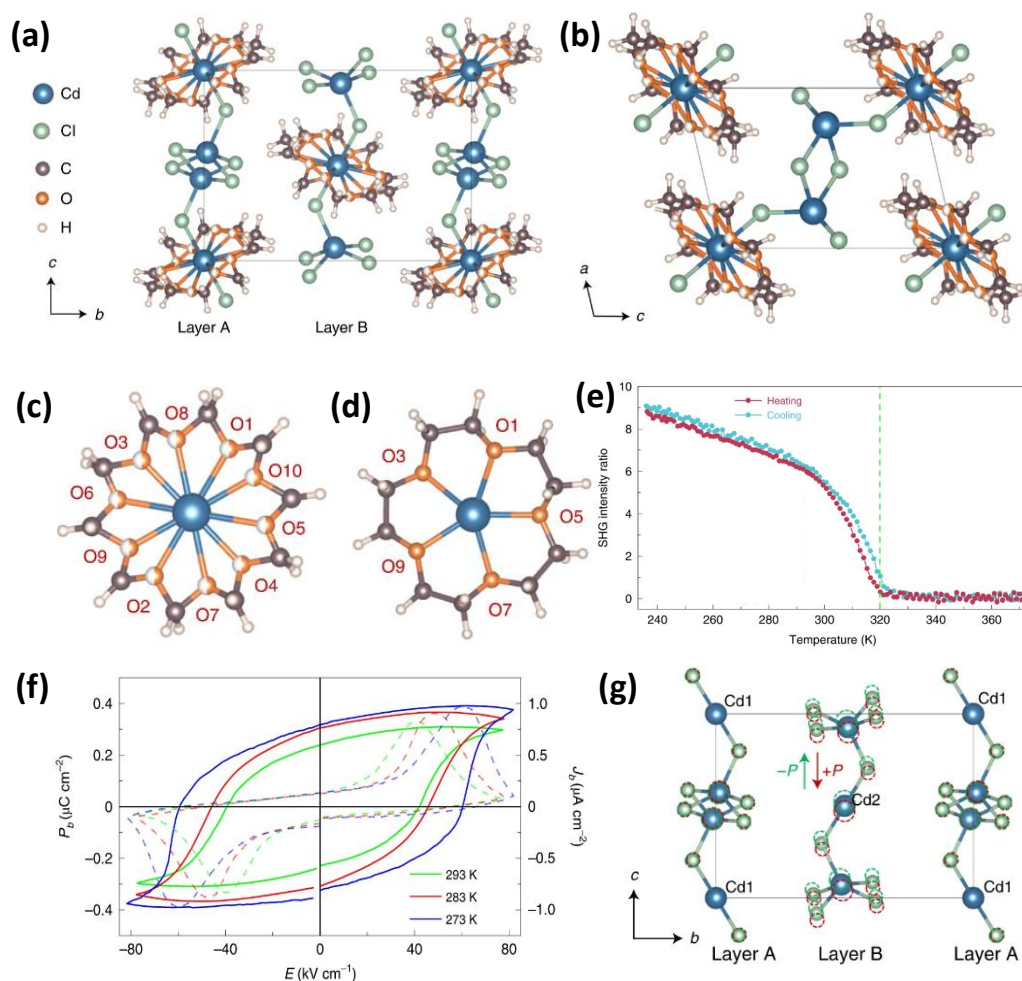


Figure 1.12 Single-crystal X-ray diffraction structure of CCC in HTP (a) with the van der Waals stacking along the b-axis (b) Top view of an individual layer. Top view of crown-ether in HTP (c) and (d) LTP. (e) The SHG intensity of the powder sample of CCC as a function of temperature. (f) The P-E hysteresis loop along with the leakage current plot. (g) The ion displacements of CdCl_2 chains. Solid outlines, HTP; dashed outlines, LTP ($\pm P$). For clarity, the organic parts are not shown. The arrows indicate the sliding directions with respect to Cd1 and not the polarisation directions. Adapted with permission from ref. 63 Copyright © 2022, The Author(s), under exclusive licence to Springer Nature Limited

1.9 Applications of Ferroelectric Materials

Ferroelectric materials are utilised in various domains since their polarisation can be switched under an external electric field. Ferroelectric materials are used in non-volatile memory devices, such as ferroelectric random access memory (FeRAM) and ferroelectric field-effect transistors (FE-FETs). These devices offer high-density storage and fast data access.^{23, 24, 64, 65}

In addition, the diverse physical characteristics of piezoelectricity, pyroelectricity, dielectric permittivity, and nonlinear optical behaviour allow ferroelectric materials to be used in a variety of additional applications (Figure 1.13).^{22, 66-72} Ferroelectric materials are used in the field of non-linear optics due to their large second-order non-linear susceptibility and high non-linear electro-optic coefficients. These properties make ferroelectric materials suitable for use in devices such as frequency converters, optical modulators, and optical switches. Owing to the inherent pyroelectric nature of ferroelectric materials, their use as infrared detectors is well understood. These detectors are used in a variety of applications, such as thermal imaging, night vision, and temperature sensing, pertaining to their high pyroelectric coefficients and their ability to generate an electrical charge in response to infrared radiation.

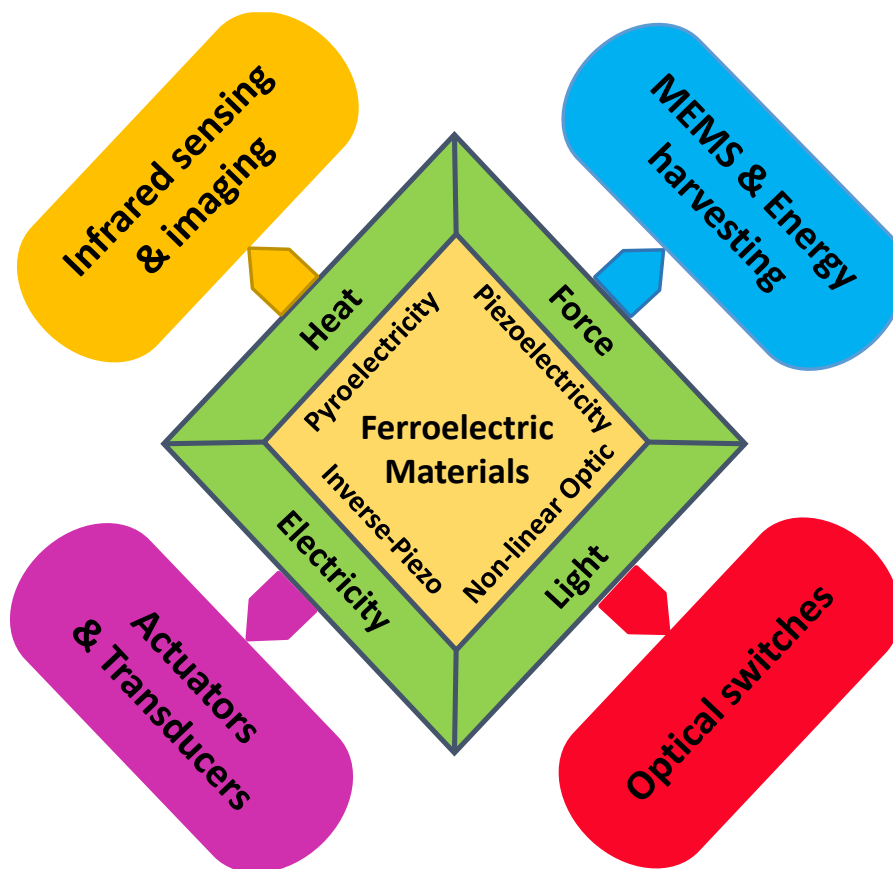


Figure 1.13 Numerous uses for non-linear dielectric materials, including piezo, pyro, and ferroelectric materials.

Ferroelectric materials are used frequently in transducers, actuators, microsensors, microphones, micro speakers, micro-electro-mechanical systems (MEMS), etc., because of their intrinsic piezoelectricity. Furthermore, nowadays, there is a lot of focussed interest on

harvesting and converting waste mechanical energy due to the electromechanical coupling of ferroelectric materials.⁷³

Ferroelectric materials are therefore set to be innovative materials for the creation of flexible self-powered electronics in the future. In view of this, the following section elaborates on using piezo- and ferroelectric materials for mechanical energy harvesting applications.

1.10 Piezo and Ferroelectric Properties for Mechanical Energy Harvesting Applications

Energy is one of the important resources that dictate the quality of our life. Energy consumption increases drastically day by day, which is largely fulfilled by non-renewable resources like fossil fuels. Due to the excessive consumption of the fast fuel reserves, there is a need to develop energy resources that are renewable and eco-friendly. There are various energy resources like solar, thermal, wind, biomass, and mechanical energy which can be collected and utilised.⁷⁴⁻⁷⁷

Among them, mechanical energy exists abundantly in our local environment, but the majority of it gets wasted and ignored, such as human body motions, walking, breathing, arm stretching and folding, etc.^{78, 79} These electromechanical responses can be harnessed by a small portable device called nanogenerator and further can be utilised as an energy source for wearable electronics and sensors in biomedical applications.⁸⁰

The semiconducting ZnO nanowires were discovered as the first piezoelectric nanogenerator by Zhang et al.⁸¹ The nanowires are deflected in response to conductive atomic force microscopy in contact mode. The area of 10 μm x 10 μm was scanned, and an output voltage of 8 mV and output power of 0.5 pW was obtained with an applied frequency of 1 MHz. However for commercial purposes, the output performance is very low, presumably due to its low piezoelectric coefficient ($d_{33} = 12$ pC/N). It is noteworthy that the d_{33} is directly proportional to the remnant polarisation ($d_{33} \propto \epsilon P_r$) of the materials. Since piezo- and ferroelectric materials have permanent dipole moments and high spontaneous polarisation are demanded to level up the overall performance of the device.

Inspired by the discovery of ZnO nanowires as a nanogenerator, researchers explored various ferroelectric materials made up of inorganic oxide ceramics such as lead zirconate titanate, lead titanate, barium titanate and sodium niobate as mechanical energy harvester.^{78, 82-84} Despite their high performance, the requirement of high-temperature synthesis, the longevity of processing time, the requirement of high voltage poling procedures, and the presence heavy and toxic metal atom such as lead impede their widespread use in wearable electronics.

To overcome this, organic polymers like polyvinylidene fluoride (PVDF) and its co-polymers have been utilised as piezoelectric energy harvester. However, achieving the enhancement of the polarisable β -phase itself is a challenging task.³¹⁻³³ Interestingly, the metal-ligand hybrid materials with high polarisation render an attractive approach as an alternative due to their facile synthesis, easy processing, lightweight, low cost etc.

Dipankar Mandal and co-workers utilised the crystalline naphthyl amine bridged [Cd(II)- μ -I₄] two-dimensional (2D) metal-organic framework (MOF) to reinforce the electroactive β -phase of PVDF for piezoelectric energy harvesting applications (Figure 1.14a).⁸⁵ The piezoelectric coefficient of these composite nanofibres was 41 pC/N due to the large interfacial interaction of $-\text{CH}_2-/-\text{CF}_2-$ dipoles of PVDF with 2D MOF. The highly flexible composite film was then electroded by using Cu-Ni plated polyester fabric and then finally encapsulated with PDMS (Figure 1.14b). The highest open-circuit voltage of 22 V and corresponding power density of $22 \mu\text{W}/\text{cm}^2$ under applied stress of 22 kPa (Figure 1.14c,d). Further, they have also explored its acoustoelectric performance, which demonstrates its ability to act as an active sensor that is sensitive to different acoustic vibrations.

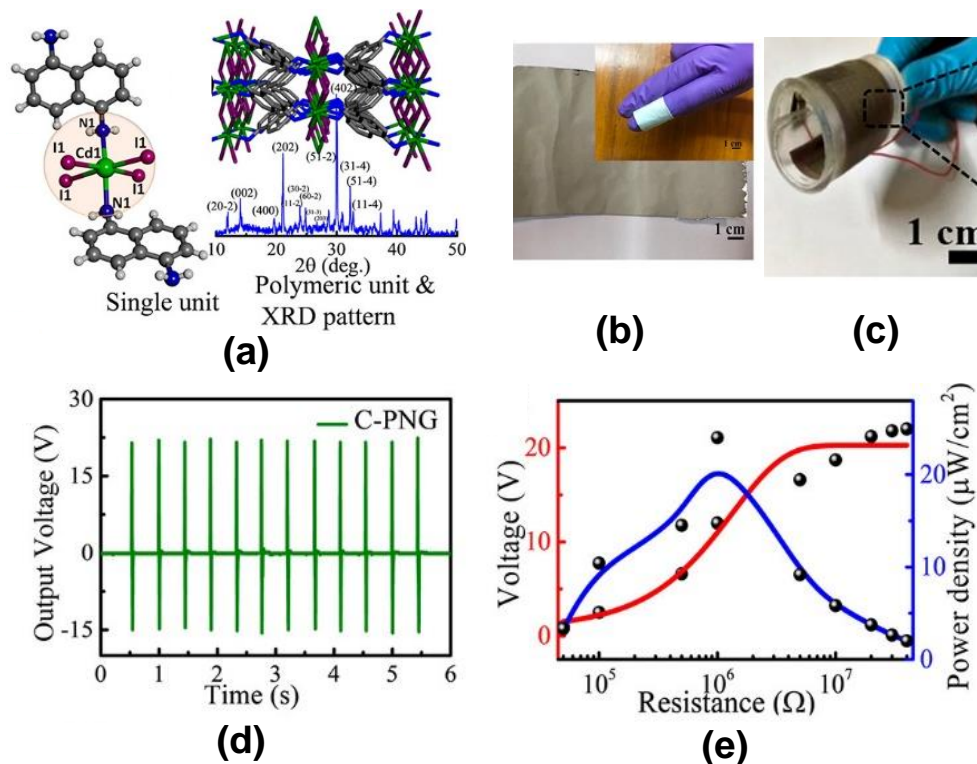


Figure 1.14 (a) Schematic diagram of the as-synthesised MOF with its X-ray diffraction pattern. (b) Photograph of the electrospun fiber mat in a combination of MOF with PVDF. (c) Photograph of the encapsulated fabricated device with PDMS along with the flexibility and

rollability. (d) The open-circuit voltage of the composite assembly under a pressure of 22 kPa. (e) Output voltage and corresponding power density across various load resistances. Adapted with permission from ref. 85. Copyright © 2021, American Chemical Society

Boomishankar and co-workers explored the ferroelectric and piezoelectric properties of A_4BX_6 type lightweight metal ion containing organic-inorganic hybrid salt composed of phosphonium cations and Ni^{II} isothiocyanate ions and demonstrated its piezoelectric energy harvesting properties (Figure 1.15a).⁸⁶ The rectangular ferroelectric hysteresis loop was obtained on the sawyer-tower circuit having remnant polarisation of $18.71 \mu\text{C cm}^{-2}$ (Figure 1.15b). The stable charge-separated structure comprising of octahedrally coordinated $[Ni(NCS)_6]^{4-}$ ions and cationic phosphorous centers and the polarisable non-covalent interactions between them is responsible for high polarisation in them. They have embedded this hybrid material in flexible piezo-inactive TPU (Thermoplastic polyurethane) polymer, which exhibits the maximum output of 19.29V and power density of 2.51 mW cm^{-3} of 15 wt% hybrid device (Figure 1.15c,d). Further, the generated output voltages from this hybrid device was utilised for charging different rated capacitors.

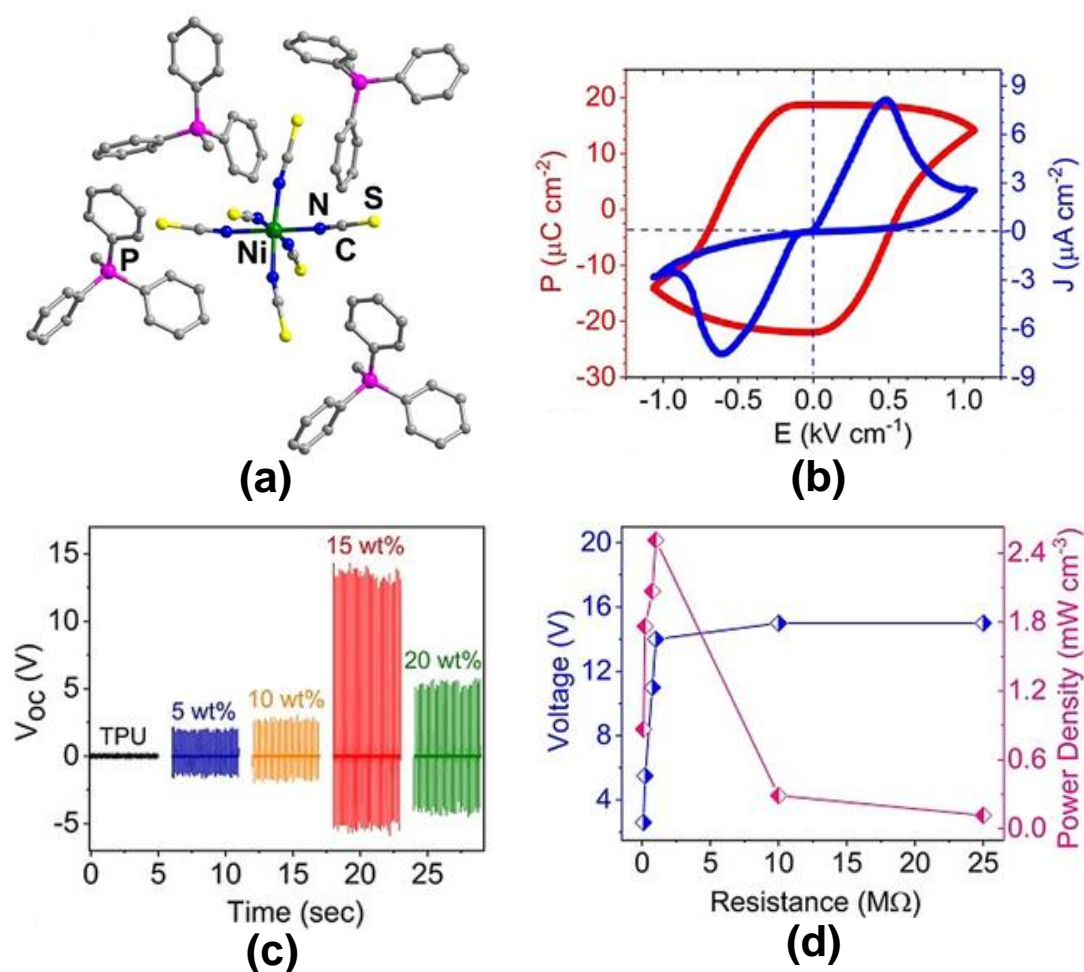


Figure 1.15 A_4BX_6 type organic-inorganic hybrid salt composed of phosphonium cations and Ni^{II} isothiocyanate ions. (b) P-E hysteresis loop. (c) Piezoelectric energy harvesting performance of different weight percentages of hybrid material composite in combination with TPU polymer. (d) The voltages and their corresponding power density across different load resistances. Adapted with permission from ref. 86. Copyright © 2020 Wiley-VCH Verlag GmbH & Co. KGaA, Weinheim

Recently, Gazit and co-workers have demonstrated nanogenerators constructed from a Zn-peptide-based coordination polymer, in which the output performance was governed by the choice of guest molecules (Figure 1.16a).⁸⁷ They demonstrated that MeCN among the five different guest solvents, namely dimethylformamide (DMF), acetonitrile (MeCN), isopropyl alcohol (IPA), acetone, and ethanol (EtOH), act as a structure-directing agent and alter the symmetry of the unit cell (Figure 1.16b). They designed and fabricated the Zn-peptide-based coordination polymer with MeCN solvent crystals between the two gold-coated silicon dioxide

substrates and finally encapsulated them with the Kapton tape to protect them from external interference (Figure 1.16c). The output signal of 1.42 V was obtained when periodically compressed with 25 N force (Figure 1.16d).

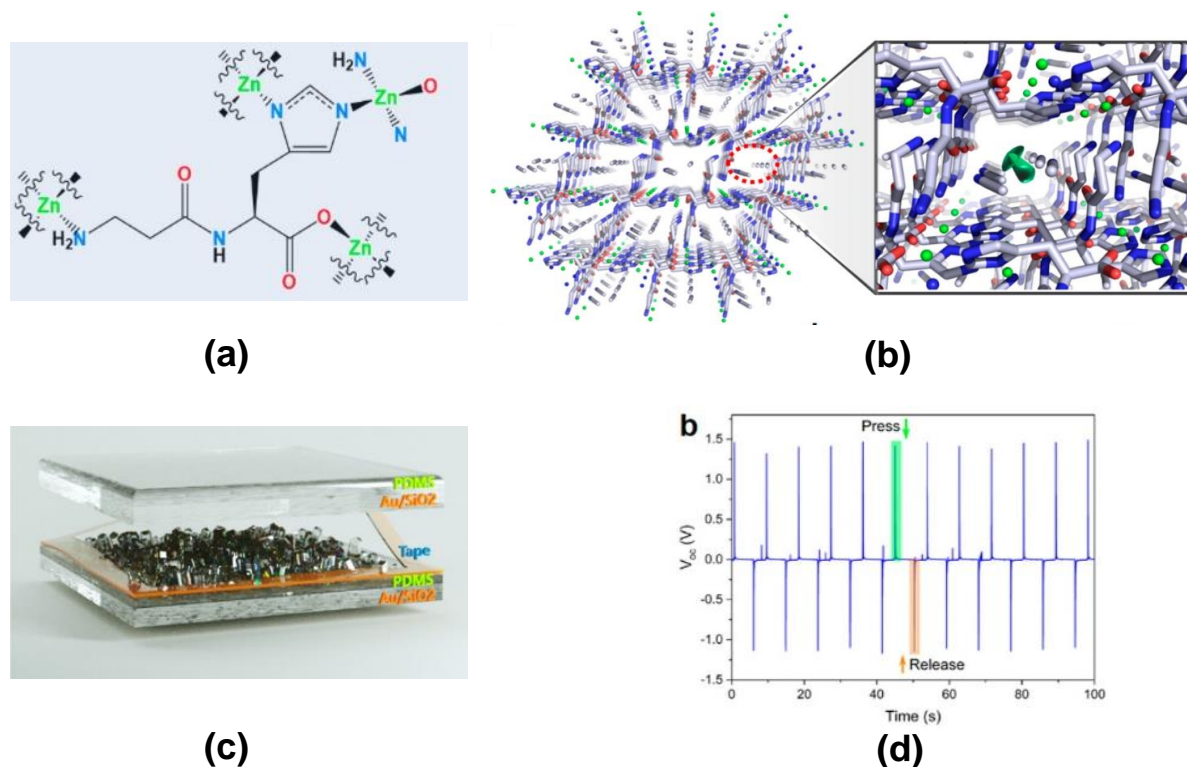


Figure 1.16 (a) Zn-peptide based coordination polymer. (b) The alignment of guest solvent MeCN in the Zn-peptide framework channel is circled in red along with the resultant molecular dipole along the a-axis (green arrow). (c) Schematic fabrication of the piezoelectric nanogenerator using the Zn-peptide MOF. (d) Piezoelectric energy harvesting performance of the composite of Zn-peptide MOF. Adapted with permission from ref. 87. Copyright © 2022, American Chemical Society

From all the above mentioned studies, it is evident that there are very limited number of examples of MOFs and high performing metal complexes that show ferroelectric behaviour. Importantly, MOF based polymer composite devices are unknown for non-piezoelectric polymers for piezoelectric energy harvesting applications. In view of this, the objectives of the present thesis are outlined as below.

1.11 Objectives of the Thesis

The thesis demonstrates the design and synthesis of ferroelectric metal-ligand architectures and their piezoelectric energy harvesting studies. [Chapter 2](#) will discuss the synthesis of discrete and its 2D connected cage framework by employing a flexible tripodal phosphoramidate ligand. Earlier work in this field showed ferroelectricity in such octahedral cage and its 1D-connected cage framework. Use of a more flexible ligand [PO(NHCH₂³Py)₃] gave rise to a 2D-connected cage framework of these cages upon ligand exchange that shows ferroelectric properties as expected for these series of compounds. [Chapter 3](#) will describe the synthesis of new discrete Co- and Ni-based discrete octahedral cages using tripodal ligand [PS(NH³Py)₃], which display excellent ferroelectric and piezoelectric properties. For the first time, the flexible polymer composites of these cages were shown for mechanical energy harvesting applications with a polydimethylsiloxane (PDMS) matrix. [Chapter 4](#) will discuss the synthesis of a two-dimensional coordination network by employing a flexible dipodal phosphoramidate ligand [PhPO(NHCH₂³Py)₂] with 4-pyridyl functionalities. This metal-ligand assembly was shown to exhibit excellent ferroelectric and piezoelectric properties analysed by piezoresponse force microscopy analysis. Further, the flexible polymeric composites of this assembly were prepared in combination with (thermoplastic polyurethane) TPU polymer for piezoelectric energy harvesting applications. [Chapter 5](#) will describe the synthesis of a neutral one-dimensional coordination network templated by a carboxyl-functionalised dipodal phosphoramidate ligand [PhPO(NHC₆H₅COOH)₂] and an N-donor bipyridyl ligand. The ferroelectric and piezoelectric properties of this assembly were analysed by the Sawyer-Tower circuit and Piezoresponse force microscopy analysis. Further, the mechanical energy harvesting performance was tested by preparing the flexible polymer composites of these hybrid materials with TPU.

Thus, the present thesis focus:

- To synthesise the low symmetric pyridyl and carboxylate functionalised dipodal or tripodal phosphoramidate ligand and its coordination assemblies with transition metal ions.
- To study their non-symmetric nature, ferroelectric, dielectric, and piezoelectric properties.
- To explore these hybrid materials for mechanical energy harvesting applications in the form of piezoelectric nanogenerator embedded in non-piezoelectric polymers.

1.12 References

1. G. M. Whitesides and M. Boncheva, *Proc. Natl. Acad. Sci. U.S.A.*, 2002, **99**, 4769-4774.
2. T. R. Cook, Y.-R. Zheng and P. J. Stang, *Chem. Rev.*, 2013, **113**, 734-777.
3. S. I. Stupp and L. C. Palmer, *Chem. Mater.*, 2014, **26**, 507-518.
4. J. R. Long and O. M. Yaghi, *Chem. Soc. Rev.*, 2009, **38**, 1213-1214.
5. X. Zou, H. Ren and G. Zhu, *Chem. Commun.*, 2013, **49**, 3925-3936.
6. J. Liu, L. Chen, H. Cui, J. Zhang, L. Zhang and C.-Y. Su, *Chem. Soc. Rev.*, 2014, **43**, 6011-6061.
7. A.-B. Xia, D.-Q. Xu, C. Wu, L. Zhao and Z.-Y. Xu, *Chem. Eur. J.*, 2012, **18**, 1055-1059.
8. D. Ajami and J. Rebek Jr., *Angew. Chem. Int. Ed.*, 2007, **46**, 9283-9286.
9. C. Müller, J. A. Whiteford and P. J. Stang, *J. Am. Chem. Soc.*, 1998, **120**, 9827-9837.
10. H. Cai, M. Li, X.-R. Lin, W. Chen, G.-H. Chen, X.-C. Huang and D. Li, *Angew. Chem. Int. Ed.*, 2015, **54**, 10454-10459.
11. H. Yang, B. Yuan, X. Zhang and O. A. Scherman, *Acc. Chem. Res.*, 2014, **47**, 2106-2115.
12. T. Hang, W. Zhang, H.-Y. Ye and R.-G. Xiong, *Chem. Soc. Rev.*, 2011, **40**, 3577-3598.
13. T. Akutagawa, S. Nishihara, N. Takamatsu, T. Hasegawa, T. Nakamura and T. Inabe, *J. Phys. Chem. B*, 2000, **104**, 5871-5873.
14. A. Trujillo, M. Fuentealba, D. Carrillo, C. Manzur, I. Ledoux-Rak, J.-R. Hamon and J.-Y. Saillard, *Inorg. Chem.*, 2010, **49**, 2750-2764.
15. C.-C. Chueh, C.-I. Chen, Y.-A. Su, H. Konnerth, Y.-J. Gu, C.-W. Kung and K. C. W. Wu, *J. Mater. Chem. A*, 2019, **7**, 17079-17095.
16. S.-W. Cheong and M. Mostovoy, *Nature Mater*, 2007, **6**, 13-20.
17. R. Ramesh, *Nature*, 2009, **461**, 1218-1219.
18. W. Eerenstein, N. D. Mathur and J. F. Scott, *Nature*, 2006, **442**, 759-765.
19. A. K. Tagantsev, V. O. Sherman, K. F. Astafiev, J. Venkatesh and N. Setter, *Journal of Electroceramics*, 2003, **11**, 5-66.
20. Y. Yuan, Z. Xiao, B. Yang and J. Huang, *J. Mater. Chem. A*, 2014, **2**, 6027-6041.
21. J. Hoffman, X. Pan, J. W. Reiner, F. J. Walker, J. P. Han, C. H. Ahn and T. P. Ma, *Adv. Mater.*, 2010, **22**, 2957-2961.

22. C. R. Bowen, H. A. Kim, P. M. Weaver and S. Dunn, *Energy Environ. Sci.*, 2014, **7**, 25-44.
23. C. A. P. de Araujo, J. D. Cuchiari, L. D. McMillan, M. C. Scott and J. F. Scott, *Nature*, 1995, **374**, 627-629.
24. S. Das and J. Appenzeller, *Nano Lett.*, 2011, **11**, 4003-4007.
25. Y. Zhang, P. T. T. Phuong, E. Roake, H. Khanbareh, Y. Wang, S. Dunn and C. Bowen, *Joule*, 2020, **4**, 301-309.
26. J. Valasek, *Phys. Rev.*, 1921, **17**, 475-481.
27. S. Horiuchi and Y. Tokura, *Nature Mater*, 2008, **7**, 357-366.
28. M. Safaei, H. A. Sodano and S. R. Anton, *Smart Mater. Struct.*, 2019, **28**, 113001.
29. Y. Bai, H. Jantunen and J. Juuti, *Adv. Mater.*, 2018, **30**, 1707271.
30. H. Liu, J. Zhong, C. Lee, S.-W. Lee and L. Lin, *Applied Physics Reviews*, 2018, **5**, 041306.
31. S.-H. Park, H. B. Lee, S. M. Yeon, J. Park and N. K. Lee, *ACS Appl. Mater. Interfaces*, 2016, **8**, 24773-24781.
32. N. R. Alluri, A. Chandrasekhar, J. H. Jeong and S.-J. Kim, *J. Mater. Chem. C*, 2017, **5**, 4833-4844.
33. J. H. Park, N. Kurra, M. N. AlMadhoun, I. N. Odeh and H. N. Alshareef, *J. Mater. Chem. C*, 2015, **3**, 2366-2370.
34. D. W. Richerson, *CRC press*, 2005.
35. H. M. Rosenberg, *Oxford University Press*, 1988.
36. S. O. Kasap, *McGraw-Hill New York:* , 2006, **784**.
37. K. Uchino, *Woodhead Publishing Ltd.:*, Cambridge, UK, 2010.
38. A. M. Manjón-Sanz and M. R. Dolgos, *Chem. Mater.*, 2018, **30**, 8718-8726.
39. W. P. Mason, *J. Acoust. Soc. Am.*, 1981, **70**, 1561-1566.
40. W. Zhang and R.-G. Xiong, *Chem. Rev.*, 2012, **112**, 1163-1195.
41. G. Busch and P. Scherrer, *Naturwissenschaften*, 1935, **23**, 737-737.
42. T. Mitsui, *Landolt-Bornstein, Series*, 1982, **16**, 99.
43. M. E. G. Lines, A. M., *Clarendon press Oxford:* , 1977.
44. H. S. Nalwa, *CRC Press:*, 1995.
45. K. Noda, K. Ishida, A. Kubono, T. Horiuchi, H. Yamada and K. Matsushige, *J. Appl. Phys. Rev.*, 2003, **93**, 2866-2870.

46. P. Jain, N. S. Dalal, B. H. Toby, H. W. Kroto and A. K. Cheetham, *J. Am. Chem. Soc.*, 2008, **130**, 10450-10451.
47. G.-C. Xu, X.-M. Ma, L. Zhang, Z.-M. Wang and S. Gao, *J. Am. Chem. Soc.*, 2010, **132**, 9588-9590.
48. G.-C. Xu, W. Zhang, X.-M. Ma, Y.-H. Chen, L. Zhang, H.-L. Cai, Z.-M. Wang, R.-G. Xiong and S. Gao, *J. Am. Chem. Soc.*, 2011, **133**, 14948-14951.
49. D. Di Sante, A. Stroppa, P. Jain and S. Picozzi, *J. Am. Chem. Soc.*, 2013, **135**, 18126-18130.
50. P. Jain, A. Stroppa, D. Nabok, A. Marino, A. Rubano, D. Paparo, M. Matsubara, H. Nakotte, M. Fiebig, S. Picozzi, E. S. Choi, A. K. Cheetham, C. Draxl, N. S. Dalal and V. S. Zapf, *npj Quant Mater*, 2016, **1**, 16012.
51. K. Asadi and M. A. van der Veen, *Eur. J. Inorg. Chem.*, 2016, **2016**, 4332-4344.
52. X.-Y. Dong, B. Li, B.-B. Ma, S.-J. Li, M.-M. Dong, Y.-Y. Zhu, S.-Q. Zang, Y. Song, H.-W. Hou and T. C. W. Mak, *J. Am. Chem. Soc.*, 2013, **135**, 10214-10217.
53. M. Mon, J. Ferrando-Soria, M. Verdaguer, C. Train, C. Paillard, B. Dkhil, C. Versace, R. Bruno, D. Armentano and E. Pardo, *J. Am. Chem. Soc.*, 2017, **139**, 8098-8101.
54. A. Yadav, A. K. Srivastava, P. Kulkarni, P. Divya, A. Steiner, B. Praveenkumar and R. Boomishankar, *J. Mater. Chem. C*, 2017, **5**, 10624-10629.
55. A. K. Srivastava, P. Divya, B. Praveenkumar and R. Boomishankar, *Chem. Mater.*, 2015, **27**, 5222-5229.
56. A. K. Srivastava, B. Praveenkumar, I. K. Mahawar, P. Divya, S. Shalini and R. Boomishankar, *Chem. Mater.*, 2014, **26**, 3811-3817.
57. A. K. Srivastava, T. Vijayakanth, P. Divya, B. Praveenkumar, A. Steiner and R. Boomishankar, *J. Mater. Chem. C*, 2017, **5**, 7352-7359.
58. F. Xue, J. Cao, X. Li, J. Feng, M. Tao and B. Xue, *J. Mater. Chem. C*, 2021, **9**, 7568-7574.
59. B. He, M. M. Sadiq, M. P. Batten, K. Suzuki, M. Rubio-Martinez, J. Gardiner and M. R. Hill, *Chem. Eur. J.*, 2019, **25**, 13184-13188.
60. P. A. Bayliss, I. A. Ibarra, E. Pérez, S. Yang, C. C. Tang, M. Poliakoff and M. Schröder, *Green Chem.*, 2014, **16**, 3796-3802.
61. M. Taddei, D. A. Steitz, J. A. van Bokhoven and M. Ranocchiari, *Chem. Eur. J.*, 2016, **22**, 3245-3249.

62. A. S. Munn, P. W. Dunne, S. V. Y. Tang and E. H. Lester, *Chem. Commun.*, 2015, **51**, 12811-12814.
63. L.-P. Miao, N. Ding, N. Wang, C. Shi, H.-Y. Ye, L. Li, Y.-F. Yao, S. Dong and Y. Zhang, *Nat. Mater.*, 2022, **21**, 1158-1164.
64. S.-T. Han, Y. Zhou and V. A. L. Roy, *Adv. Mater.*, 2013, **25**, 5425-5449.
65. J. F. Scott and C. A. Paz de Araujo, *Science*, 1989, **246**, 1400-1405.
66. C. Wan and C. R. Bowen, *J. Mater. Chem. A*, 2017, **5**, 3091-3128.
67. Y. Zhang, M. Xie, J. Roscow, Y. Bao, K. Zhou, D. Zhang and C. R. Bowen, *J. Mater. Chem. A*, 2017, **5**, 6569-6580.
68. C. R. Bowen, J. Taylor, E. LeBoulbar, D. Zabek, A. Chauhan and R. Vaish, *Energy Environ. Sci.*, 2014, **7**, 3836-3856.
69. Z. Fan, K. Sun and J. Wang, *J. Mater. Chem. A*, 2015, **3**, 18809-18828.
70. B. Chen, J. Shi, X. Zheng, Y. Zhou, K. Zhu and S. Priya, *J. Mater. Chem. A*, 2015, **3**, 7699-7705.
71. Y. Bai, T. Siponkoski, J. Peräntie, H. Jantunen and J. Juuti, *Appl. Phys. Lett.*, 2017, **110**, 063903.
72. W. Jie and J. Hao, *Nanoscale*, 2014, **6**, 6346-6362.
73. F. R. Fan, W. Tang and Z. L. Wang, *Adv. Mater.*, 2016, **28**, 4283-4305.
74. H. Ryu and S.-W. Kim, *Small*, 2021, **17**, 1903469.
75. T. Cheng, Q. Gao and Z. L. Wang, *Adv. Mater. Technol.*, 2019, **4**, 1800588.
76. H. Ryu, H.-J. Yoon and S.-W. Kim, *Adv. Mater.*, 2019, **31**, 1802898.
77. X. Huang, L. Wang, H. Wang, B. Zhang, X. Wang, R. Y. Z. Stening, X. Sheng and L. Yin, *Small*, 2020, **16**, 1902827.
78. K.-I. Park, J. H. Son, G.-T. Hwang, C. K. Jeong, J. Ryu, M. Koo, I. Choi, S. H. Lee, M. Byun, Z. L. Wang and K. J. Lee, *Adv. Mater.*, 2014, **26**, 2514-2520.
79. R. Yang, Y. Qin, C. Li, G. Zhu and Z. L. Wang, *Nano Lett.*, 2009, **9**, 1201-1205.
80. Z. L. Wang, *Mater. Today*, 2017, **20**, 74-82.
81. Z. L. Wang and J. Song, *Science*, 2006, **312**, 242-246.
82. J. H. Jung, M. Lee, J.-I. Hong, Y. Ding, C.-Y. Chen, L.-J. Chou and Z. L. Wang, *ACS Nano*, 2011, **5**, 10041-10046.
83. S. Xu, Y.-w. Yeh, G. Poirier, M. C. McAlpine, R. A. Register and N. Yao, *Nano Lett.*, 2013, **13**, 2393-2398.
84. A. Koka and H. A. Sodano, *Adv. Energy Mater.*, 2014, **4**, 1301660.

85. K. Roy, S. Jana, Z. Mallick, S. K. Ghosh, B. Dutta, S. Sarkar, C. Sinha and D. Mandal, *Langmuir*, 2021, **37**, 7107-7117.
86. T. Vijayakanth, F. Ram, B. Praveenkumar, K. Shanmuganathan and R. Boomishankar, *Angew. Chem. Int. Ed.*, 2020, **59**, 10368-10373.
87. Y. Chen, S. Guerin, H. Yuan, J. O'Donnell, B. Xue, P.-A. Cazade, E. U. Haq, L. J. W. Shimon, S. Rencus-Lazar, S. A. M. Tofail, Y. Cao, D. Thompson, R. Yang and E. Gazit, *J. Am. Chem. Soc.*, 2022, **144**, 3468-3476.

Chapter 2

Ferroelectric Behavior of an Octahedral Metal-Ligand Cage and Its 2D-Connected Cage Framework

2.1 Introduction

Ferroelectricity is the property of polar crystalline substances exhibiting spontaneous electric polarization, which can be reversed by sweeping the direction of the electric field.¹ Ferroelectric materials find many technological applications, such as in memory devices and sensors.²⁻⁵ Recent studies explored ferroelectrics as solar- and mechanical-energy harvesting systems.⁶⁻⁹ Most commercial ferroelectrics utilize ceramic metal oxide systems.¹⁰⁻¹² However, these materials are mostly brittle, require high processing temperatures and often contain heavy and toxic elements. Aiming to overcome these issues, molecular and polymeric systems have been explored to achieve better flexibility, light weight character, low temperature synthesis and processing techniques.¹³⁻²¹ Metal-organic frameworks are promising ferroelectrics because of the many ways in which their structures can be constructed and modified.^{22, 23} However, uncovering the mechanism behind their ferroelectric behavior is challenging because of the complexity of their structures.^{8, 24-26}

Our group has been interested in the ferroelectric behavior of metal-organic assemblies supported by di- and tripodal phosphoramidate ligands of the type [PhPO(NHPy)₂], (Py = 3-pyridyl (³Py) or 4-pyridyl (⁴Py)) and [PS(NH³Py)₃].^{8, 27, 28} We were able to obtain axially symmetric octahedral M₆L₈ cages using the tripodal [PS(NH³Py)₃] ligand and reversibly connect these cages to form hierarchical frameworks of discrete, 1D, 2D and 3D-structures.²⁶ While the discrete and 1D-frameworks exhibited ferroelectric behavior, this could not be established for the 2D and 3D-frameworks of this series since these were plagued by poor crystal quality that hampers the electrical measurements on them. Hence, we focused on the design of new ligands to improve the structural integrity and the ferroelectric response of these materials. Herein, we report the synthesis and ferroelectric behavior of the octahedral cage assembly [Cu₆(H₂O)₁₂(TPPA)₈](NO₃)₁₂·45H₂O (**1**) and its 2D-cage connected framework [{Cu₆Cl₄(H₂O)₆(TPPA)₈}(NO₃)₈·60H₂O]_n (**2**). These are supported by the tris(N-(3-picolyl))phosphoramidate ligand (NHCH₂-(3-Py))₃PO (TPPA). The ligand is more flexible due to the introduction of internal CH₂ groups that connect the bridge-head P=O unit with the three coordinating pyridyl rings. Crystals of **1** and **2** gave the remnant polarization (P_r) values of 27.27 and 29.09 μC/cm², respectively. This is the first report on the observation of ferroelectric behavior in a 2D-framework of octahedral cages. The observation of ferroelectric behavior in these cage-derived systems reinforces the effect of disordered anions and solvates in governing the polarization in supramolecular metal-ligand systems.

2.2 Experimental section

2.2.1 General remarks

All manipulations involving phosphorous halides were performed under dry nitrogen or argon atmosphere in standard Schlenk-glassware. The solvent toluene was dried over sodium. 3-picolyamine was purchased from Aldrich and used as received. POCl_3 was purchased locally and was distilled prior to use. $\text{Cu}(\text{NO}_3)_2 \cdot 3\text{H}_2\text{O}$ was purchased from Aldrich and used as received. NMR spectra were recorded on a Jeol 400 MHz spectrometer (^1H NMR, 400.13 MHz; $^{13}\text{C}\{^1\text{H}\}$ NMR, 100.62 MHz; $^{31}\text{P}\{^1\text{H}\}$ NMR, 161.97 MHz) at room temperature using SiMe_4 (^1H , ^{13}C) and 85% H_3PO_4 (^{31}P). The MALDI-TOF spectra were obtained on an Applied Biosystem MALDI-TOF/TOF spectrometer. The powder X-ray diffraction (PXRD) data were obtained from a Bruker-D8 Advance diffractometer. Thermal analysis (TGA) data have been obtained from a Perkin-Elmer STA-6000 thermogravimetric analyzer. The measurement of the second harmonic generation was carried out by using the method of Kurtz and Perry. The fundamental wavelength is 1064 nm generated by a Q-switched Nd:YAG laser with a frequency doubling at 532 nm. The samples were filled into a capillary tube and a powdered potassium dihydrogen phosphate (KDP) sample was used as the reference. Elemental analyses were performed on a Vario-EL cube elemental analyzer. FT-IR in attenuated total reflectance (ATR) mode was taken on neat samples on a Bruker Alpha spectrophotometer. Melting points were obtained using an Electro thermal melting point apparatus and were uncorrected.

2.2.2 Synthesis

2.2.2.1 Synthesis of tris(N-(3-picoly))phosphoramidate (TPPA): To a stirred solution of 3-picolyamine (3.80 mL, 4.042g, 37.38 mmol) in toluene (~ 100 mL) at 0 °C, POCl_3 (0.5 mL, 0.82 g, 5.34 mmol) in 10 mL of toluene was added drop wise through a pressure equalizer funnel and the reaction mixture was refluxed for overnight until a white precipitate was formed. The toluene was decanted and the solids were extracted in dichloromethane three times. The combined dichloromethane extracts were evaporated under reduced pressure to yield the pure ligand. Crystals of TPPA were obtained by slow evaporation of a solution from methanol. Yield: 1.56 g (79.18%). M.P.: 105-110 °C. ^1H NMR (CDCl_3): δ 8.45 (d, 3H, CH(pyridyl)), δ 8.34 (dd, 3H, CH(pyridyl)), δ 7.56 (td, 3H, CH (pyridyl)), δ 7.12 (dd, 3H, CH (pyridyl)), δ 4.07 (t, 3H, NH), δ 3.59 (d, 6H, CH_2). $^{13}\text{C}\{^1\text{H}\}$ NMR (CDCl_3): δ 42.77, 123.63, 135.36, 135.88, 148.53, 148.87. ^{31}P NMR (162 MHz, $\{(\text{CD}_3)_2\text{SO}\}$): δ 16.78. MALDI-TOF: 391.12 (M

+ Na)⁺, 407.09 (M + K)⁺ Anal. Calcd. for C₁₈H₂₁N₆OP: C, 58.69; H, 5.75; N, 22.81. Found: C, 56.38; H, 3.261; N, 20.89.

2.2.2.2 Synthesis of Compound 1: To a stirred solution of TPPA (50 mg, 0.135 mmol) in MeOH (3 mL), Cu(NO₃)₂·3H₂O (98.25 mg, 0.407 mmol) in H₂O was added. An initially formed bluish green precipitate was dissolved by adding water (2-3 drops) giving rise to a blue-colored solution. The resulting solution was stirred for 2 h and was filtered through a thick pad of celite. Blue crystals suitable for SCXRD analysis were obtained from the filtrate after five days. Yield: 80%. M.P. 82-87 °C. FT-IR data on powder (cm⁻¹): 3457, 3238, 1601, 1425, 1314, 1178, 1079, 882, 784, 702, 599, 552. Anal. Calcd. for C₁₄₄H₂₈₂N₆₀O₁₀₁P₈Cu₆: C, 33.92; H, 5.57; N, 16.48. Found: C, 32.26; H, 2.323; N, 15.10.

2.2.2.3 Synthesis of Compound 2: To a stirred solution of TPPA (50 mg, 0.135 mmol) in MeOH (3 mL), Cu(NO₃)₂·3H₂O (98.25 mg, 0.407 mmol) in H₂O (0.5 mL) was added. An initially formed bluish green precipitate was dissolved by adding water (2-3 drops) giving rise to a blue-colored solution. After 30 minutes of stirring, an aqueous solution of NaCl (excess) was added to the mixture. The resulting solution was stirred for 2 h and was filtered through a thick pad of celite. Blue crystals suitable for SCXRD analysis were obtained from the filtrate after five days. Yield: 85%. M.P. 92-98 °C. FT-IR data on powder (cm⁻¹): 3431, 3230, 1606, 1423, 1329, 1166, 1096, 874, 794, 698, 640. Anal. Calcd. for C₁₄₄H₃₀₀Cl₄N₅₆O₉₈P₈Cu₆: C, 33.55; H, 5.87; N, 15.22. Found: C, 32.72; H, 4.72; N, 16.08.

2.2.3 Crystallography: Reflections were collected on a Bruker Smart Apex Duo diffractometer at 100 K using MoK α radiation ($\lambda = 0.71073 \text{ \AA}$). Structures were refined by full-matrix least squares against F² using all data using SHELX.²⁹ All non-hydrogen atoms were refined anisotropically if not stated otherwise. The phosphoryl oxygen atom in **2** is disordered over two sites. The nitrates ions in the asymmetric units of both **1** and **2** were disordered. The disordered fragments were refined with the similar distances and the similar U-restraints by using the SIMU/SAME command of the Shelx. Crystals of **1** and **2** were weakly diffracting at higher angles and hence their data were truncated to $2\theta = 50^\circ$. Hydrogen atoms were constrained in geometric positions to their parent atoms. (Table 2.1)

Table 2.1: Crystallography data table for TPPA, compound 1 and 2.

Compound	TPPA	1	2
Chemical formula	C ₁₈ H ₂₁ N ₆ OP	C ₁₄₄ H ₂₈₂ Cu ₆ N ₆₀ O ₁₀₁ P ₈	C ₁₄₄ H ₃₀₀ Cl ₄ Cu ₆ N ₅₆ O ₉₈ P ₈
Formula weight	368.38	5099.8	5155.2
Temperature	100(2) K	100(2) K	100(2) K
Crystal system	Monoclinic	Cubic	Tetragonal
Space group	P 2 ₁ /n	Pn -3 n	I 4 2 2
a (Å); α (°)	10.7016(16); 90	23.1600(19); 90	20.236(6); 90
b (Å); β (°)	9.1589(13); 96.172(4)	23.1600(19); 90	20.236(6); 90
c (Å); γ (°)	18.330(3) ; 90	23.1600(19); 90	29.872(9); 90
V (Å ³); Z	1786.2(4); 4	12423(3); 2	12232(8); 1
ρ (calc.) mg m ⁻³	1.370	1.363	1.400
μ(Mo K _α) mm ⁻¹	0.175	0.654	0.706
2θ _{max} (°)	50.042	50.048	50.052
R(int)	0.0671	0.0888	0.0861
Completeness to θ	100 %	99.4 %	99.7 %
Data / param.	3152 / 254	1835 / 135	5420 / 327
GOF	1.040	1.113	1.202
R1 [F>4σ(F)]	0.0603	0.1292	0.1163
wR2 (all data)	0.1590	0.3813	0.3537
max.peak/hole (e.Å ⁻³)	1.209/-1.042	0.851/-0.595	1.469/-0.667

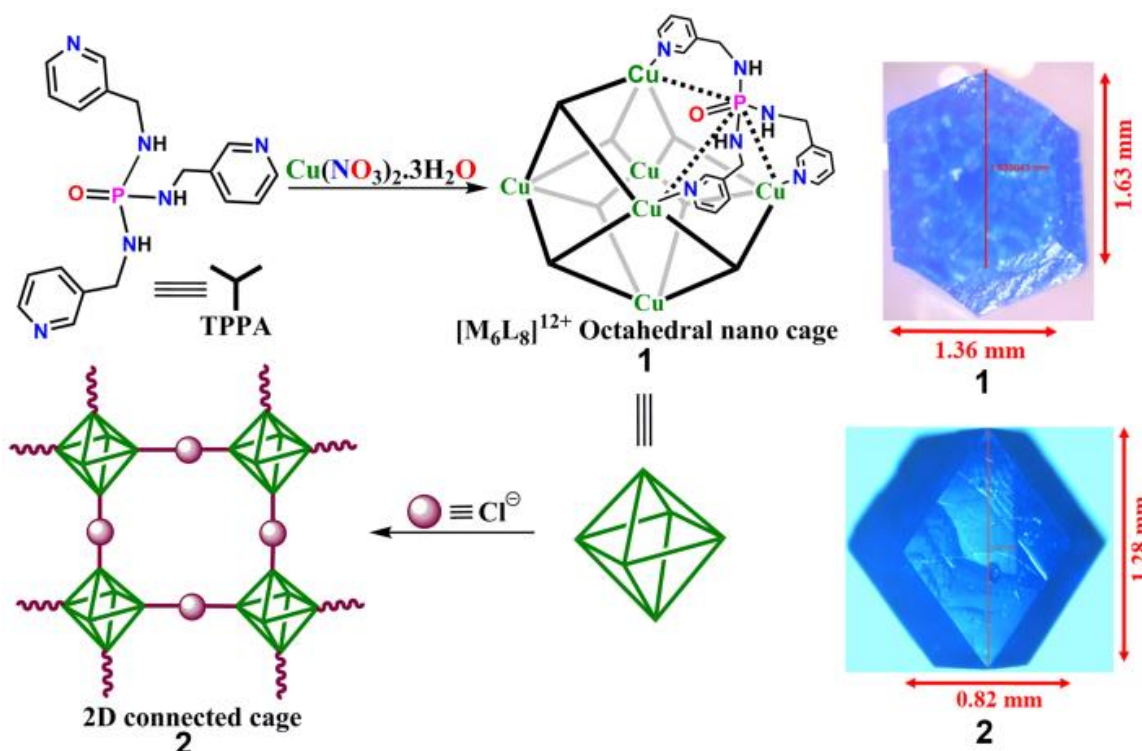
2.2.4 Ferroelectric and Dielectric measurements: The ferroelectric hysteresis loops for **1** and **2** were measured on single crystals of dimensions 1.36 x 1.63 x 0.65 and 1.28 x 0.82 x 0.60 mm, respectively, by using a Sawyer-Tower circuit. The measurements pertaining to the polarization and fatigue cycles were recorded using hysteresis loop analyzer (TF Analyzer 2000E, aixACCT, Germany). Leakage currents were measured dynamically for various voltage steps during the hysteresis loop measurements. Powder samples of **1** and **2** were compacted in the form of discs (of approximately 10 mm diameter and 1 mm thickness) to measure dielectric

properties. The compacted discs were subsequently electroded using aluminum adhesive foils for both measurements. The dielectric characteristics for **1** and **2** were measured using the Novocontrol, Dielectric Spectrometer.

2.3 Results and Discussion

2.3.1 Synthesis and crystal structures

The ligand TPPA was synthesized by refluxing 3-picolylamine and POCl₃ in toluene (Scheme 1). The ³¹P NMR of the ligand yields a single signal at δ 16.78 ppm while MALDI-TOF spectra showed m/z values of 391.12 and 407.19 corresponding to [M+Na] and [M+K] ions (See Figures 2A.1-2A.3, Appendix 2). Treatment of TPPA with Cu(NO₃)₂·3H₂O in 1:3 ratio in MeOH/H₂O mixtures gave [Cu₆(H₂O)₁₂(TPPA)₈](NO₃)₁₂·45H₂O (**1**), which consists of discrete octahedral cages. Reaction of **1** with NaCl in MeOH/H₂O yielded the 2D-connected cage framework [{Cu₆Cl₄(H₂O)₆(TPPA)₈}]₈·60H₂O (**2**); in it every cage is connected to four others via chloride bridges between Cu(II) centers. Both **1** and **2** were obtained as blue crystals from the slow evaporation of their reaction mixtures (Scheme 2.1).



Scheme 2.1: Schematic diagram showing the formation of cage **1** and its 2D-connected cage framework **2**. Images of the crystals of **1** and **2** under the microscope and their dimensions are given on the right side.

Single crystal X-ray structure analysis reveals that compound **1** crystallizes in cubic space group $Pn\bar{3}n$. Each Cu(II) center of the cationic cage $[\text{Cu}_6(\text{H}_2\text{O})_{12}(\text{TPPA})_8]^{12+}$ shows a Jahn-Teller-distorted octahedral coordination (Figure 2.1a and Appendix 2, Figures 2A.4-2A.5). Its equatorial positions are occupied by the N-atoms of four TPPA ligands while the axial positions bind two water molecules. The discrete cages have chiral octahedral symmetry (point group O). The six Cu^{2+} ions coincide with the 4-fold rotation axes while the TPPA ligands occupy the 3-fold rotation axes. The P=O groups are oriented towards the cavity of the cage. Hence, the crystal is a racemate containing cages of opposite handedness, which form a cubic pseudo-body-centered packing (Figure 2.1b and Appendix 2, Figure 2A.6). The solvent accessible volume of the cavity inside the cage measures 436 \AA^3 which is 7.0 % of the total volume (Appendix 2, Figure 2A.7a). It is occupied by disordered water molecules forming a cage like hydrogen bonded network that is connected to the P=O groups and the copper bound water molecules (Appendix 2, Figure 2A.8). However, the bulk of the void volume is found between the cages. It forms an extended 3D-channel structure that occupies 39.4 % of the total volume; it contains nitrate anions and water molecules (Appendix 2, Figure 2A.7b). They form a hydrogen bonded network that also involves cage bound NH groups and Cu-coordinated water ligands (Figure 2.1c and Appendix 2, Figure 2A.9). The contents of both internal and external voids are highly disordered.

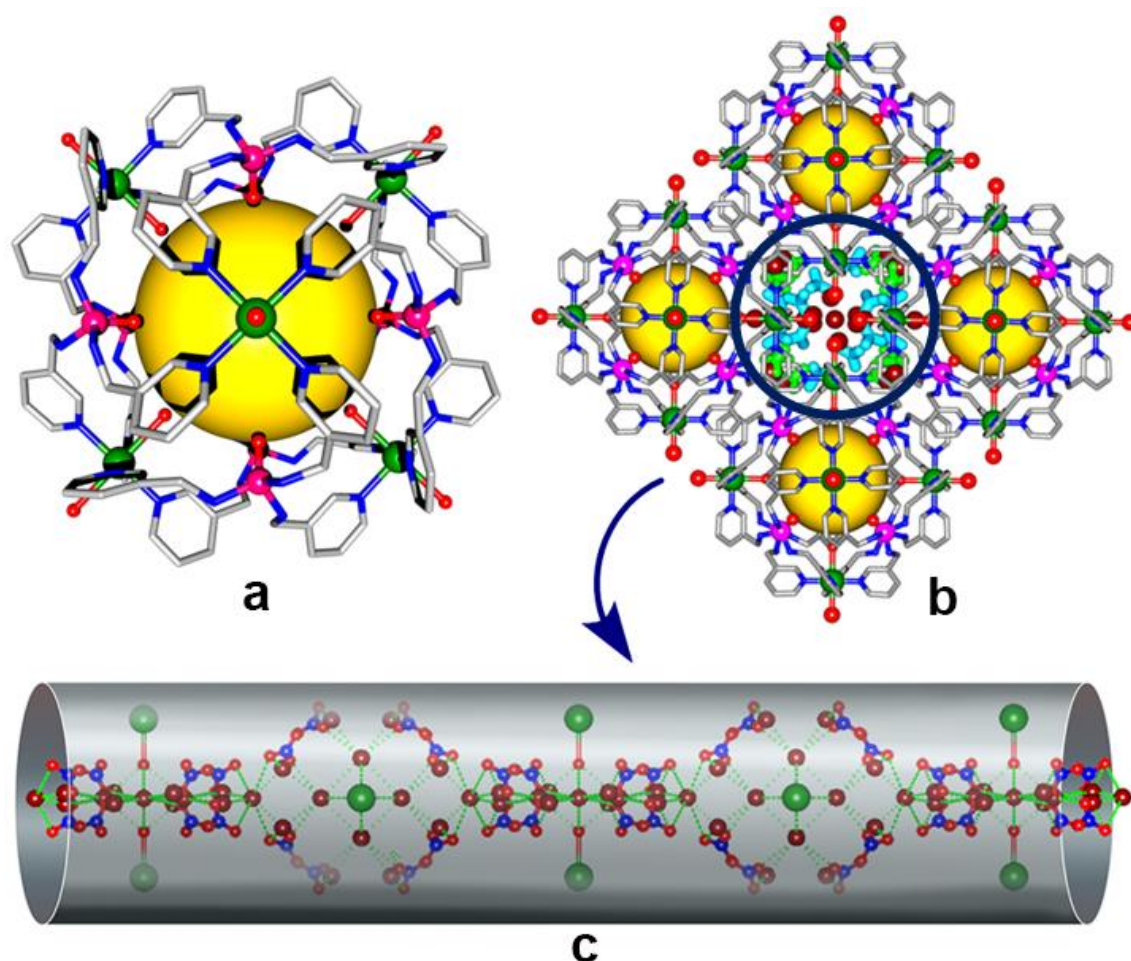


Figure 2.1: (a) Octahedral core structure of **1**. (b) Packing view of **1** showing the extrinsic voids filled with disordered nitrate anions and solvated water molecules. (c) Closer view of the H-bonded chains of nitrate anions and water molecules (both solvated and coordinated) that are responsible for the long-range polar order.

Crystals of **2** exhibit space group symmetry $I422$. The cages are linked via Cu-Cl-Cu bridges resulting in a two-dimensional square-grid type framework (Figure 2.2a). These grids are packed on top of each other so that nodes of one layer sit above squares of the next layer resembling the layered structure of SnF_4 ($I4/mmm$), (Appendix 2, Figure 2A.10).³⁰ The homochiral nature of the grid shows that the handedness is passed on from one cage to another via the chloride bridges. Neighboring layers have the same handedness which contrasts the racemic nature of the earlier reported 2D-framework that is supported by ligands $\text{PS}(\text{NH}^3\text{Py})_3$ (Appendix 2, Figure 2A.11).²⁸ Crystals of **2** have the composition $[\{\text{Cu}_6\text{Cl}_4(\text{H}_2\text{O})_6(\text{TPPA})_8\}(\text{NO}_3)_8 \cdot 60\text{H}_2\text{O}]_n$. The two non-bridging Cu-coordination sites are

occupied by water molecules. The endo sites bind chloride and water molecules with varying site-occupancies. As a result, the inside void of the cages is slightly smaller than **1** and measures 371 \AA^3 (6.1 % of total volume), while the external void volume, which again forms a 3D-channel network, makes up 37.1 % of the total volume (Appendix 2, Figure 2A.12). Similar as in **1** the inner voids are filled with water molecules, while the external channels contain nitrate ions and water molecules. Again, the contents of the voids are highly disordered; nitrate ions are distributed over two sites in pockets of the hydrogen bonded network (Figure 2.2b and Appendix 2, Figure 2A.13).

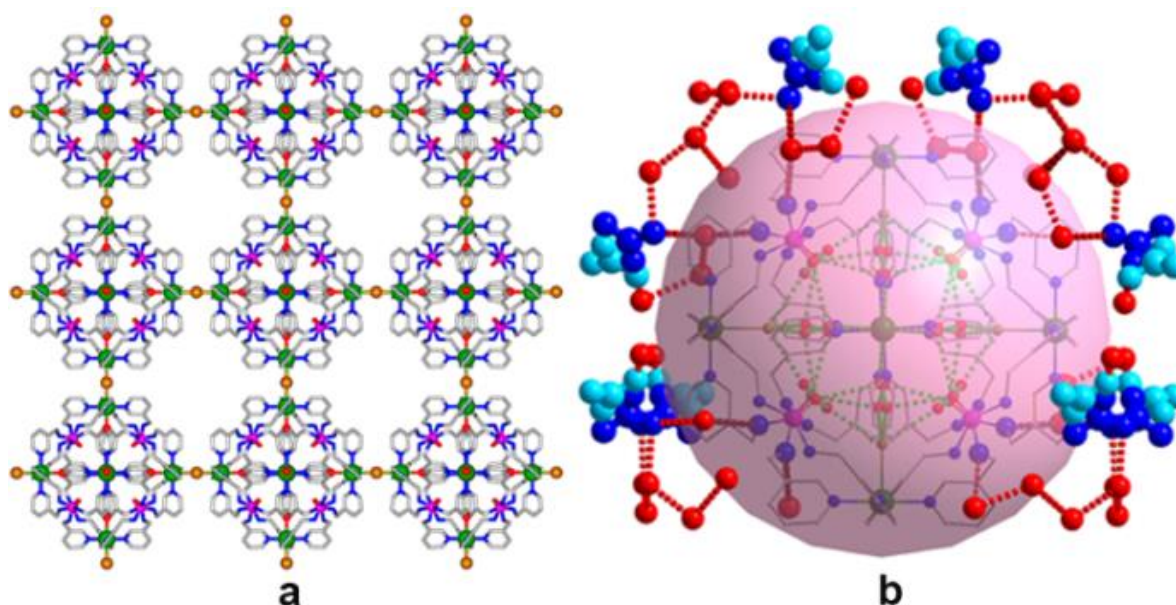


Figure 2.2: (a) View of the 2D-framework in **2** along the c-axis. b) View of disordered nitrate ions at the extrinsic pores of **2** and their interactions with disordered water molecules.

2.3.2 Ferroelectric and dielectric studies

The polarization in these compounds result from the toggling of nitrate ions as part of a hydrogen-bonded network with water molecules hosted by the mainly static framework of cages. It should be pointed out that the non-polar space groups of these compounds only reflect the symmetry of the rigid frameworks of cages, but not the disordered ions and molecules occupying the void spaces. Attempts to resolve the disorder by performing X-ray diffraction on polarized crystals remained futile due to the very low scattering contributions and diffuse character of nitrate ions and water molecules occupying the voids. The P-E hysteresis loops of **1** and **2** were measured on single crystals by using a Sawyer-Tower circuit at room temperature.

For **1**, the measurements can be performed along any of the two opposite crystal faces due to its cubic symmetry. The measurements on **2** were performed across the larger face that coincides with the [1 0 -1] plane (Appendix 2, Figure 2A.14). The nitrate anions and H-bonded solvated water molecules run parallel to this plane giving rise to long-range polar order that is reversible (Figure 2.2b).

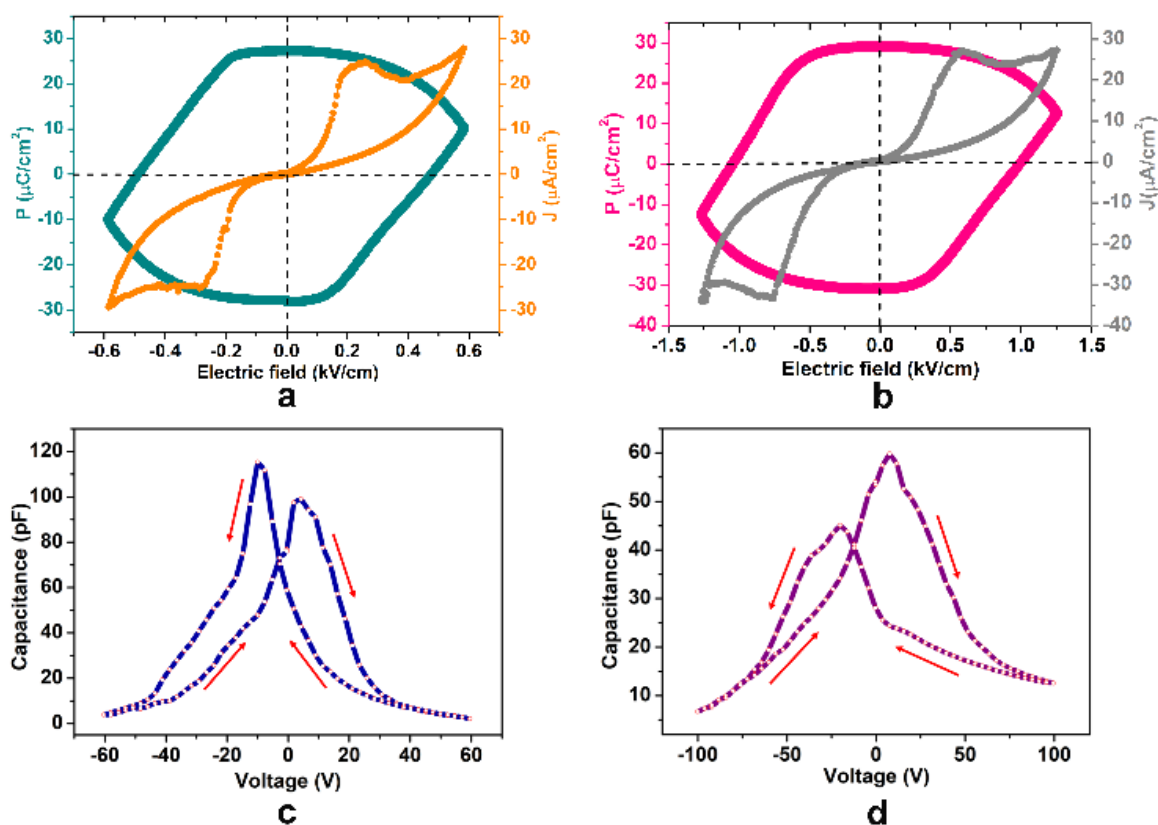


Figure 2.3: P-E hysteresis loop and the corresponding leakage current plots for the single crystals of (a) **1** and (b) **2**. The C-V curves of (c) **1** (d) **2**.

The P-E loop measured on single crystals of **1** at 0.1 Hz shows a high remnant polarization (P_r) value of $27.27 \mu\text{C}/\text{cm}^2$ (Figure 2.3a). The plot of current density (J) vs. electric field (E) gives two opposite peaks at the coercive fields (E_c) corresponding to two stable states with opposite polarity. Based on the J-E curves, the saturation polarization (P_s) and the coercive field (E_c) were found to be $25.91 \mu\text{C}/\text{cm}^2$ and $0.22 \text{ kV}/\text{cm}$, respectively. Similar measurements on **2** at 0.1 Hz, gave a P_r value of $29.09 \mu\text{C}/\text{cm}^2$ at room temperature. Also, from the obtained J-E curves, the P_s and E_c values were estimated to be $26.79 \mu\text{C}/\text{cm}^2$ and $0.56 \text{ kV}/\text{cm}$, respectively (Figure 2.3b). The considerably small coercive fields (E_c) suggest swift switching of the

ferroelectric domains in both these crystals. As observed in most supramolecular ferroelectrics, the obtained P_r values are smaller than the P_s for both **1** and **2**. Normally, the elastic energy of the bonds plays a vital role in domain evolution and the field dependent polarization switch. As a result, the supramolecular ferroelectrics based on weak interactions may often exhibit higher P_r than P_s due to the slower switching of polarization in comparison with those of the conventional oxide ferroelectrics.³¹

In addition to the P-E hysteresis curves, capacitance vs. voltage (C-V) curves were also measured for both these assemblies. The C-V characteristics were measured by sweeping the voltages up and down between 0 and ± 60 V and 0 and ± 100 V, respectively, on the crystals of **1** and **2** (Figures 2.3c and 2.3d). During the measurements, the capacitance peaks are observed upon ramping up the dc voltages and are absent when the dc voltages are brought down. Also, the C-V curves of **1** and **2** indicate hysteresis behavior with a characteristic butterfly like shape because of the reversal of polarization direction in the developed domain structure. The voltages corresponding to the capacitance peaks are related to the coercive field while the polarization switching matches closely with those obtained in their corresponding P-E loops and J-E curves. The switching asymmetry observed in the P-E loops and J-E curves can also be seen in the obtained C-V curves.³²⁻³⁴

The ferroelectric fatigue measurements on the crystals of **1** and **2** shows the retention of more than 50% of the P_r values even after 10^4 switching cycles (Figures 2.4a). Furthermore, the temperature dependent P-E hysteresis loop measurements supported the ferroelectric nature of the obtained P-E loops in **1**. For this, the thermal hysteresis measurement (THM) data were obtained on **1** in which remnant polarization is measured against temperature. Generally with increase in temperature, the P_r decreases. However, the polarization in **1** increases from 7.25 to 28.83 $\mu\text{C}/\text{cm}^2$ at 0.8 Hz along the same driving voltage when the temperature is increased from 299.5 K to 321.7 K (Figures 2.4b). Such increments in P_r may be attributed to the alignment of some randomly oriented domains with rising temperature.³⁵ With further increase in temperature, crystals develop cracks and loss of crystallinity. For **2**, such measurements gave inconsistent values probably due to the random loss of solvates upon heating the sample. In addition, room temperature second harmonic generation (SHG) experiments were performed on the finely grounded and unsieved powder samples of cages. The observed SHG efficiencies of 7.2% and 9.0% for **1** and **2**, respectively, corresponding to the standard potassium dihydrogen phosphate (KDP) sample confirms the ferroelectric nature of these materials.

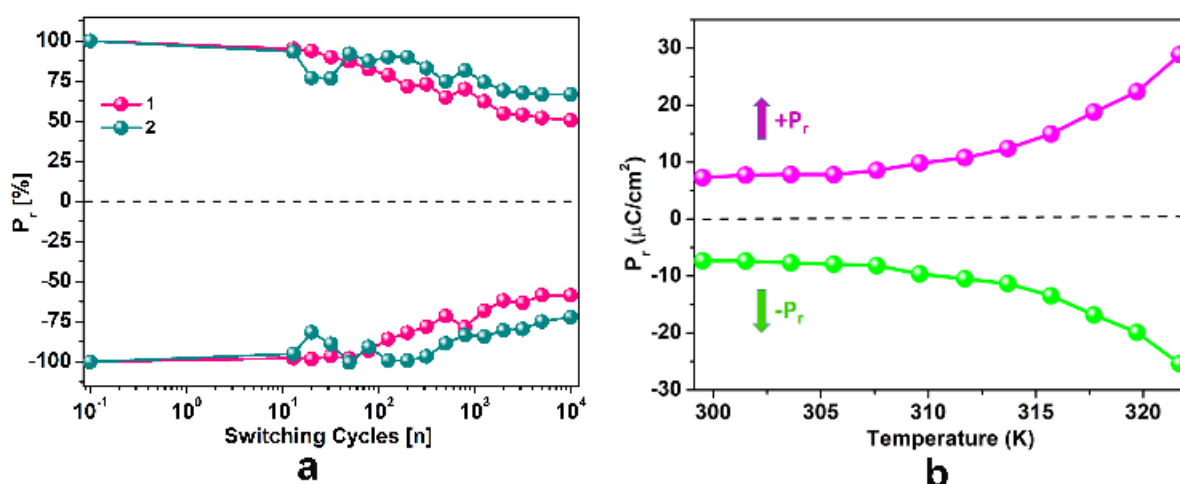


Figure 2.4: (a) Ferroelectric fatigue data for **1** and **2**. (b) Observed trends in the obtained remnant polarization (P_r) values of **1** as a function of temperature from the thermal hysteresis measurement (THM).

The temperature dependent dielectric permittivity measurements were carried out at various frequencies in the range of $10^3 - 10^6$ Hz on compact polycrystalline pellets of **1** and **2**. Figures 5a and 5b shows the dielectric curves for **1** and **2** with the anomaly peaks centered on 353 and 363 K, respectively. As with other similar cages,²⁶ the broad nature of these anomaly peaks is attributed to the desolvation of the framework. The observed ϵ' values at 1 kHz for **1** and **2** at 298 K are 55 and 32, respectively, shooting up to 635 and 111 at their respective anomaly points. The motional dynamics of the polar water molecules and the anions located in the pockets of cages could, in principal, result in such high relative permittivity values at higher temperatures.^{36, 37} Furthermore, the frequency independent behavior of the anomaly peaks implies that both **1** and **2** behave as relaxor-free dielectric materials. The plot of ϵ' vs. frequency for **1** and **2** shows a decreasing trend in the dielectric permittivity values with increasing frequencies indicating the engagement of all polarization mechanisms (Appendix 2, Figures 2A.15-2A.16.).^{1, 38} The corresponding dielectric loss ($\tan \delta$) plots also follow the same trend and support the high dielectric and ferroelectric nature of these assemblies (Appendix 2, Figures 2A.17-2A.20).

2.3.3 Solvent-dependent studies

In contrast to the previously reported cages,^{26, 28} the desolvation assisted dielectric transitions in **1** and **2** occur over much narrower temperature ranges. Variable temperature PXRD

measurements on the bulk samples of **1** and **2** indicate loss of crystallinity above the transition temperatures. The crystallinity, however, is restored after a few drops of the mother liquor were added (Figure 2.6 and Appendix 2, Figure 2A.21). The reversible switching between solvated crystalline and desolvated amorphous phases is mirrored in the FT-IR spectra recorded in the ATR mode. They show signals in the region of 3600-3100 cm^{-1} due to solvated molecules of water, which mostly disappear in the desolvated phase, but then re-emerge to their original intensity upon addition of mother liquor (Appendix 2, Figures 2A.22-2A.23). The 298 K single-crystal X-ray diffraction analyses of **1** and **2** indicate that the space group symmetries of their crystals remain unchanged and their unit cell parameters were closely similar to those obtained from 100 K data. In fact, the crystal structure of **1** could be solved at 298 K that shows large thermal ellipsoids particularly to the organic parts of the molecule (Appendix 2, Table 2A.21-2A.2 and Figure 2A.24).

The TGA of **1** and **2** shows the initial weight loss of around 18% at 70 °C due to the loss of both solvated and coordinated water molecules. Both **1** and **2** were found to be stable up to 170 °C. The TGA of the desolvated samples of **1** and **2** (**1**_{desolvated} and **2**_{desolvated}) shows no major weight losses at the initial temperatures and shows the stability of the frameworks up to 170 °C. However, the original TGA profiles of **1** and **2** were almost restored upon resolution by adding a few drops of their corresponding mother liquor. (Appendix 2, Figures 2A.25-2A.28). Furthermore, the P-E loop measurements performed on compacted pellet samples of **1**_{desolvated} and **2**_{desolvated} shows resistor-type behaviour, signifying the role of the solvate molecules in the packing structure of **1** and **2** in restoring the long-range order responsible for their ferroelectric polarization (Appendix 2, Figures 2A.29).²⁷

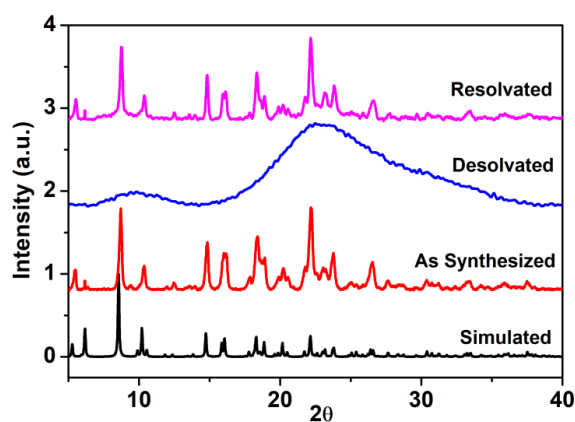


Figure 2.6: Powder X-ray diffraction (PXRD) pattern for the various samples of **2**.

2.4 Conclusion

In conclusion, we have synthesized an octahedral Cu_6L_8 cage containing the more flexible tripodal tris(N-(3-picolyl))phosphoramidate ligand. Formation of the 2D-framework was achieved by introducing bridging chloride ions. Both **1** and **2** showed ferroelectric response due to the toggling of nitrate anions within a hydrogen bonded network with water molecules. The observed P_r values of $27.27 \mu\text{C}/\text{cm}^2$ (**1**) and $29.09 \mu\text{C}/\text{cm}^2$ (**2**) are consistent with those reported for similar types of cage compounds. The ferroelectric nature in **1** and **2** were further confirmed by butterfly-like hysteresis loops obtained in C-V measurements as well as by the thermal hysteresis measurements in the case of **1**. The observation of high relative permittivity supports the presence of stable dipoles in both of these assemblies. These results shed further light on the role of unconventional type of mechanisms such as toggling of anions that control the origin of ferroelectric behavior in metal-ligand assemblies.

2.5 References

1. A. M. Glass, M. E. Lines, 1977.
2. Y. Yuan, Z. Xiao, B. Yang and J. Huang, *J. Mater. Chem. A* 2014, **2**, 6027-6041.
3. C. A. P. de Araujo, J. D. Cuchiaro, L. D. McMillan, M. C. Scott and J. F. Scott, *Nature*, 1995, **374**, 627-629.
4. S. Das and J. Appenzeller, *Nano Lett.*, 2011, **11**, 4003-4007.
5. L. W. Martin and A. M. Rappe, *Nat. Rev. Mater.*, 2016, **2**, 16087.
6. S. Deswal, S. K. Singh, P. Rambabu, P. Kulkarni, G. Vaitheeswaran, B. Praveenkumar, S. Ogale and R. Boomishankar, *Chem. Mater.*, 2019, **31**, 4545-4552.
7. T. Vijayakanth, A. K. Srivastava, F. Ram, P. Kulkarni, K. Shanmuganathan, B. Praveenkumar and R. Boomishankar, *Angew. Chem. Int. Ed.*, 2018, **57**, 9054-9058.
8. A. Yadav, A. K. Srivastava, P. Kulkarni, P. Divya, A. Steiner, B. Praveenkumar and R. Boomishankar, *J. Mater. Chem. C*, 2017, **5**, 10624-10629.
9. T. Vijayakanth, F. Ram, B. Praveenkumar, K. Shanmuganathan and R. Boomishankar, *Chem. Mater.*, 2019, **31**, 5964-5972.
10. R. Ramesh, J. Lee, T. Sands, V. G. Keramidas and O. Auciello, *Appl. Phys. Lett.*, 1994, **64**, 2511-2513.
11. B. H. Park, B. S. Kang, S. D. Bu, T. W. Noh, J. Lee and W. Jo, *Nature*, 1999, **401**, 682-684.

12. J. Zylberberg, A. A. Belik, E. Takayama-Muromachi and Z.-G. Ye, *Chem. Mater.*, 2007, **19**, 6385-6390.
13. T. Furukawa, M. Date and E. Fukada, *J. Appl. Phys.*, 1980, **51**, 1135-1141.
14. G.-C. Xu, X.-M. Ma, L. Zhang, Z.-M. Wang and S. Gao, *J. Am. Chem. Soc.*, 2010, **132**, 9588-9590.
15. P. Jain, N. S. Dalal, B. H. Toby, H. W. Kroto and A. K. Cheetham, *J. Am. Chem. Soc.*, 2008, **130**, 10450-10451.
16. X. Duan, Q. Meng, Y. Su, Y. Li, C. Duan, X. Ren and C. Lu, *Chem. – Eur. J.*, 2011, **17**, 9936-9943.
17. L. Wen, L. Zhou, B. Zhang, X. Meng, H. Qu and D. Li, *J. Mater. Chem.*, 2012, **22**, 22603-22609.
18. D.-W. Fu, H.-L. Cai, Y. Liu, Q. Ye, W. Zhang, Y. Zhang, X.-Y. Chen, G. Giovannetti, M. Capone, J. Li and R.-G. Xiong, *Science*, 2013, **339**, 425-428.
19. S. Horiuchi and Y. Tokura, *Nat. Mater.*, 2008, **7**, 357.
20. S. Horiuchi, F. Ishii, R. Kumai, Y. Okimoto, H. Tachibana, N. Nagaosa and Y. Tokura, *Nat. Mater.*, 2005, **4**, 163-166.
21. A. S. Tayi, A. K. Shveyd, A. C. H. Sue, J. M. Szarko, B. S. Rolczynski, D. Cao, T. J. Kennedy, A. A. Sarjeant, C. L. Stern, W. F. Paxton, W. Wu, S. K. Dey, A. C. Fahrenbach, J. R. Guest, H. Mohseni, L. X. Chen, K. L. Wang, J. F. Stoddart and S. I. Stupp, *Nature*, 2012, **488**, 485.
22. W. Zhang, H.-Y. Ye and R.-G. Xiong, *Coord. Chem. Rev.*, 2009, **253**, 2980-2997.
23. W. Zhang and R.-G. Xiong, *Chem. Rev.*, 2012, **112**, 1163-1195.
24. X.-Y. Dong, B. Li, B.-B. Ma, S.-J. Li, M.-M. Dong, Y.-Y. Zhu, S.-Q. Zang, Y. Song, H.-W. Hou and T. C. W. Mak, *J. Am. Chem. Soc.*, 2013, **135**, 10214-10217.
25. S. Horiuchi, Y. Tokunaga, G. Giovannetti, S. Picozzi, H. Itoh, R. Shimano, R. Kumai and Y. Tokura, *Nature*, 2010, **463**, 789.
26. A. Yadav, P. Kulkarni, B. Praveenkumar, A. Steiner and R. Boomishankar, *Chem. – Eur. J.*, 2018, **24**, 14639-14643.
27. A. K. Srivastava, P. Divya, B. Praveenkumar and R. Boomishankar, *Chem. Mater.*, 2015, **27**, 5222-5229.
28. A. K. Srivastava, B. Praveenkumar, I. K. Mahawar, P. Divya, S. Shalini and R. Boomishankar, *Chem. Mater.*, 2014, **26**, 3811-3817.
29. G. M. Sheldrick, *Acta Crystallogr. A*, 2008, **64**, 112-122.

30. A. F. WELLS, 2012.
31. H. Ma, W. Gao, J. Wang, T. Wu, G. Yuan, J. Liu and Z. Liu, *Adv. Electron. Mater.*, 2016, **2**, 1600038.
32. L. Filip, L. Pintilie, V. Stancu and I. Pintilie, *Thin Solid Films*, 2015, **592**.
33. L. Pintilie, M. Lisca and M. Alexe, *Appl. Phys. Lett.*, 2005, **86**, 192902.
34. K. Liang, A. Buditama, D. Chien, J. Cui, P. L. Cheung, S. Goljahi, S. H. Tolbert, J. P. Chang and C. S. Lynch, *J. Appl. Phys.*, 2015, **117**, 174107.
35. Q. Pan, Z.-B. Liu, H.-Y. Zhang, W.-Y. Zhang, Y.-Y. Tang, Y.-M. You, P.-F. Li, W.-Q. Liao, P.-P. Shi, R.-W. Ma, R.-Y. Wei and R.-G. Xiong, *Adv. Mater.*, 2017, **29**, 1700831.
36. M. Usman, C.-H. Lee, D.-S. Hung, S.-F. Lee, C.-C. Wang, T.-T. Luo, L. Zhao, M.-K. Wu and K.-L. Lu, *J. Mater. Chem. C* 2014, **2**, 3762-3768.
37. H. Cui, B. Zhou, L.-S. Long, Y. Okano, H. Kobayashi and H. Tanaka, *Angew. Chem. Int. Ed.*, 2008, **47**, 3376-3380.
38. I. Stassen, N. Burtch, A. Talin, P. Falcaro, M. Allendorf and R. Ameloot, *Chem. Soc. Rev.*, 2017, **46**, 3185-3241.

Chapter 3

**Visualization of Domain Structure and
Piezoelectric Energy Harvesting in a
Ferroelectric Metal-Ligand Cage**

3.1 Introduction

Developing clean and renewable energy scavenging methods is of growing interest to meet the global mandate of reducing the carbon footprint. Mechanical force is an abundant energy resource that is readily available in our environment and yet remains unprocessed.^{1, 2} Miniaturized energy conversion systems (nanogenerators) based on ferroelectrics are attractive since materials with high remnant polarization and low rigidity yield significant piezoelectric responses.³⁻⁶ Until now, most commercial piezoelectric nanogenerators have been mainly assembled from traditional inorganic ceramics such as BaTiO₃ and organic polymers such as polyvinylidene fluoride (PVDF) because of their high polarization.⁴⁻⁷ Despite that, with the increasing demand for devices based on thin films, the use of inorganic ferroelectrics for this application is hampered by their heavy metal content and complicated film-forming procedures. In contrast, PVDF films require external additives and a high-voltage poling process.⁸⁻¹⁰ Thus, alternate materials such as single-component organics, two-component hybrids and metal-ligand assemblies have been investigated for their ferroelectric properties and nanogenerator applications.^{11, 12} In this context, the use of polar metal-ligand systems is desirable as they can be easily assembled from environmentally benign light-weight transition metal ions and simple organic ligands. Our group has been interested in the design of ferroelectric [M^{II}₆L₈]¹²⁺ type metal-ligand octahedral cages supported by tripodal N-donor ligands.¹³⁻¹⁵ Though the ferroelectricity in these axially symmetric cages was probed by typical P-E hysteresis loop measurements, visualization of ferroelectric domain structures and piezoelectric energy harvesting on their thin films were not explored until now due to the challenges associated with the solution stability of these framework assemblies.

Herein, we report a new Co(II) and Ni(II)-based ferroelectric metal-organic cage [Co₆(H₂O)₁₂(TPTA)₈](NO₃)₁₂·48H₂O (**1**) [Ni₆(H₂O)₁₂(TPTA)₈](NO₃)₁₂·37H₂O (**2**) along with the entire portfolio of studies on its noncentrosymmetric structure, ferroelectric behaviour, and piezoelectric energy harvesting functionality. Ferroelectric hysteresis loop measurements on a single crystal of **1** and **2** showed a saturated polarization (P_s) of 3.72 and 15.58 μC/cm² respectively. By employing the piezoresponse force microscopy (PFM) technique, we could visualize the ferroelectric phase and amplitude images on its micrometer-scaled crystalline thin film grown on a Pt substrate. We have also demonstrated the switchable stress-voltage hysteresis of **1** and **2** using the PFM spectroscopy. Moreover, we were successful in obtaining flexible composites of **1** and **2** with polydimethylsiloxane (PDMS) polymer, which gave a

maximum open-circuit voltage (V_{pp}) of 9.54 V for 20 wt% in case of **1**-PDMS and 25.35 V for its 10 weight percent (wt%) **2**-PDMS nanogenerator device. Energy storage was demonstrated by harvesting the output voltages obtained from the 10 wt% **2**-PDMS device for charging electrolytic capacitors. To the best of our knowledge, this is the first report on a discrete metal-ligand cage that reports both the visualization of ferroelectric domain structures and the fabrication of its polymer composite devices as electric energy nanogenerators.

3.2 Experimental Section

3.2.1 General Remarks

All manipulations involving phosphorous halides and solvent purification were performed under a dry nitrogen atmosphere in standard Schlenk-glassware. The precursors $\text{Ni}(\text{NO}_3)_2 \cdot 6\text{H}_2\text{O}$, $\text{Co}(\text{NO}_3)_2 \cdot 6\text{H}_2\text{O}$ and 3-aminopyridine was purchased from Merck and used as received. PSCl_3 was purchased locally and was distilled prior to use. The ligand **TPTA** was synthesized by following our earlier reported procedure.¹⁴ The powder X-ray diffraction (PXRD) data were obtained from a Bruker-D8 Advance diffractometer. Thermal analysis (TGA) data have been obtained from a Perkin-Elmer STA-6000 thermogravimetric analyzer. Elemental analyses were performed on a Vario-EL cube elemental analyzer. FT-IR in attenuated total reflectance (ATR) mode was taken on neat samples on a Bruker Alpha spectrophotometer. Melting points were obtained using an Electro thermal melting point apparatus and they were uncorrected.

3.2.2 Synthesis

3.2.2.1 Compound 1: To a stirred solution of **TPTA** (40 mg, 0.116 mmol) in MeOH (4 mL), $\text{Co}(\text{NO}_3)_2 \cdot 6\text{H}_2\text{O}$ (102 mg, 0.350 mmol) in H_2O (1 mL) was added dropwise. The resulting blue solution was filtered through a cellite pad and left for crystallization. The suitable blue block crystals for SCXRD analysis were obtained after five days. Yield: 65 %. M.P. 190-195 °C. FT-IR data on powder (cm^{-1}): 3396, 3224, 1583, 1327, 1270, 1116, 1062, 1031, 941, 807, 693, 603. Anal. Calcd. for $\text{C}_{120}\text{H}_{252}\text{N}_{58}\text{Co}_6\text{O}_{96}\text{P}_8\text{S}_8$: C, 29.41; H, 5.18; N, 16.57; S, 5.23. Found: C, 28.42; H, 5.20; N, 16.51; S, 5.12.

3.2.2.2 Compound 2: To a stirred solution of **TPTA** (40 mg, 0.116 mmol) in MeOH (4 mL), $\text{Ni}(\text{NO}_3)_2 \cdot 6\text{H}_2\text{O}$ (102 mg, 0.350 mmol) in H_2O (1 mL) was added dropwise. The resulting blue solution was filtered through a cellite pad and left for crystallization. The suitable blue block crystals for SCXRD analysis were obtained after five days. Yield: 62 %. M.P. 190-195 °C. FT-

IR data on powder (cm⁻¹): 535.75, 693.60, 942.20, 1117.05, 1195.83, 1324.91, 1387.76, 1502.48, 1584.56, 1627.16, 2966.77, 3189.22. Anal. Calcd. for C₁₂₀H₂₁₈N₆₀O₈₅P₈S₈Ni₆: C, 30.55; H, 4.66; N, 17.81; S, 5.44. Found: C, 30.82; H, 4.94; N, 17.62; S, 5.35.

3.2.3 Crystallography

Reflections of **1** and **2** were collected on a Bruker Smart Apex Duo diffractometer at 100 K using MoK α radiation ($\lambda = 0.71073$ Å). Structures were refined by full-matrix least squares against F² using all data using SHELX. All non-hydrogen atoms were refined anisotropically if not stated otherwise. Hydrogen atoms of water molecules were therefore omitted in the refinement due to the high ambiguity in their positions. The nitrate anions and solvates were disordered in the asymmetric unit. The disordered fragments were refined by using similar distances and similar U-restraints (SAME/SIMU) routines of the SHELXL.

Table S1. Crystallographic data for **1**.

Compound	1	2
Chemical formula	C ₁₂₀ H ₂₅₂ N ₅₈ Co ₆ O ₉₆ P ₈ S ₈	C ₁₂₀ H ₂₁₈ N ₆₀ Ni ₆ O ₈₅ P ₈ S ₈
Formula weight	4768.56	4718.03
Temperature	100 K	100 K
Crystal system	Tetragonal	Tetragonal
Space group	I4	I4
a (Å); α (°)	21.021(6) Å; 90°	21.034(8) Å; 90°
b (Å); β (°)	21.021(6) Å; 90°	21.034(8) Å; 90°
c (Å); γ (°)	24.278(6) Å; 90°	24.440(9) Å; 90°
V (Å ³); Z	10728(6) Å ³ ; 2	10813(9) Å ³ ; 2
ρ (calc.) mg m ⁻³	1.475	1.449
μ (Mo K α) mm ⁻¹	0.680	0.747
2 θ _{max} (°)	50.484	50.484
R(int)	0.1014	0.0978
Completeness to θ	99.5 %	100 %
Data / param.	13276/611	9530/602
GOF	1.066	1.066

R1 [$F > 4\sigma(F)$]	0.1639	0.1147
wR2 (all data)	0.3364	0.2865
max.peak/hole ($e \cdot \text{\AA}^{-3}$)	0.908/-1.088	1.617/-1.191

3.2.4 Non-linear Optical Measurements

Non-linear optical studies were performed using an attenuated output from a Coherent Astrella Ti:sapphire regenerative amplifier providing 800 nm laser pulses at a 1 kHz repetition rate and of 75 fs duration. A Kurtz-Perry test¹⁶ was performed at 293 K. Potassium dihydrogen phosphate (KDP) was used as a second harmonic generation (SHG) reference. The single crystals of **1** and **2**; and those of KDP were crushed with a spatula and sieved through a mini-sieve set (Aldrich), collecting a microcrystal size fraction of 250–177 μm . Next, size-graded samples were fixed between microscope glass slides (forming tightly packed layers), sealed, and mounted to the sample holder. Average power of an 800 nm beam, equal to 245 mW, - with a spot area of 0.5 cm^2 was employed. The laser beam was directed onto samples at 45° and was unfocused in all cases. Signal-collecting optics, mounted to the glass optical fiber, were placed perpendicularly to the plane of the sample (backscattering geometry), which was placed on a horizontally aligned holder. Scattered pumping radiation was suppressed using a 750 nm short-pass dielectric filter (FESH0750, Thorlabs). The emission spectra were recorded by an Ocean Optics Flame T spectrograph.

3.2.5 Preparation of the Thin Film Crystallites of **1** and **2** for PFM Measurements

The compound **1** and **2** (10 mg) was taken along with 0.5 mL of distilled water in an Eppendorf and sonicated until the dissolution of **1**. The solution was subsequently drop-casted on the Pt substrate and left to stand at room temperature. The pink and blue-coloured micrometer-sized crystallites of **1** and **2** respectively were observed on the Pt substrate after one hour.

3.2.6 Piezoresponse Force Microscopy Characterization

PFM visualization of the ferroelectric domain structure on **1** and **2** microcrystal surface and the thin film was carried out using a commercial AFM system [MFP-3D, Asylum Research in the contact mode (Vector mode)]. A conductive Pt-coated silicon probe was used for domain imaging in lateral and vertical orientation [SCM-PIT-V2 by Bruker, (Pt/Ir coated tip) with a spring constant of 2.8 N/m and a tip radius of 25 nm]. Resonance-enhanced PFM mode was used to enhance the signal with a frequency of 285 kHz and an AC amplitude of 2 V. The d_{33}

values were calculated by recording amplitude the signal at the first contact resonance of the cantilever by changing the tip bias voltage. For non-centrosymmetric materials, due to the converse piezoelectric effect, the $\text{Amp (cantilever)} = d_{33} \times V_{AC} \times Q_{\text{factor (tip)}}.$ ¹⁷ We obtained the amplitude signal by varying the AC bias, and later calculated the d_{33} values using the above equation. The switching ability of the domains on thin films was checked by the application of external DC bias of ± 50 V using the PFM tip in contact mode.

3.2.7 Ferroelectric and Dielectric Measurements

The ferroelectric hysteresis loops for **1** and **2** were measured on single crystals of dimensions of 2.33 mm and 2.72 mm by using a Sawyer-Tower circuit. The single crystals were electroded by sticking the aluminium tape on the broad facets of the crystal. The measurements pertaining to the polarization were recorded using a hysteresis loop analyser (TF Analyser 2000E, aixACCT Germany). Leakage current was measured dynamically for various voltage steps during the hysteresis loop measurements.

The dielectric measurements were performed on a powder-pressed sample of **1** and **2** compacted in the form of discs (of approximately 10 mm diameter and 1 mm thickness). The compacted discs were subsequently electroded using aluminium adhesive foils for the measurements. The dielectric characteristics of **1** and **2** were measured using the Novocontrol, Dielectric Spectrometer.

3.2.8 Preparation of the 1-PDMS and 2-PDMS Composite Films and Testing of the Composite Devices

Firstly, the PDMS solution was prepared by adding the silicone elastomer base (Sylgard 184A) and silicone elastomer curing agent (Sylgard 184B) in a 10:1 ratio as stated in the Dow Sylgard 184 Kit. Pre-calculated amounts of **1** and **2** were then dispersed into the PDMS to prepare composites of varying (1, 5, 10, 15) weight percent (wt %) compositions. After uniform mixing, the formulated composites were drop-casted onto the aluminium integrated PET sheet with area of $2.5 \times 2.5 \text{ cm}^2$ and let it dry for 24 hours followed by placing the aluminium tape of size $2 \times 2 \text{ cm}^2$ on the cured composite film. The aluminium integrated PET sheet serves as a bottom electrode and aluminium tape serves as a top electrode. The final device architecture was achieved by establishing electrical contacts to the end of the electrodes followed by the enclosure of the entire device with the Kapton tape to protect the device from any physical damages. Further, the energy harvesting performance of all the **1**-PDMS and **2**-PDMS

composite devices was measured by using a home-built impact measurement setup. The output voltages were measured using a Tektronix 2024 mixed-signal oscilloscope operating at an input impedance of 1 M Ω .

3.3 Results and Discussions

3.1 Synthesis, Characterization and Crystal Structures: The Co-cage (**1**) and Ni-cage (**2**) of formula $[\text{Co}_6(\text{H}_2\text{O})_{12}(\text{TPTA})_8] \cdot (\text{NO}_3)_{12} \cdot 48\text{H}_2\text{O}$ and $[\text{Ni}_6(\text{H}_2\text{O})_{12}(\text{TPTA})_8] \cdot (\text{NO}_3)_{12} \cdot 37\text{H}_2\text{O}$ was isolated at room temperature as hexagonal-shaped pink and blue crystals respectively in a 3:1 reaction mixture containing the ligand (TPTA)^{13, 14} and $\text{Ni}(\text{NO}_3)_2 \cdot 6\text{H}_2\text{O}$ in MeOH/H₂O (Figures 3.1a-d). The single-crystal X-ray diffraction (SCXRD) analysis reveals that **1** and **2** both crystallizes in the tetragonal polar space group *I4*. The IR spectrum of **1** and **2** gives characteristic peaks for all the functional groups in it and its bulk phase purity was confirmed by powder X-ray diffraction (PXRD) analysis (Figures A.1, A.2, Appendix 3). All the metal ions of the $[\text{Co}_6(\text{H}_2\text{O})_{12}(\text{TPTA})_8]^{12+}$ and $[\text{Ni}_6(\text{H}_2\text{O})_{12}(\text{TPTA})_8]^{12+}$ cage core exhibit the characteristic Jahn-Teller distorted octahedral geometry. Each Co^{2+} and Ni^{2+} in the cationic cage is coordinated equatorially with the four $\text{N}_{\text{pyridyl}}$ functionalities from the four distinct TPTA ligands, and aqua ligands establish their axial contacts.

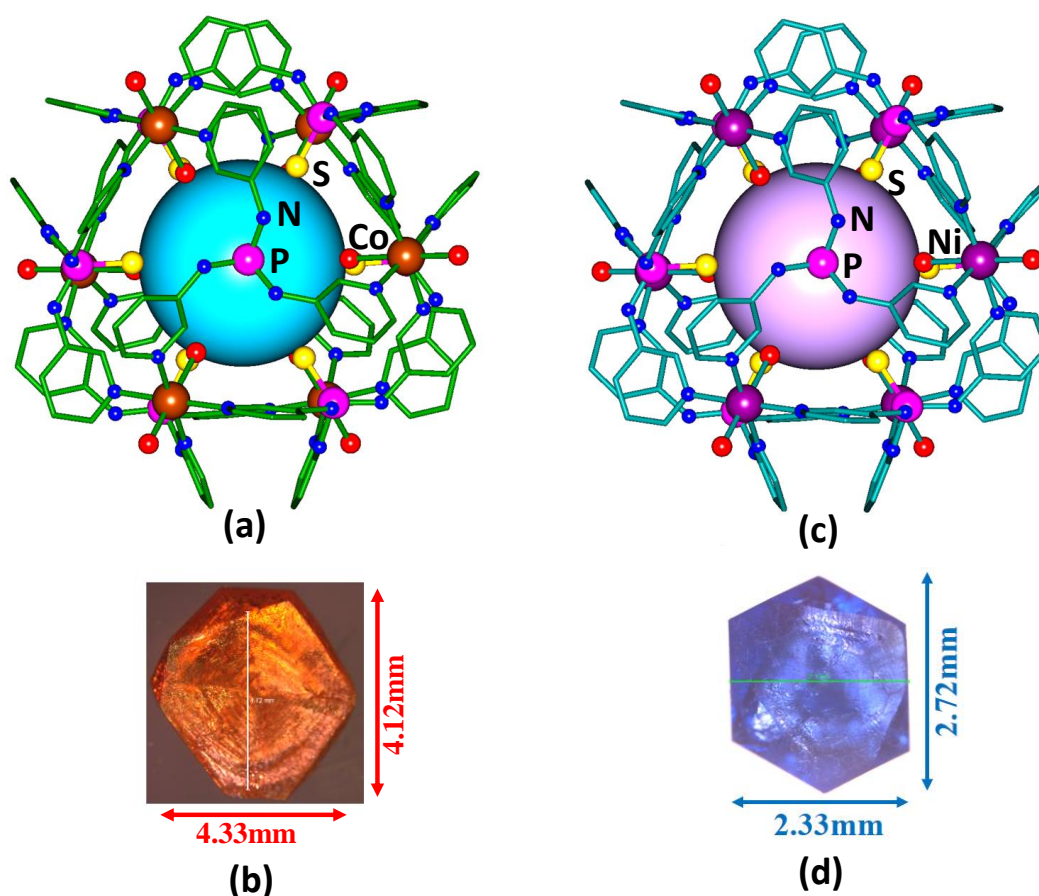


Figure 3.1: Crystal structure of **1** (a) and **2** (c) viewed along the three-fold axes. Microscope images of single crystals of **1** (b) and **2** (d).

All eight TPTA ligands adopt a *syn* coordination mode with the M^{2+} ions and their P=S bonds are directed inward towards the centre of the cage. The symmetry of the cationic cage is cubic (432 point group, octahedral O), in which the six M^{2+} occupy the three 4-fold axes and the P=S motifs of the ligands are located on the 3-fold axes. However, the crystal exhibits a reduced symmetry (tetragonal C_4) due to the presence of disordered nitrate anions and solvate water molecules in its lattice. Furthermore, the charge-balancing nitrate anions and water molecules interact with the cage via hydrogen bonding with the metal-bound aqua ligands and the amido and thiophosphoryl groups of the TPTA ligand.

3.3.2 SHG, Ferroelectric, Dielectric and Piezoelectric Studies

Apart from the SCXRD data, the non-centrosymmetric structure of **1** and **2** is firmly evidenced by the second harmonic generation (SHG) experiments, which gave a clear signal at 400 nm with a relative SHG efficiency of 0.03 for **1** and 0.08 for **2** versus the KDP reference upon

irradiation with 800 nm femtosecond laser pulses (Figure A3.3, Appendix 3). The ferroelectric P-E loop measurements at room temperature were performed on a single crystal of **1** and **2** along its larger facet oriented in the crystallographic (-1 0 1) plane (Figure A3.4, Appendix 3). A characteristic rectangular hysteresis loop was observed for **1** and **2**, with a saturation polarization value of 3.72 and 15.58 $\mu\text{C}/\text{cm}^2$. The leakage current density versus electric field plot (J-E) shows a very low leakage all along the measurements and peaks only at the coercive fields (Figures 3.2a,b). Such attributes confirm the ferroelectric origin of the observed hysteresis loop. The coercive field of the measurement is only 0.55 and 0.28 kV/cm, indicating the facile switching of the polarizable domains in **1** and **2** respectively at low electric fields.

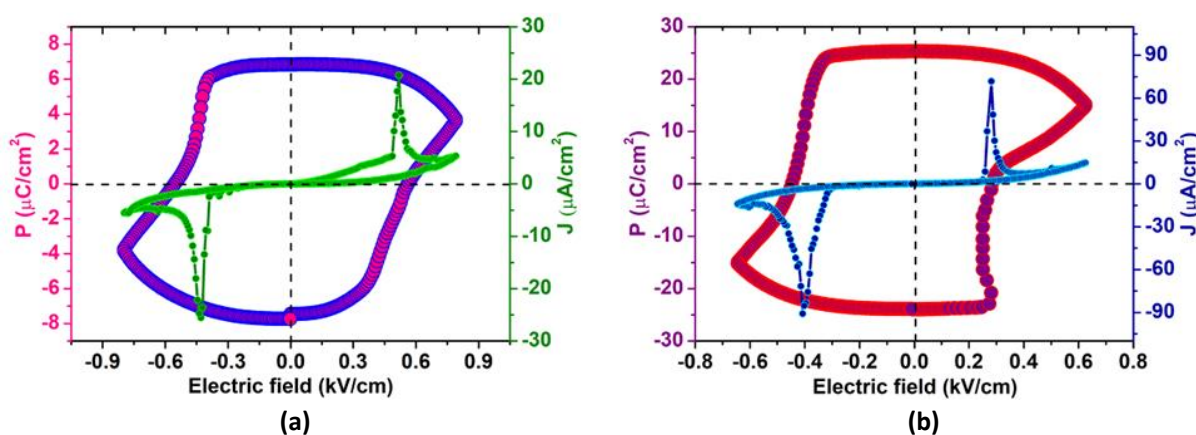


Figure 3.2: P-E hysteresis loop and its corresponding leakage current density plot for a single-crystal of **1** (a) and **2** (b).

Furthermore, the dielectric permittivity studies on a compacted polycrystalline sample of **1** and **2** were performed to understand the polarization of the bulk material. The real part of dielectric permittivity vs. temperature (ϵ' vs. T) plots at various frequencies show broad peaks for a wide range of temperatures (Figure 3.3a,b). A maximum ϵ' value of 120.4 and 73.90 is observed for **1** and **2** at 40 °C at a 1 kHz frequency. The broad nature of the dielectric peak and large ϵ' values signify the change in the polarizability of loosely placed solvate molecules (of the lattice) with temperature.¹⁸⁻²⁰ It is apparent that the dielectric permittivity maxima decrease as the frequency increases from 1 kHz to 1 MHz, while the maxima show the marginal shift to higher temperatures. Such shifts in intensity maxima were also observed for $\tan \delta$ (dielectric loss factor) vs. T plot (Figures 3.3c,d). This behaviour can be attributed to the gradual desolvation at higher temperatures, leading to a dielectric relaxation in **1** and **2**.²¹⁻²³ The

desolvation-assisted anomaly is further confirmed by the TGA, DSC and VT-PXRD (Figures A3.5-A3.7, Appendix 3). The frequency-dependent measurements gave higher ϵ' values at lower frequencies due to the contribution of all four polarization mechanisms (Figure A3.8, Appendix).²⁴

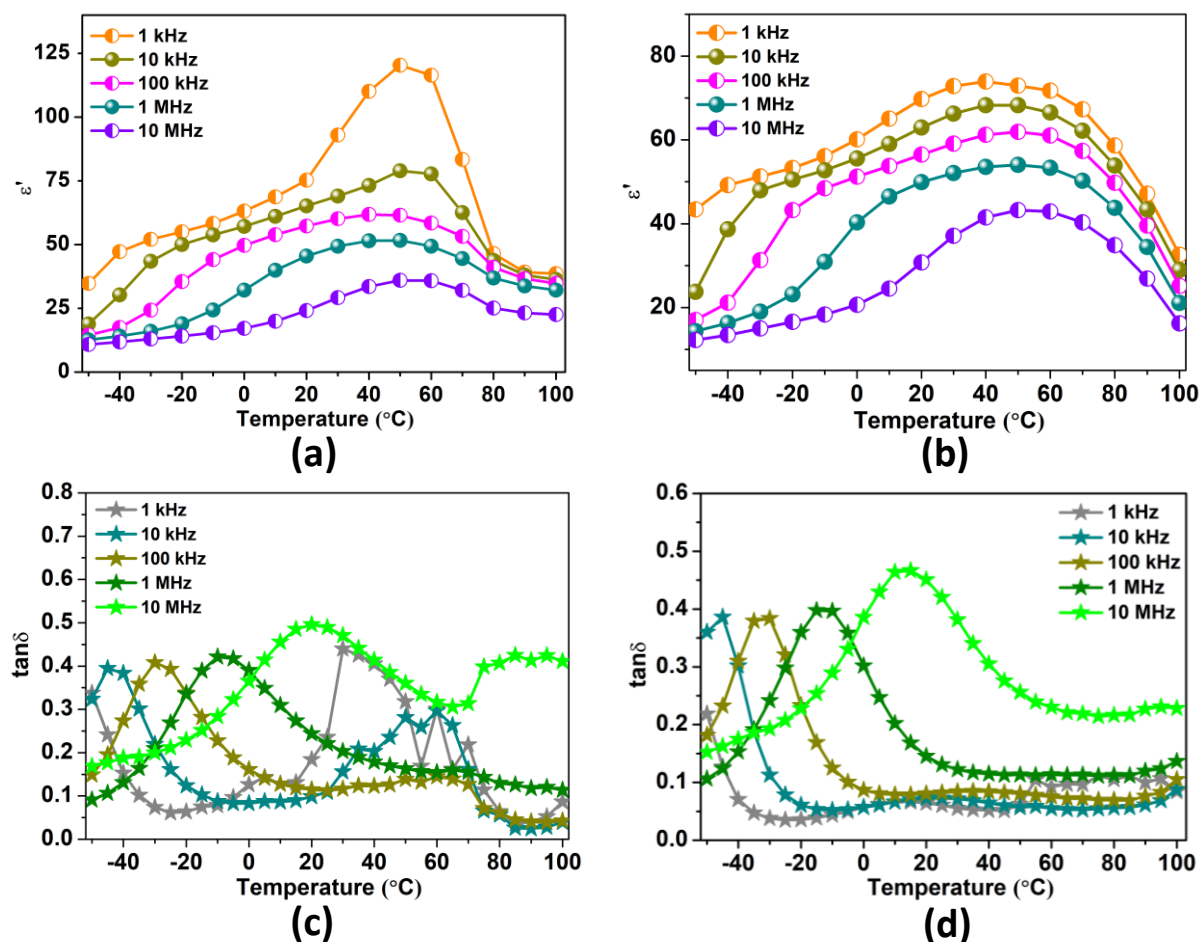


Figure 3.3: The ϵ' vs. T plots for **1** (a) and **2** (b) at various frequencies. The loss factor ($\tan\delta$) of **1** (c) and **2** (d).

It has been reported that non-covalent bonds are often polar due to a disparity in the electron densities between the interacting motifs.^{25,26} However, to establish a long-range order, such induced dipoles must reside within an ordered noncentrosymmetric structure. In the case of **1** and **2**, the polarity originates from the switching (toggling) of nitrate anions and some of the solvates between two unique positions, generating two domains of the opposite polarity. Interestingly, one of the two domains exists predominantly under each of the sweeping

directions of the electric field, resulting in the net polarization of the crystal (Figure A3.9, Appendix 3).

To further probe the polarization dynamics, PFM experiments in the vertical and lateral PFM (VPFM and LPFM) modes were performed.^{27, 28} For this experiment, a thin film of **1** and **2** was prepared on a Pt substrate by the drop-casting method (Figure A3.10). Figures 3.4a,b,c shows the 3D topography, vertical amplitude and phase mappings for **1**; Figures 3.4 d,e,f shows the topography, vertical amplitude and phase mappings for **2**. Also, the VPFM performed directly on a bulk single crystal of **2** indicates the presence of multiple domains on its surface (Figure A3.11, Appendix 3).

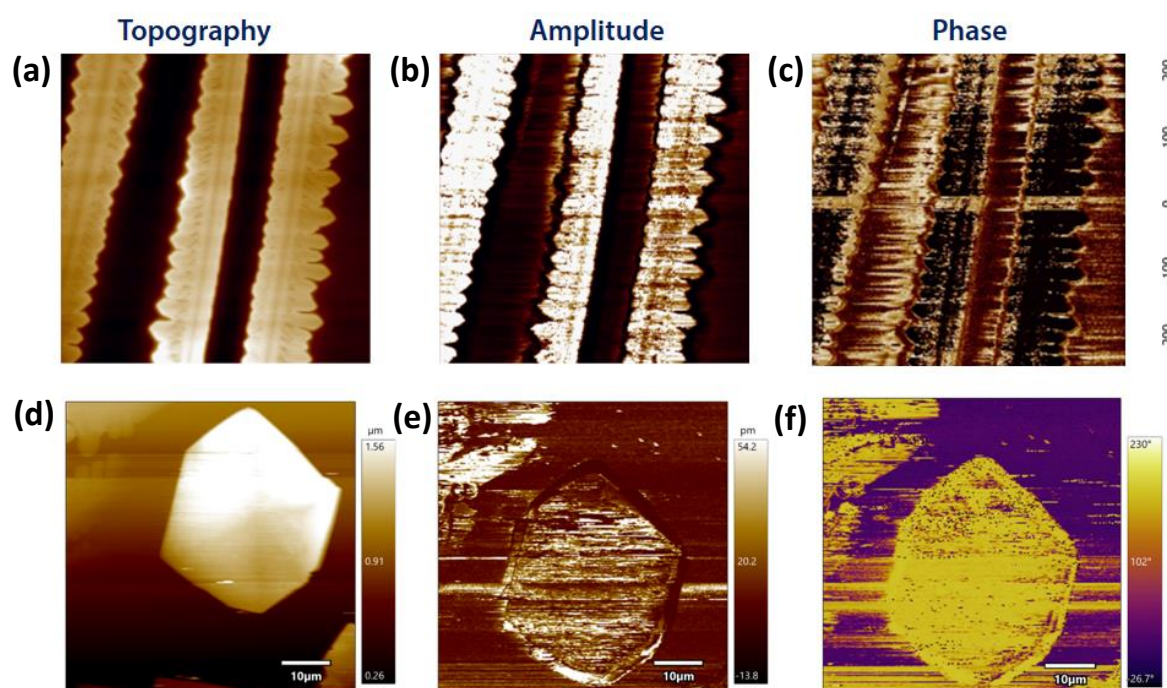


Figure 3.4: PFM data on the thin film sample of **1** and **2**. Topography, amplitude and phase images of **1** (a), (b) and (c) and **2** (d), (e) and (f) respectively.

We then carried out PFM spectroscopy on a single point of the thin film crystallite to study polarization switching and the local piezoresponse as a function of the bias tip voltage. A well-resolved off-field²⁹ butterfly-shaped amplitude loop and a hysteretic phase loop evidence the robust ferroelectricity in **1** and **2** (Figure 3.5a-d). The asymmetry of the obtained loops, estimated from the local coercive voltage (E_c) values of the negative and positive voltage sweeps, is presumably due to the different electrostatic boundary conditions commonly

observed for thin-film samples.³⁰ Overall, the PFM results unambiguously establish the existence of stable and switchable polarization in a thin film of **1** and **2**, unprecedented among metal-organic cages.

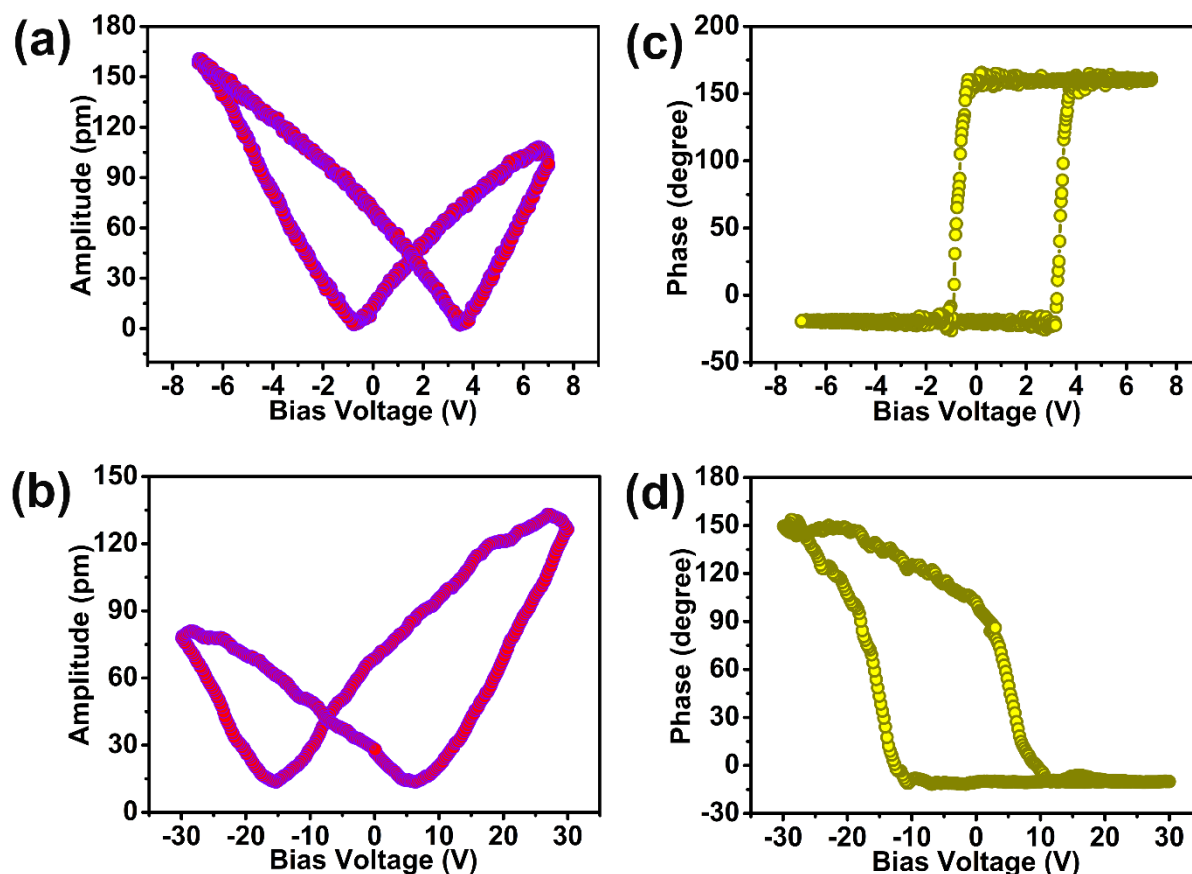


Figure 3.5: Local piezoresponse force spectroscopy on selected point of **1** and **2**. Amplitude ‘butterfly’ loop for **1** (a) and **2** (b); phase hysteresis loops on a selected point of **1** (c) and **2** (d).

Further, the domain switching for **2** was further evidenced by writing experiments using a PFM tip DC bias +25V, albeit with a weak response (Figure A3.12, Appendix).

The bulk piezoelectric coefficient (d_{33}) of a crystal of **2** has been obtained by the quasi-static method. At the tapping frequency of 110 Hz and applied force of 0.25 N, the d_{33} value was measured to be 4.2 pC/N.

3.3.3 Device Fabrication Process

Motivated by the dielectric, ferroelectric, and piezoelectric properties of these cages, we set out to probe the utility of the hybrid framework of **1** and **2** as a mechanical energy harvesting device in the form of piezoelectric nanogenerators (PENGs). For this application, flexible

polymer composites with various (1, 5, 10, 15) wt% of **1** and **2** were prepared with PDMS, a non-piezoelectric polymer. Note that the high crystallinity of **1** and **2** facilitated the formation of its homogenous composite films with PDMS, which is rare among MOFs and coordination cages. Simple multilayer **1**-PDMS and **2**-PDMS composite devices were prepared by drop-casting a mixture of **1** and **2** and PDMS onto the Al foil integrated PET, which serves as a bottom electrode. After curing the mixture for 24 h at room temperature, aluminum adhesive tape was pasted on the cured composite film as a top electrode (Figure A3.13, Appendix 3). The whole arrangement was wrapped with polyimide adhesive tape to keep the electrodes intact and insulate them from external interference. All of the composite films' PXRD profiles agree with that of the pristine sample of **2** (Figure A3.14, Appendix 3). Moreover, the increase in the intensity of the diffraction peaks with an increase in the loading (wt%) of **2** is evident from the PXRD profiles. Mechanical operations like folding, two-fold bending, and twisting demonstrate the flexibility of the composite film (Figure A3.15, Appendix 3). The cross-sectional SEM image of a **2**-PDMS device shows an approximate thickness of 1.15 mm for the sandwich structure (Figure A3.16, Appendix 3).

3.3.4 Mechanical Energy Harvesting Studies

The electromechanical performance of all the fabricated non-poled devices, with an active area of 4 cm², was assessed at an applied mechanical excitation of (21 N, 8 Hz) using a home-built mechanical force stimulator. During these measurements, the **1**-PDMS and **2**-PDMS composites generate an electric potential under external stress, while the ferroelectric particles of **1** and **2** serve as the energy sources. The maximum output peak-to-peak voltage (V_{PP}) of 9.54 V and 25.35 V is observed for the 20 wt% and 10 wt% composites of **1**-PDMS and **2**-PDMS, respectively (Figures 3.6a-b; A3.17-3.18, Appendix 3). Similar measurements on a blank device made of a pure PDMS film showed no apparent piezoelectric output. Therefore, the high output piezoelectric performance can be ascribed to the high piezoelectric coefficient of **1** and **2** present in the composite matrix of PDMS. It is worth noting that the improvement in the output voltages from 10 to 20 wt% for **1** and 1 to 10 wt% for **2** is mainly attributed to the significant increase in the ferroelectric content in the composite material and, to some extent, to the uniform distribution of **2** inside the matrix. Beyond this limit, aggregation of the polar crystallites takes place, as seen from the SEM images of the composites (Figure 3.19, Appendix 3). Though such agglomerations may lead to an increase in the dielectric permittivity, it causes a reduction in the field concentration effect due to the solidification of the dipoles.

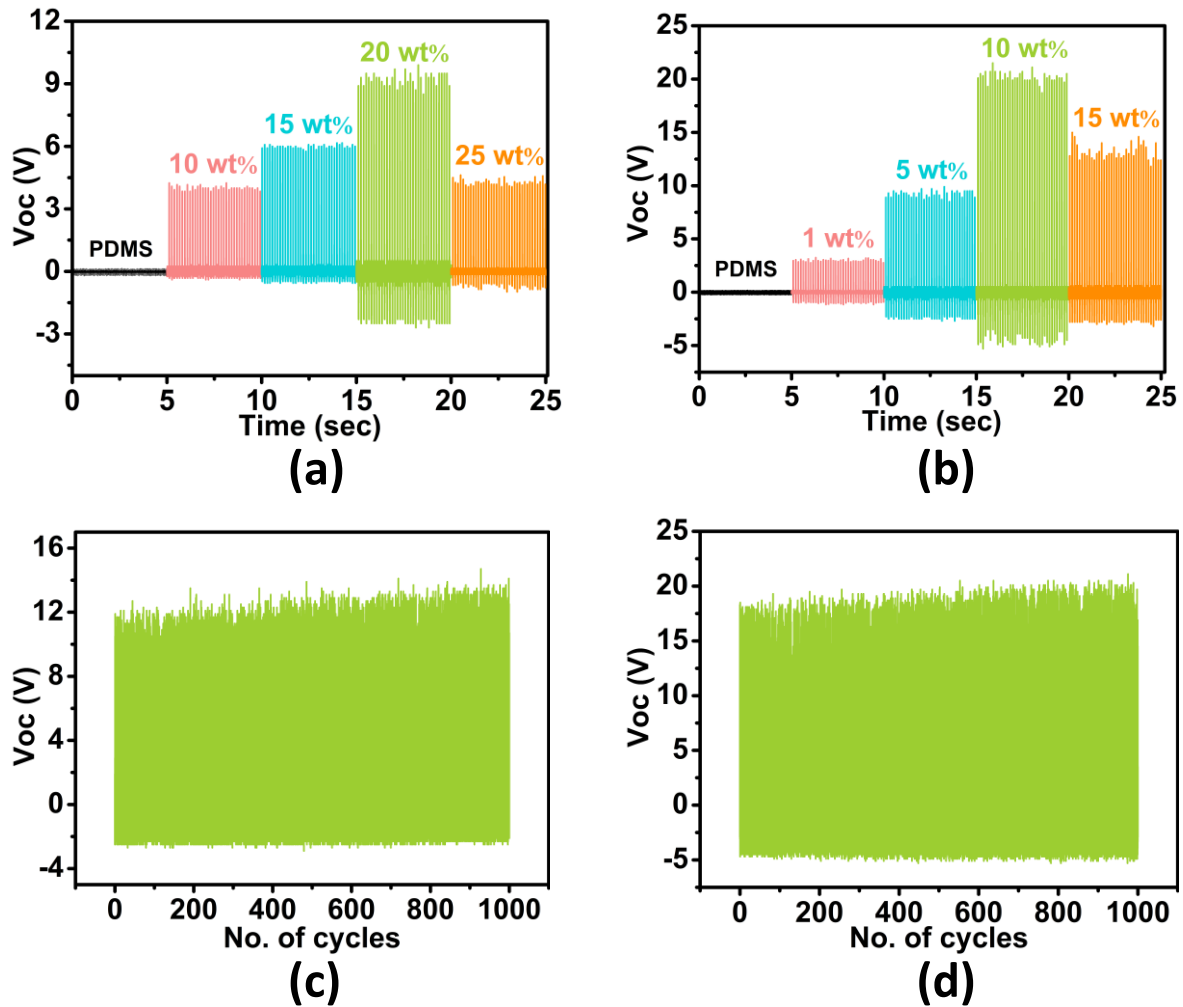


Figure 3.6: Piezoelectric output open-circuit voltages recorded for the various wt% **1**-PDMS (a) and **2**-PDMS (b) composite devices.

This effect eventually weakens the electromechanical coupling and polarizability of the composite films.³¹ The observed trend in the V_{PP} values correlates well with obtained d_{33} values of 6.5, 10.5, 26.4, and 21.2 pC/N for the composite films 1, 5, 10, and 15 wt % **2**-PDMS, respectively (Figure 3.20, Appendix 3). Notably, the highest d_{33} value of 26.4 pC/N is obtained for the best-performing 10 wt % **2**-PDMS film. Furthermore, no change in the amplitude of the voltage signals was observed upon testing the best-performing device up to 1000 cycles (Figures 3.6c-d). It clearly shows the reliability of the obtained signals and the excellent durability of the device.

Subsequently, we have performed the load resistance (R_L) dependent voltage measurements (in the range of 0.1 to 50 M Ω) along with the current density (CD) and power density (PD) analysis to determine the actual impedance matching of the best-performing 10 wt% device. These calculations gave a maximum PD of 79.33 $\mu\text{W}/\text{cm}^2$ at the R_L value of 0.9 M Ω , which is identified as the optimal load-matching resistance (Figure 3.21, Appendix 3). The output performance of the 10 wt % **2**-PDMS device is the highest among all MOF-based devices known so far and some of the best performing hybrid PENGs (Table A3.1, Appendix3). The practical utility of the best-performing 10 wt% PENG device was further tested by the capacitor charging experiments using a full-wave bridge rectifier circuit (Figure 3.22, Appendix 3). Three different capacitors with capacitances of 10, 22, and 47 μF were shown to complete charging within 5 minutes (Figure 3.23, Appendix 3). A maximum stored charge of 4.15 μC was recorded for the high-rated 47 μF capacitor.

3.4 Conclusion

In conclusion, we have reported the ferroelectric behaviour of a Co(II) and Ni(II)-based octahedral cage **1** and **2** that exhibits a remnant polarization of 7.35 and 25.31 $\mu\text{C}/\text{cm}^2$, respectively. Furthermore, visualization of the clear domain structures due to the ferro- and the piezoelectric nature of **1** and **2** was probed by the PFM measurements on its micrometer-sized crystalline thin films. PFM spectroscopy at a single point of the film shows the characteristic amplitude ‘butterfly’ and phase hysteresis loops. Furthermore, PDMS polymer composites of **1** and **2** were fabricated and employed as PENGs. The maximum open-circuit voltage of 9.54 V and 25.35 V were observed from **1** and **2**, respectively. The output voltages from the impact measurements were utilized for charging various aluminum electrolytic capacitors, demonstrating the practical utility of the cage. These results promise the potential deployment of metal-organic cages as lead-free piezoelectric nanogenerators for small-scale energy harvesting applications.

3.5 References

1. S. R. Anton and H. A. Sodano, *Smart Mater. and Struct.*, 2007, **16**, R1-R21.
2. M. Lee, C.-Y. Chen, S. Wang, S. N. Cha, Y. J. Park, J. M. Kim, L.-J. Chou and Z. L. Wang, *Adv. Mater.*, 2012, **24**, 1759-1764.
3. H. Li, C. R. Bowen and Y. Yang, *Adv. Funct. Mater.*, 2021, **31**, 2100905.

4. K.-I. Park, J. H. Son, G.-T. Hwang, C. K. Jeong, J. Ryu, M. Koo, I. Choi, S. H. Lee, M. Byun, Z. L. Wang and K. J. Lee, *Adv. Mater.*, 2014, **26**, 2514-2520.
5. S.-H. Shin, Y.-H. Kim, M. H. Lee, J.-Y. Jung and J. Nah, *ACS Nano*, 2014, **8**, 2766-2773.
6. Z. L. Wang and J. Song, *Science*, 2006, **312**, 242-246.
7. Y. Bai, H. Jantunen and J. Juuti, *Adv. Mater.*, 2018, **30**, 1707271.
8. C. Wang, X. Ke, J. Wang, R. Liang, Z. Luo, Y. Tian, D. Yi, Q. Zhang, J. Wang, X.-F. Han, G. Van Tendeloo, L.-Q. Chen, C.-W. Nan, R. Ramesh and J. Zhang, *Nat Commun*, 2016, **7**, 10636.
9. J. Junquera and P. Ghosez, *Nature*, 2003, **422**, 506-509.
10. V. Garcia, S. Fusil, K. Bouzehouane, S. Enouz-Vedrenne, N. D. Mathur, A. Barthélémy and M. Bibes, *Nature*, 2009, **460**, 81-84.
11. T. Vijayakanth, D. J. Liptrot, E. Gazit, R. Boomishankar and C. R. Bowen, *Adv. Funct. Mater.*, 2022, **32**, 2109492.
12. N. Prajesh, V. B. Sharma, S. S. Rajput, C. K. Singh, P. Dixit, B. Praveenkumar, J. K. Zaręba, D. Kabra, S. Ogale and R. Boomishankar, *ACS Sustainable Chem. Eng.*, 2022, **10**, 9911-9920.
13. A. Yadav, P. Kulkarni, B. Praveenkumar, A. Steiner and R. Boomishankar, *Chem. Eur. J.*, 2018, **24**, 14639-14643.
14. A. Yadav, A. K. Srivastava, P. Kulkarni, P. Divya, A. Steiner, B. Praveenkumar and R. Boomishankar, *J. Mater. Chem. C*, 2017, **5**, 10624-10629.
15. N. Prajesh, A. Yadav, R. Gourkhede, B. Praveenkumar, A. Steiner and R. Boomishankar, *Chem. Asian J.*, 2020, **15**, 3275-3280.
16. S. K. Kurtz and T. T. Perry, *J. Appl. Phys.*, 1968, **39**, 3798-3813.
17. Y. Zhang, X.-J. Song, Z.-X. Zhang, D.-W. Fu and R.-G. Xiong, *Matter*, 2020, **2**, 697-710.
18. H. Cui, Z. Wang, K. Takahashi, Y. Okano, H. Kobayashi and A. Kobayashi, *Journal of the American Chemical Society*, 2006, **128**, 15074-15075.
19. M. Sánchez-Andújar, S. Yáñez-Vilar, B. Pato-Doldán, C. Gómez-Aguirre, S. Castro-García and M. A. Señarís-Rodríguez, *The Journal of Physical Chemistry C*, 2012, **116**, 13026-13032.
20. H. Cui, B. Zhou, L.-S. Long, Y. Okano, H. Kobayashi and A. Kobayashi, *Angewandte Chemie International Edition*, 2008, **47**, 3376-3380.

21. T. R. Shrouf and J. Fielding, 1990.
22. J. Hlinka, J. Petzelt, S. Kamba, D. Noujmi and T. Ostapchuk, *Phase Transitions*, 2006, **79**, 41-78.
23. Z. G. Ye, *Key Engineering Materials*, 1998, **155-156**, 81-122.
24. A. A. BOKOV and Z.-G. YE, *Journal of Advanced Dielectrics*, 2012, **02**, 1241010.
25. A. S. Tayi, A. Kaeser, M. Matsumoto, T. Aida and S. I. Stupp, *Nature Chem*, 2015, **7**, 281-294.
26. L. Pan, G. Liu, H. Li, S. Meng, L. Han, J. Shang, B. Chen, A. E. Platero-Prats, W. Lu, X. Zou and R.-W. Li, *J. Am. Chem. Soc.*, 2014, **136**, 17477-17483.
27. T. Jungk, Á. Hoffmann and E. Soergel, *New J. Phys.*, 2009, **11**, 033029.
28. F. Johann, T. Jungk, M. Lilienblum, Á. Hoffmann and E. Soergel, *Appl. Phys. Lett.*, 2010, **97**, 102902.
29. H. Qiao, O. Kwon and Y. Kim, *Appl. Phys. Lett.*, 2020, **116**, 172901.
30. Y.-H. Hsieh, F. Xue, T. Yang, H.-J. Liu, Y. Zhu, Y.-C. Chen, Q. Zhan, C.-G. Duan, L.-Q. Chen, Q. He and Y.-H. Chu, *Nat Commun*, 2016, **7**, 13199.
31. H. Hammami, M. Arous, M. Lagache and A. Kallel, *J. Alloys Compd.*, 2007, **430**, 1-8.

Chapter 4

A Ferroelectric Two-Dimensional Metal-Organic Coordination Polymer Showing Efficient Piezoelectric Energy Harvesting Properties

4.1 Introduction

The harvesting and conversion of energy from sustainable sources is vital in meeting global energy demands. The last two decades have witnessed several breakthroughs in solar, wind, electrochemical and mechanical energy harvesting and storage. Mechanical energy harvesting is one of the simplest forms of renewable source as it is abundantly available in all life forms. Ferroelectric materials are a special class of dielectrics that exhibits switchable spontaneous polarization under the influence of a sweeping electric field. They show the polarization dependence in the presence of external stimuli forces like temperature, pressure, and optical signals. These materials are utilized in various electronic components including piezoelectric actuators and transducers, infrared sensors, capacitors, random access memories (RAMs), and electro-optic light valves.¹ Ferroelectric materials with robust polarization attributes usually have good piezoelectric performance and are efficient for mechanical energy harvesting and their devices are commonly known as piezoelectric nanogenerators (PENGs). The commercially employed conventional inorganic ceramics have superior electromechanical, ferroelectric and piezoelectric properties but suffer from their toxicity, high cost, and difficult film forming procedures. Hence, unconventional ferroelectrics such as polymers, organic-inorganic hybrids and metal-organic materials have gained immense attraction in search of improved energy efficiency, increased integration, and enhanced versatility.

Supramolecular metal-organic frameworks (MOFs) and related architectures are an emerging class of engineering materials because they are endowed with inherent design flexibility. The potential of these materials for integration into microelectronics lies in their ability to adopt to the materials requirements of light-weight and flexible (thin and soft) characteristics and bio-friendliness in the resultant devices.²⁻⁴ Nevertheless, exploring ferroelectric and piezoelectric properties in MOFs is still embryonic as they often do not follow the conventional order-disorder or displacive type polarization mechanisms. Typically, the polarization mechanisms in the known examples of MOF-based ferro- and piezoelectrics originated from the presence of rotatable dipolar groups in their linkers,^{5, 6} doping of the metal ions in the lattice nodes of MOFs⁷, displacement of switchable coordination bonds, the choice of counter anions and incorporation of polar guest molecules.^{8,9-12} In this effort, our group has been involved in the design of lower symmetric di- or tripodal (N-donor or O-donor) phosphoramidate ligands such as [PhPO(NHPy)₂], (Py = 3-pyridyl (³Py) or 4-pyridyl (⁴Py)), [PS(NH₃Py)₃], [PO(NHCH₂³Py)₃] and [PhPO(NH-(C₆H₄COOH))₂] for the development of coordination networks with ferro- and piezoelectric properties. Utilizing these lower-symmetric ligands, we

have developed noncentrosymmetric metal-organic cages and their connected cage frameworks, one and two-dimensional polar coordination networks in which polarization was found to originate from the charge-separated structures or the distortions around the metal centre.¹³⁻²¹

In this chapter, we show that the relative displacement of a weakly bonded counter anion nitrate is responsible for ferroelectricity in a two-dimensional metal-ligand coordination polymer [Cu(PhPONHCH₂(³Py)₂)(NO₃)₂·2H₂O (**1**)] assisted by the flexibility of the framework. The compound **1** was synthesized by the treatment of a flexible noncentrosymmetric dipodal ligand [PhPONHCH₂(³Py)₂] (**L**) containing picolyl substituents with copper(II) nitrate. The piezoresponsive force (PFM) measurements reveal an excellent ferro- and piezoelectric response for the 2D polymer **1**. The longitudinal converse piezoelectric coefficient (d_{33}) was observed to be 82 pm/V for the single-crystalline thin film of **1**, which is remarkable for MOF-based piezoelectric materials. Furthermore, the polymer composites of **1** with TPU (Thermoplastic polyurethane) showed attractive PENG performance with a maximum output voltage of 25.05 V with an estimated power density of 48.69 $\mu\text{W}/\text{cm}^2$ for the optimized champion device of 10 wt% (**1**-TPU). Additionally, the best performing 10 wt% device was utilized for charging the aluminum-based electrolytic capacitors. These results demonstrate a new type of coordination driven mechanism for polarization in MOFs and related materials and their utility in PENG applications.

4.2 Experimental Section

4.2.1 General Remarks. All manipulations involving phosphorous halides were performed under dry nitrogen atmosphere in standard Schlenk-glassware. The solvent toluene was dried over sodium. 3-Picolylamine was purchased from Aldrich and used as received. PhPOCl₂ and Cu(NO₃)₂·3H₂O were purchased from Acros-Organics and Merck, respectively, and used as received. NMR spectra were recorded on a Jeol 400 MHz spectrometer (¹H NMR, 400.13 MHz; ¹³C ¹H NMR, 100.62 MHz; ³¹P ¹H NMR, 161.97 MHz) at room temperature using SiMe₄ (¹H, ¹³C) and 85% H₃PO₄ (³¹P). The MALDI-TOF spectra were obtained on an Applied Biosystem MALDI-TOF/TOF spectrometer. The powder X-ray diffraction (PXRD) data were obtained from a Bruker-D8 Advance diffractometer. Thermal analysis (TGA) data have been obtained from a PerkinElmer STA-6000 thermogravimetric analyzer. Elemental analyses were performed on a Vario-EL cube elemental analyzer. FT-IR spectra were taken on a PerkinElmer

spectrophotometer with samples prepared as KBr pellets. Melting points were obtained using an Electro thermal melting point apparatus and were uncorrected.

4.2.2 Synthesis. L: To a stirred solution of 3-picolyamine (4.575 g, 0.0423 mol) in toluene (~110 mL) at 0 °C, PhPOCl₂ (1 mL, 1.375 g, 0.00705 mol) in 10mL of toluene was added dropwise through a pressure equalizer funnel under inert atmosphere, and the reaction mixture was refluxed for 4 h. The toluene solution was filtered and obtained white precipitate washed with dichloromethane three times. The filtrate and washings were evaporated under reduced pressure to yield a white precipitate of the **L**, which was then dried and collected. Yield: 1.56 g (79.18%). M.P.: 105-110 °C. ¹H NMR (CDCl₃): δ 8.45 (d, 2H, CH(pyridyl)), δ 8.4 (dd, 2H, CH(pyridyl)), δ 7.6 (td, 2H, CH (pyridyl)), δ 7.12 (dd, 2H, CH (pyridyl)), δ 3.44 (t, 2H, NH), δ 4.1 (d, 4H, CH₂), δ 7.43 (1H, phenyl), δ 7.5 (2H, phenyl), δ 7.8 (2H, phenyl). ¹³C {¹H} NMR (CDCl₃): δ 42.3, 123.5, 128.7, 131.6, 132, 135.3, 148.7, 148.9. ³¹P NMR (162 MHz, {(CD₃)₂SO}): δ 21.14. MALDI-TOF: 361.35 (M + Na)⁺, 377.35 (M + K)⁺ Anal. Calcd. for C₁₈H₁₉N₄OP: C, 63.9; H, 5.66; N, 16.56. Found: C, 62.5; H, 5.44; N, 17.12.

4.2.2.1: To a stirred solution of **L** (30 mg, 0.088 mmol) in MeOH (3mL), Cu(NO₃)₂·3H₂O (14 mg, 0.057 mmol) in H₂O (1 mL) was added. The resulting solution was subsequently stirred for 2 h and filtered through celite pad. The filtrate was left for crystallization. The suitable blue crystals for X-ray analysis were obtained after 2-3 weeks. Yield: 45.4% (23.6 mg), based on Cu. Calcd. for C₃₆H₄₀N₁₀O₁₀P₂Cu: C, 48.14; H, 4.49; N, 15.59. Found: C, 55.96; H, 3.810; N, 8.04. FT-IR data on powder (cm⁻¹): 3859, 3737, 3608, 2310, 1736, 1692, 1516, 1070, 897, 796.

4.2.3 Ferroelectric and Dielectric Measurements. In order to determine the dielectric and ferroelectric properties, the powdered sample of this compound was compacted in the form of disc (of approximately 13 mm diameter and 0.131 mm thickness). The compacted discs were subsequently electroded using silver paint for both measurements. The frequency dependent dielectric characteristics for **1** at various temperatures was measured using the Novocontrol dielectric spectrometer.

The ferroelectric hysteresis loop in **1** were measured by using a Sawyer-Tower circuit. The polarization studies were recorded using a hysteresis loop analyzer (TF Analyzer 2000, aixACCT Germany).

4.2.4 Crystallography: Reflections were collected on a Bruker Smart Apex Duo diffractometer at 100 K using MoK α radiation ($\lambda = 0.71073 \text{ \AA}$). Structures were refined by

full-matrix least squares against F^2 using all data using SHELX.²² All non-hydrogen atoms were refined anisotropically if not stated otherwise. The nitrates ions in the asymmetric units of both **1** were disordered. The disordered fragments were refined with the similar distances and the similar U-restraints by using the SIMU/SAME command of the Shelx. Crystals of **1** were weakly diffracting at higher angles and hence their data were truncated to $2\theta = 50^\circ$. Hydrogen atoms were constrained in geometric positions to their parent atoms. (Table 4.1)

Table 4.1: Crystallographic data for the ligand **L**, **1 (120 K)** and **1 (298 K)**.

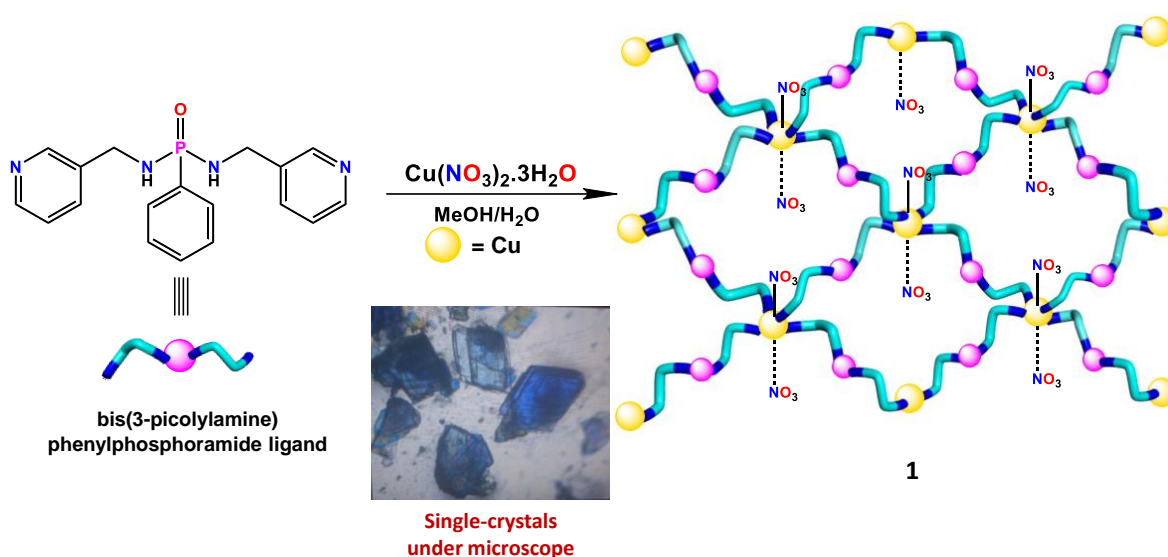
Compound	L	1 (120 K)	1 (308 K)
Chemical formula	C ₁₈ H ₁₉ N ₄ OP	C ₃₆ H ₄₂ N ₁₀ O ₁₀ P ₂ Cu	C ₃₆ H ₄₀ N ₁₀ O ₁₀ P ₂ Cu
Formula weight	338.34	900.27	898.26
Temperature	120 K	100 K	308 K
Crystal system	Orthorhombic	Monoclinic	Orthorhombic
Space group	Pca2 ₁	Pc	Aba2
a (Å); α (°)	16.208(3) Å, 90°	13.012(17) Å, 90°	16.0506(6) Å, 90°
b (Å); β (°)	5.3177(9) Å, 90°	16.42(2) Å, 114.16°	23.656(9) Å, 90°
c (Å); γ (°)	38.178(7) Å, 90°	10.653(14) Å, 90°	10.421(3) Å, 90°
V (Å ³); Z	3290.5(10); 8	2077(5); 2	4069(2); 4
ρ (calc.) mg m ⁻³	1.366	1.439	1.466
μ(Mo Kα) mm ⁻¹	0.180	0.670	0.684
2θ _{max} (°)	40.778	50.05	50.484
R(int)	0.0731	0.0776	0.0505
Completeness to θ	100 %	99.5 %	99.4 %
Data / param.	3238/433	5353/509	4839/261
GOF	1.127	1.022	1.053
R1 [F > 4σ(F)]	0.0394	0.1337	0.1270

wR2 (all data)	0.1038	0.2133	0.2110
max.peak/hole ($e \cdot \text{\AA}^{-3}$)	0.239/-0.268	1.304/-0.617	0.553/-0.985

4.3 Results and Discussions

4.3.1 Synthesis, Characterization and Crystal Structure

The flexible dipodal ligand **L** was synthesized by refluxing 3-picolyamine and PhPOCl₂ in toluene. The ligand was characterized by NMR spectroscopy, mass spectrometry and single-crystal X-ray diffraction analysis (Appendix 4, Figures 4A.1). The 2D coordination polymer **1** was isolated as blue colored crystals in a 2:1 reaction mixture involving **L** and Cu(NO₃)₂·3H₂O in MeOH/H₂O solvent medium at room temperature (Scheme 4.1).



Scheme 4.1. Schematic diagram showing the formation of two-dimensional coordination polymer **1** from the tripodal picolyl-based phosphoramidate ligand **L**. Images of the crystals of **1** under the microscope showing the layered morphology.

Furthermore, we analyzed the structure of the compound **1** using the single-crystal X-ray diffraction (SCXRD) and the variable temperature X-ray powder diffraction (PXRD) measurements. At 120 K, the compound **1** crystallizes in the monoclinic non-centrosymmetric polar space group *Pc* ($a = 13.012(17) \text{ \AA}$, $b = 16.42(2) \text{ \AA}$, $c = 10.653(14) \text{ \AA}$; $\alpha = 90^\circ$, $\beta = 114.16^\circ$, $c = 90^\circ$, $V = 2077(5) \text{ \AA}^3$) (Figure 4.1a). The asymmetric unit contains one Cu²⁺ ion with full occupancy, two phosphoramidate ligands, two nitrate anions with full occupancy and two water molecules. The Cu²⁺ ion is equatorially coordinated with the four N_{pyridyl} ligands belonging to

the four different ligand motifs and axially coordinated with the nitrate anion, which corroborates the formation of distorted square pyramidal geometry with a τ value of 0.26. This trigonal index was calculated using the formula $\tau = (\beta - \alpha)/60^\circ$ previously defined by Addison et al²³, where τ infers the values of 0 or 1 for ideal square-pyramidal and trigonal-bipyramidal geometries, respectively. The apically coordinated nitrate anion is at a distance of 2.306(16) Å from Cu²⁺ and a deviation from the basal plane of 0.2725 Å (Figure 4.1). This axial elongation is due to the Jahn Teller effect typical of Cu²⁺ complexes.²⁴ Each Cu²⁺ ions is bonded to two molecules of **L** with four N_{pyridyl} contacts to yield a 2D layer containing channels which are occupied by the water molecules and uncoordinated nitrate anions, which is responsible for restoring the charge of the cationic framework. Both the coordinated and uncoordinated nitrate anions were disordered over two positions. The uncoordinated nitrate anion is located somewhat closer to the other axial site of the Cu²⁺ ion at a distance of 2.98 Å. The water molecules present in the channel are involved in the H-bonding interactions with the uncoordinated nitrate anions and phosphoryl oxygen-atoms of the ligand **L**.

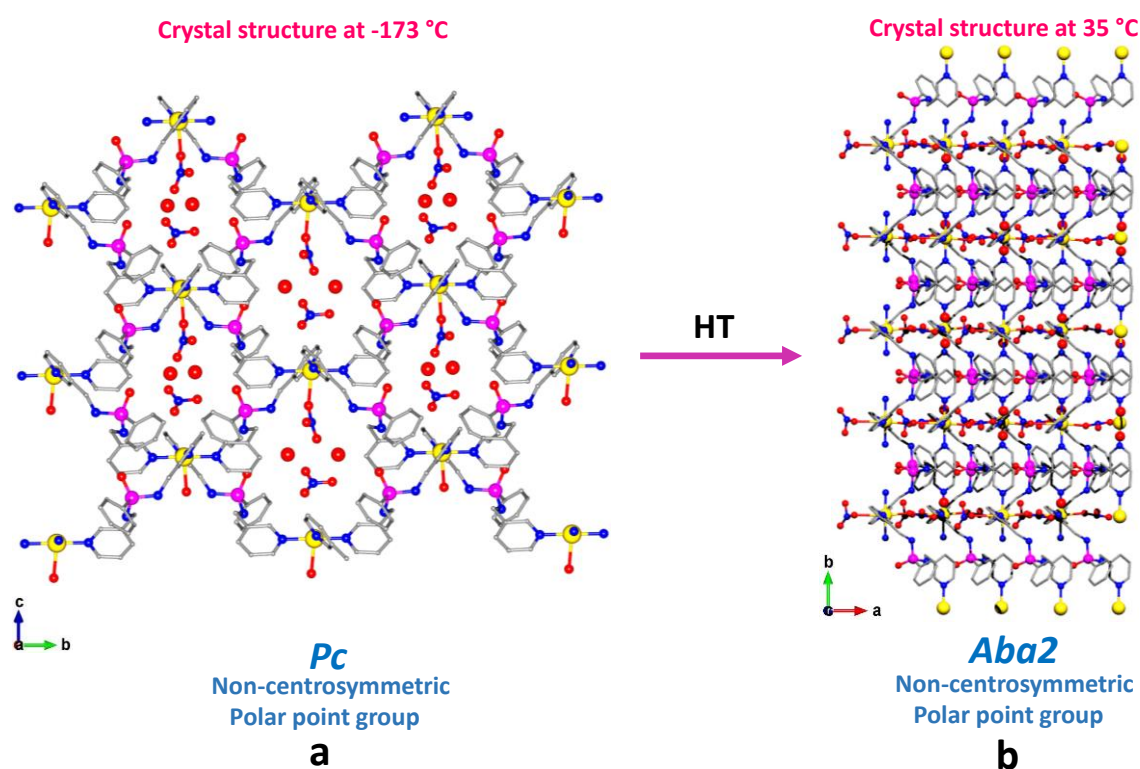


Figure 4.1: Single-crystal X-ray data (SCXRD) data at (a) -173 °C and (b) 35 °C.

The crystal structure of **1** at 308 K was solved in a higher symmetric orthorhombic unit cell, yet again in the polar and non-centrosymmetric space group *Aba2* ($a = 16.506(6)$ Å, $b =$

23.656(9) Å, $c = 10.421(3)$ Å; $\alpha = 90^\circ$, $\beta = 90^\circ$, $\gamma = 90^\circ$, $V = 4069(2)$ Å³) (Figure 4.1b). The asymmetric unit contains one Cu²⁺ ion with half occupancy, one phosphoramidate ligand, two nitrate anions each with half occupancy and one water molecule. The square-pyramidal polyhedra was distorted but with a τ value less than the value at low temperature which is of 0.22. The apically occupied nitrate anion was at a distance of 2.21(3) Å (Figure 4.2b). Interestingly, the uncoordinated nitrate anion forms a weak coordination bond to Cu²⁺ which is at a reduced distance of 2.754 Å (Figure 4.2). This is due to the diffused electron density due to the disorder at room temperature and larger thermal ellipsoids. Also, it is worth noting that the stacking sequence of the 2D-layers has changed from an AAAA type to ABAB type during this phase change, which helped in pushing the uncoordinated nitrate anions towards the metal centers (Figure 4.2).

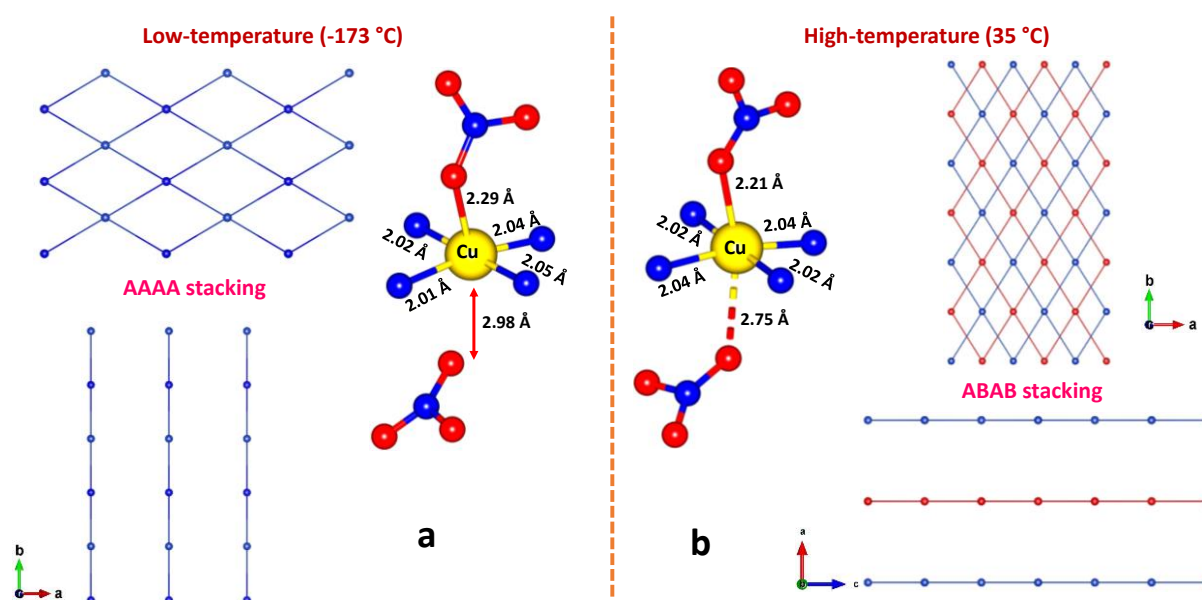


Figure 4.2: SCXRD analysis of **1** (a) low temperature at (-173 °C) and (b) high temperature at (35 °C)

Due to the weak diffraction of the crystals of compound **1** at high temperature, the variable-temperature PXRD was performed on the powder sample of **1** to verify the phase transition. As can be seen in Figure 4.3, the measured diffraction peaks at 35 °C are in coherence with the simulated pattern at the same temperature. It can also be noted that the simulated pattern at 173 °C does not match with the experimental peaks at 35 °C. Multiple hkl peaks around 18.58° and 21.46° were merged into one diffraction peak indicative of the emergence of the new phase when going from -173 °C to 35 °C. The VT-PXRD show that the orthorhombic phase was

stable upto 100 °C. Interestingly, no notable curie points (ferroelectric to paraelectric) were observed until 120 °C which is attributed to its greater structure stability.

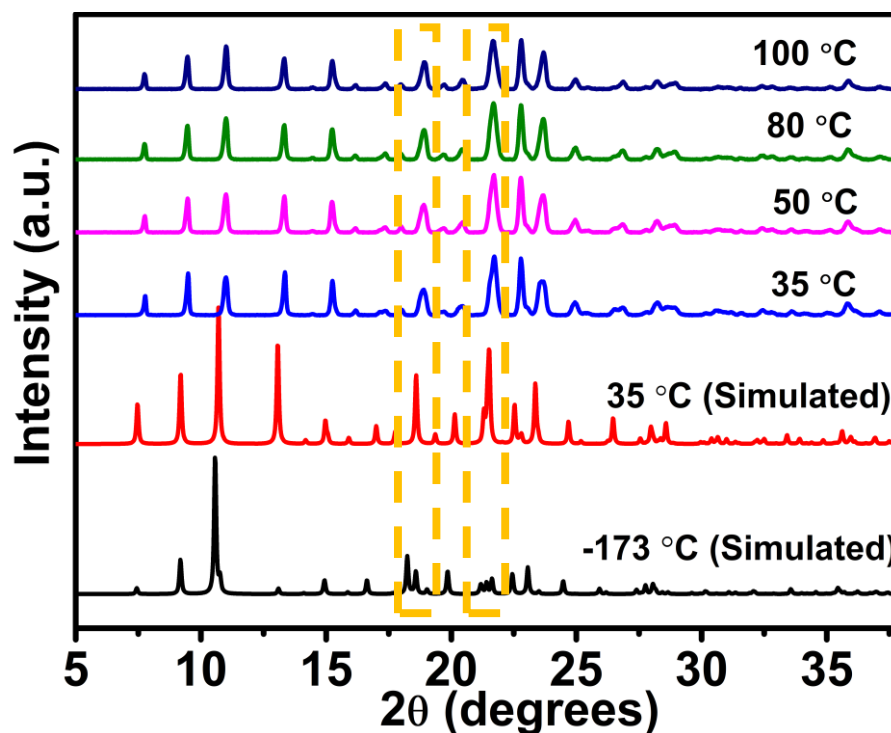


Figure 4.3: Variable-temperature powder X-ray diffraction (VT-PXRD) data of **1**.

The thermogravimetric analysis data of **1** shows a good thermal stability up to 160 °C (Appendix 4, Figure 4A.2). Furthermore, the differential scanning calorimetry (DSC) measurements show a reversible anomaly at 27 °C / 40 °C in the heating / cooling runs indicating a reversible phase transition (Figure 4.4a). The broad and small anomalous peak in the endothermic / exothermic process is indicative of second-order phase transition.^{25, 26}

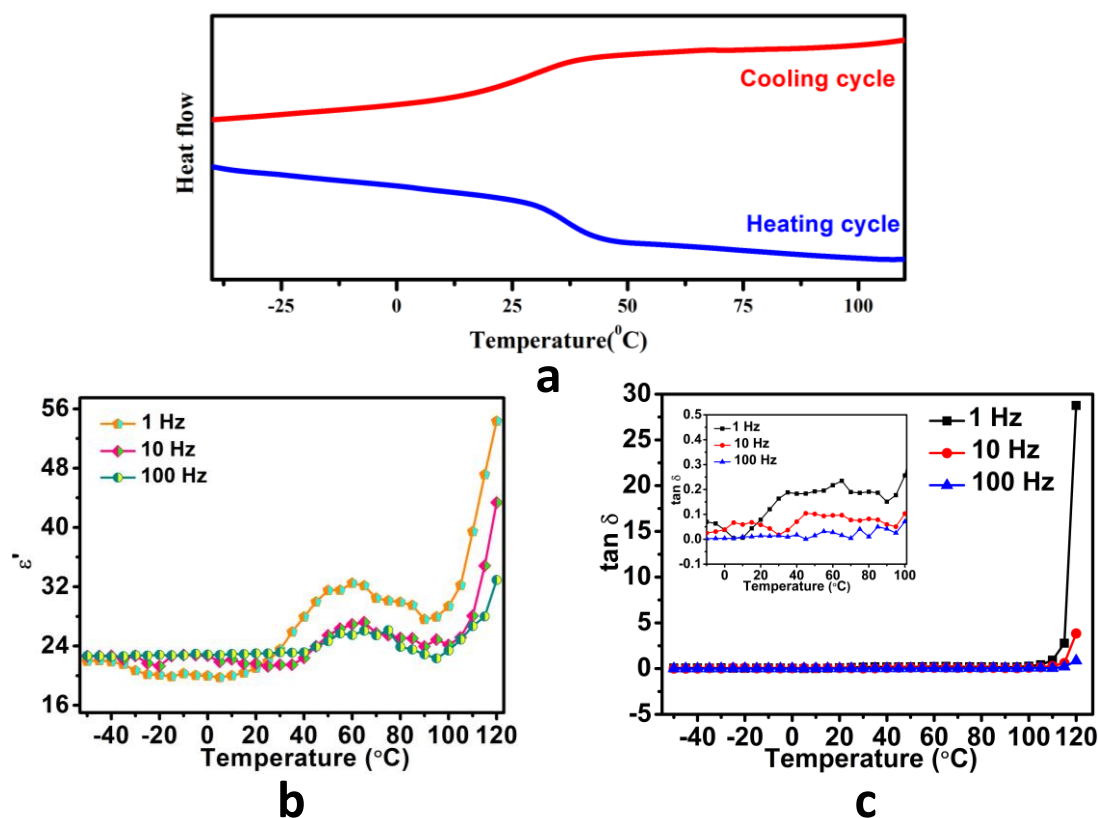


Figure 4.4: (a) DSC measurements on **1**. (b) Temperature-dependent dielectric permittivity measurements on the compact crystalline pellet of **1**. (c) Dielectric loss factor ($\tan \delta$) of **1** as a function of temperature.

The temperature dependent dielectric measurements on **1** was performed on the polycrystalline compact powder-pressed sample to further understand this phase behaviour. The real part (ϵ') of the complex dielectric permittivity displays a broad anomalous peak in a temperature range from 20 to 95 °C and beyond that temperature it shows an abrupt rise upto 120 °C (Figure 4.4b). The first anomaly is indicative of a dielectric phase transition. The subsequent onset in the dielectric permittivity was observed due to the increase in the polarizability of water molecules and non-conductive charge carriers near its melting point. The broad anomalous peak with respect to frequency was found to be slightly shifted towards higher temperatures accompanying with the decrease in the maxima of ϵ' values. This relaxation type behavior appears due to the slow dipole (ionic or molecular) motion in **1**, which is common in many dielectric MOFs.²⁷ A similar trend has also been observed in the corresponding temperature-dependent dielectric loss factor ($\tan \delta$) plot as well (Figure 4.4c). Moreover, the frequency dependent dielectric measurements (ϵ' and $\tan \delta$) gave similar trends as observed from the

temperature-dependent measurements (Appendix 4, Figures 4A.3 and 4A.4). However, the measured dielectric permittivity value of ca. 22.9 at room temperature and low dissipation factor ($\tan\delta$) indicates that **1** is a good dielectric material and suitable for practical aspects.

4.3.2 Piezoresponse Force Microscopy (PFM) Studies

The point group symmetry of compound **1** in the orthorhombic phase at room temperature is C_{2v} , which belongs to one of the 10 polar point groups (C_1 , C_s , C_2 , C_{2v} , C_3 , C_{3v} , C_4 , C_{4v} , C_6 and C_{6v}) compatible for exhibiting ferroelectric and piezoelectric properties. The piezoresponse force microscopy (PFM) has long been established as a non-destructive tool to characterize the piezo- as well as ferroelectric materials using a combination of surface probe imaging and spectroscopy modes.^{28, 29} The PFM technique is based on the local converse piezoelectric effect. The main parts of PFM image includes amplitude and phase parameters, related to the strength of the piezoelectric coefficient and the direction of polarization in each domains, respectively.³⁰ The vector-mode vertical-PFM (VPFM) measurements were carried out on the as-grown drop-casted single-crystalline thin film sample of **1**. The as-prepared film shows good crystallinity as verified by PXRD (Appendix 4, Figure 4A.5), and the measured area just contains a few single crystals. The obtained topography has found to exhibit a layered morphology as shown in Figure 4.5a on the as-grown thin film of **1**. Figures 4.5b, c shows the corresponding PFM amplitude and phase images, respectively. The stripe-like shape of the ferroelectric domain pattern in single-crystalline thin film can be seen from the contrast in the amplitude images, which do not show cross-talk with the topography. The ferroelectric behavior can be explored through the PFM spectroscopy performed at a selected point by applying a dc voltage of ± 40 V with superimposed 2.5 V ac voltage to obtain both the on-field and off-field loops. The off-field loops are expected to contain electromechanical response induced solely by piezoelectricity rather than the mixture of piezoelectricity and electrostatic effects typically obtained in the on-field mode.³¹ The hysteresis loops obtained in Figure 4.5d in the off-field mode thus rules out the artefact induced by electrostatic effects, which confirms the existence of ferroelectricity in compound **1**. The rectangular, clear and successive reversals of phase hysteresis loop observed in Figure 4.5d confirms the swift switching of the polarization by 180° back and forth supporting the robust ferroelectricity in thin films of **1**. From the amplitude butterfly loops in Figure 4.5d, the existence of piezoelectricity in **1** is confirmed. Furthermore, the slope of the amplitude curve reflects the magnitude of the piezoresponse and for **1** it is found to be 82 pm/V. This value is unprecedented among metal-ligand coordination networks. From the point charge model analysis of the crystal structure of

1 at room temperature (Table 4.1), the value of polarization is estimated to be $3.088 \mu\text{C}/\text{cm}^2$. Due to the charge separated nature of **1**, the origin of polarization in it can be tracked to the subtle displacement of the un-bound nitrate anions near the metal center under the applied electric field that gives rise to two distinctly reversible domains along the axial direction. The quasi-static method (known as Berlincourt method) was employed to deduce the macroscopic d_{33} on the polycrystalline compact pellet which comes out to be $0.22 \text{ pC}/\text{N}$. The apparent disparity in the magnitudes of d_{33} obtained from the PFM and Berlincourt method is due to the brittle nature of the neat crystals of **1** under an external force, precluding the measurements at higher impact forces and the poor packing density of its pellets in comparison with ceramics.

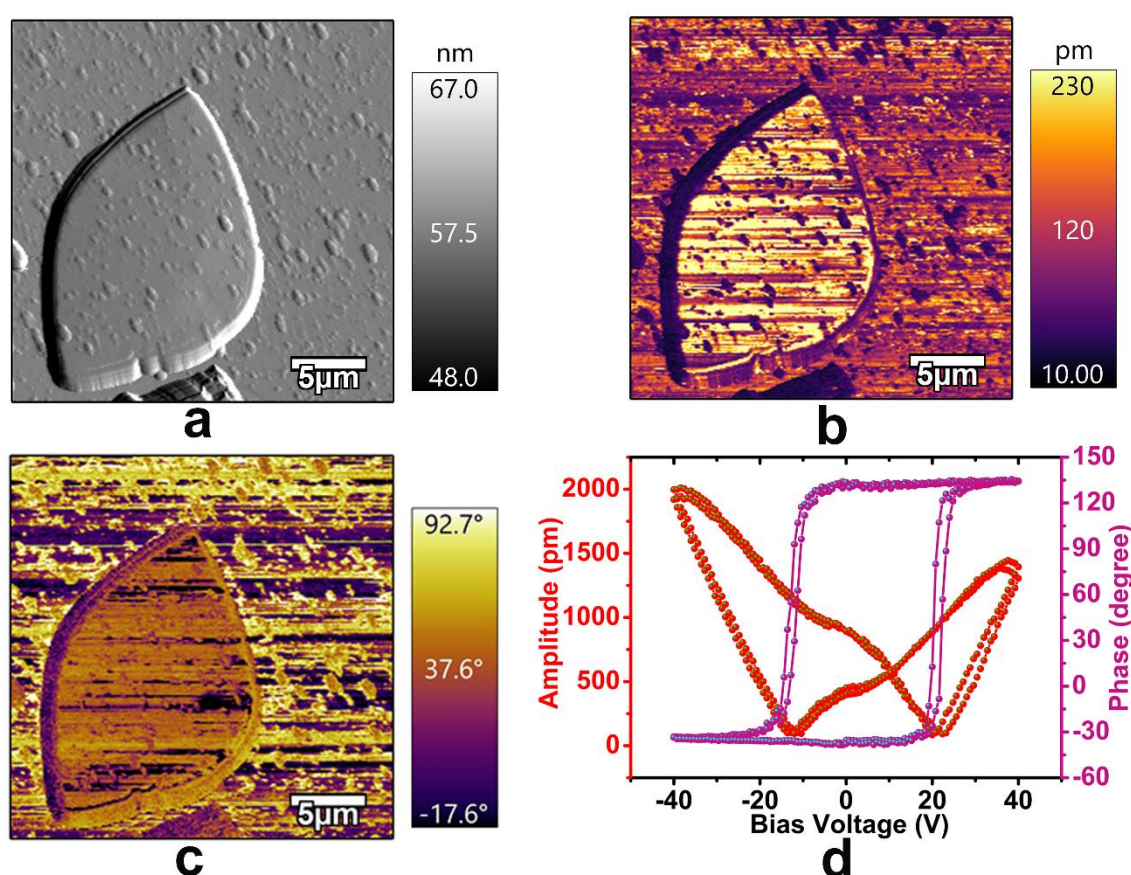


Figure 4.5: Vertical PFM data of **1**. (a) topography, (b) amplitude and (c) phase images for a $30 \times 30 \mu\text{m}$ region in the as-grown single crystalline thin film. (d) Vertical PFM amplitude and phase as a function of dc bias for a selected point of **1**, displaying local amplitude butterfly and phase hysteresis loops with a coercive voltage of about 20 V.

4.3.3 Characterization of 2D MOF-Based Power Generator

Due to the presence of inherent ferro- and piezoelectricity in **1**, we set out to explore this hybrid network towards mechanical energy harvesting application in the form of its flexible polymer composite. To make a composite film, we have employed a piezoelectric inactive TPU (Thermoplastic polyurethane) polymer as a polymer substrate. The flexible polymer composites with varying weight percentages (1, 5, 10, 15, 20 wt%) of **1** were obtained by dispersing its powdered crystals into the homogeneous solution of TPU in THF. The mixed slurry were then poured onto the PET sheet, dried at room temperature and then subsequently peeled off (Figure 4.6a). The blue-colored composite films were found to be mechanically robust and flexible during the folding, rolling, multi-fold bending and twisting operations (Figure 4.6b and Appendix 4, Figure 4A.6). A thin layer of Au/Cr (100/5 nm) was magnetron sputtered on both the sides of composite films as the top and bottom electrode. The device connections were finally made by soldering the copper wires onto the copper tape adhered to the electrodes. Then the whole device was encapsulated in the thin PDMS layer to avoid formation of air gaps or contact separation during the impacting process, thus eliminating the potential interference of triboelectricity to the maximum extent possible (Figure 4.6b). The PXRD profiles of all the composite films exhibits the signature peaks of the bulk material signifying the retention of the crystallinity of **1** in the composite films. Additionally, as the loading of the ferroelectric particles increasing in the composite films, the improvement in the intensity of all the diffraction peaks can be seen, which indicates the increased content of the crystalline material in the composite films at higher loading (Figure 4.6c). The cross-sectional SEM image reveals the thickness of ~ 0.22 mm of the composite film in the devices (Appendix, 4A. Figure 4A.6).

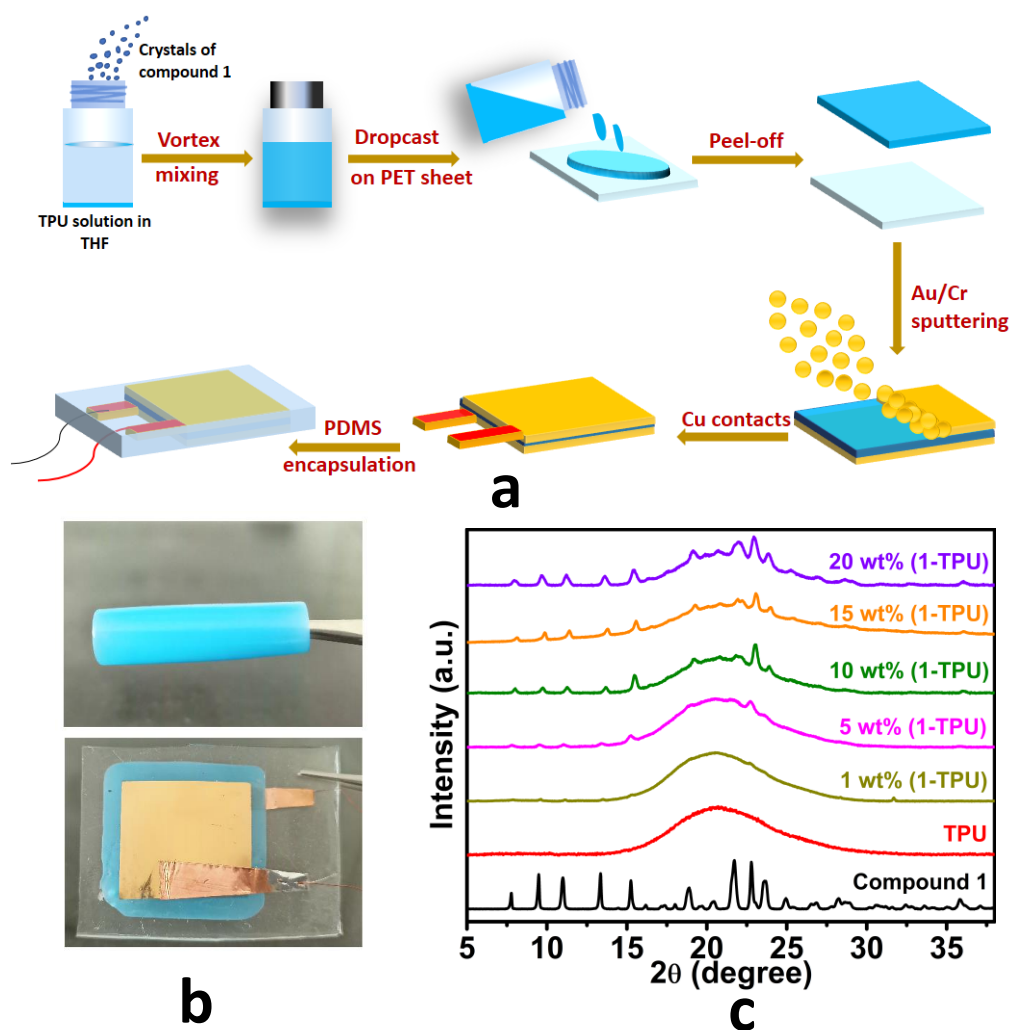


Figure 4.6: (a) Schematic diagram illustrating the preparation and fabrication of the composite films of **1** in TPU. (b) Photographs of the as-made blue composite film showing flexibility as rolling (top) and **1**-TPU fabricated device (bottom). (c) PXRD profiles of various (1, 5, 10, 15, 20) wt% **1**-TPU composite films and its comparison with pristine compound of **1**. The broad profile of a neat TPU film showing its amorphous structure.

All the fabricated devices were tested under a compressive force of 21 N from a home-built setup. For optimal energy harvesting, electrical poling is crucial to align the dipoles in piezoelectric materials. Every device was poled with an electric field of 6 kV/cm for eight hours to strengthen dipole alignment. The energy harvesting performance of each poled device was examined under similar force conditions, and the results can be seen in Figure 4.7a. The 10 wt% (**1**-TPU) device exhibited the maximum electrical response (V_{PP}) of 25.05 V evidencing that the % loading level in this device is optimal for energy harvesting. The asymmetry between the positive and negative peaks were observed in the process of pressing

or releasing process. This can be attributed to the fact that the pressing process is dependent upon the external force, whereas the releasing process is predominated by the flexibility of the piezocomposites themselves.³² The reinforcement of the output voltages with increase in the concentration of **1** is due to the enhancement of the interfacial polarization occurring at the interfaces between the hybrid piezoelectric contents and the TPU matrix upto the 10 wt%.^{33, 34} However, beyond 10 wt%, the aggregation of the ferro-/piezoelectric particles occurs as can be seen in SEM images in (Appendix 4, Figure 4A.9) leading to the poor stress transfer with lowered output performance. Remarkably, the observed trend in the V_{PP} values is consistent with the d_{33} values (3.4, 16.5, 31.1, 22.7, 5.3 pC/N) obtained for all the 1, 5, 10, 15, 20 wt% **1**-TPU composite films from the direct method (Berlincourt technique) (Figure 7b).

For evaluate the potential of the **1**-TPU device under practical operating conditions, we measured the output voltage across different external resistances ranging from 0.1 to 40 M Ω . From Figures 4.7c and Appendix 4, Figure 4A.11; it can be seen that the output voltage gradually increases initially and then tends to saturate with the rise of loading resistance, while the current density showing the opposite trend. The maximum instantaneous power calculated by the product of output voltage and current density came out to be 48.69 $\mu\text{W}/\text{cm}^2$ at the loading resistance of 0.9 M Ω . Further, the mechanical stability test of the PENG was estimated by continuous supply of compressive and release cycles. The stability of the signal amplitude upto 1000 cycles makes it reliable for practical applications under ambient environment (Figure 4.7d).

Moreover, the energy generated from the champion 10 wt% **1**-TPU device from the whole series was then used to charge commercially available capacitors (10, 47 and 100 μF). The capacitors were connected to the PENG through a full-wave bridge rectifier which operates in altering the AC output signals of the PENG to direct signals for charging the capacitors (Figure 4.8a). The charging speed is higher for smaller load capacitor and it reaches the saturation voltage quickly within 180 s (Appendix 4, Figure 4A.12). The stored charges on different load capacitors were calculated by using this relation, $Q = C_L V$, as shown in Figure 8b. Various trends are observed for the stored charges among the different rated capacitors. The load capacitor of 10 μF stores minute amount of charge and quickly reaches the saturation value. As the value of load capacitor is increased, then their storage capacity is also increased, and the curve is elevated until it becomes linear. In addition, the load capacitor of 100 μF stored the maximum charges of 13.44 μC in a given time of 450 s.

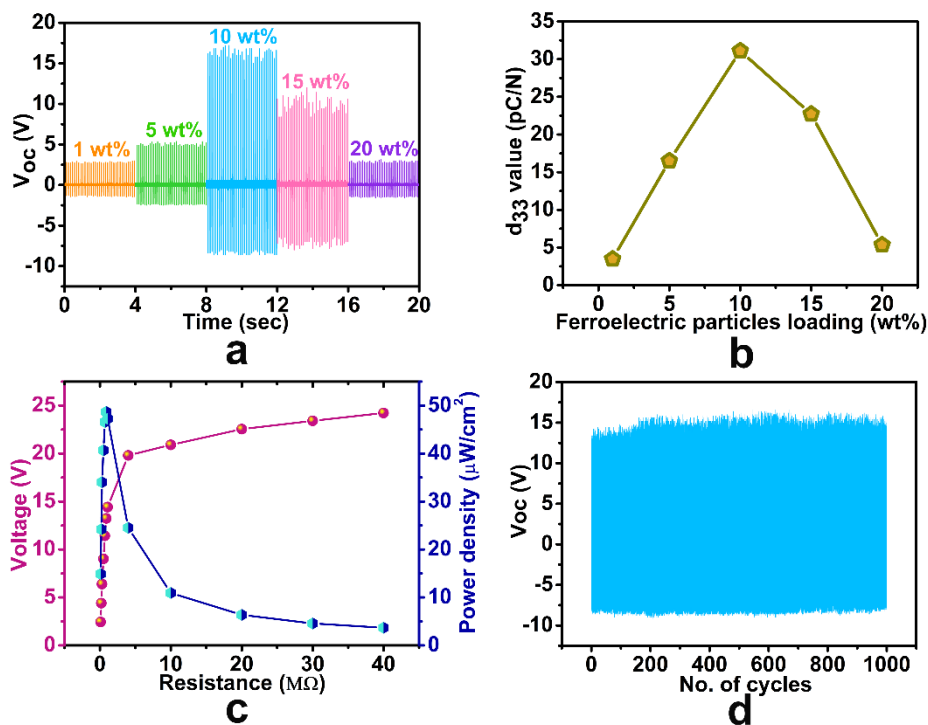


Figure 4.7: (a) Piezoelectric composites of the poled 1-TPU composite devices. (a) Open-circuit voltages recorded for various wt% 1-TPU composite devices. (b) Longitudinal piezoelectric coefficient values obtained from the quasi-static method for all the wt% 1-TPU composite films. (c) Output voltage and power density of the 10 wt% 1-PDMS composite device under different load resistances (solid lines are a guide to the eye). (d) Long-term durability test of the upstanding 10 wt% 1-TPU device with a continuous applied force of 21 N upto 1000 cycles.

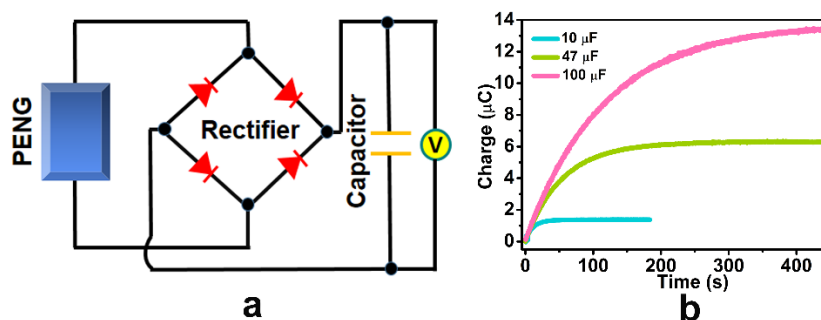


Figure 4.8: (a) Schematic drawing representation of the charging of the capacitor using a 1-TPU device connected through a full-wave four diode bridge rectifier circuit. (b) Plots representing the calculated charge for three different capacitors using output voltages from the 10 wt% 1-TPU device.

4.4 Conclusion

In summary, we have synthesized a polar two-dimensional coordination polymer **1** by employing a noncentrosymmetric flexible dipodal picolyl phosphoramidate ligand **L**. PFM spectroscopy at a single point shows a characteristic butterfly shaped amplitude loop and rectangular shaped phase hysteresis loop. The obtained longitudinal piezoelectric coefficient (d_{33}) value of 82 pm/V is unprecedented in the field of MOFs. Furthermore, the TPU polymer composites of **1** were fabricated and employed as piezoelectric nanogenerators. The maximum open-circuit voltage of 25.05 V and power density output of 48.69 $\mu\text{W}/\text{cm}^2$ were extracted from the optimized 10 wt% (**1**-TPU) composite device. The output voltages were then used to charge the aluminum electrolytic capacitors. The presence of ferro- and piezoelectric behavior in the 2D MOF **1** is substantiated by the PFM measurements and energy harvesting experiments, which indicates the spontaneous polarization in such aggregates. This unfolds the use of MOFs and related materials as a source for renewable electricity generators.

4.5 References

1. K. Uchino, *Ferroelectric devices*, CRC press, 2018.
2. A. Bétard and R. A. Fischer, *Chem. Rev.*, 2012, **112**, 1055-1083.
3. P. Falcaro, R. Ricco, C. M. Doherty, K. Liang, A. J. Hill and M. J. Styles, *Chem. Soc. Rev.*, 2014, **43**, 5513-5560.
4. V. Stavila, A. A. Talin and M. D. Allendorf, *Chem. Soc. Rev.* **43**, 5994–6010 (2014), 2014, **43**, 5994-6010.
5. F. Xue, J. Cao, X. Li, J. Feng, M. Tao and B. Xue, *J. Mater. Chem. C*, 2021, **9**, 7568-7574.
6. J. P. Dürholt, B. F. Jahromi and R. Schmid, *ACS Cent. Sci.*, 2019, **5**, 1440-1448.
7. J. Liang, M. Liu, X. Xu and Z. Liu, *Chem. Commun.*, 2021, **57**, 2515-2518.
8. Y. Chen, S. Guerin, H. Yuan, J. O'Donnell, B. Xue, P.-A. Cazade, E. U. Haq, L. J. W. Shimon, S. Rencus-Lazar, S. A. M. Tofail, Y. Cao, D. Thompson, R. Yang and E. Gazit, *J. Am. Chem. Soc.*, 2022, **144**, 3468-3476.
9. W.-P. Zhao, C. Shi, A. Stroppa, D. Di Sante, F. Cimpoesu and W. Zhang, *Inorg. Chem.*, 2016, **55**, 10337-10342.
10. A. S. Tayi, A. Kaeser, M. Matsumoto, T. Aida and S. I. Stupp, *Nature Chem*, 2015, **7**, 281-294.

11. P.-P. Shi, Y.-Y. Tang, P.-F. Li, W.-Q. Liao, Z.-X. Wang, Q. Ye and R.-G. Xiong, *Chemical Society Reviews*, 2016, **45**, 3811-3827.
12. O. Sato, *Nature Chem*, 2016, **8**, 644-656.
13. A. K. Srivastava, B. Praveenkumar, I. K. Mahawar, P. Divya, S. Shalini and R. Boomishankar, *Chem. Mater.*, 2014, **26**, 3811-3817.
14. A. K. Srivastava, P. Divya, B. Praveenkumar and R. Boomishankar, *Chem. Mater.*, 2015, **27**, 5222-5229.
15. A. Yadav, A. K. Srivastava, P. Kulkarni, P. Divya, A. Steiner, B. Praveenkumar and R. Boomishankar, *J. Mater. Chem. C*, 2017, **5**, 10624-10629.
16. A. Yadav, P. Kulkarni, B. Praveenkumar, A. Steiner and R. Boomishankar, *Chem. Eur. J.*, 2018, **24**, 14639-14643.
17. A. Yadav, A. K. Srivastava, P. Kulkarni, P. Divya, A. Steiner, B. Praveenkumar and R. Boomishankar, *Journal of Materials Chemistry C*, 2017, **5**, 10624-10629.
18. N. Prajesh, V. B. Sharma, S. S. Rajput, C. K. Singh, P. Dixit, B. Praveenkumar, J. K. Zaręba, D. Kabra, S. Ogale and R. Boomishankar, *ACS Sustainable Chem. Eng.*, 2022, **10**, 9911-9920.
19. N. Prajesh, A. Yadav, R. Gourkhede, B. Praveenkumar, A. Steiner and R. Boomishankar, *Chem. Asian J.*, 2020, **15**, 3275-3280.
20. R. Gourkhede, N. Prajesh, R. Gupta and R. Boomishankar, *J Chem Sci*, 2022, **134**, 115.
21. N. Prajesh, D. R. Naphade, A. Yadav, V. Kushwaha, B. Praveenkumar, J. K. Zaręba, T. D. Anthopoulos and R. Boomishankar, *Chem. Commun.*, 2023, DOI: 10.1039/D3CC00098B.
22. G. M. Sheldrick, *Acta Crystallogr. A*, 2008, **64**, 112-122.
23. A. W. Addison, T. N. Rao, J. Reedijk, J. van Rijn and G. C. Verschoor, *J. Chem. Soc., Dalton Trans.*, 1984, DOI: 10.1039/DT9840001349, 1349-1356.
24. J. Conradie, M. M. Conradie, K. M. Tawfiq, S. J. Coles, G. J. Tizzard, C. Wilson and J. H. Potgieter, *New J. Chem.*, 2018, **42**, 16335-16345.
25. C.-R. Huang, X. Luo, W.-Q. Liao, Y.-Y. Tang and R.-G. Xiong, *Inorg. Chem.*, 2020, **59**, 829-836.
26. D.-W. Fu, H.-L. Cai, S.-H. Li, Q. Ye, L. Zhou, W. Zhang, Y. Zhang, F. Deng and R.-G. Xiong, *Phys. Rev. Lett.*, 2013, **110**, 257601.
27. W. Zhang and R.-G. Xiong, *Chem. Rev.*, 2012, **112**, 1163-1195.
28. A. Gruverman, M. Alexe and D. Meier, *Nat Commun*, 2019, **10**, 1661.

29. H.-Y. Zhang, X.-J. Song, X.-G. Chen, Z.-X. Zhang, Y.-M. You, Y.-Y. Tang and R.-G. Xiong, *J. Am. Chem. Soc.*, 2020, **142**, 4925-4931.
30. Z.-H. Wei, Z.-T. Jiang, X.-X. Zhang, M.-L. Li, Y.-Y. Tang, X.-G. Chen, H. Cai and R.-G. Xiong, *J. Am. Chem. Soc.*, 2020, **142**, 1995-2000.
31. H.-Y. Zhang, X.-G. Chen, Y.-Y. Tang, W.-Q. Liao, F.-F. Di, X. Mu, H. Peng and R.-G. Xiong, *Chem. Soc. Rev.*, 2021, **50**, 8248-8278.
32. K. Shi, X. Huang, B. Sun, Z. Wu, J. He and P. Jiang, *Nano Energy*, 2019, **57**, 450-458.
33. M. Arous, H. Hammami, M. Lagache and A. Kallel, *J. Non-Cryst. Solids*, 2007, **353**, 4428-4431.
34. K. Y. Lee, D. Kim, J.-H. Lee, T. Y. Kim, M. K. Gupta and S.-W. Kim, *Adv. Funct. Mater.*, 2014, **24**, 37-43.

Chapter 5

**Flexible Piezoelectric Nanogenerators
Based on One-Dimensional Neutral
Coordination Network Composites**

5.1 Introduction

Piezoelectricity is a macroscopic property exhibited by intrinsically non-centrosymmetric crystals, in which the polarization is induced by the application of an external mechanical stress. Most commercial piezoelectrics are based on oxide ceramics and are utilized in microelectronics, telecommunication devices, medical ultrasonic imaging units, field-effect transistors (FETs), energy storage, photovoltaics etc.¹⁻⁵ However, due to the presence of heavy and toxic metal in conventional ceramics, and their high processing temperatures, alternative materials that possess environmentally benign elements are investigated for piezoelectric applications.⁶⁻⁸ In this regard, material selection spans from organic polymers, for example commercially available semi-crystalline polyvinylidene fluoride (PVDF), to custom-made single-component organics, organic co-crystals, acid-base adducts, two-component salts (organic and hybrid organic-inorganic) and various supramolecular architectures, all of which have been investigated for their notable piezoelectric behavior.⁹⁻¹⁴ Typically, these materials can be combined with piezoelectric or non-piezoelectric polymers to yield flexible composites and optimized multi-layered structures toward maximized energy scavenging performance.^{15, 16}

Metal-ligand coordination assemblies are among the emerging families of supramolecular systems that find a wide range of applications in chemical sensing,¹⁷ gas adsorption and separation,¹⁸ biomedicine,¹⁹ luminescence,²⁰ but also non-linear optics.²¹⁻²³ One of the key attributes of these materials is their efficacy to exhibit compositional tunability and structural diversity that can play a vital part in the design of framework solids with ferro- and piezoelectric properties. However, unlike traditional all-inorganic materials, it is challenging to impart ferroelectricity to the metal-ligand systems, as structure-function relationships for them can only be drawn tentatively.^{24, 25} Despite the lack of highly dependable design rules, polar order in coordination networks can be achieved preferentially by systematic tuning of the nature of metal ions, coordinating ligands, counterions and guest molecules.^{7, 26, 27} However, attaining ferroelectricity in neutral framework materials derived from carboxylate-based ligands has thus far been a challenging task, hence such systems are far less explored than those with charged networks. The polarity in neutral MOFs can be induced by the incorporation of polar functional groups in carboxylate ligands or via encapsulation of polar solvent molecules like water and DMF (N, N-dimethylformamide), which interacts with the frameworks via non-

covalent interactions.^{25, 28-30} Our group has been engaged in the design efforts of polar metal-ligand materials based on pyridyl donor ligands such as [PhPO(NHPy)₂], (Py = 3-pyridyl (³Py) or 4-pyridyl (⁴Py)), [PS(NH³Py)₃] and [PO(NHCH₂³Py)₃], in which the piezo- and ferroelectricity originates from their stable charge-separated structure and the low symmetry of the employed phosphoramidate scaffold.³¹⁻³⁶ Hence, we reasoned that developing pseudo-C₂ and C₃ symmetric phosphoramidate ligands containing carboxylic acid functional groups, would result in the generation of neutral noncentrosymmetric coordination networks suitable for ferro- and piezoelectric studies. In this contribution, we describe a new neutral one-dimensional zinc coordination network {[Zn(L¹)(bpy)]•(H₂O)_{1.5∞}} (**1**), employing the flexible carboxylate functionalized dipodal P-N ligand [PhPO(NH-(C₆H₄COOH))₂] (**L¹H₂**), which crystallizes in the polar non-centrosymmetric space group *R3c*. The piezoelectric behavior and the domain structure of **1** could be extracted at a microscopic level using the piezoresponse force microscopy (PFM) technique. Measurements of second-harmonic generation (SHG) at 800 nm not only provided independent, nonlinear optical evidence of structural non-centrosymmetry of **1**, but also demonstrated two-photon excited luminescence (2PEL), pointing to its multifunctional behavior. Furthermore, flexible composites comprising the framework **1** in different weight percentages (wt%) were prepared with thermoplastic polyurethane (TPU) polymer and examined for piezoelectric energy harvesting application. A highest open-circuit voltage (*V_{oc}*) of 5.6 V and power density output of 14.6 μW/cm² was achieved for the poled 5 wt% **1**-TPU nanogenerator device. Energy storage was demonstrated by charging the capacitors using the output voltages obtained from the 5 wt% **1**-TPU device. These findings are prominent contributions to the emerging area of metal-organic electricity nanogenerators.

5.2 Experimental Section

5.2.1 General Remarks

All reactions and work-up involving PhPOCl₂ were carried out under dry N₂ atmosphere in Schlenk-type glassware. Ethyl 3-aminobenzoate, Zn(NO₃)₂·6H₂O and PhPOCl₂ was purchased from Merck chemical company and used as received. Dry solvents and PhPOCl₂ were distilled prior to use. All NMR spectra were recorded at room temperature using a Jeol 400 MHz spectrometer with operating frequencies of 400.13, 100.62 and 161.97 MHz for the respective ¹H, ¹³C and ³¹P{¹H} nuclei. For the ¹H, ¹³C spectra, SiMe₄ was employed as the internal

standard, while for ^{31}P spectra, the 85% H_3PO_4 was used as the standard. The MALDI-TOF spectra of the ligands **L** and **L¹H₂** were recorded by using an Applied Biosystem MALDI-TOF/TOF spectrometer. The powder X-ray diffraction (PXRD) data of **1** were measured on a Bruker-D8 Advance diffractometer. A Perkin-Elmer STA-6000 thermogravimetric analyzer was used to obtain the TGA of **1**. Elemental analyses **L**, **L¹H₂** and **1** were performed on a Vario-EL cube elemental analyzer. The melting points of **L**, **L¹H₂** and **1** were determined from an Electro thermal melting point apparatus. FT-IR spectra were recorded on a Bruker Alpha spectrophotometer in the attenuated total reflectance (ATR) mode for the neat samples of **L**, **L¹H₂** and **1**.

5.2.2 Synthesis

2.2.2.1 (L): To a solution of ethyl 3-aminobenzoate (7.37 mL, 8.160 g, 24.53 mmol) in toluene (100 mL) kept stirring at 0 °C under inert atmosphere, PhPOCl_2 (1 mL, 1.375 g, 3.52 mmol) in 10 mL of toluene was added dropwise using a pressure equalizer funnel. The resultant mixture was refluxed for 4 h until a white precipitate of the amine-hydrochloride was formed. The residue was filtered off and the resulting filtrate was left standing at room temperature for 2-3 h to precipitate the ester compound **L**. It was then filtered off, washed 3-4 times with distilled water and dried. Yield 1.71 g (54 %). ^1H NMR (400 MHz, CD_3OD) δ 7.84 (dd, $J = 13.6, 6.9$ Hz, 2H), 7.74 – 7.73 (m, 2H), 7.53 – 7.47 (m, 1H), 7.46 – 7.40 (m, 4H), 7.30 (dd, $J = 7.6, 2.3$ Hz, 2H), 7.17 (t, $J = 7.9$ Hz, 2H), 4.19 (q, $J = 7.1$ Hz, 4H), 1.22 (t, $J = 7.1$ Hz, 6H). ^{13}C NMR (101 MHz, CD_3OD) δ 168.0, 142.9, 133.8, 133.0, 132.9, 132.5, 130.2, 129.8, 124.1, 123.5, 120.5, 62.1, 14.7. $^{31}\text{P}\{^1\text{H}\}$ NMR (162 MHz, CD_3OD) δ 12.01. MALDI-TOF: 475.31 ($\text{M}+\text{Na}$)⁺, 491.31 ($\text{M}+\text{K}$)⁺. M.P.: 190°C. Anal. Calcd. for $\text{C}_{24}\text{H}_{25}\text{N}_2\text{O}_5\text{P}$: C, 63.71; H, 5.57; N, 6.19. Found: C, 63.84; H, 5.177; N, 6.04.

5.2.2.2 (L¹H₂): The **L** (0.50 g) was dissolved in methanol (35 ml) and water (15 ml). Sodium hydroxide (400-500 mg) was added and the resulting mixture was stirred overnight at room temperature. The MeOH/H₂O was removed using a rotary evaporator, the precipitate obtained was re-dissolved in 1 mL of H₂O and re-precipitated by adding an excess amount of 1M solution of HCl. The product **L¹H₂** as a white solid was isolated by filtration and washing multiple times with water. Yield 0.295 g (59 %). ^1H NMR (400 MHz, DMSO-d_6) δ 12.78 (s, 2H), 8.28 (d, $J = 11.5$ Hz, 2H), 7.87 (dd, $J = 7.3, 5.8$ Hz, 1H), 7.83 (t, $J = 1.7$ Hz, 3H), 7.59 (td,

$J = 7.4, 1.4$ Hz, 1H), 7.56 – 7.50 (m, 2H), 7.41 (dt, $J = 6.9, 1.8$ Hz, 4H), 7.27 (t, $J = 7.9$ Hz, 2H). ^{13}C NMR (101 MHz, DMSO- d_6) δ 167.3, 142.5, 133.0, 132.1, 131.7, 131.4, 129.0, 128.5, 122.1, 121.4, 118.6, 39.5. $^{31}\text{P}\{^1\text{H}\}$ NMR (162 MHz, DMSO- d_6) δ 8.77. MALDI-TOF: 420.01 ($\text{M}+\text{Na}$) $^+$, 434.11 ($\text{M}+\text{K}$) $^+$ M.P.: 220 °C. Anal. Calcd. for $\text{C}_{20}\text{H}_{17}\text{N}_2\text{O}_5\text{P}$: C, 60.61; H, 4.32; N, 7.07. Found: C, 60.19; H, 4.168; N, 6.98.

5.2.2.3 Compound 1: To a solution of L^1H_2 (50 mg, 0.126 mmol) and 2,2'-bipyridine (19.5 mg, 0.126 mmol) stirred in N,N-dimethylformamide (DMF) (3 mL), $\text{Zn}(\text{NO}_3)_2 \cdot 6\text{H}_2\text{O}$ (111.55 mg, 0.378 mmol) in H_2O (3 mL) was added. This mixture was sealed in a 10 mL teflon-lined stainless steel reactor and heated to 100 °C for 48 h in a programmable oven. The reaction system was cooled for 24 h. Fine needle like white crystals suitable for SCXRD analysis were collected from the bottom of the reactor vessel. Yield: 70%. M.P. 229 °C. Calcd. for $\text{C}_{30}\text{H}_{26}\text{N}_4\text{O}_{6.5}\text{PZn}$: C, 56.05; H, 4.08; N, 8.71. Found: C, 55.96; H, 3.810; N, 8.04. FT-IR data on powder (cm^{-1}): 3228, 2361, 1580, 1382, 1207, 1126, 956, 814, 734, 685, 626.

5.2.3 Crystallography

The single-crystal X-ray diffraction data for **L**, L^1H_2 and **1** were collected at 100 K on a Bruker Smart Apex Duo diffractometer using MoK α radiation ($\lambda = 0.71073$ Å). All the structures were refined using SHELX by full-matrix least-squares against F^2 on all data. All the non-hydrogen atoms of **L**, L^1H_2 and **1** were refined anisotropically except for some of the atoms of L^1H_2 . Four carbon atoms in L^1H_2 had poor thermal ellipsoids and hence they were refined with partial isotropic characteristics. The crystals of **L**, L^1H_2 and **1** exhibited weak diffractions at higher angles. Hence, their data were reduced to $2\theta = 50^\circ$ for **L** and $2\theta = 45^\circ$ for L^1H_2 and **1**.

Table 5.1: Crystallographic data for the ligand **L**, L^1H_2 and **1**.

Compound	L	L^1H_2	1
Chemical formula	$\text{C}_{24}\text{H}_{25}\text{N}_2\text{O}_5\text{P}$	$\text{C}_{40}\text{H}_{30}\text{N}_4\text{O}_{10}\text{P}_2$	$\text{C}_{30}\text{H}_{26}\text{N}_4\text{O}_{6.5}\text{PZn}$
Formula weight	452.43	788.62	642.89
Temperature	100(2)	120(2)	100(2)
Crystal system	Monoclinic	Triclinic	Trigonal
Space group	$\text{P}2_1/\text{c}$	$\text{P} - 1$	$\text{R}3\text{c}$

a (Å); α (°)	12.390(2); 90	8.601(3); 94.00(8)	30.362(11); 90
b (Å); β (°)	40.435(8); 89.990(5)	12.264(4); 93.48(8)	30.362(11); 90
c (Å); γ (°)	8.9559(16); 90	17.179(6); 92.34(8)	15.620(6); 120
V (Å ³); Z	4486.7(14); 8	1802.4(11); 2	12470(10); 18
ρ (calc.) mg m ⁻³	1.340	1.453	1.541
μ (Mo K α) mm ⁻¹	0.161	0.189	0.999
2 θ_{\max} (°)	50.054	45.024	45.022
R(int)	0.1060	0.1897	0.2289
Completeness to θ	94.8 %	99.4 %	99.3 %
Data / param.	7492/581	4699/505	3611/359
GOF	0.919	1.115	1.026
R ₁ [F > 4 σ (F)]	0.0525	0.1191	0.0476
wR ₂ (all data)	0.0917	0.3375	0.1075
max.peak/hole (e.Å ⁻³)	0.212/-0.320	1.362/-0.594	0.385/-0.392

5.2.4 Ferroelectric, Dielectric and Piezoelectric Measurements

The ferroelectric P-E hysteresis loops measurements along with the leakage current plots for framework **1** were performed on its drop-casted film by using a commercial Sawyer-Tower circuit (TF Analyzer 2000E, aixACCT, Germany). The dielectric permittivity data for **1** was obtained on its polycrystalline pellets of 10 mm diameter using a Solartron analytical 1260 model impedance analyzer attached to a 1269A model dielectric interface. Janis 129610A model cryostat integrated with a Lakeshore 336 model temperature controller was used as the sample holder. The d_{33} values of the poled composite films of **1**, of ~0.47 mm thickness, were extracted on a PM300 Piezotest meter.

5.2.5 Second Harmonic Generation Study

The laser source used for SHG measurements was a Coherent Astrella Ti:sapphire regenerative amplifier generating 800 nm, 75 fs laser pulses (repetition rate of 1 kHz). Semi-quantitative assessment of SHG efficiency was performed at 293K following a modified Kurtz-Perry (Graja) powder test methodology. Potassium dihydrogen phosphate (KDP) was employed as a

SHG standard. The single-crystalline materials of **1** and that of KDP were manually powdered and size-graded by sieving through an Aldrich mini-sieve set into 250–177 μm size range. Subsequently, sieved powders of **1** and KDP were placed in-between microscope glass slides (forming tightly packed layers) sealed and placed on horizontally-aligned sample holder. Mean power density of 800 nm laser beam was 0.49 Wcm^{-2} , with a spot area of 0.5 cm^2 . The unfocused laser beam was directed at samples at 45° . Collimating optics, attached to the 400 μm optical fiber, were positioned at a right angle to the plane of the sample, allowing for detection of backscattered SHG signal. Scattered 800 nm pumping beam was attenuated using a 750 nm short-pass hard-coated Thorlabs optical filter (FESH0750, O.D. > 5 at 800nm), which was placed in front of the signal collecting lens ($f = 25.4 \text{ mm}$). Ocean Optics Flame T-XR fiber-coupled spectrometer (200 μm entrance slit) was used to record SHG signal.

5.2.6 Piezoresponse Force Microscopy Characterization

Piezoelectric characterizations of 1 and 5 wt% (**1**-TPU) film were studied under the Asylum research MFP-3D atomic force microscopy (AFM) system. The contact mode AFM (c-AFM) was done to obtain piezoresponse of the films. The measurement was done using RMN-12PT300B measurement cantilever probes with 1.12 N/m spring constant and $< 8 \text{ nm}$ tip diameter. The PFM data collected was based on the vertical PFM measurements (VPFM) where AC voltage was applied to the conductive AFM tip keeping the bottom electrode grounded. The PFM images were collected at resonance frequency of $300 \pm 20 \text{ kHz}$ with 2.5V applied bias. The measurements were done in dual ac resonance tracking (DART) mode PFM.

5.2.7 Computational Details

The preliminary first-principles study for the electric polarization calculations were performed by employing the Berry phase method using the Quantum Espresso software code.³⁷ The nonrelativistic norm-conserving pseudopotentials with Perdew-Burke-Ernzerhof (PBE) exchange-correlation functional were applied for the calculations.^{38, 39} The calculations were done using the modern theory of polarization on a discrete Zn(II) polyhedral core at the center of a box $18 \times 18 \times 18 \text{ \AA}^3$ with a sufficient amount of vacuum in the free space to tackle the periodic effect. The change in dipoles was calculated upon changing the geometry around the Zn-core from ideal square-pyramidal to distorted square-pyramidal core as observed in the structure of **1**. Nevertheless, it should be emphasized that the overall dipole moment and the

polarization of the system will include the collective contributions of the metal-ion, ligand systems and the solvate atoms. Such calculations could not be performed due to the presence of atoms in huge number by the system. The structural graphics were acquired by using the VESTA software.⁴⁰

5.2.8 Preparation of the 1-TPU Composite Films and Testing of the Composite Devices

Flexible polymeric composite films were prepared by the solution casting method. A constant quantity of TPU (1 g) was dissolved in N,N-dimethylformamide (6 mL, DMF) and heated at 90 °C for 60 minutes until a clear homogeneous solution was formed. A precalculated amount (for example, 53.47 mg for 5 wt% composite) of ferroelectric crystals were added into a transparent homogeneous TPU mixture and then performed vortex mixing for 5 minutes. The suspension was continuously stirred at room temperature for 4 hours, until the complete dispersion of the crystals. Afterwards, the homogeneous composite mixture was poured into an aluminium mould and let it dry in an oven for 24 h at 60 °C. A completely dried free-standing milky white composite film from the aluminum mould was scraped off. A similar procedure was followed to prepare 1, 5, 10, 15 wt% composite films. Further, the composite devices were fabricated with an appropriate selected area of 1.3 x 2 cm² and a thickness of \approx 0.47 mm. The copper tapes with conductive adhesive were pasted on either side of the films using a hot-press method. The final device architecture for each wt% of the composite devices were encapsulated with a Kapton tape to protect the device from any physical damages. Further, by using a home-built impact measurement setup, the piezoelectric performance of all the composite devices of the framework **1** were carried out. The piezoelectric output voltages of the **1**-TPU films were recorded on a mixed-signal oscilloscope model Tektronix 2024 working at 1 M Ω input impedance. The currents generated during these measurements were monitored using a Keithley multimeter model number DMM7510 7.5.

5.3 Results and Discussion

5.3.1 Synthesis, Characterization and Crystal Structures

The flexible dipodal ligand **L¹H₂** was synthesized by reacting PhPOCl₂ with ethyl 3-aminobenzoate followed by hydrolysis (Scheme 5A.1, Appendix 5). The ligands were characterized by NMR spectroscopy, mass spectrometry and single-crystal X-ray diffraction analysis (Figures 5A.1-5A.7, Appendix 5). Hydrothermal treatment of **L¹H₂** with

$\text{Zn}(\text{NO}_3)_2 \cdot 6\text{H}_2\text{O}$ and 2,2'-bipyridine at 100 °C affords a one-dimensional zinc coordination network **1**, (Scheme 5A.2, Appendix 5). The single crystal X-ray diffraction analysis of **1** reveal that it crystallizes in the trigonal $R\bar{3}c$ space group ($a = 30.36 \text{ \AA}$, $c = 15.62 \text{ \AA}$, $\gamma = 120^\circ$). The cationic charge of the Zn(II) center is canceled out by two carboxylate anions, while the 2,2'-bipyridine completes its coordination sphere. The Zn(II) ion is located in a penta-coordinated environment and exhibits a geometry in-between trigonal bipyramidal and square pyramidal, but slightly inclined towards the latter, with the Addison parameter $\tau = 0.53$ ($\tau = (\beta - \alpha)/60^\circ$, where β and α are the two greatest valence angles around coordinated metal center).⁴¹

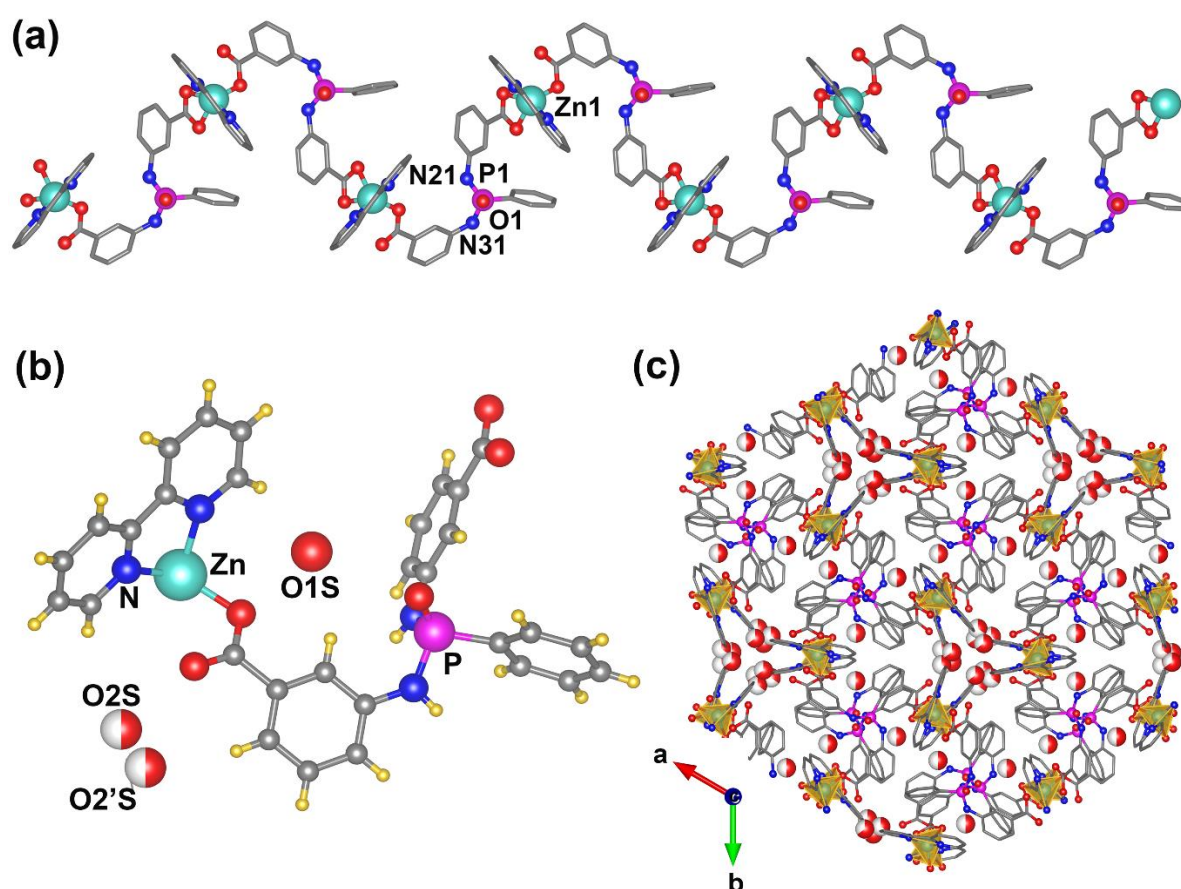


Figure 5.1: (a) Crystal structure of **1** showing its zig-zag one-dimensional coordination network. (b) Asymmetric unit of **1**. (c) The hexagonal packing structure of **1** viewed along the c-axis. Color code: ligand backbone, grey; small blue spheres, nitrogen atoms; small red spheres, ligand oxygen atoms; zinc polyhedron, yellow; disordered water molecules, mixed white and red.

The coordination sphere around the Zn(II) center consists of two nitrogen atoms from 2,2'-bipyridine ligand, and three carboxylate oxygen atoms from two L^1 fragments. The two oxygen atoms from one arm of the dipodal ligand assume chelating coordination mode and one oxygen atom from another L^1 fragment lies in a terminal coordination (Figure 5A.8, Appendix 5). Each unit of L^1 interacts with two adjacent Zn(II) centers and give rise to the framework of a 1D-*zig zag* chain structure (Figure 2.1a). Furthermore, the asymmetric unit of **1** contains 1.5 H₂O molecules, of which one of them is disordered over two positions (Figure 2.1b). These water molecules are involved in H-bonding interactions with both the coordinated and uncoordinated carboxylate O-atoms and result in the formation of H-bonded trigonal 3D-network along the c-axis (Figure 2.1c). A closer look at the coordination polyhedron around the Zn(II) center shows that both the equatorial (chelating) Zn-O bonds are equivalent in distance (Zn-O21: 2.134(7) and Zn-O22: 2.172(8)), while the apical Zn-O contact (Zn-O31: 1.955(8)) is shorter by 9.2 %. By contrast, one of the equatorial Zn-N distance of the 2,2'-bipyridine (Zn-N41: 2.084(6)) ligand is longer over the other one (Zn-N52: 2.007(7)) by 4.4%. The average of out-of-plane bond angles, namely O-Zn-O and N-Zn-O, are 106.32(3)° and 113.975(3)°, respectively, are much larger than those found in typical square pyramidal geometries. In the absence of its typical charge-separated structure, these geometric distortions around the metal-center could act as one of the factors causing polarization in **1**.

To check whether these distortions generate any dipole in the structure, we performed preliminary ab-initio calculations on the polyhedral Zn(II) core of **1**.⁴²⁻⁴⁵ These calculations yielded a change in dipole moment of 30.68 eÅ upon changing the Zn(II) core from an ideal square-pyramidal to distorted square-pyramidal geometry, as shown in Figure 2.2a. The location of the positive and negative charge densities obtained due to the distortions are displayed in Figure 2.2b. Interestingly, these dipoles align in the propagation direction of the 1D-chain in **1** along the polar c-axis (Figure 5A.9, Appendix 5). Furthermore, a long-range order of these dipoles is established via H-bonding interactions with solvent molecules (Figure 2.2c). Nevertheless, it should be emphasized that the overall dipole moment and the polarization of the system will include the collective contributions of the metal-ions, ligand systems and the solvate molecules.

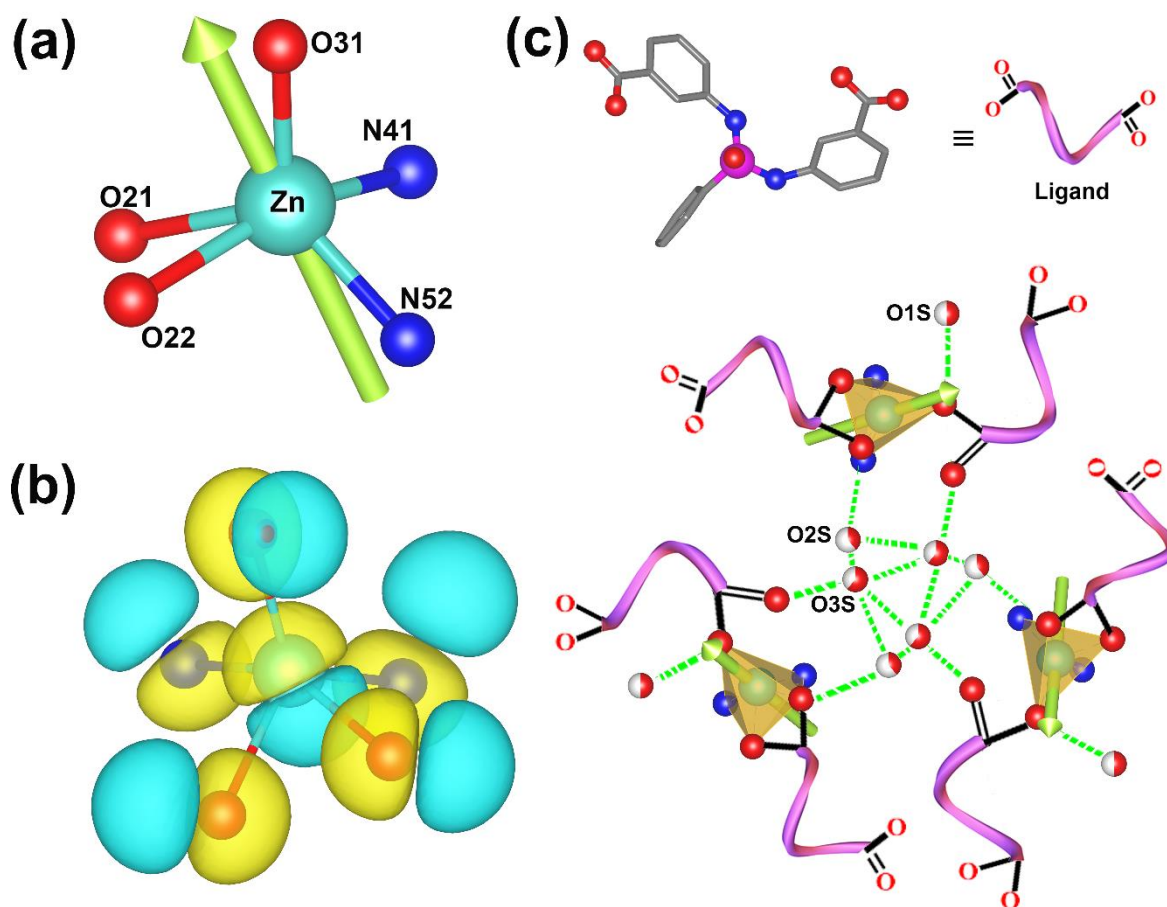


Figure 5.2: (a) View of the Zn(II) core of **1** showing (a) the orientation of its dipole and (b) the charge-density plot with the separation of positive (yellow) and negative (cyan) charges. (c) Long-range ordering of the dipoles around the metal-centers assisted by H-bonding interactions.

5.3.2 SHG, Ferroelectric, Dielectric and Piezoelectric Studies

The noncentrosymmetric nature of **1** was further verified by Kurtz-Perry (Graja) powder method.^{46, 47} The 800 nm fs laser pulses were employed to obtain second harmonic generation (SHG) signals in size-graded samples of **1** and KDP ($\lambda_{\text{SHG}} = 400$ nm) at 293 K. The calculated integral intensities of SHG signals yielded a relative SHG efficiency of **1** equal to 0.23 versus that of the KDP reference material (Figure 5A.10, Appendix 5).

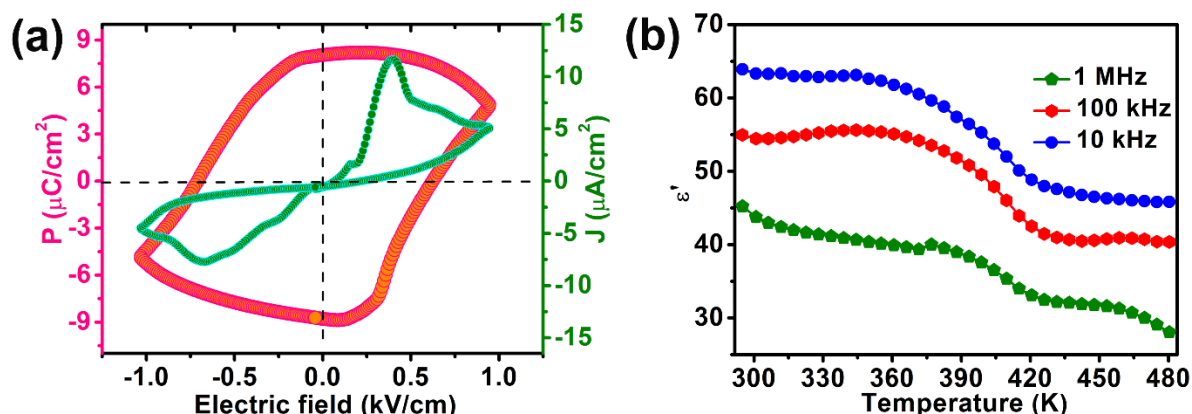


Figure 5.3: (a) P-E hysteresis loop measurements of **1** at room temperature along with the leakage current-density plot. (b) Temperature-dependent of ϵ' for **1** under different frequencies.

The compound **1** exhibits a molecular symmetry of C_{3v} , which belongs to the combined class of ten polar point groups that are capable to show ferroelectric property. To establish the ferroelectric nature of **1**, the polarization vs. electric field (P-E) measurements were performed for **1** on its drop-casted thin films on Al substrate (Figures 5A.15-5A.16, Appendix 5).⁴⁸ These measurements yielded a nearly rectangular shaped P-E hysteresis loop for the thin-film sample of **1**, indicating its ferroelectric nature. A saturation polarization (P_s) value of $4.80 \mu\text{C}/\text{cm}^2$ at a coercive field of $0.62 \text{ kV}/\text{cm}$ was obtained for **1** (Figure 2.3a). The current density measured as a function of electric field along the P-E loop trace shows low leakage currents and gave peaks due the coercive fields indicating the presence of switchable polarization.

To further explore the polarization characteristics, the dielectric permittivity analysis were done on the compacted disc of **1**. The real part of the dielectric permittivity (ϵ') as a function of temperature showed a broad anomalous peak at the temperature ranging from 308 to 423 K, which is attributed to desolvation of the solvated water molecules present in **1**. Further rise in the temperature shows no additional peak anomaly, signifying the absence of any ferroelectric to paraelectric phase transition until 573 K (Figure 2.3b). The thermogravimetric analysis shows an initial weight loss of about 5% onset at 318 K and a subsequent weight loss of around 38 % at 578 K due to its decomposition (Figure 5A.17, Appendix 5). The powder X-ray diffraction data of framework **1** collected at temperatures between 300 and 493 K shows no change in its peak profiles, indicating the crystallinity and the structural stability of the

framework is retained even after desolvation (Figure 5A.18, Appendix 5). Furthermore, the frequency-dependent permittivity measurements recorded in the range of 10 kHz to 1 MHz, show an increasing trend in the ϵ' values, signifying the existence of all four polarization mechanisms in **1**. Particularly, the polarizability of solvated water molecules and the mobility of ions gave higher polarization at lower frequencies (Figure 5A.19, Appendix 5). The dielectric loss factor ($\tan \delta$), that indicates the dissipation of electrical energy as heat, was observed to be very low in both temperature and frequency dependent measurements (Figures 5A.20 and 5A.21, Appendix 5).

With the aim to investigate the local polarization state of **1**, vertical piezoresponse force microscopy (VPFM) experiments were done on polycrystalline disc of **1** mounted on the Pt substrate. PFM provides the information regarding strength of the electromechanical coupling and direction of polarization in each domain.^{49, 50} An external dc bias of 50 V with a superimposed constant alternating current voltage of 2.5 V from the metal coated conducting tip perpendicular to the pellet surface was applied to record the polarization attributes (Figure 5A.22a, Appendix 5). The obtained amplitude and phase images of **1** with an active area of 5 x 5 μm^2 are shown in the Figures 2.4a and 2.4c, respectively (for topography, please see Figure 5A.22b, Appendix 5). Subsequently, PFM spectroscopy was performed at a fixed location on **1** by applying an additional dc bias of 50 V at the cantilever tip. Figure 4b shows the typical butterfly-shaped amplitude-bias loop, which corresponds to the strain-voltage phenomenon of piezoelectric materials. The difference between phases of the opposite signals is nearly 180°, which shows the inverse domain switching of the polarization (Figure 2.4d). These results support the existence of ferroelectric behavior in **1**. Such observations for the domain structures at the nanoscale are rare among metal-ligand coordination polymers.²⁹ Furthermore, the piezoelectric coefficient d_{33} , (a quantitative measure of the piezoelectric deformation, which is directly proportional to the amplitude) was calculated to be 19.4 pm/V. The observation of ferroelectric domains and sizable piezoelectric coefficient values are quite rare among single-component metal-ligand assemblies (Table 5A.1, Appendix 5).

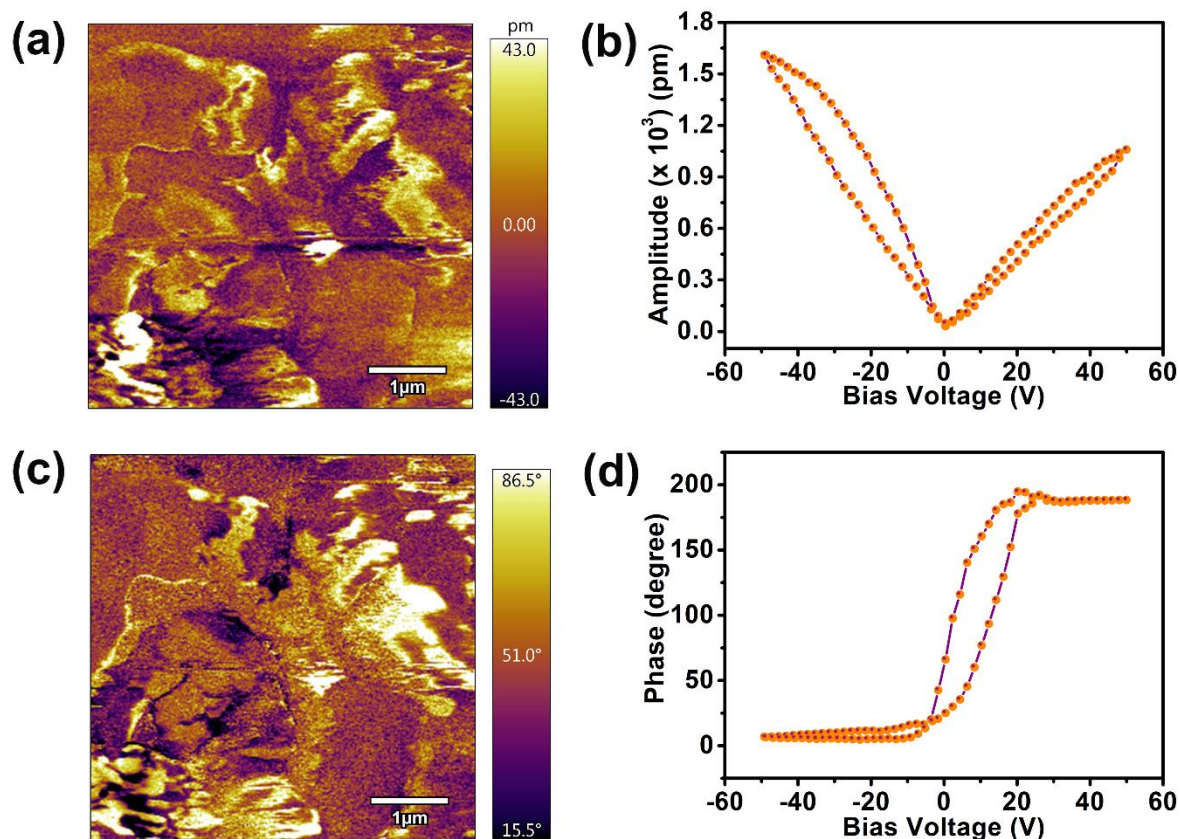


Figure 5.4: PFM data of **1**. (a) Amplitude image (b) Amplitude-bias ‘butterfly’ loop (c) Phase contrast image (d) Phase hysteresis loop.

5.3.3 Fabrication and Characterization of the 1-TPU Composites

Spurred by the promising ferro- and piezoelectric attributes of **1**, we set out to utilize this framework for the fabrication of flexible piezoelectric nanogenerators. For this purpose, composites with various (1, 5, 10 and 15) weight percentages (wt%) of **1** were prepared in combination with the piezoelectrically inactive polymeric TPU.⁵¹ These composites were obtained by mixing the calculated amount of **1** into a DMF solution of TPU. The homogeneous mixtures were poured into an aluminum mould, heated at 60 °C for 24 hours and the formed films were subsequently peeled off (Table 5A.2, Figure 5A.23, Appendix 5). The exceptional flexibility of all these as-made composite films were examined by subjecting them to the various mechanical stretching, rolling and bending operations (Figure 2.5a and Figure 5A.24, Appendix 5). Furthermore, a good dispersion of **1** in TPU matrix is observed from the confocal microscope image of the 5 wt% **1**-TPU composite, which is favorable for the effective stress

transfer during the mechanical energy generation process.^{52, 53} The PXRD profiles of these films show that all hkl diffraction peaks of **1** are intact in the composite films, serving as direct evidence for the presence of crystalline particles embedded in the composite films (Figure 2.5b, Figure 5A.25, Appendix 5).

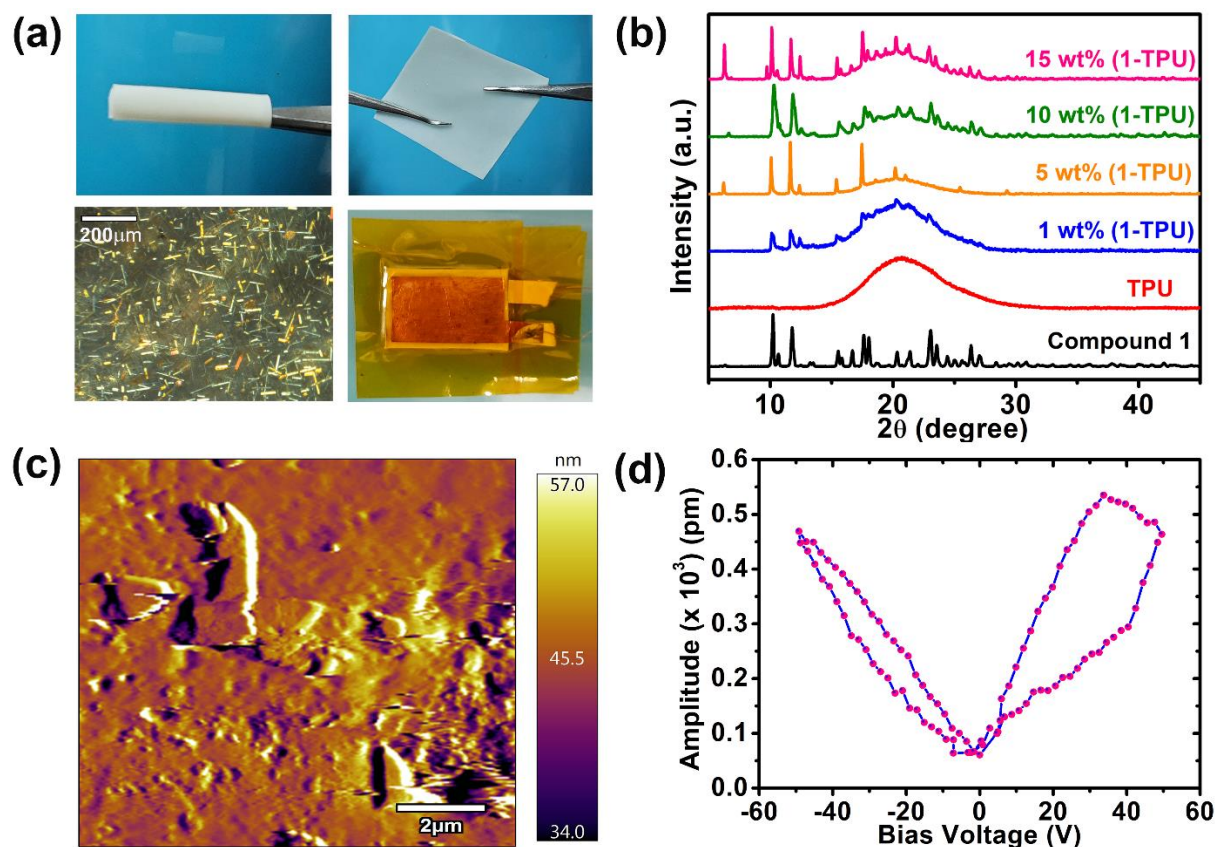


Figure 5.5: (a) (From top to bottom) Pictures demonstrating the flexibility of a representative 1-TPU film toward rolling and stretching functions. The 1-TPU film photograph taken under the polarizing microscope at a magnification scale of 200 μm. Photograph of the device showing the sandwich structure of 1-TPU between Cu electrodes encapsulated with Kapton tape. (b) PXRD profiles of composite films of 1-TPU with various wt% of **1**. (c) Topography image at a 10 x 10 μm² area of the 5 wt% 1-TPU composite film. (d) Amplitude-bias voltage ‘butterfly’-shaped loop.

To confirm whether the piezoelectric properties of **1** are preserved in the composite films, the PFM experiments were performed on the 5 wt% 1-TPU film. The amplitude image shows the presence of the domain structures with upward and downward polarizations. The PFM

spectroscopy performed at a single point on the film shows the characteristic butterfly-shaped amplitude loop (Figures 2.5c, d and Figure 5A.26, Appendix 5). The slope of the amplitude curve yielded the converse piezoelectric coefficient (d_{33}) value of 16.7 pm/V.

The device architectures for these composite films were made by placing copper adhesive tapes which serves as top and bottom electrodes (Figure 2.5a). Finally, the fabricated nanogenerator devices were sealed with Kapton tape to keep the electrodes and the composite films intact and provide insulation to the devices from the external environment. The cross-sectional SEM images of a representative **1**-TPU device indicate the thickness of the **1**-TPU thin-film to be \approx 0.47 mm (Figure 5A.27, Appendix 5). The output performance of all these **1**-TPU devices was estimated by applying constant compressive force from an home-built impact stimulator.⁵⁴ Prior to the experiment, all the **1**-TPU composite films were subjected to a poling process at an electric field of 25 kV/cm for about two hours at room temperature to orient the disordered electric dipoles along the electric field direction. The open-circuit voltage (V_{oc}) of the devices were recorded under an impact force of 40 N at a frequency of 17 Hz, from each of the devices with an active area of 1.3 x 2 cm². Figure 2.6a presents the output voltages generated from all the **1**-TPU devices along with a blank device fabricated from a pristine TPU layer (for individual data please see Figure 5A.28, Appendix 5). It is evident that the electric performance is strongly correlated with the concentration of the piezoelectric fillers. An initial increase in the V_{oc} from 3.24 V to 5.65 V is noticed as the mass fraction is varied from 1 wt% to 5 wt% of **1**. Subsequently, it drops to 4.22 V and 3.05 V as the content of **1** is increased further to 10 wt% and 15 wt%, respectively. This clearly signifies that compositional optimization is essential for yielding the best performance in piezoelectric nanogenerators. In this case, the champion device is the 5 wt% **1**-TPU hybrid material, which shows a maximum output of 5.65 V. Also, an examination of the output voltages of this best-performing device under various external impact forces (28, 35, 40 N) showed again the highest open-circuit voltage of 5.6 V at the optimal 40 N force (Figure 5A.29, Appendix 5).

By contrast, the reference device involving only pure TPU shows a negligible V_{oc} of \sim 400 mV. Since TPU is non-piezoelectric, the observed small electrical signals from it can be tracked to the residual electrostatic charges at the electrodes. Nevertheless, this effect can be neglected, given the large contrast provided by the robust piezoelectric effect seen for **1**. Furthermore, we

carried out a polarity-switching test (by reversing the connections to oscilloscope) on the best-performing 5 wt% **1**-TPU device to verify the observed electric signals are purely due to the piezoelectric effect (Figure 5A.30, Appendix 5).^{55, 56} Figure 2.6b illustrates that the V_{oc} values of nearly same magnitude are observed from nanogenerator in the forward and reverse connections. The insets of this figure exhibit a close view of a single pulse demonstrating the reversibility of the positive and negative piezoelectric potential responses during the compression and release cycles. Also, the obtained V_{oc} from the non-poled devices is found to be much lower than that for poled devices (Figure 5A.31, Appendix 5).

The variations in the voltage outputs of these **1**-TPU films can be understood as follows. During the piezoelectric impact stress and release operation, free electrons produced at the electrodes will be driven to flow back and forth to screen the induced piezopotential difference and maintain electrostatic equilibrium between the two electrodes. An alternating output voltage is generated to counter the flow of free electrons in an external circuit. The disproportion in the positive and negative voltage peaks can be ascribed to the variation between the external force applied and the restoring force. When the concentration of **1** is increased, an augmentation in the Maxwell-Wagner-Sillars (MWS) phenomena takes place due to the increase in the interface area.⁵⁷ A further increase in the piezoelectric content beyond a threshold limit, however, results in the aggregation of the particles. Although this effect improves permittivity, it also causes the field concentration effect and dipole mobility in an adverse way, leading to a decrease in the output performance.^{56, 58, 59} The scanning electron microscopy (SEM) images recorded on all the **1**-TPU composites show a homogeneous distribution of **1** in the TPU matrix at lower concentrations and indicate the aggregate formation for particle loadings of 10 wt% and above (Figure 5A.32, Appendix 5). To corroborate this, the dielectric permittivity values of all the composite films of **1**-TPU were measured and compared. These measurements showed an increase in the ϵ' values for upto 5 wt% of **1** in the polymer matrix. However, it was found to decrease in the higher 10 and 15 wt% composites confirming a reduction of the bulk polarization in them (Figure 5A.33, 5A.34, 5A.35 Appendix 5).

To further confirm the concentration effect of **1** on the device output characteristics, direct piezoelectric coefficient (d_{33}) measurements were performed using Berlincourt method. The d_{33} values were extracted by a quasi-static piezometer on the various wt% composite films of

1 with an externally applied force of 0.25 N which operates at a frequency of 110 Hz. These measurements yielded the d_{33} values of 4.20, 11.70, 9.06, 3.30 pC/N for the composite films 1, 5, 10, 15 wt% 1-TPU, respectively (Figure 2.6c, Figure 5A.36, Appendix 5). Notably, the highest d_{33} value of 11.70 pC/N is acquired for the best performing 5 wt% 1-TPU film. Also, the observed trends in the d_{33} values again validates the reduction of dipoles due to the increase in the concentration of the particles, which correlates well with the V_{oc} values obtained for the 1-TPU composite devices.

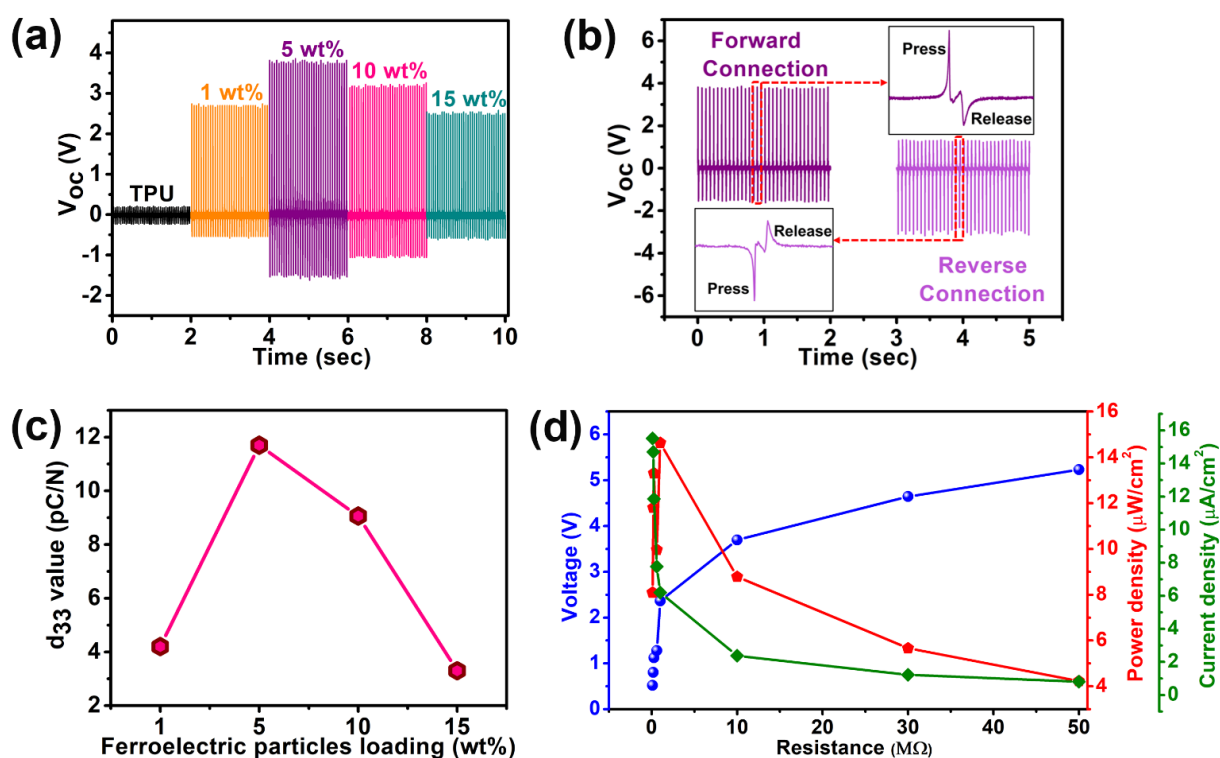


Figure 5.6: Piezoelectric characterizations of the poled 1-TPU-based composite devices. (a) Open-circuit voltages (V_{oc}) of all the devices generated under a periodic mechanical tapping on a shifted-time axis. (b) The polarity-switching tests using the forward and reverse connections to the oscilloscope (c) Longitudinal Piezoelectric coefficient (d_{33}) measurements of various 1-TPU films. (d) The load resistance dependent output voltage, current density and power density data of the best performing 5 wt% 1-TPU film. The solid lines connecting the points in plots of (c) and (d) serve as a guide to the eye.

To determine the appropriate matching impedance of working efficiency, the electrical output responses (such as voltage, current density and power density) for the best performing device 5 wt% were extracted by employing various resistors ranging from 0.1 to 50 M Ω (Figure 2.6d). The applied pushing force and frequency were maintained constant during the measurements at 40 N and 17 Hz, respectively. With an increment in the load resistance, the output voltages (V) of the 5 wt% **1**-TPU device were found to increase. Concomitantly, the peak-to-peak current density (J) values of the **1**-TPU device is decreased from 15.5 to 0.8 $\mu\text{A}/\text{cm}^2$, with an increase in the resistance loads from 0.1 to 50 M Ω due to the ohmic loss (Figure 5A.37, Appendix 5). Furthermore, the instantaneous peak power density ($P = V \times J$) of the device was calculated, as shown in Figure 6d. The highest power density value of 14.6 $\mu\text{W}/\text{cm}^2$ was obtained at 1 M Ω for the 5 wt% **1**-TPU, which is identified as an optimized matching resistance useful for real-life applications. The fatigue experiments on this 5 wt% composite device showed substantial durability exhibiting the retention of the open-circuit voltages even after 400 cycles with a constant external impact of 40 N (Figure 5A.38, Appendix 5).

Despite the fact that metal-organic frameworks (MOFs) and coordination polymers have been utilized in the past as mechanical energy harvesters, most of them have been employed either as additives to PVDF, to enhance its performance via the enhancement of its electroactive β -phase, or as triboelectric nanogenerators.^{60, 61} However, there are only a few examples of piezoelectric nanogenerators known that employ MOFs or coordination polymers. Recently, Gazit and co-workers have demonstrated nanogenerators constructed from a Zn-peptide based coordination polymer, in which the output performance was governed by the choice of guest molecules.⁶² In this regard, the 5 wt% **1**-TPU device exhibits much higher output voltage and power density values, promising the utility of such neutral coordination polymers for future technological applications (Table 5A.3, Appendix 5).

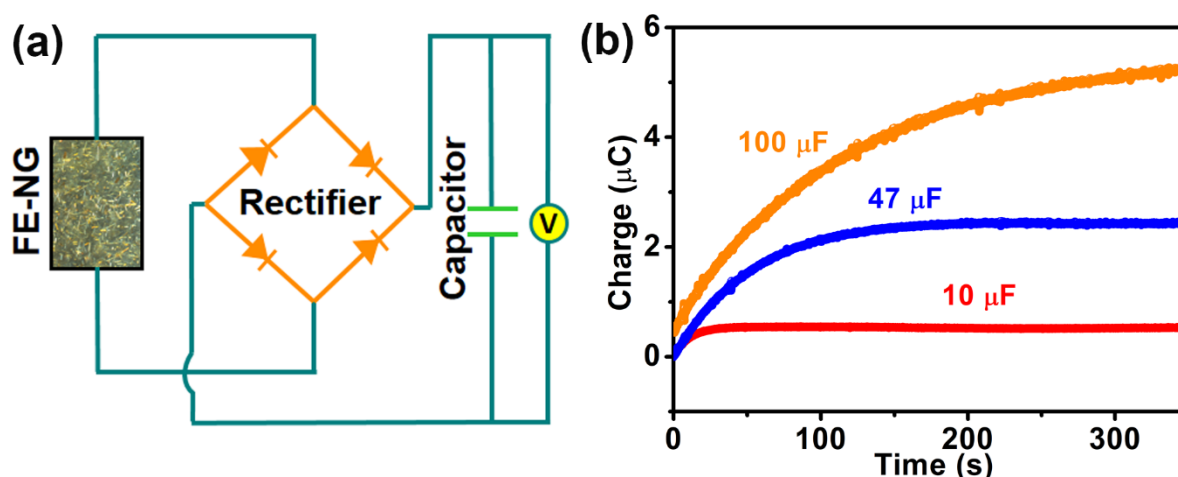


Figure 5.7: (a) Drawing representing the charging of a capacitor using a 1-TPU device connected through a full-wave bridge rectifier circuit. (b) Calculated charge of the 5 wt% 1-TPU device at different load capacitances.

The energy storage efficacy of the 1-TPU 5 wt% device was further examined through the charging of capacitors with different capacitance values. A full-wave bridge rectifier circuit was employed to connect the device to the capacitor which convert the ac potentials to dc voltages (Figure 5.7a). The voltages in the capacitors were found to increase as a function of time and the obtained saturation voltages were found to be very close for most of the load capacitors (Figure 5A.39, Appendix 5). The charging rate is higher for a lower value capacitor as its saturation charge is attained quicker than the other higher loading capacitors. Note that the voltage measured across these capacitors is much lower than the corresponding output voltage due to the voltage consumed in rectification of the diodes and/or leakage of the stored energy in the capacitors.^{63, 64} Furthermore, the stored charges (Q) on the capacitors (C_L) were calculated by the formula, $Q = C_L V$ (Figure 5.7b). A linear relationship between the strength of the load capacitor and the storage capacity is observed in all of them showing a gradual increase in the energy storage until the curves become saturated.^{65, 66} Again, the 10 µF capacitor stores only a small amount of charge and attains the saturation value very quickly. A maximum stored charge of 5.22 µC is noted for the highest rated 100 µF capacitor at a given time of 350 s.

2.4 Conclusion

In summary, we have synthesized a neutral noncentrosymmetric one-dimensional coordination network **1** that exhibits both piezo- as well as ferroelectric properties. The electromechanical coefficient value of 19.4 pm/V extracted from the PFM measurements is remarkable for its neutral framework structure. The existence of a dipole moment in **1** can be tracked down to the distortions of Zn(II)-center, as inferred from preliminary DFT calculations. Also, the P-E loop measurements yielded a P_r value of 8.04 $\mu\text{C}/\text{cm}^2$ supporting its ferroelectric properties. Furthermore, flexible composite materials of **1** were prepared and employed as piezoelectric energy devices. The highest open-circuit voltage of 5.6 V and power density output of 14.6 $\mu\text{W}/\text{cm}^2$ were recorded for the optimized champion device containing 5 wt% of **1** in the TPU matrix. The potential of this framework-based device for small-scale energy storage was demonstrated via capacitor charging experiments. These findings demonstrate the potential of lead-free ferroelectric metal-organic frameworks with light-weight metal ions for fabricating piezoelectric nanogenerator devices for use in future multifunctional electronics.

2.5 REFERENCES

1. C. R. Kagan, D. B. Mitzi and C. D. Dimitrakopoulos, *Science*, 1999, **286**, 945-947.
2. M. M. Lee, J. Teuscher, T. Miyasaka, T. N. Murakami and H. J. Snaith, *Science*, 2012, **338**, 643-647.
3. S.-T. Han, Y. Zhou and V. A. L. Roy, *Adv. Mater.*, 2013, **25**, 5425-5449.
4. J. F. Scott and C. A. P. d. Araujo, *Science*, 1989, **246**, 1400-1405.
5. T. A. Vanderah, *Science*, 2002, **298**, 1182-1184.
6. A. S. Tayi, A. Kaeser, M. Matsumoto, T. Aida and S. I. Stupp, *Nat. Chem.*, 2015, **7**, 281-294.
7. W. Zhang and R.-G. Xiong, *Chem. Rev.*, 2012, **112**, 1163-1195.
8. H.-Y. Liu, H.-Y. Zhang, X.-G. Chen and R.-G. Xiong, *J. Am. Chem. Soc.*, 2020, **142**, 15205-15218.
9. T. Vijayakanth, D. J. Liptrot, E. Gazit, R. Boomishankar and C. R. Bowen, *Adv. Funct. Mater.*, 2022, **32**, 2109492.
10. L. Lu, W. Ding, J. Liu and B. Yang, *Nano Energy*, 2020, **78**, 105251.

11. Y. Zhang, M. A. Hopkins, D. J. Liptrot, H. Khanbareh, P. Groen, X. Zhou, D. Zhang, Y. Bao, K. Zhou, C. R. Bowen and D. R. Carbery, *Angew. Chem. Int. Ed.*, 2020, **59**, 7808-7812.
12. C. R. Bowen, H. A. Kim, P. M. Weaver and S. Dunn, *Energy Environ. Sci.*, 2014, **7**, 25-44.
13. R. Pandey, G. Sb, S. Grover, S. K. Singh, A. Kadam, S. Ogale, U. V. Waghmare, V. R. Rao and D. Kabra, *ACS Energy Lett.*, 2019, **4**, 1004-1011.
14. T. Vijayakanth, D. J. Liptrot, E. Gazit, R. Boomishankar and C. R. Bowen, *Adv. Funct. Mater.*, **n/a**, 2109492.
15. V. Vivekananthan, N. R. Alluri, Y. Purusothaman, A. Chandrasekhar and S.-J. Kim, *Nanoscale*, 2017, **9**, 15122-15130.
16. G. Vats, A. Kumar, N. Ortega, C. R. Bowen and R. S. Katiyar, *Energy Environ. Sci.*, 2016, **9**, 1335-1345.
17. S. Das, S. Xu, T. Ben and S. Qiu, *Angew. Chem., Int. Ed.*, 2018, **57**, 8629-8633.
18. L. Alaerts, C. E. A. Kirschhock, M. Maes, M. A. van der Veen, V. Finsy, A. Depla, J. A. Martens, G. V. Baron, P. A. Jacobs, J. F. M. Denayer and D. E. De Vos, *Angew. Chem., Int. Ed.*, 2007, **46**, 4293-4297.
19. W. Morris, W. E. Briley, E. Auyeung, M. D. Cabezas and C. A. Mirkin, *J. Am. Chem. Soc.*, 2014, **136**, 7261-7264.
20. J. Xiao, J. Liu, M. Liu, G. Ji and Z. Liu, *Inorg. Chem.*, 2019, **58**, 6167-6174.
21. J. K. Zaręba, M. Nyk and M. Samoć, *Adv. Opt. Mater.*, 2021, **9**, 2100216.
22. R. Medishetty, J. K. Zaręba, D. Mayer, M. Samoć and R. A. Fischer, *Chem. Soc. Rev.*, 2017, **46**, 4976-5004.
23. L. R. Mingabudinova, V. V. Vinogradov, V. A. Milichko, E. Hey-Hawkins and A. V. Vinogradov, *Chem. Soc. Rev.*, 2016, **45**, 5408-5431.
24. S. Horiuchi, Y. Tokunaga, G. Giovannetti, S. Picozzi, H. Itoh, R. Shimano, R. Kumai and Y. Tokura, *Nature*, 2010, **463**, 789-792.
25. X.-Y. Dong, B. Li, B.-B. Ma, S.-J. Li, M.-M. Dong, Y.-Y. Zhu, S.-Q. Zang, Y. Song, H.-W. Hou and T. C. W. Mak, *J. Am. Chem. Soc.*, 2013, **135**, 10214-10217.
26. T. Hang, W. Zhang, H.-Y. Ye and R.-G. Xiong, *Chem. Soc. Rev.*, 2011, **40**, 3577-3598.
27. W. Zhang, H.-Y. Ye and R.-G. Xiong, *Coord. Chem. Rev.*, 2009, **253**, 2980-2997.

28. F. Xue, J. Cao, X. Li, J. Feng, M. Tao and B. Xue, *J. Mater. Chem. C*, 2021, **9**, 7568-7574.
29. Y. Sun, Z. Hu, D. Zhao and K. Zeng, *Nanoscale*, 2017, **9**, 12163-12169.
30. Y. Sun, J. Gao, Y. Cheng, Y.-W. Zhang and K. Zeng, *J. Phys. Chem. C*, 2019, **123**, 3122-3129.
31. A. K. Srivastava, P. Divya, B. Praveenkumar and R. Boomishankar, *Chem. Mater.*, 2015, **27**, 5222-5229.
32. A. K. Srivastava, B. Praveenkumar, I. K. Mahawar, P. Divya, S. Shalini and R. Boomishankar, *Chem. Mater.*, 2014, **26**, 3811-3817.
33. A. K. Srivastava, T. Vijayakanth, P. Divya, B. Praveenkumar, A. Steiner and R. Boomishankar, *J. Mater. Chem. C*, 2017, **5**, 7352-7359.
34. A. Yadav, A. K. Srivastava, P. Kulkarni, P. Divya, A. Steiner, B. Praveenkumar and R. Boomishankar, *J. Mater. Chem. C*, 2017, **5**, 10624-10629.
35. A. Yadav, P. Kulkarni, B. Praveenkumar, A. Steiner and R. Boomishankar, *Chem. Eur. J.*, 2018, **24**, 14639-14643.
36. N. Prajesh, A. Yadav, R. Gourkhede, B. Praveenkumar, A. Steiner and R. Boomishankar, *Chem. Asian J.*, 2020, **15**, 3275-3280.
37. P. Giannozzi, S. Baroni, N. Bonini, M. Calandra, R. Car, C. Cavazzoni, D. Ceresoli, G. L. Chiarotti, M. Cococcioni, I. Dabo, A. Dal Corso, S. de Gironcoli, S. Fabris, G. Fratesi, R. Gebauer, U. Gerstmann, C. Gougoussis, A. Kokalj, M. Lazzeri, L. Martin-Samos, N. Marzari, F. Mauri, R. Mazzarello, S. Paolini, A. Pasquarello, L. Paulatto, C. Sbraccia, S. Scandolo, G. Sclauzero, A. P. Seitsonen, A. Smogunov, P. Umari and R. M. Wentzcovitch, *J. Phys.: Condens. Matter*, 2009, **21**, 395502.
38. D. R. Hamann, *Phys. Rev. B*, 2013, **88**, 085117.
39. J. P. Perdew, K. Burke and M. Ernzerhof, *Phys. Rev. Lett.*, 1996, **77**, 3865-3868.
40. K. Momma and F. Izumi, *J. Appl. Crystallogr.*, 2011, **44**, 1272-1276.
41. A. W. Addison, T. N. Rao, J. Reedijk, J. van Rijn and G. C. Verschoor, *J. Chem. Soc., Dalton Trans.*, 1984, DOI: 10.1039/DT9840001349, 1349-1356.
42. R. D. King-Smith and D. Vanderbilt, *Phys. Rev. B*, 1993, **47**, 1651-1654.
43. J. B. Neaton, C. Ederer, U. V. Waghmare, N. A. Spaldin and K. M. Rabe, *Phys. Rev. B*, 2005, **71**, 014113.

44. N. A. Spaldin, *J. Solid State Chem.*, 2012, **195**, 2-10.
45. D. Di Sante, A. Stroppa, P. Jain and S. Picozzi, *J. Am. Chem. Soc.*, 2013, **135**, 18126-18130.
46. S. K. Kurtz and T. T. Perry, *J. Appl. Phys.*, 1968, **39**, 3798-3813.
47. A. Graja, *phys. stat. sol. (b)*, 1968, **27**, K93-K97.
48. J. F. Scott, *J. Phys.: Condens. Matter*, 2007, **20**, 021001.
49. W.-Q. Liao, D. Zhao, Y.-Y. Tang, Y. Zhang, P.-F. Li, P.-P. Shi, X.-G. Chen, Y.-M. You and R.-G. Xiong, *Science*, 2019, **363**, 1206-1210.
50. Y.-M. You, W.-Q. Liao, D. Zhao, H.-Y. Ye, Y. Zhang, Q. Zhou, X. Niu, J. Wang, P.-F. Li, D.-W. Fu, Z. Wang, S. Gao, K. Yang, J.-M. Liu, J. Li, Y. Yan and R.-G. Xiong, *Science*, 2017, **357**, 306-309.
51. T. Vijayakanth, F. Ram, B. Praveenkumar, K. Shanmuganathan and R. Boomishankar, *Angew. Chem., Int. Ed.*, 2020, **59**, 10368-10373.
52. C. K. Jeong, K.-I. Park, J. Ryu, G.-T. Hwang and K. J. Lee, *Adv. Funct. Mater.*, 2014, **24**, 2620-2629.
53. S. Siddiqui, D.-I. Kim, L. T. Duy, M. T. Nguyen, S. Muhammad, W.-S. Yoon and N.-E. Lee, *Nano Energy*, 2015, **15**, 177-185.
54. S. K. Singh, S. Muduli, D. Dhakras, R. Pandey, R. Babar, A. Singh, D. Kabra, M. Kabir, R. Boomishankar and S. Ogale, *Sustain. Energy Fuels*, 2019, **3**, 1943-1950.
55. M. Wu, T. Zheng, H. Zheng, J. Li, W. Wang, M. Zhu, F. Li, G. Yue, Y. Gu and J. Wu, *J. Mater. Chem. A*, 2018, **6**, 16439-16449.
56. K.-I. Park, M. Lee, Y. Liu, S. Moon, G.-T. Hwang, G. Zhu, J. E. Kim, S. O. Kim, D. K. Kim, Z. L. Wang and K. J. Lee, *Adv. Mater.*, 2012, **24**, 2999-3004.
57. S. Kim, M. K. Gupta, K. Y. Lee, A. Sohn, T. Y. Kim, K.-S. Shin, D. Kim, S. K. Kim, K. H. Lee, H.-J. Shin, D.-W. Kim and S.-W. Kim, *Adv. Mater.*, 2014, **26**, 3918-3925.
58. K. Y. Lee, D. Kim, J.-H. Lee, T. Y. Kim, M. K. Gupta and S.-W. Kim, *Adv. Funct. Mater.*, 2014, **24**, 37-43.
59. J. Nie, L. Zhu, W. Zhai, A. Berbille, L. Li and Z. L. Wang, *ACS Appl. Electron. Mater.*, 2021, **3**, 2136-2144.
60. G. Khandelwal, A. Chandrasekhar, N. P. Maria Joseph Raj and S.-J. Kim, *Adv. Energy Mater.*, 2019, **9**, 1803581.

61. S. Hajra, M. Sahu, A. M. Padhan, I. S. Lee, D. K. Yi, P. Alagarsamy, S. S. Nanda and H. J. Kim, *Adv. Funct. Mater.*, 2021, **31**, 2101829.
62. Y. Chen, S. Guerin, H. Yuan, J. O'Donnell, B. Xue, P.-A. Cazade, E. U. Haq, L. J. W. Shimon, S. Rencus-Lazar, S. A. M. Tofail, Y. Cao, D. Thompson, R. Yang and E. Gazit, *J. Am. Chem. Soc.*, 2022, **144**, 3468-3476.
63. J. Yan and Y. G. Jeong, *ACS Appl. Mater. Interfaces*, 2016, **8**, 15700-15709.
64. S. Xu, B. J. Hansen and Z. L. Wang, *Nat. Commun*, 2010, **1**, 93.
65. S. Niu and Z. L. Wang, *Nano Energy*, 2015, **14**, 161-192.
66. S. Niu, Y. Liu, Y. S. Zhou, S. Wang, L. Lin and Z. L. Wang, *IEEE Trans. Electron Devices*, 2015, **62**, 641-647.

Chapter 6

Thesis Conclusion and Future Perspectives

In summary, this thesis describes the synthesis of non-centrosymmetric polar ferroelectric metal-ligand architectures derived from the dipodal and tripodal (N-donor or O-donor) phosphoramidate ligands and exploration of their ferroelectric and piezoelectric properties and utilized them for piezoelectric energy harvesting applications.

In the first part of the thesis, we have synthesized the less-symmetric more flexible ligand tris(N-(3-picolyl))phosphoramidate by introducing an extra CH_2 group in between the P-N scaffolds and coordinating pyridyl rings. Interestingly, a discrete octahedral cage and its 2D connected cage framework were obtained by introducing the bridging chloride ions. We have observed the ferroelectric responses of these frameworks due to the toggling of polar nitrate anions and solvated water molecules. These results further shed the light on the unconventional mechanism of ferroelectric polarization in the domain of metal-organic frameworks ([Chapter 2](#)).

In extension of [Chapter 2](#), we have explored the ferroelectric and piezoelectric behaviour of similar type of cages, a Co(II) and Ni(II)-based octahedral cages, that were templated by tripodal thiophosphoramidate ligand. For the first time, we have observed the polar domains, and characteristic butterfly amplitude loop and phase hysteresis loop on the single-crystalline thin film of these cages by piezoresponse force microscopy experiments (PFM). Further, the successful preparation of polymer composites of these cages were employed for piezoelectric energy harvesting studies. The obtained open-circuit voltage and power-density values are exceedingly high among the well-known ferroelectric MOFs ([Chapter 3](#)).

In [Chapter 4](#), we have synthesized a less-symmetric flexible dipodal picolyl-based phosphoramidate ligand and obtained its two-dimensional polar coordination polymer. For the first time, we have obtained a high longitudinal piezoelectric coefficient value which is unprecedented among the reported MOFs by employing piezoresponse force spectroscopy (PFS) experiments on the single-crystalline thin films. Besides good ferroelectric and piezoelectric attributes, the polymer composites of this framework yielded a high open-circuit voltage and power density values in the piezoelectric energy harvesting studies.

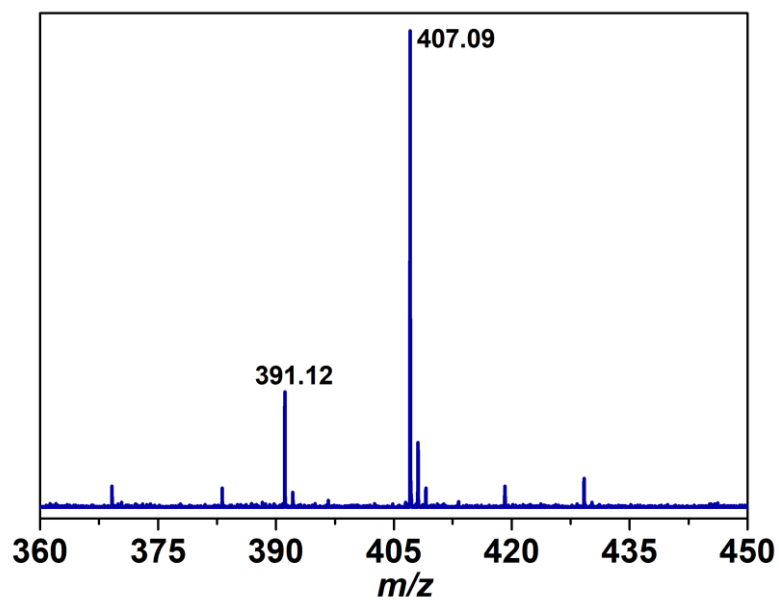
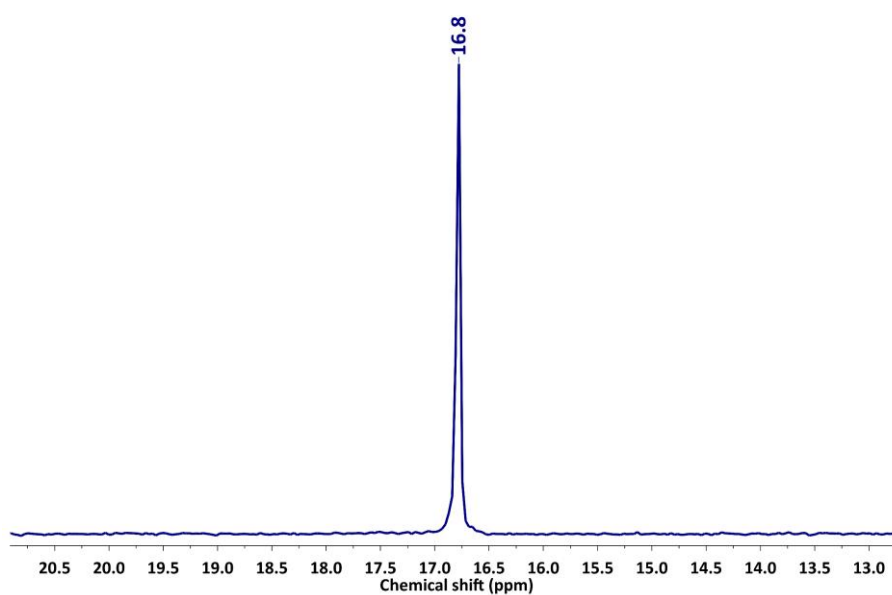
Finally, in the last chapter [Chapter 5](#), we have synthesized a neutral polar one-dimensional coordination network by employing flexible dipodal carboxylate-based phosphoramidate ligand along with the N-donor 2,2-bipyridine as a co-ligand. The polarization in this neutral

framework have been tracked down due to the distortions around the metal-polyhedra. The ferroelectric and piezoelectric properties were confirmed by the piezoresponse force microscopy (PFM) experiments. Further, the polymer composites of this network utilized for piezoelectric energy harvesting studies.

These findings demonstrate the potential of lead-free ferroelectric metal-ligand architectures with light-weight metal ions for fabricating piezoelectric nanogenerator devices for future multifunctional electronics.

Overall, we have understood that in order to make a ferroelectric and piezoelectric materials, there are various factors which are directly related to symmetry of metal-ligand coordination assemblies. Therefore, the design of ligand will be the key factor to develop such kind of materials. In this regard, the ligand design can be varied from (1) by introduction of more donor-sites for metal-coordination (2) introducing the conformational flexibility of binding sites (3) introducing the chiral environment within the ligand (4) position of the donor-site. We can also introduce the heavier transition metal-ions for its better coordination ability with the above-mentioned ligand designs. The choice of counter anions and solvent molecules can also induce polarization characteristics in the metal-ligand coordination assemblies. There are various possibilities to explore the field of MOFs judiciously to obtain desired output performances in the field of energy harvesting.

Appendix

Characterization data of TPPA**Figure 2A.1:** MALDI-TOF mass spectrum of TPPA**Figure 2A.2:** ³¹P spectra of TPPA.

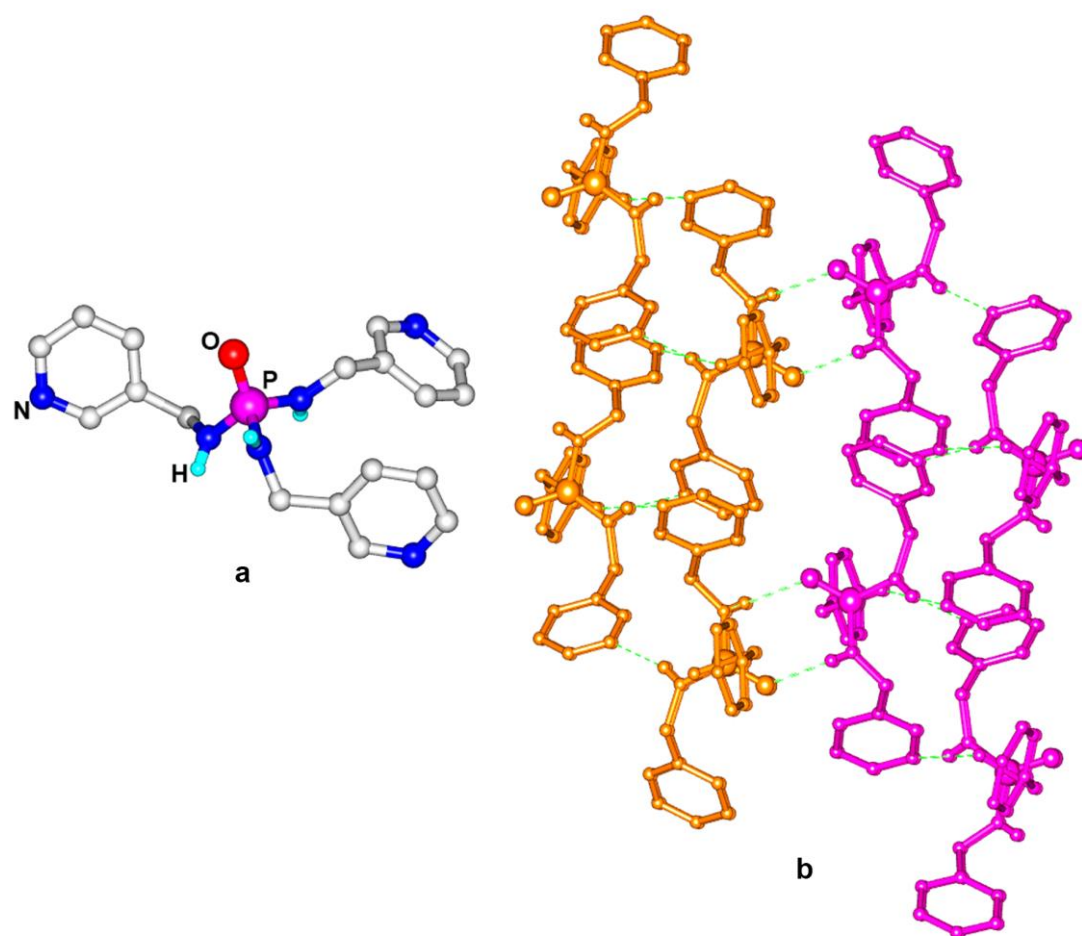


Figure 2A.3: Crystal structure of TPPA: (a) View of the monomeric unit, (b) two dimensional network formed by the N-H...N_{pyridyl} and N-H...O hydrogen bonding interactions.

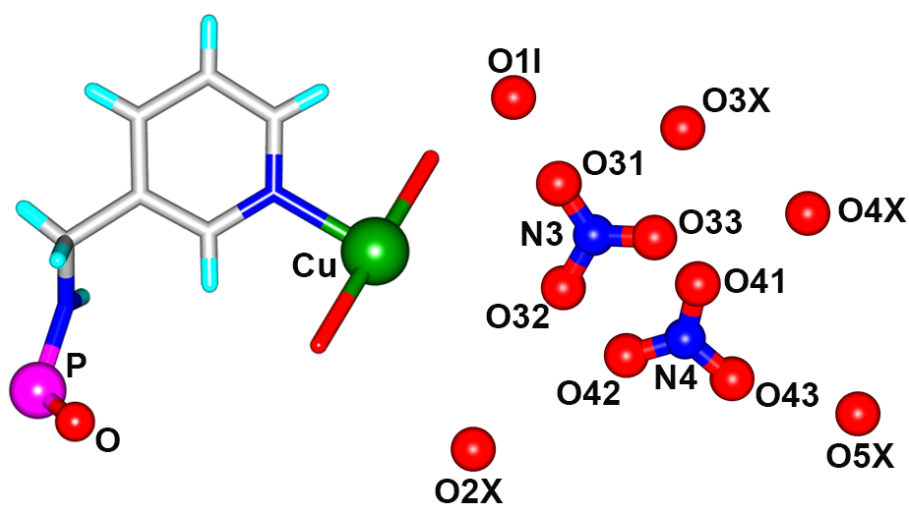


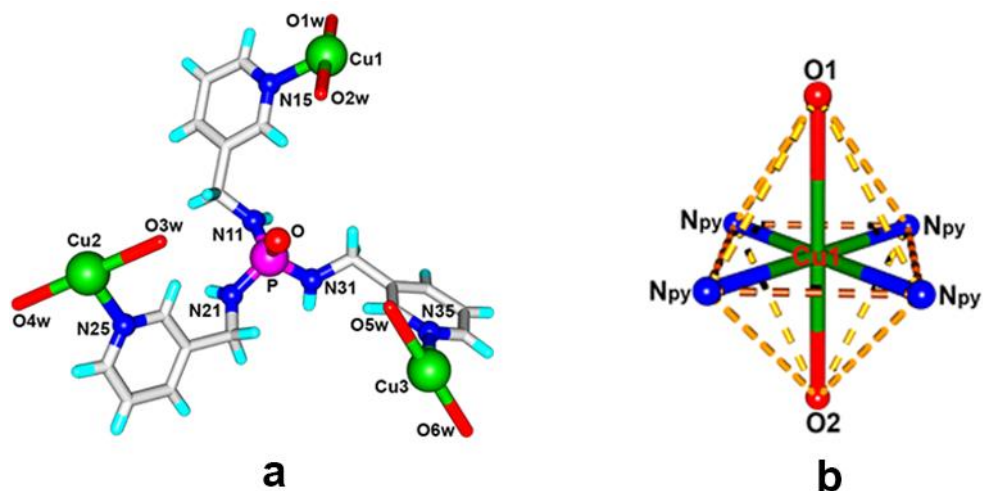
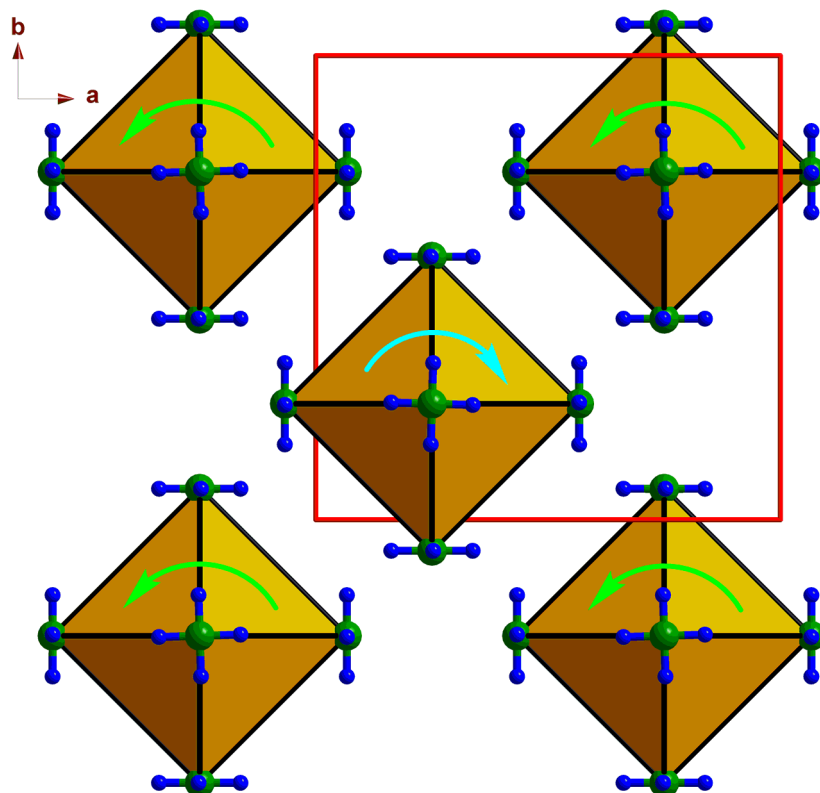
Figure 2A.4: Asymmetric unit of **1**Figure 2A.5: a) Association of the TPPA ligand with Cu^{II} ions. b) The coordination environment at the Cu^{II} centres.

Figure 2A.6: Packing view of Cu₆ octahedra in **1** along with the direction of rotation of the CuN₄ subunits in them. The organic ligands (except N_{pyridyl} atoms), anions and solvates are omitted for clarity.

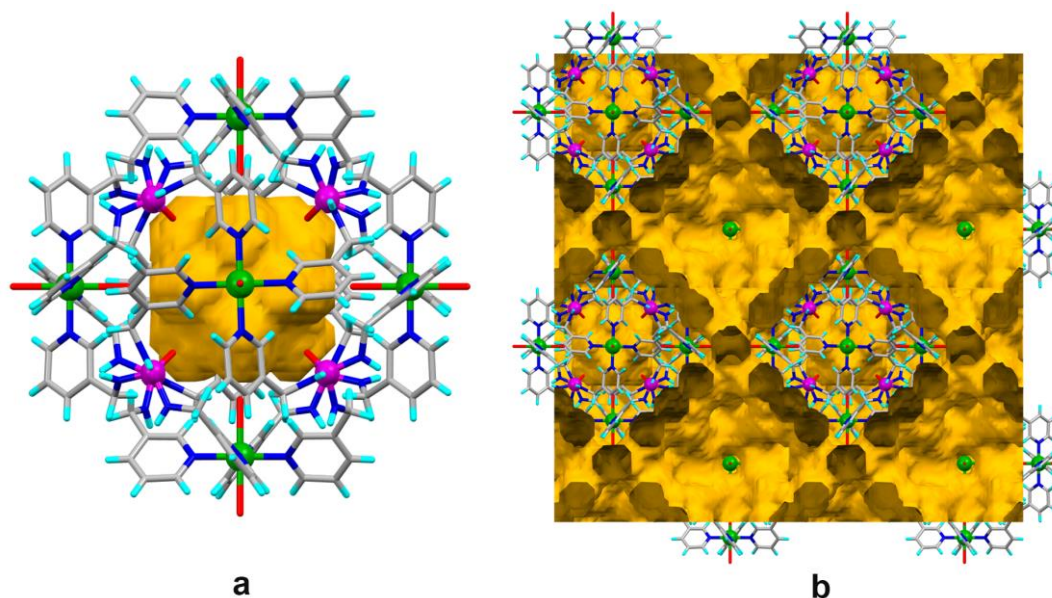


Figure 2A.7: (a) View of the solvent-accessible void surface inside the cage of **1**. (b) Connolly surface view of the void structure of **1** in 2x2x2 cell.

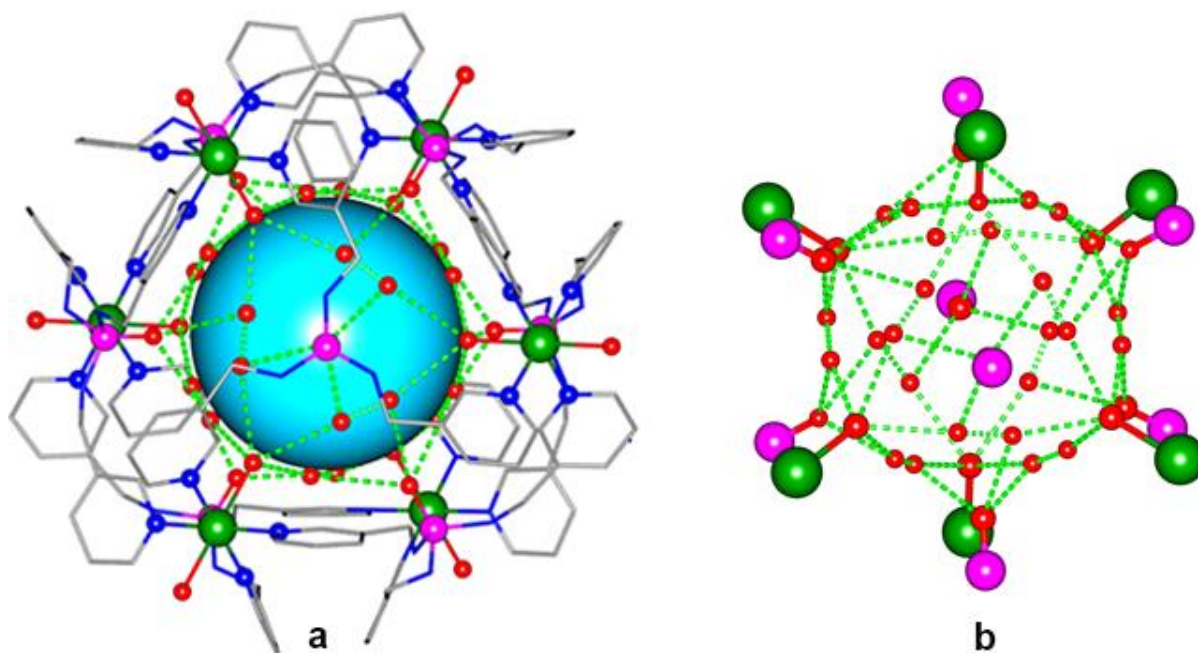


Figure 2A.8: Crystal structure of **1**: (a) Cage with internal water molecules (the internal space is highlighted). (b) Closer view of the H-bonded network of water molecules inside the cage.

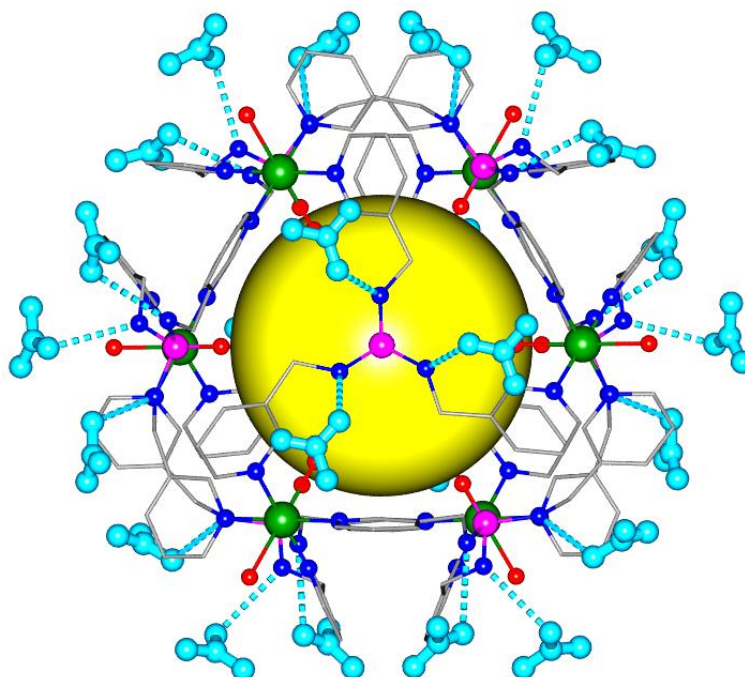


Figure 2A.9: Cage structure of **1** with nitrate anions. The disordered nitrate ions are hydrogen bonded to all $\text{P}(\text{NH}_3)_3$ ligand units.

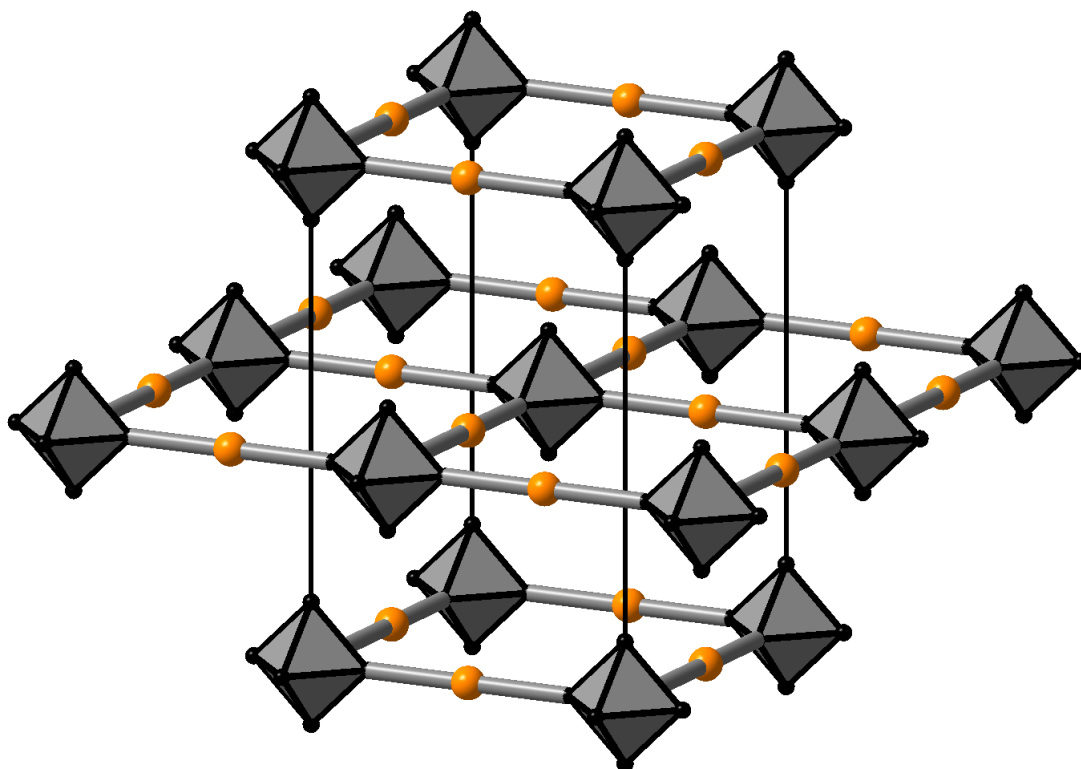


Figure 2A.10: Schematic presentation of the packing of the square-grid type framework of **2**. Layers are stacked in way that a cage of one layer sits on top of a square of the next layer.

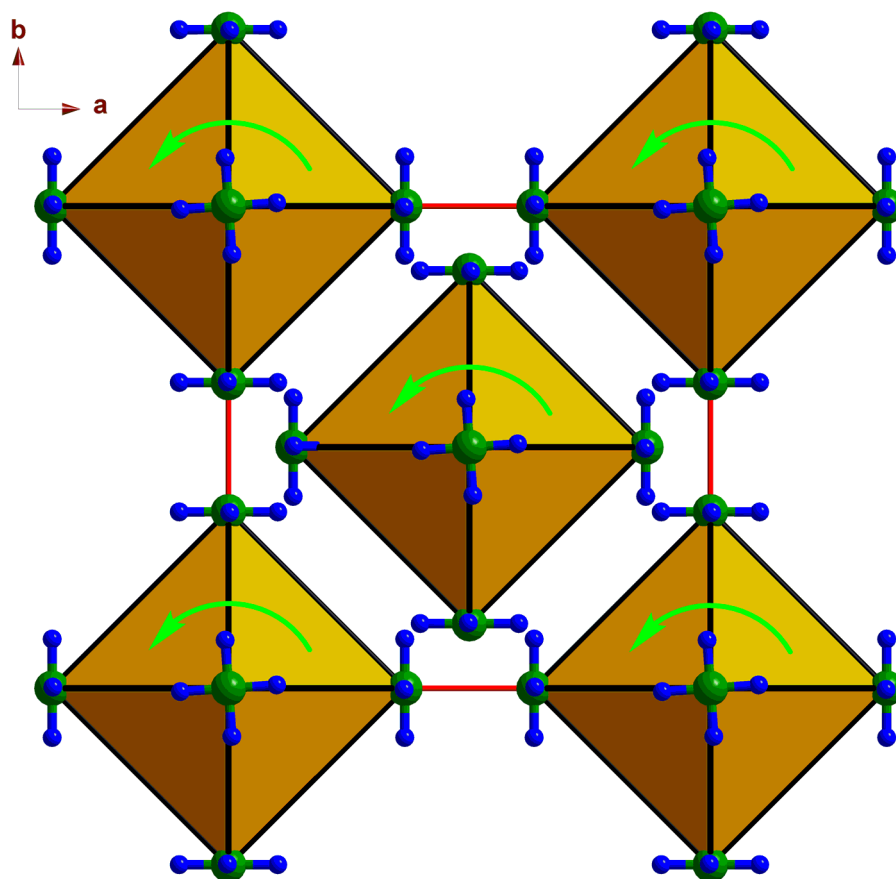


Figure 2A.11: Packing view of Cu₆ octahedra in **2** along with the direction of rotation of the CuN₄ subunits in them. The organic ligands (except those of N_{pyridyl} atoms), anions and solvates are omitted for clarity.

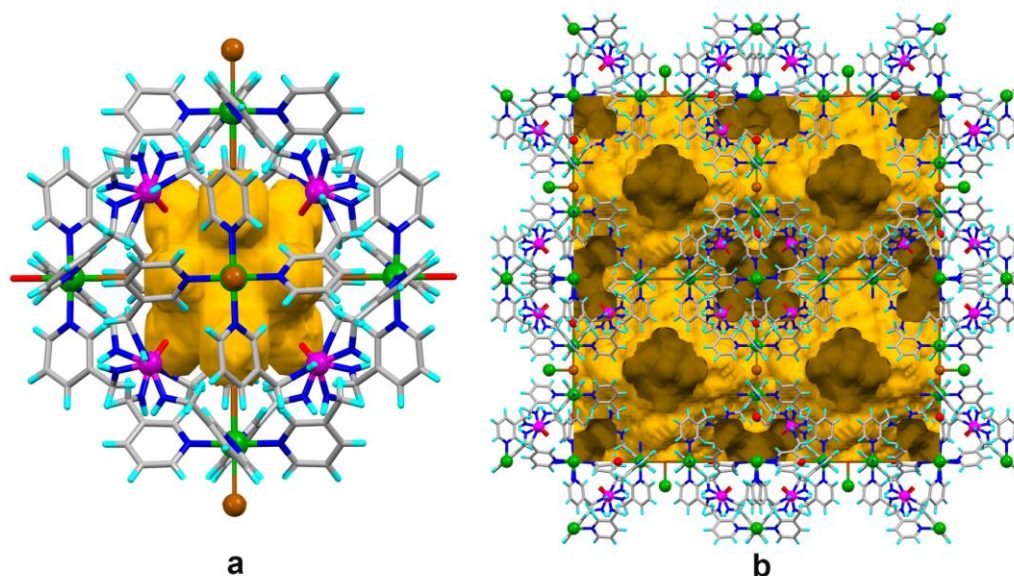


Figure 2A.12: (a) View of the solvent-accessible void surface at the cage interior of **2**. (b) Connolly surface view of the void structure of **2** in its 2x2x2 packing.

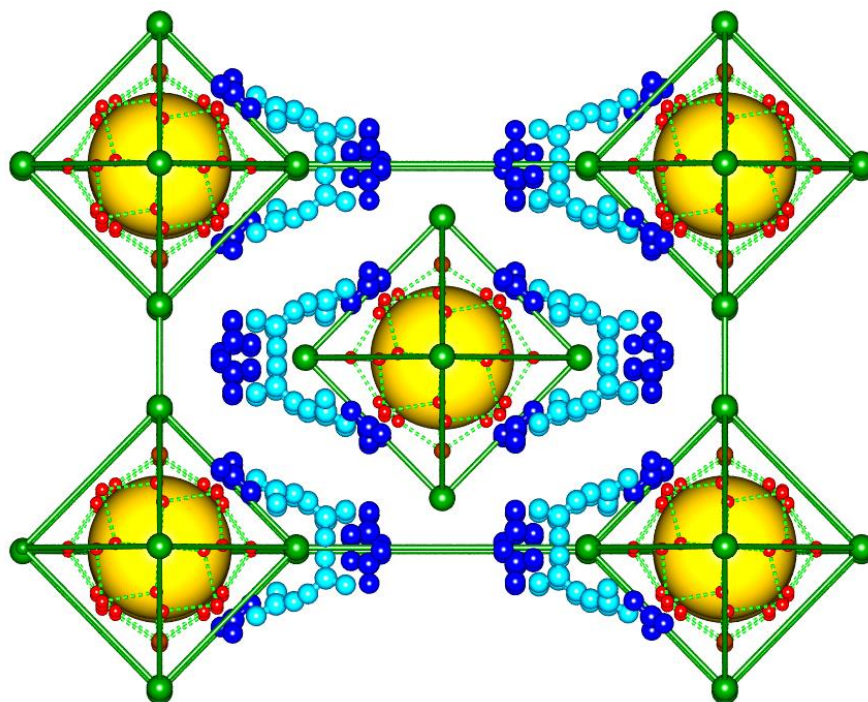


Figure 2A.13: Location of nitrate anions in the unit cell of **2** along the b-axis. Green octahedra represents the Cu_6 core and the yellow sphere represents the intrinsic cavity occupied by the disordered water molecules. The ligand atoms have been omitted for clarity. Disordered partners of the nitrate anions are shown in blue and cyan colored atoms.

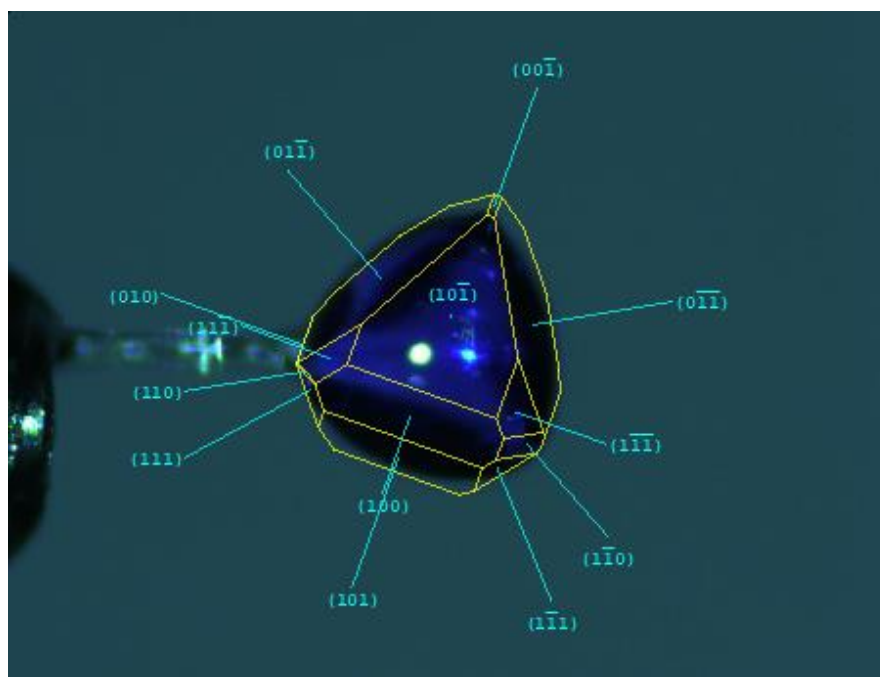


Figure 2A.14: Face indexing on **2** represents the $[1\ 0\ -1]$ plane on which the ferroelectric measurements were done.

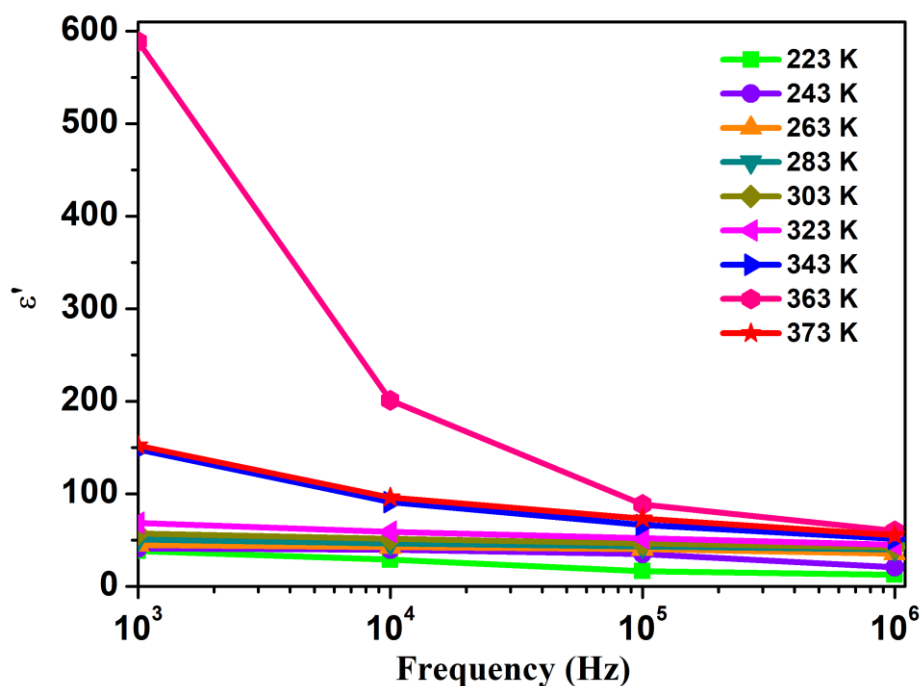


Figure 2A.15: Frequency dependent real-part of dielectric Permittivity (ϵ') of 1 at various temperatures.

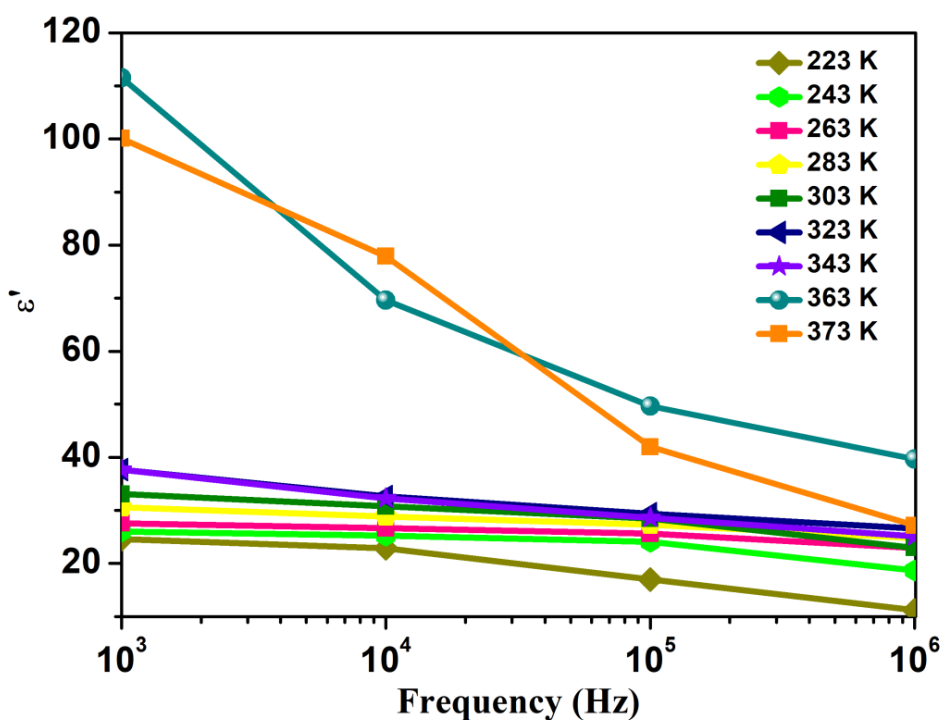


Figure 2A.16: Frequency dependent real-part of dielectric Permittivity (ϵ') of 2 at various temperatures.

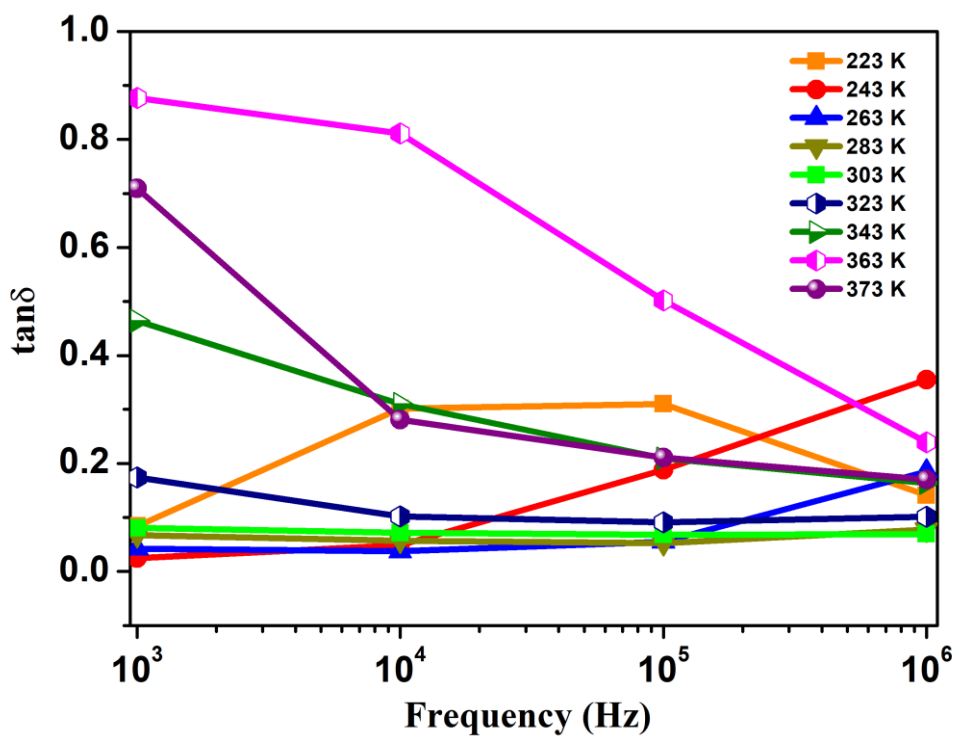


Figure 2A.17: Dielectric loss of 1 at various frequencies.

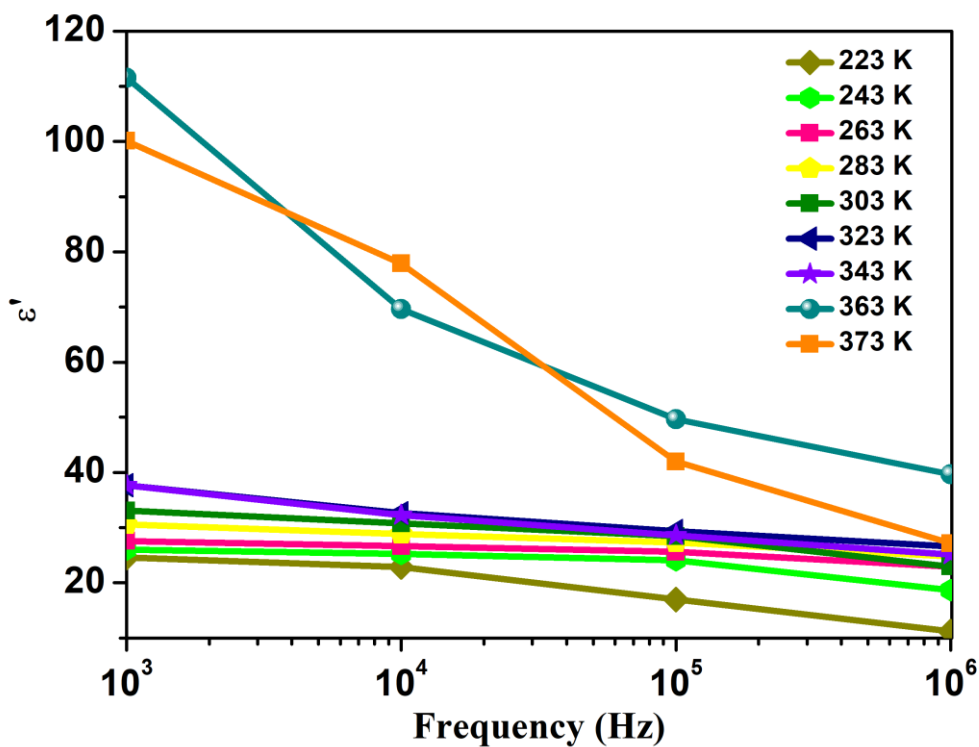


Figure 2A.18: Dielectric loss of 2 at various frequencies.

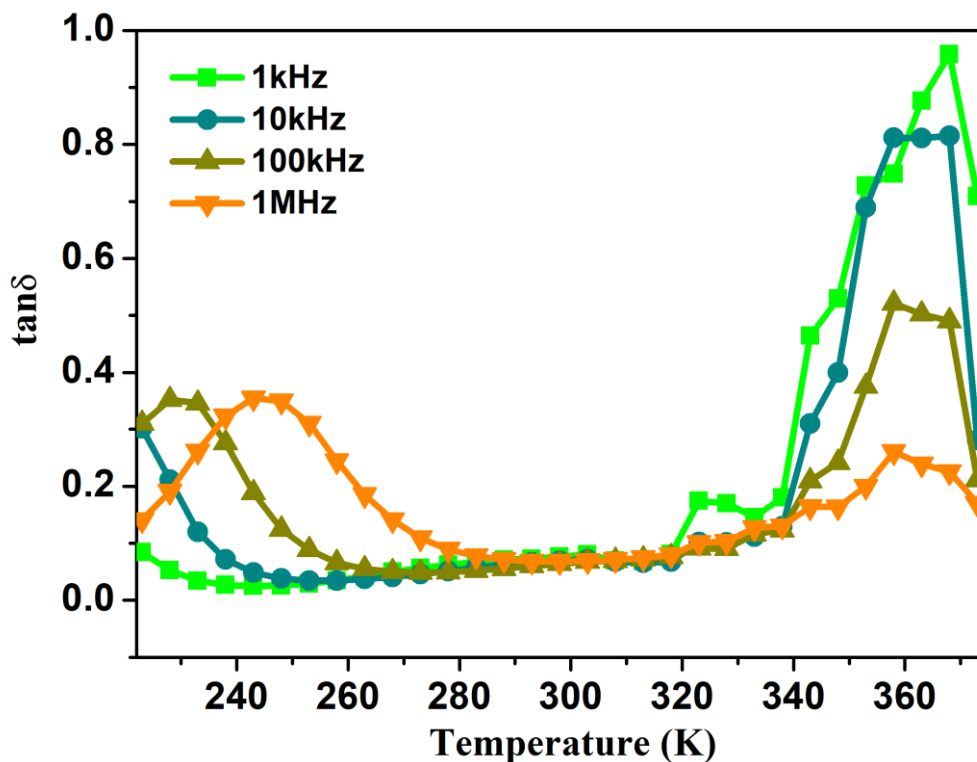


Figure 2A.19: Dielectric loss of 1 at various temperatures.

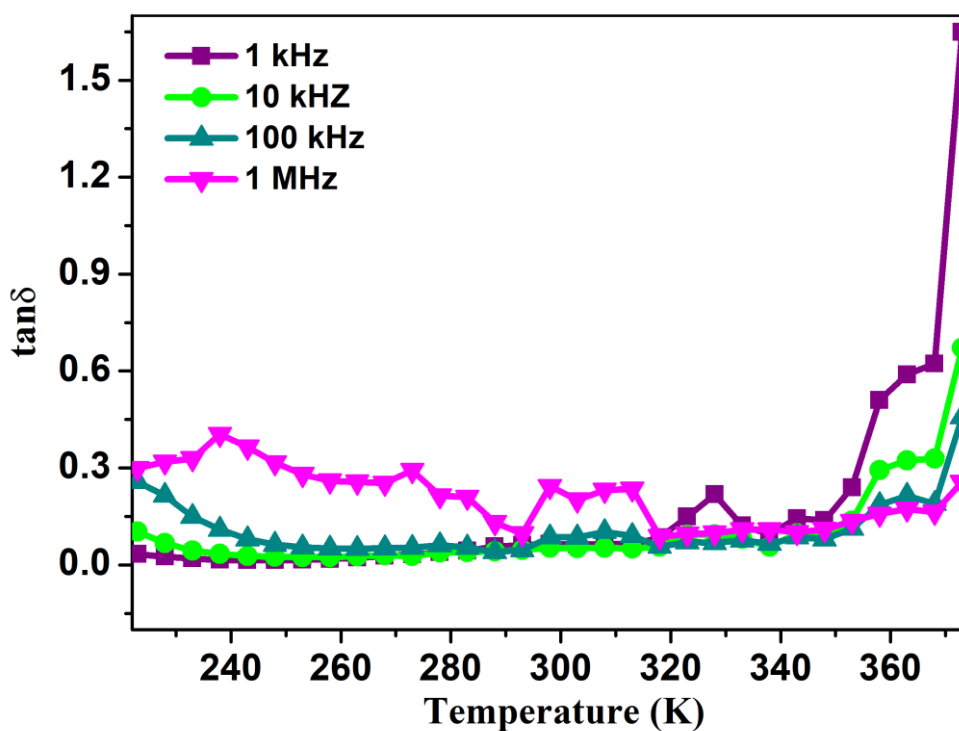


Figure 2A.20: Dielectric loss of 2 at various temperatures.

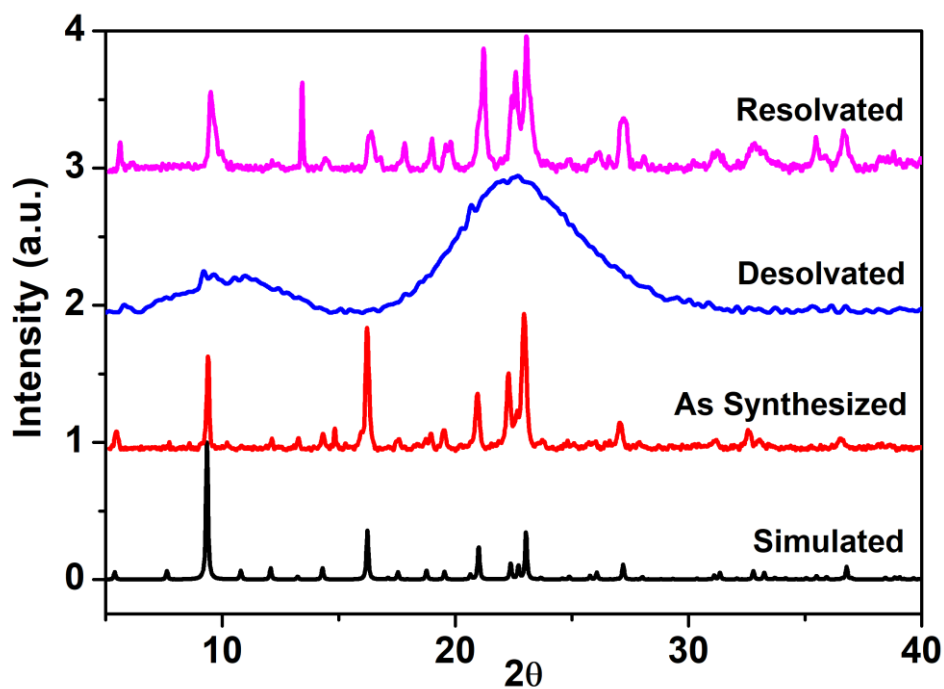


Figure 2A.21: Powder X-ray diffraction (PXRD) pattern for the various samples of **1**.

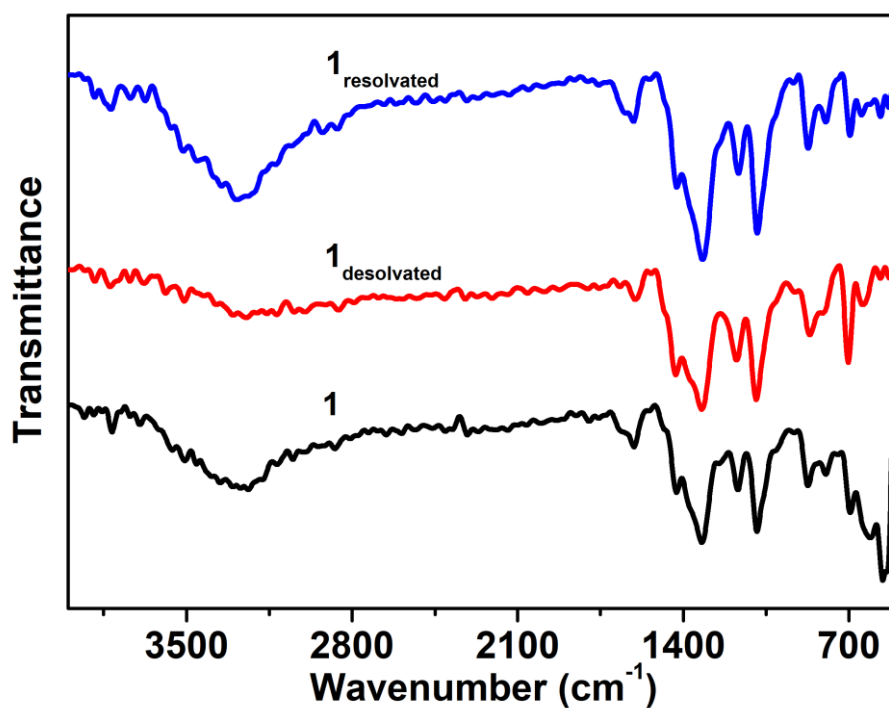


Figure 2A.22: IR spectra for **1**, **1_{desolvated}**, **1_{resolvated}**

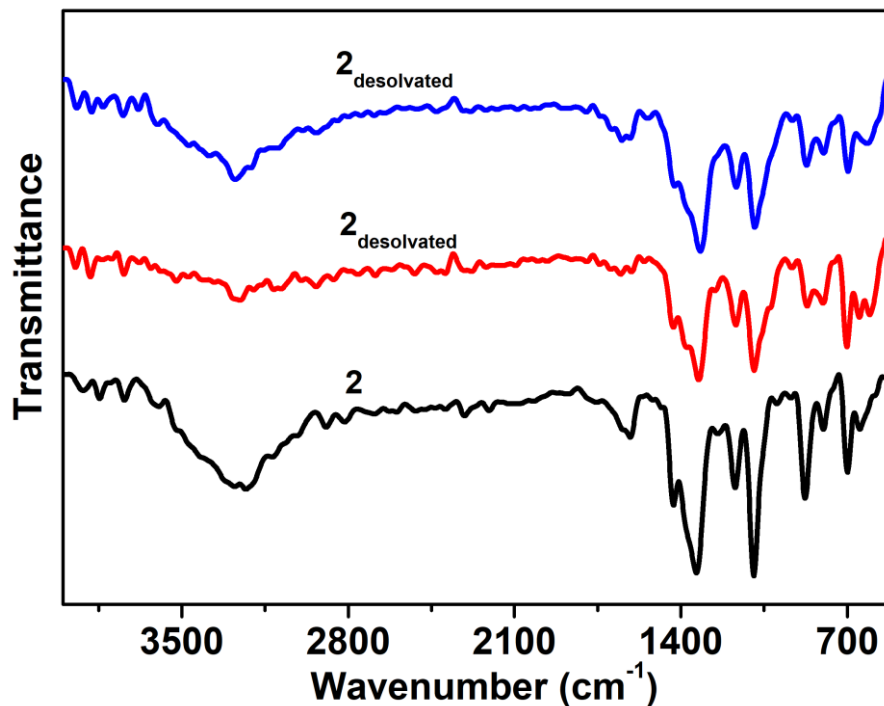


Figure 2A.23: IR spectra for **2**, **2**_{desolvated}, **2**_{resolvated}

Table 2A.1. Comparison of unit cell parameters for **1** and **2** at 100 and 298 K

2 (100 K)	2 (298 K)
$a = 20.236(6) \text{ \AA}, \alpha = 90^\circ$	$a = 19.989(19) \text{ \AA}, \alpha = 90^\circ$
$b = 20.236(6) \text{ \AA}, \beta = 90^\circ$	$b = 19.989(19) \text{ \AA}, \beta = 90^\circ$
$c = 29.872(9) \text{ \AA}, \gamma = 90^\circ$	$c = 30.48(3) \text{ \AA}, \gamma = 90^\circ$
Volume = $12232(8) \text{ \AA}^3$	Volume = $12178(26) \text{ \AA}^3$
Space group = <i>I422</i>	Space group = <i>I422</i>

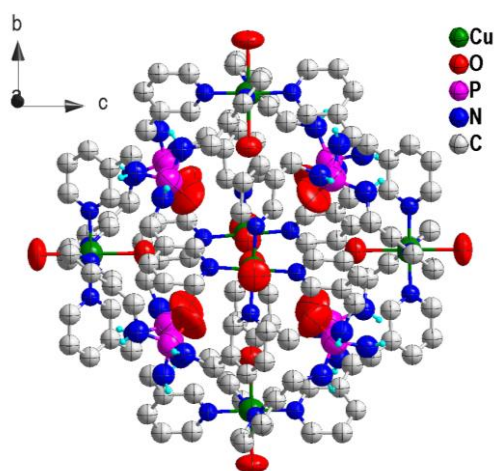


Figure 2A.24: Thermal ellipsoid diagram for **1** at 298 K. The disordered nitrate anions and solvated water molecules have been omitted for clarity. The carbon and nitrogen atoms are depicted at 30% probability ellipsoid level for a better viewing.

1 (100 K)	1 (298 K)
a = 23.1600(19) Å, $\alpha = 90^\circ$	a = 23.1600(19) Å, $\alpha = 90^\circ$
b = 23.1600(19) Å, $\beta = 90^\circ$	b = 23.1600(19) Å, $\beta = 90^\circ$
c = 23.1600(19) Å, $\gamma = 90^\circ$	c = 23.1600(19) Å, $\gamma = 90^\circ$
Volume = 12423(3) Å ³	Volume = 12423(3) Å ³
Space group = Pn-3n	Space group = Pn-3n

Table 2A.2: Crystallographic data for 1 at 298 K

Compound	1 (298K)
Chemical formula	C ₁₄₄ H ₂₈₂ Cu ₆ N ₆₀ O ₁₀₁ P ₈
Formula weight	5099.28
Temperature	296(2) K
Crystal system	Cubic
Space group	Pn -3 n
a (Å); α (°)	23.1600(19); 90
b (Å); β (°)	23.1600(19); 90
c (Å); γ (°)	23.1600(19) ; 90
V (Å ³); Z	12423(3); 2
ρ (calc.) mg m ⁻³	1.363
μ (Mo K α) mm ⁻¹	0.654
$2\theta_{\max}$ (°)	50.042
R(int)	0.2585
Completeness to θ	97.1 %
Data / param.	409 / 83
GOF	1.146
R1 [F > 4 σ (F)]	0.1393
wR2 (all data)	0.1590
max.peak/hole (e.Å ⁻³)	0.320/-0.269

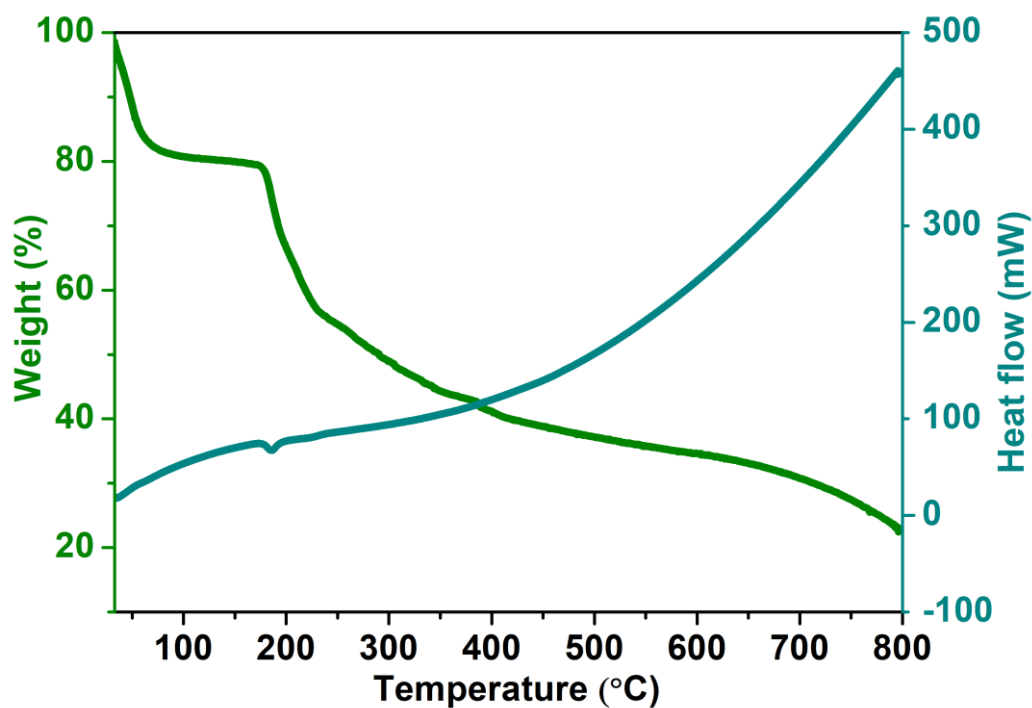


Figure 2A.25: Thermo-gravimetric analysis (TGA) plot for **1**.

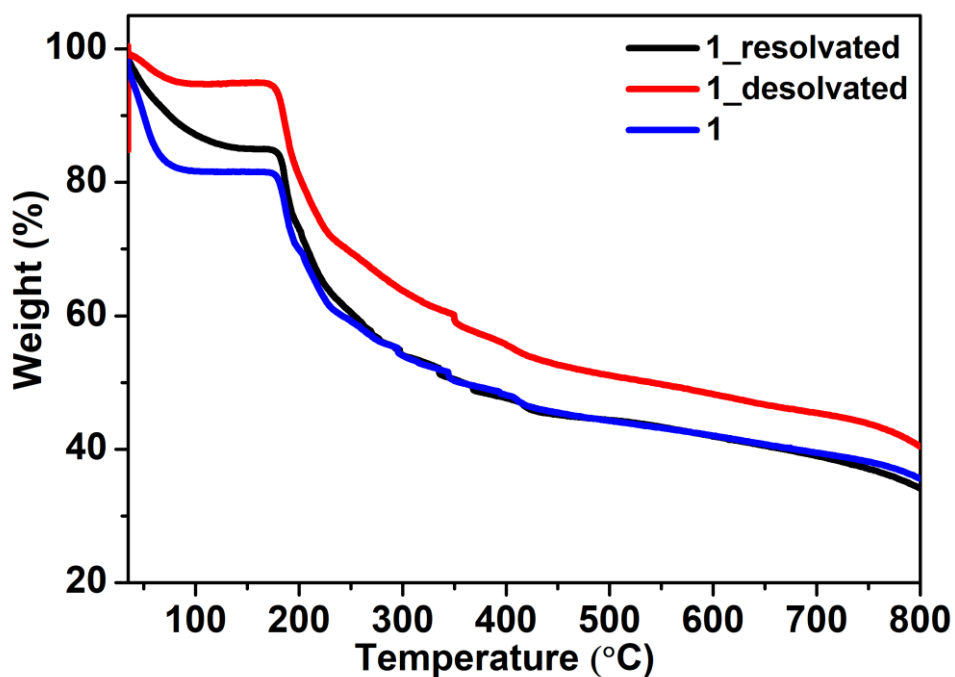


Figure 2A.26: Thermo-gravimetric analysis (TGA) plot for **1**, **1_{desolvated}** and **1_{resolvated}**.

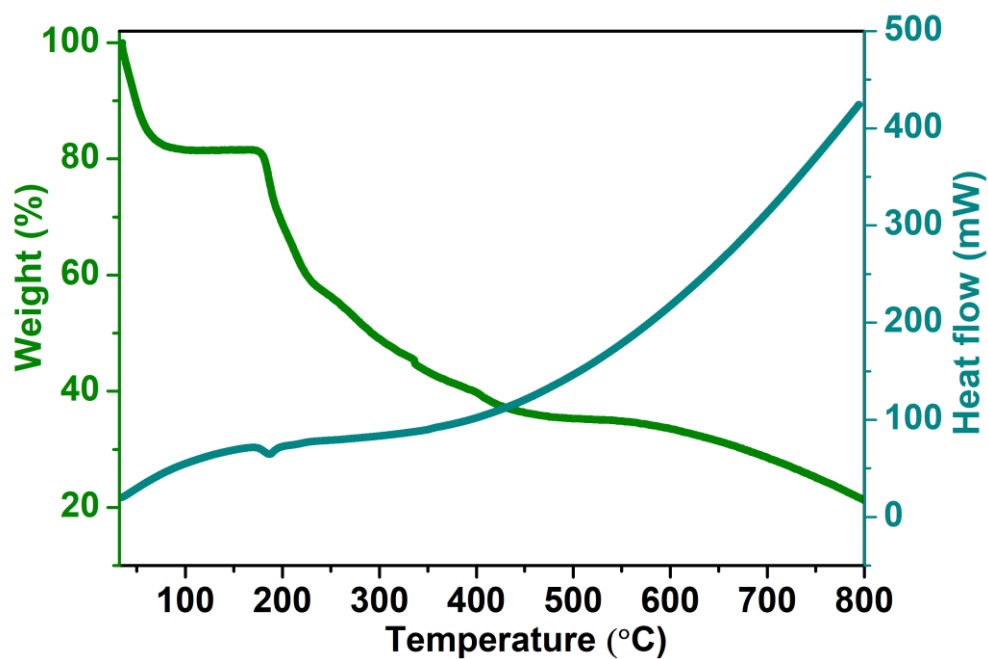


Figure 2A.27: Thermo-gravimetric analysis (TGA) plot for 2.

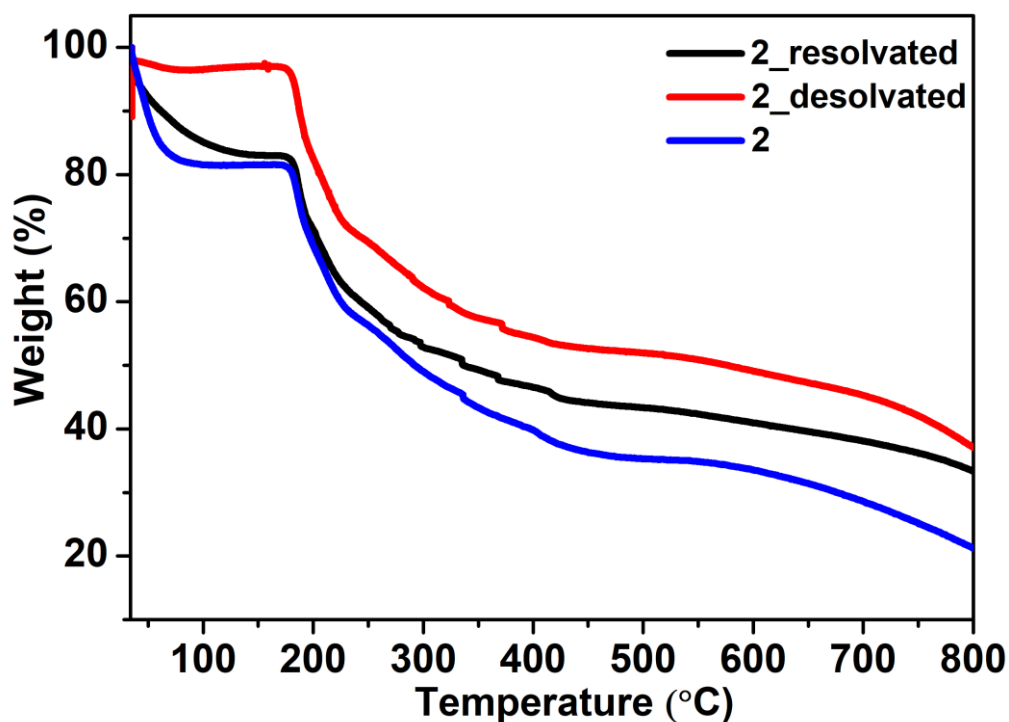


Figure 2A.28: Thermo-gravimetric analysis (TGA) plot for 2, $2_{\text{desolvated}}$ and $2_{\text{resolvated}}$.

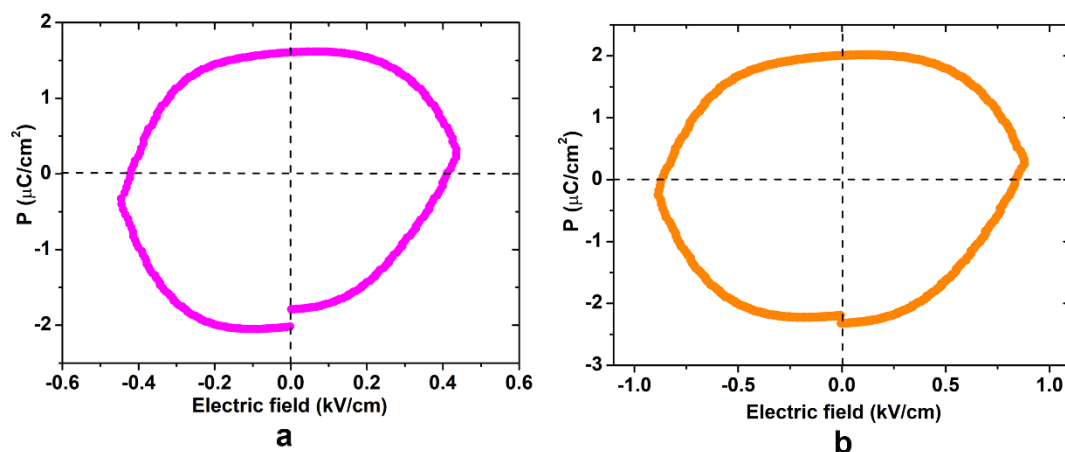


Figure 2A.29. The P-E loops of the compacted pellets of **1**_{desolvated} and **2**_{desolvated} showing the resistor-type behaviour.

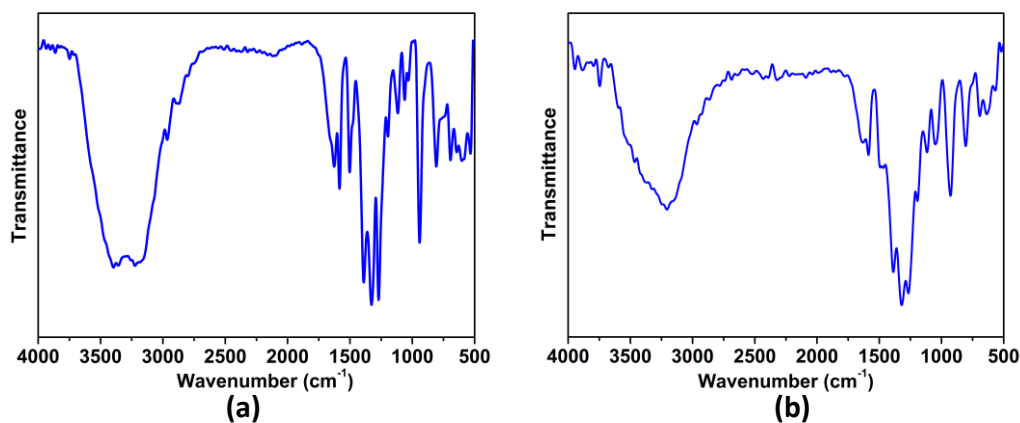


Figure A3.1: FT-IR spectra of **1** (a) and **2** (b).

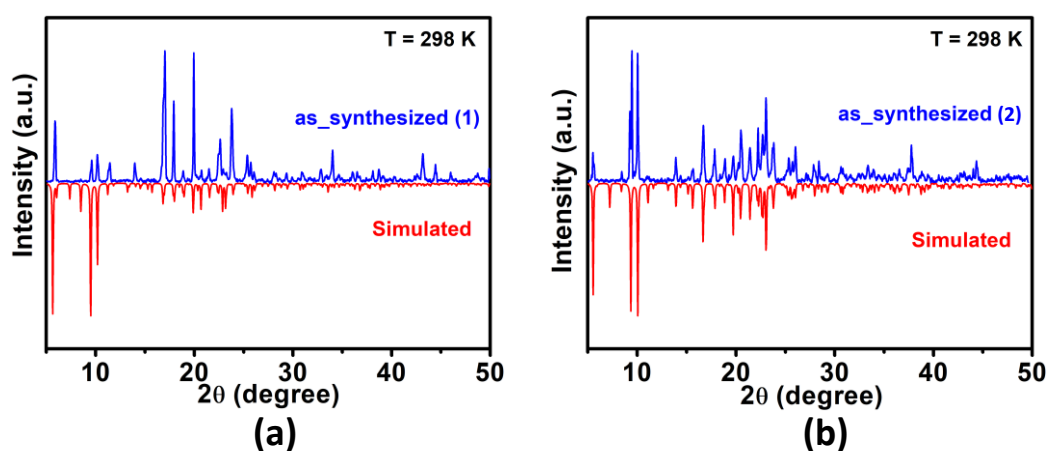


Figure A3.2: The powder X-ray diffraction profile of the as-synthesized compound **1** (a) and **2** (b) and its comparison with simulated pattern from single crystal X-ray data.

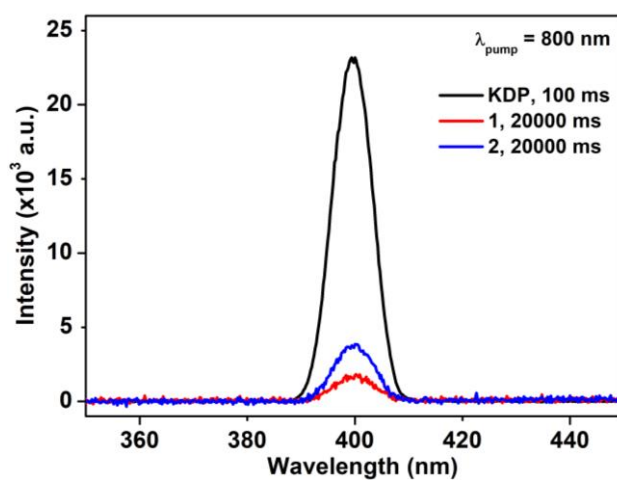


Figure A3.3: The SHG signal of **1** and **2** overlaid with that of KDP of the same particle size.

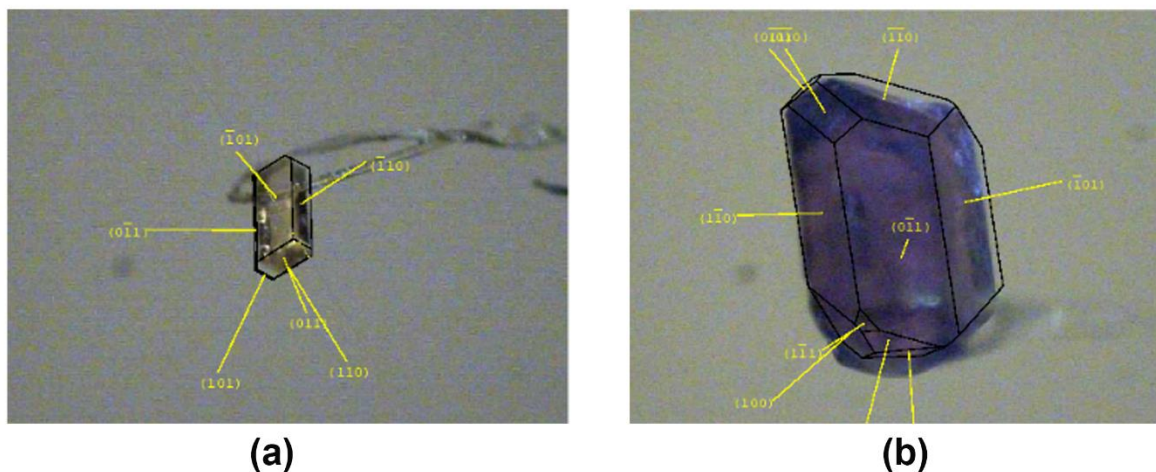


Figure A3.4: Face indexing pattern showing the various hkl planes on a single crystal of **1** (a) and **2** (b).

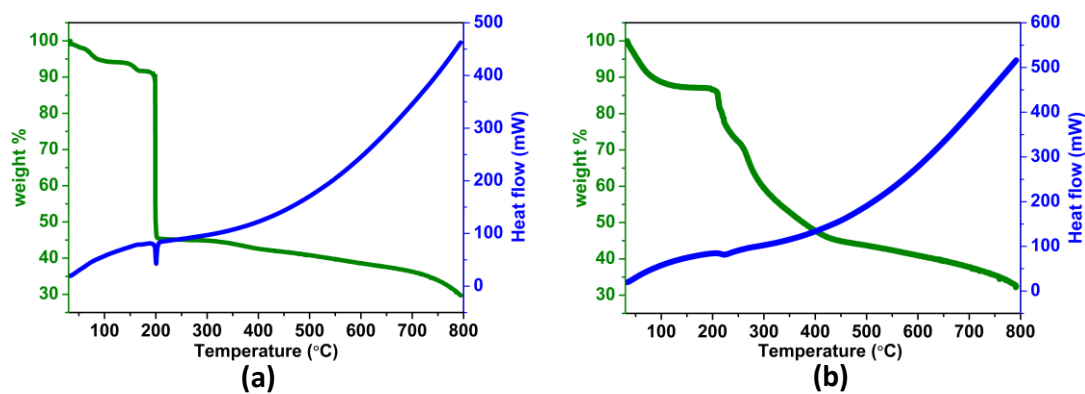


Figure A3.5: Thermo-gravimetric analysis (TGA) of **1** (a) and **2** (b).

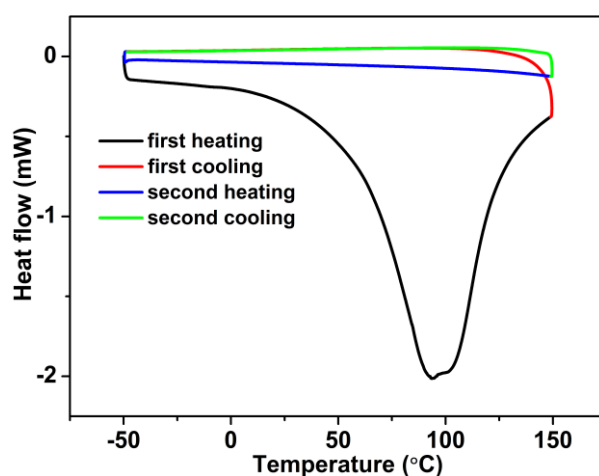
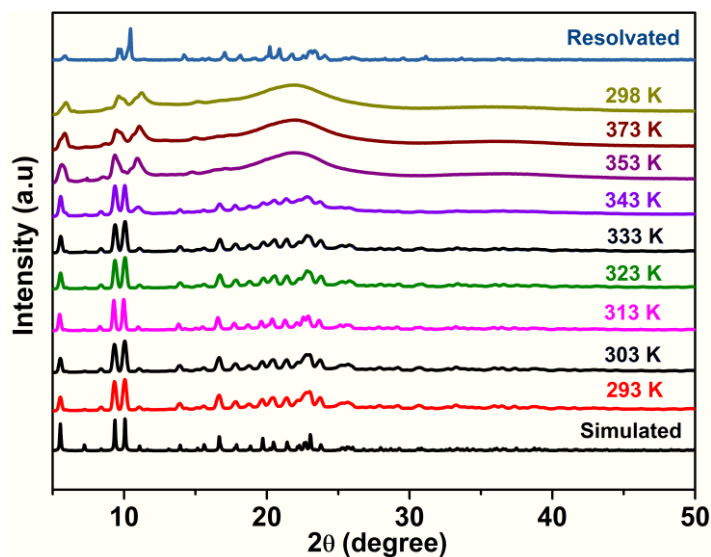
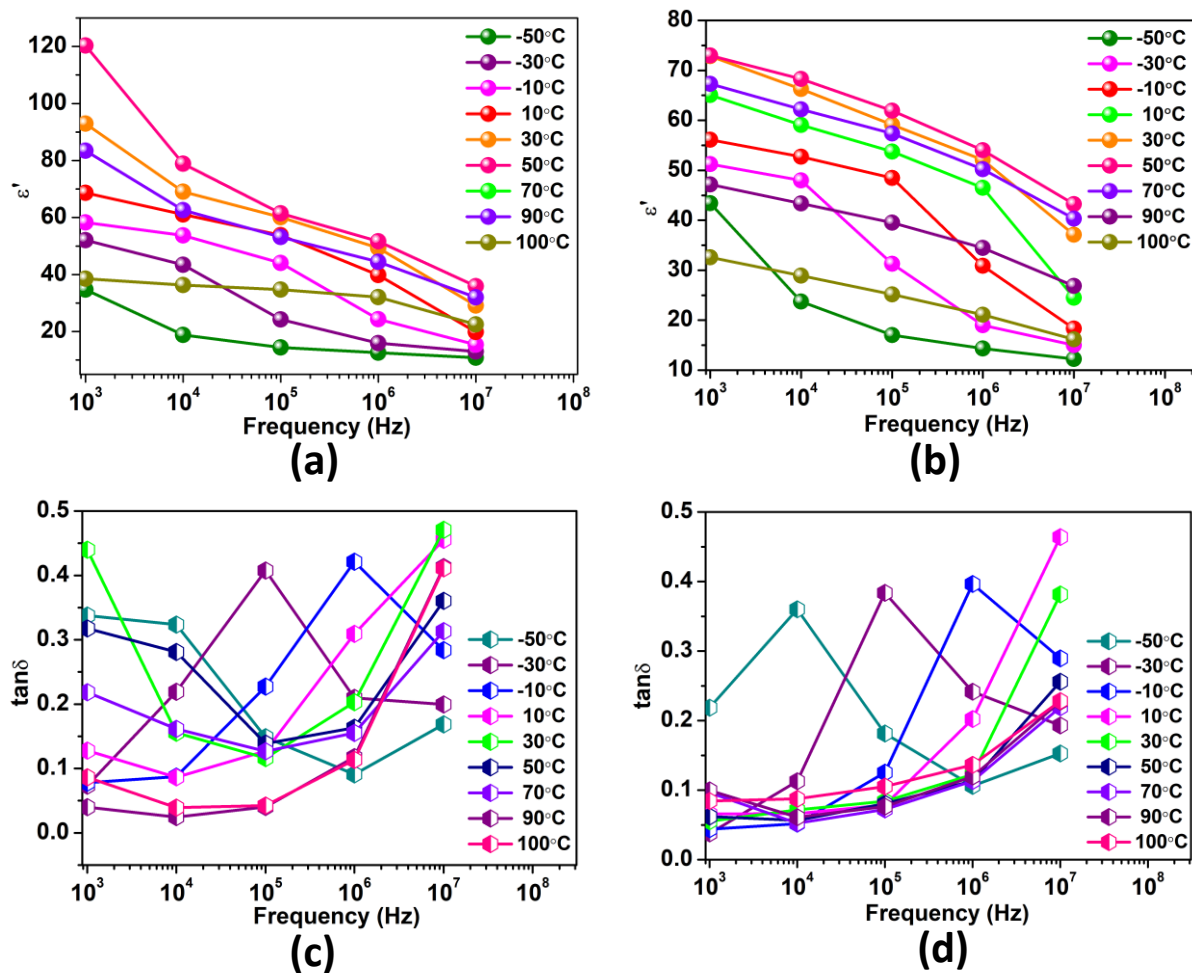


Figure A3.6: Differential Scanning Calorimetry (DSC) of **2**.

Figure A3.7: Variable-temperature PXRD of **2**.Figure A3.8: The ϵ' vs frequency plot of **1** (a) and **2** (b). Dielectric loss factor ($\tan \delta$) of **1** (a) and **2** (b) as a function of frequency.

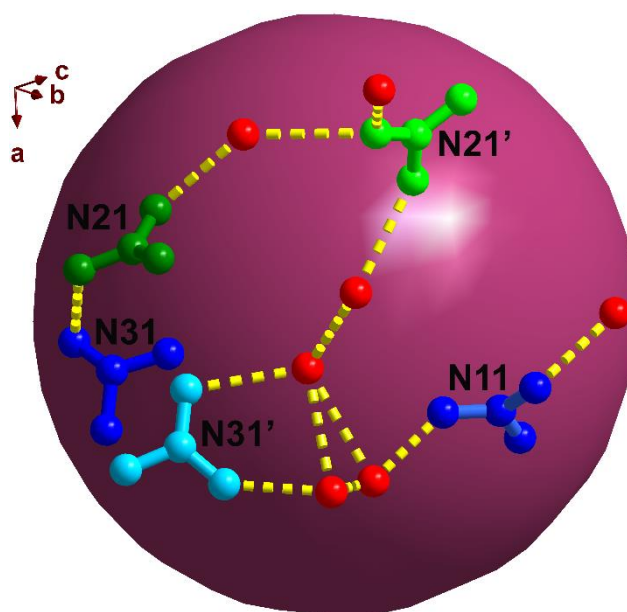


Figure A3.9: Segments of the ordered and the disordered nitrate anions of **2** and their H-bonding interactions with solvate molecules. The cyan and light green spheres indicate the disordered nitrate fragments.

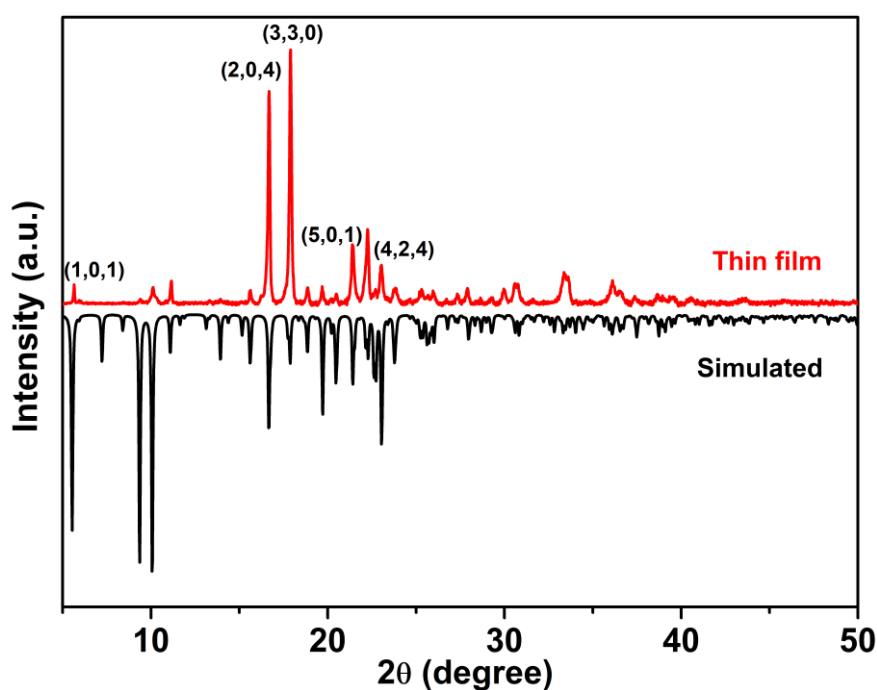


Figure A3.10: Powder X-ray diffraction pattern for the thin film of **2** and its comparison with simulated patterns from X-ray-derived structure.

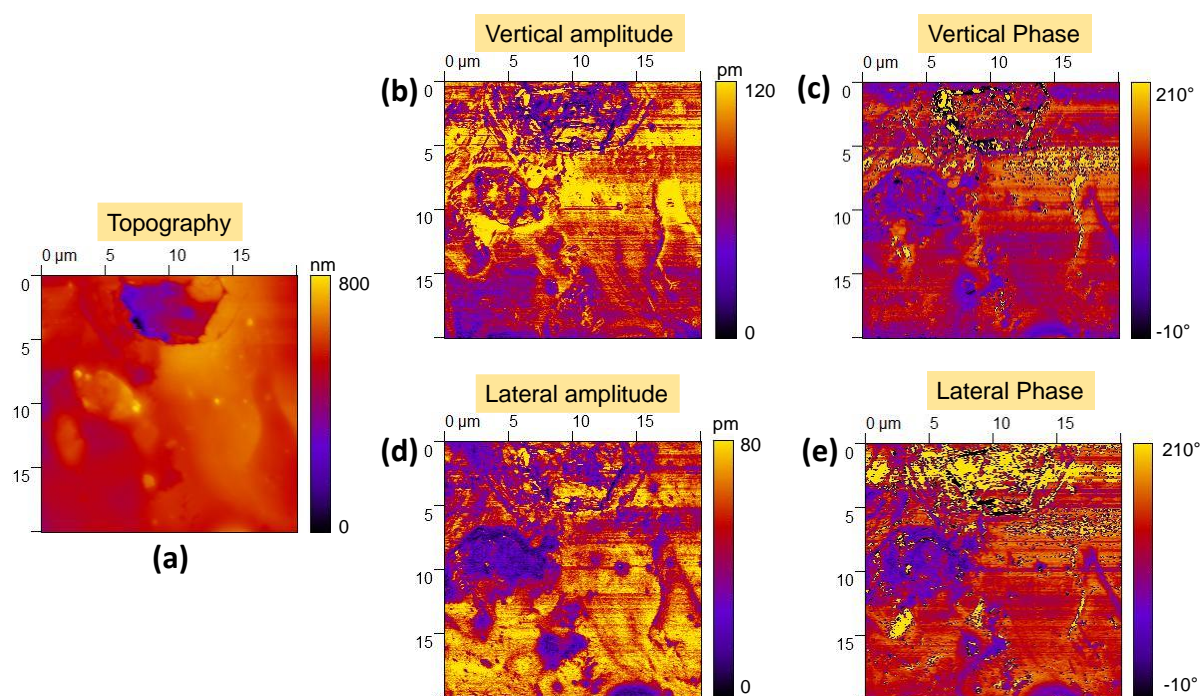


Figure A3.11: PFM measurements on the bulk single crystal of **2**. (a) Topography (b) Vertical-Amplitude (c) Vertical-Phase (d) Lateral-Amplitude (e) Lateral-Phase images.

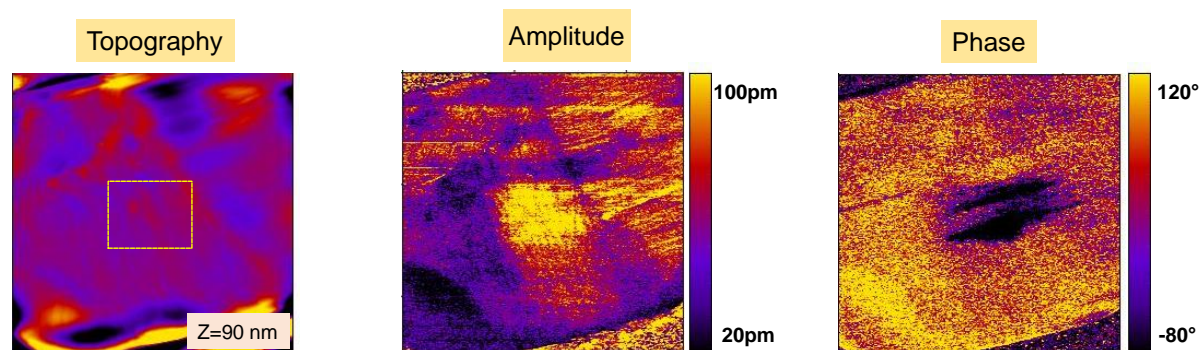


Figure A3.12: PFM writing experiments on the thin film of **2**.

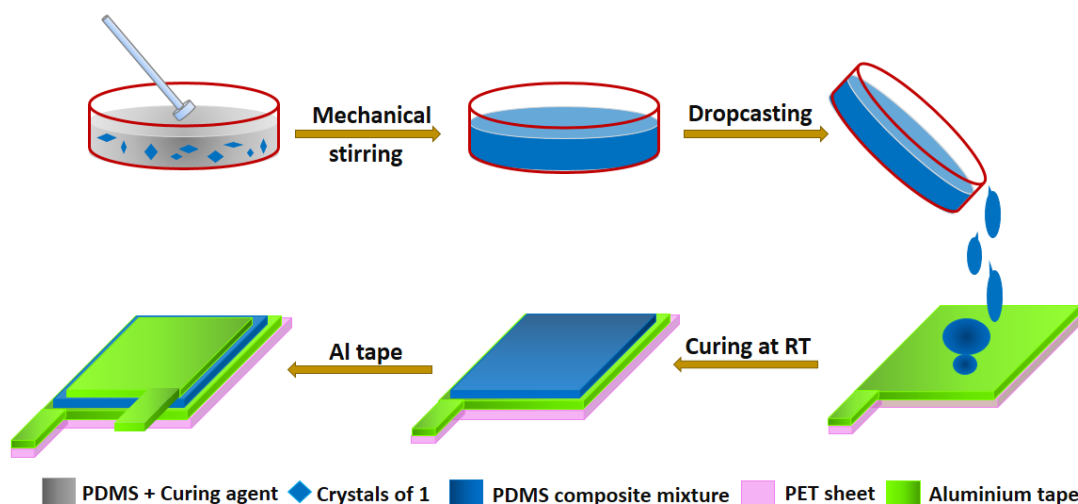


Figure A3.13: Schematic diagram illustrating the preparation and fabrication of composite films of **2** in PDMS.

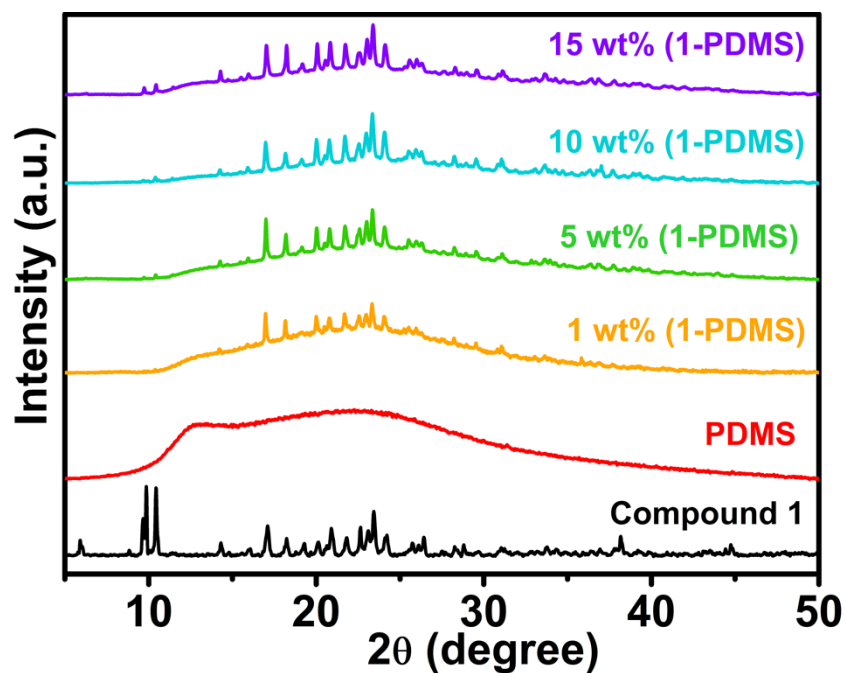


Figure A3.14: PXRD profiles of various (1, 5, 10, 15) wt% **2**-PDMS composite films and its comparison with pristine compound of **2**. The broad profile of a neat PDMS film shows its amorphous structure.

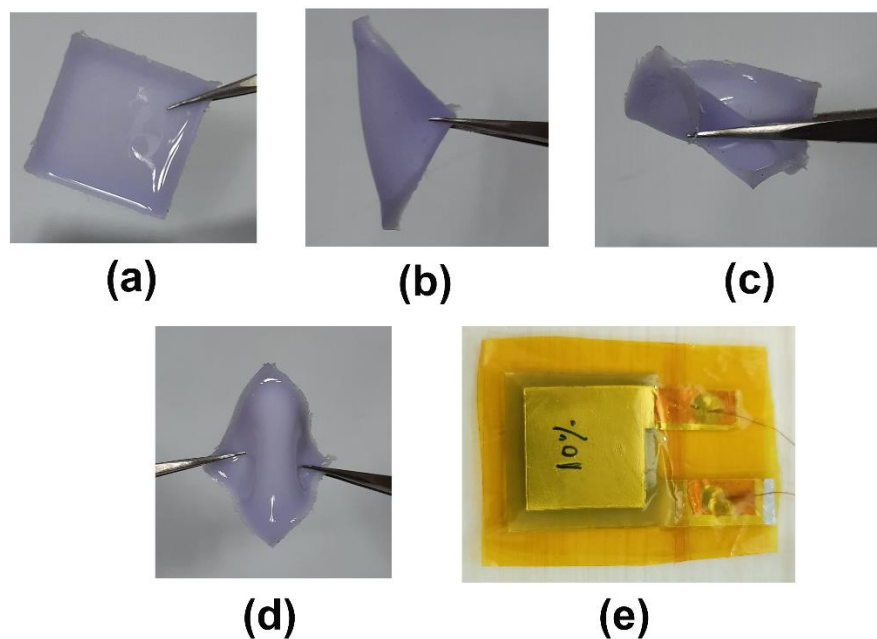


Figure A3.15: Photographs of a representative (a) as-made composite film of 2-PDMS showing its flexibility towards (b) folding, (c) two-fold bending and (d) twisting operations. (e) Photograph of a representative 2-PDMS PENG device.

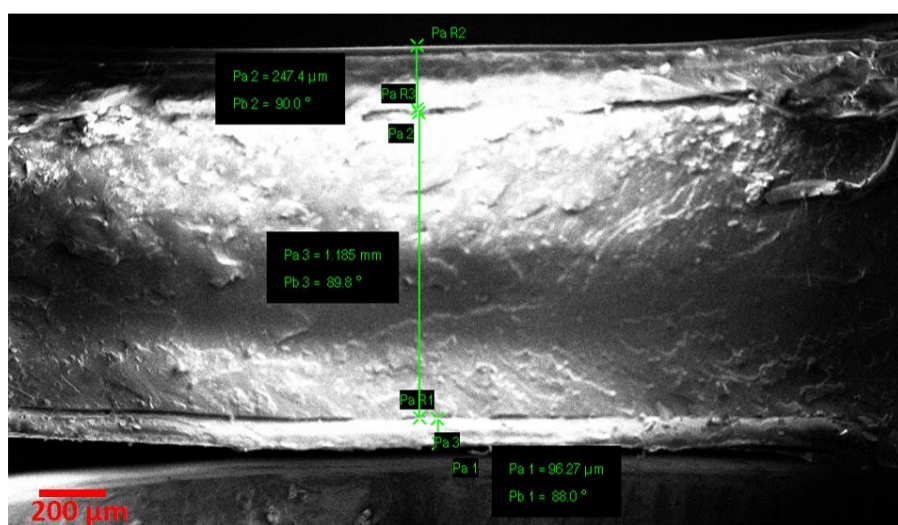


Figure A3.16: The cross-sectional image of the sandwiched structure of a representative 2-PDMS composite film showing a thickness of around 1.19 mm.

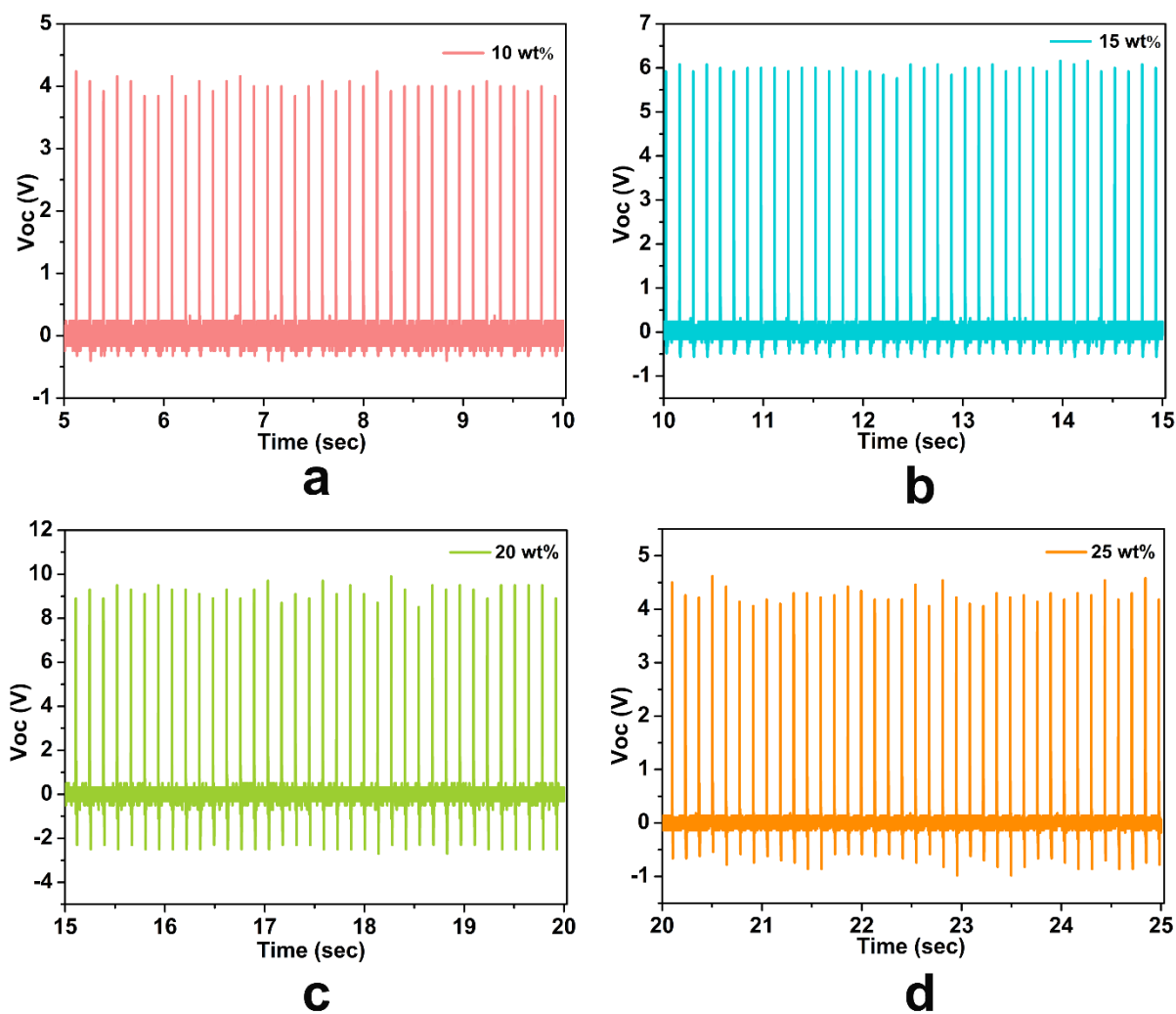


Figure A3.17: The piezoelectric output open-circuit voltages of the various 1-PDMS PENG devices.

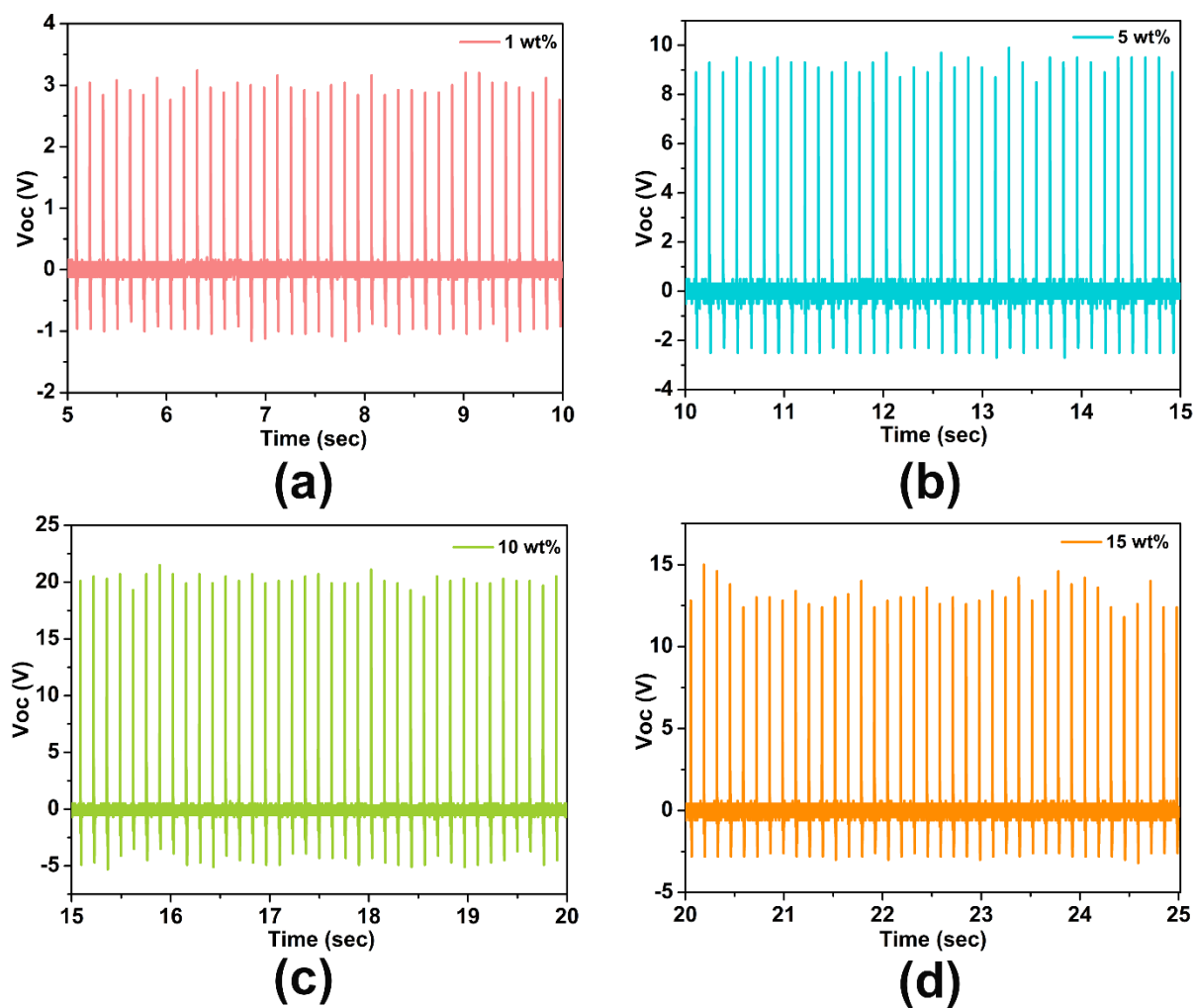


Figure A3.18: The piezoelectric output open-circuit voltages of the various 2-PDMS PENG devices.

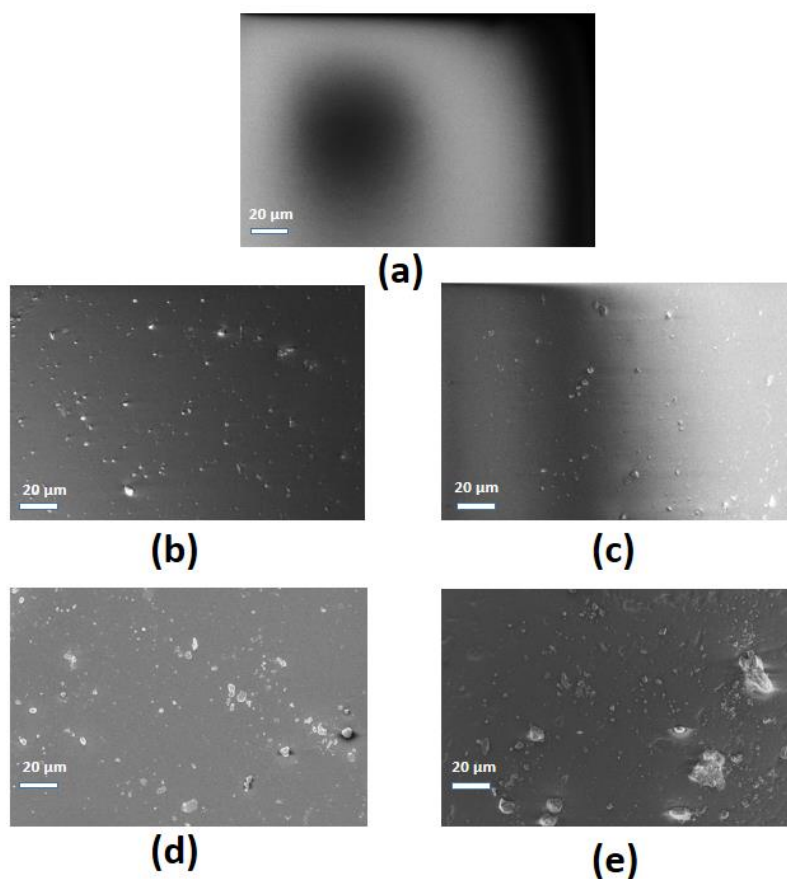


Figure A3.19: SEM images of (a) neat PDMS film and the 2-PDMS composite films of (b) 1 wt% (c) 5 wt% (d) 10 wt% (e) 15 wt% of 2.

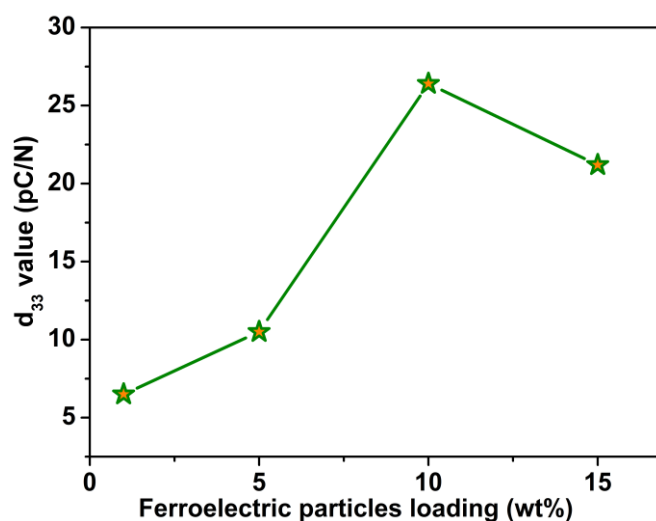


Figure A3.20: The piezoelectric coefficient (d_{33}) values obtained from the quasi-static method of the different weight percentage composite films of 2.

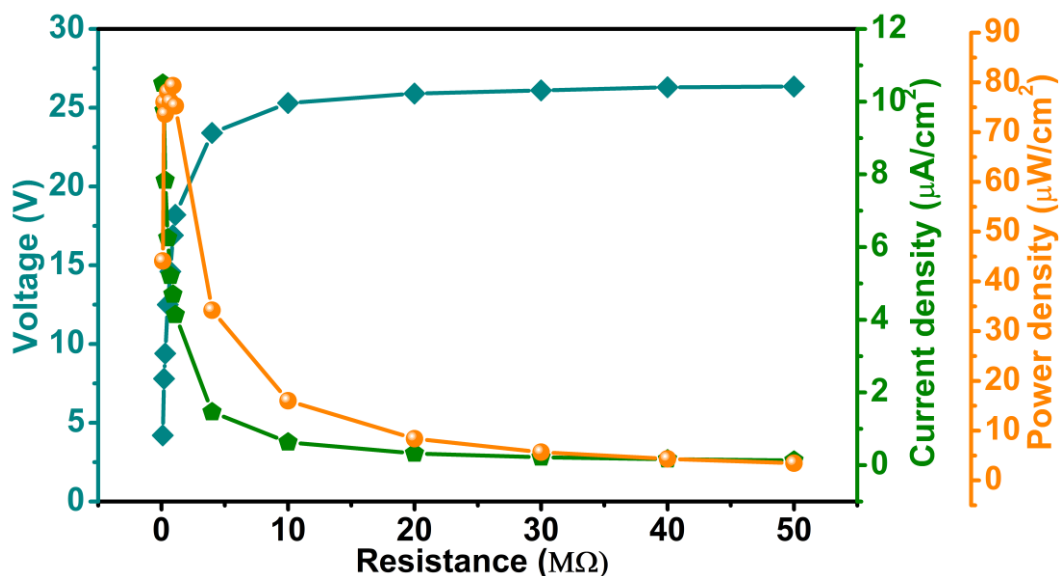


Figure A3.21: Calculated current density plot of 10 wt% 2-PDMS device across various load resistances.

Table A2.1: Comparison of output device performance of various piezoelectric energy harvesters based on metal-organic materials.

Hybrid composite materials	Output voltage (V)	Current/Current density	Power/Power density	Active Area	References
Car_Zn (MeCN)-PDMS	2.5 V	-	-	1 x 1 cm ²	1
Zr-MOF- PDMS	536 mV	-	-	2 x 1.5 cm ²	2
[Ph ₃ MeP] ₄ [Ni(NCS) ₆]-TPU	19.29 V	3.59 μA/cm ³	50.26 μW/cm ³	1.3 x 3 cm ²	3
(CdI ₂ -INH-CMe ₂)-PVDF	12 V	-	32 μW/cm ²	2 x 1 cm ²	4
MAPI-PVDF	220 mV	-	-	2.9 x 1.5 cm ²	5
(CdI ₂ -NAP)-PVDF	22 V	-	24 μW/cm ²	4 x 1.5 cm ²	6
PVDF-PLLA-SnO ₂ NF-MAPbI ₃	4.82 V	29.7 nA	-	0.25 X 0.25 cm ²	7
(TMFM)FeBr ₄	2.2 V	-	-	-	8
MASnI ₃ -PVDF	12 V	4 μA/cm ²	21.6 μW/cm ²	-	9
5 wt% ([Zn(L ¹)(bpy)]·(H ₂ O) _{1.5}) _∞ -TPU	5.6 V	6.19 μA/cm ²	14.6 μW/cm ²	1.3 x 2 cm ²	10
10 wt% (2-PDMS)	25.35 V	4.69 μA/cm²	79.33 μW/cm²	2 x 2 cm²	This work

*The overall performance of the composite devices depends on several factors, such as the dimensions of the composite films (including area, thickness), amount of piezoelectric fillers in polymer, active particles surface morphology, supporting polymer, electrodes, active surface area between electrode and composite film, magnitude of impact force and frequency.

Note – PDMS = Polydimethylsiloxane; PVDF = Polyvinyl difluoride; MAPI = Methylammonium Lead Iodide; PLLA = poly(L-lactic acid); (TMFM)FeBr₄ = trimethylfluoromethylammonium iron(III)bromide; MASnI₃ = methylammonium tin iodide.

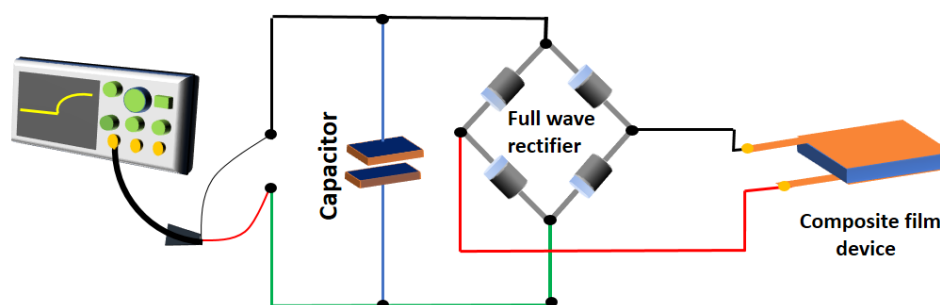


Figure A3.22: Schematic drawing depicting the capacitor charging experiment using a 2-PDMS device connected through a full-wave bridge rectifier.

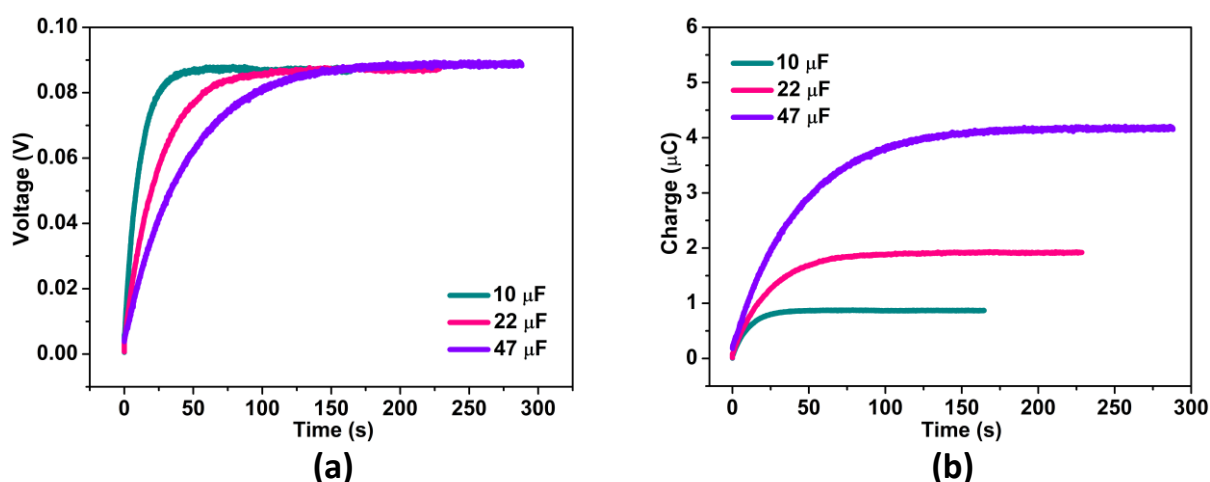


Figure A3.23: The rectified-voltage signals for the different-rated capacitors in the charging experiment obtained by the continuous impact of the 10 wt% 2-PDMS device.

A3.24 References

1. Y. Chen, S. Guerin, H. Yuan, J. O'Donnell, B. Xue, P.-A. Cazade, E. U. Haq, L. J. W. Shimon, S. Rencus-Lazar, S. A. M. Tofail, Y. Cao, D. Thompson, R. Yang and E. Gazit, *J. Am. Chem. Soc.*, 2022, **144**, 3468-3476.
2. B. H. Moghadam, M. Hasanzadeh and A. Simchi, *ACS Appl. Nano Mater.*, 2020, **3**, 8742-8752.
8. T. Vijayakanth, F. Ram, B. Praveenkumar, K. Shanmuganathan and R. Boomishankar, *Angew. Chem., Int. Ed.*, 2020, **59**, 10368-10373.
3. K. Roy, S. Jana, S. K. Ghosh, B. Mahanty, Z. Mallick, S. Sarkar, C. Sinha and D. Mandal, *Langmuir*, 2020, **36**, 11477-11489.
4. A. Sultana, S. K. Ghosh, M. M. Alam, P. Sadhukhan, K. Roy, M. Xie, C. R. Bowen, S. Sarkar, S. Das, T. R. Middy and D. Mandal, *ACS Appl. Mater. Interfaces*, 2019, **11**, 27279-27287.
5. K. Roy, S. Jana, Z. Mallick, S. K. Ghosh, B. Dutta, S. Sarkar, C. Sinha and D. Mandal, *Langmuir*, 2021, **37**, 7107-7117.
6. R. Tusiime, F. Zabihi, M. Tebyetekerwa, Y. M. Yousry, Y. Wu, M. Eslamian, S. Yang, S. Ramakrishna, M. Yu and H. Zhang, *J. Mater. Chem. C*, 2020, **8**, 2643-2658.
7. S. Ippili, V. Jella, J.-H. Eom, J. Kim, S. Hong, J.-S. Choi, V.-D. Tran, N. Van Hieu, Y.-J. Kim, H.-J. Kim and S.-G. Yoon, *Nano Energy*, 2019, **57**, 911-923.
8. N. Prajesh, V. B. Sharma, S. S. Rajput, C. K. Singh, P. Dixit, B. Praveenkumar, J. K. Zareba, D. Kabra, S. Ogale and R. Boomishankar, *ACS Sustainable Chem. Eng.*, 2022, **10**, 9911-9920

Crystal structures of **L**

The molecular structure of the ligand $\text{PhPO}(\text{NHCH}_2\text{-(3-Py)})_2$ (**L**) was solved in the orthorhombic non-centrosymmetric polar space group $Pca2_1$. The asymmetric unit contains two molecules of the ligand. It forms a tetrameric H-bonded structure due to the $\text{N-H}\cdots\text{O}$ type H-bonding interaction between the proton of the one of the amino group and the phosphoryl oxygen atom in one unit and the pyridyl N-atom in another unit.

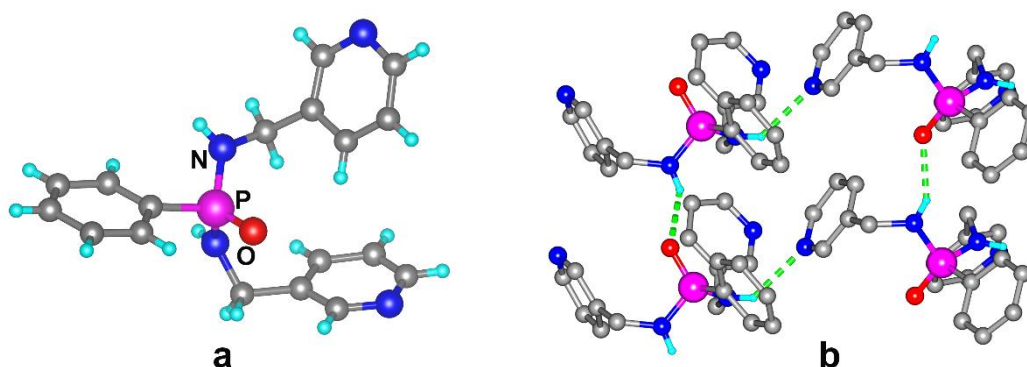


Figure 4A.1: Crystal structure of the ligand **L** (a) View of the monomeric unit of **L** (b) The hydrogen bonding interactions involving the $\text{N-H}\cdots\text{O}=\text{P}$ and $\text{N-H}\cdots^3\text{NH}_{\text{py}}$ units.

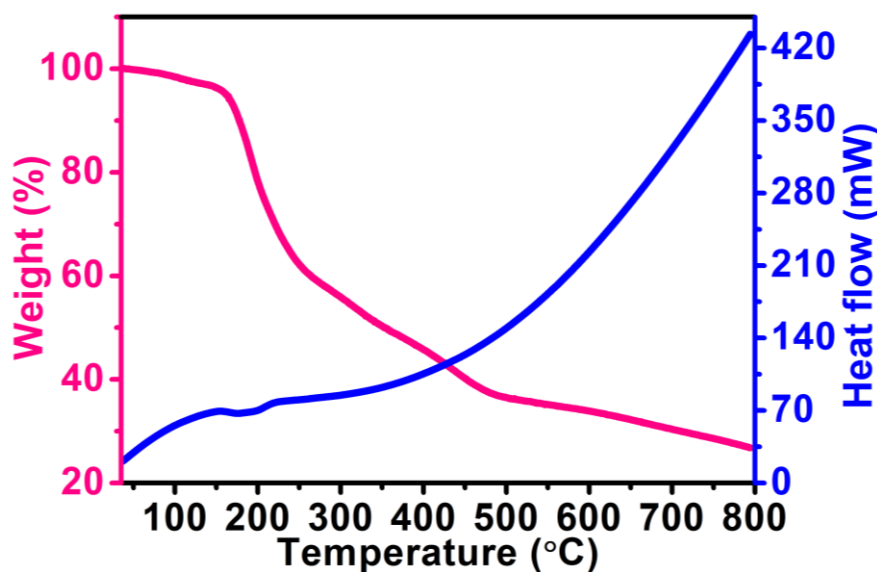


Figure 4A.2: Thermo-gravimetric analysis (TGA) plot of **1**.

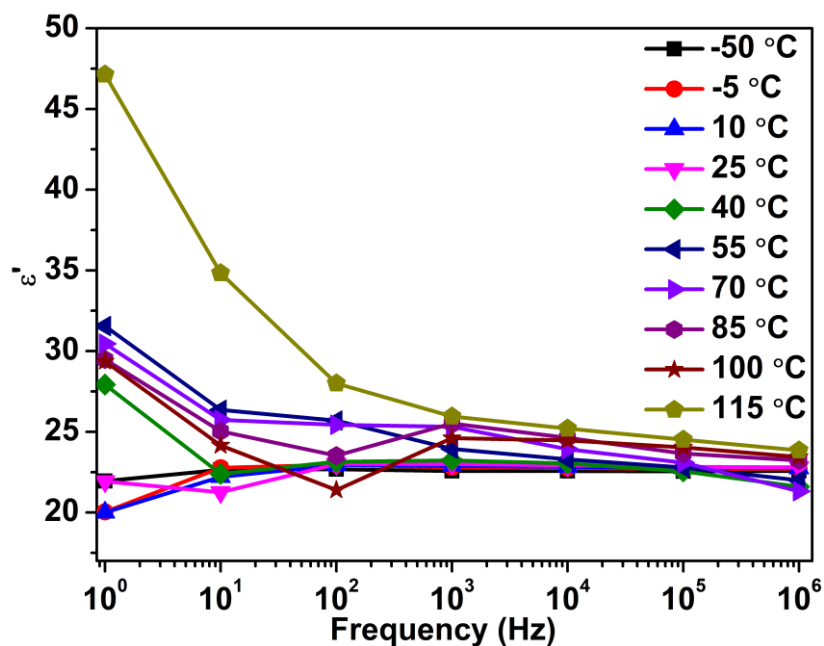


Figure 4A.3: Real part of the dielectric permittivity (ϵ') graph as a function of frequency.

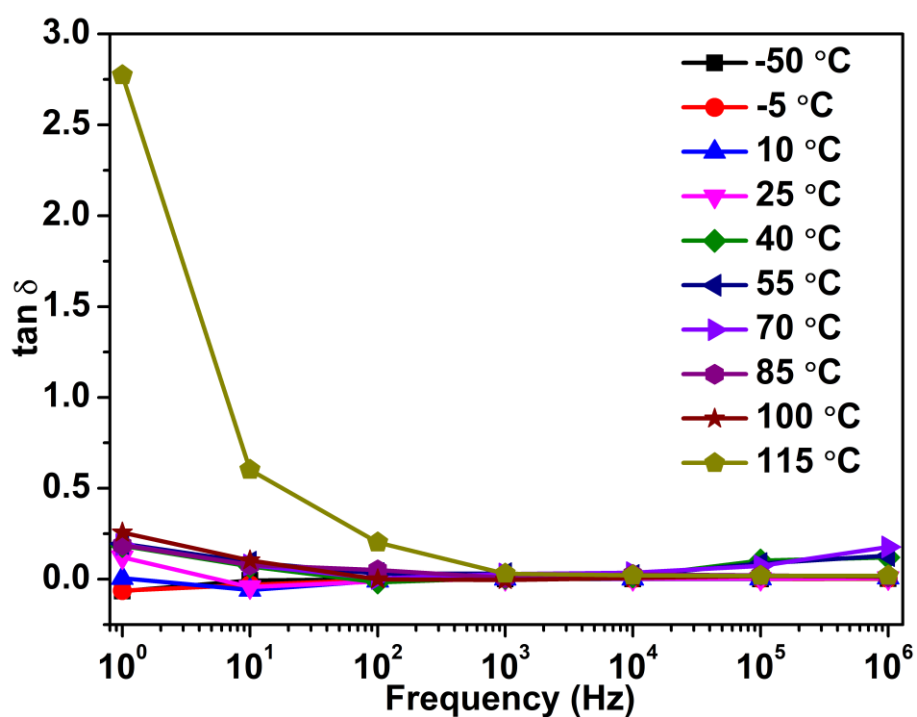


Figure 4A.4: Dielectric loss factor ($\tan \delta$) of 1 as a function of frequency.

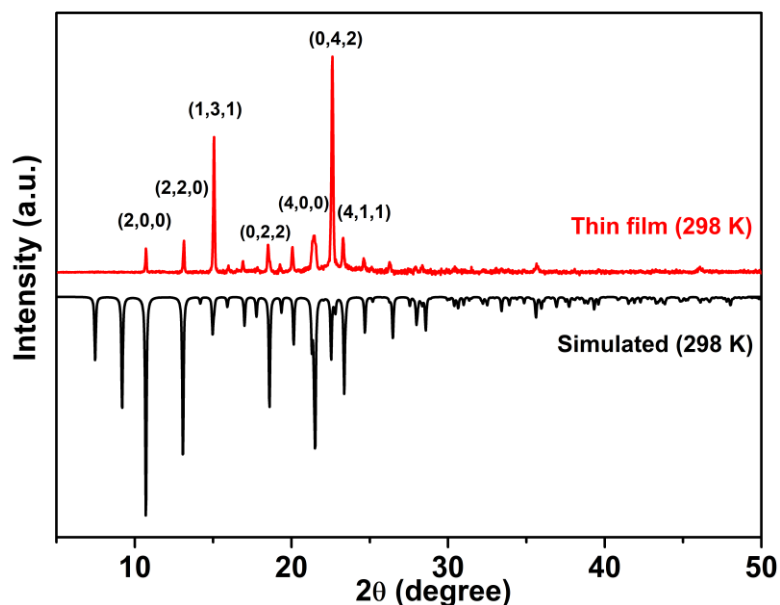


Figure 4A.5: Powder X-ray diffraction pattern for the thin film of **1** and its comparison with simulated patterns from X-ray-derived structure at 298 K.

Table S1. Coordinates of point electric charges.

Atoms	Lattice position	Coordinates		Center coordinates
Cu	Cu _E	(0.0, 0.0, 0.28037)	(0.0, 1, 0.28037)	(0.5, 0.5, 0.44704)
		(1.0, 0.0, 0.28037)	(1.0, 1.0, 0.28037)	
	Cu _F	(0.0, 0.5, .78037)	(0.5, 0.0, .78037)	
		(1.0, 0.5, .78037)	(0.5, 1.0, 0.78037)	
	Cu _B	(0.5, 0.5, 0.28037)		
N ₁	N _{1F}	(0.5, 0.99999, 0.43651)	(0.5, 0.0, 0.43651)	
		(0, 0.5, 0.43651)	(1.0, 0.5, 0.43651)	
	N _{1E}	(1.01073, 0.04185, 0.93651)	(0.98926, 0.95814, 0.93651)	
		(-0.01073, 0.95814, 0.93651)	(0.01073, 0.04185, 0.93651)	
	N _{1B}	(0.5, 0.49931, 0.93651)		
N ₂	N _{2F}	(0.5, 1.0, 0.09043)	(0.5, 0.0, 0.09043)	(0.5, 0.5, 0.36821)
		(0.0, 0.5, 0.09043)	(1.0, 0.5, 0.09043)	
	N _{2E}	(1.0, 0.0, 0.59043)	(1.0, 1.0, 0.59043)	
		(0.0, 1.0, 0.59043)	(0.0, 0.0, 0.59043)	
	N _{2B}	(0.5, 0.5, 0.59043)		

$$\begin{aligned}
P_s &= \lim \frac{1}{V} \sum q_i r_i \\
&= (q_{Cu} \Gamma_{Cu} + q_{N1} \Gamma_{N1} + q_{N2} \Gamma_{N2}) / V \\
&= [(2e \times 0.44704) + (-e \times 0.71428) + (-e \times 0.36821)] \times 4 \times c / V \\
&= [(-0.18841) \times 4 \times 1.6 \times 10^{-19} \times 10.421 \times 10^{-10} \text{ C m}] / (4069.05 \times 10^{-30} \text{ m}^3) \\
&= -12.56589 \times 10^{-29} \text{ C m} / (4069.05 \times 10^{-30} \text{ m}^3) \\
&= -0.03088 \text{ C m}^{-2} \\
|P_s| &= 3.088 \text{ } \mu\text{C cm}^{-2}
\end{aligned}$$

Table S2 Details for the preparation of various mass fractions (wt%) of 1-TPU composite films

Composite (wt%)	1 (in mg)	TPU (in mg)
1	4.03	399
5	22.21	422
10	44.88	404
15	74.10	420
20	99.5	398

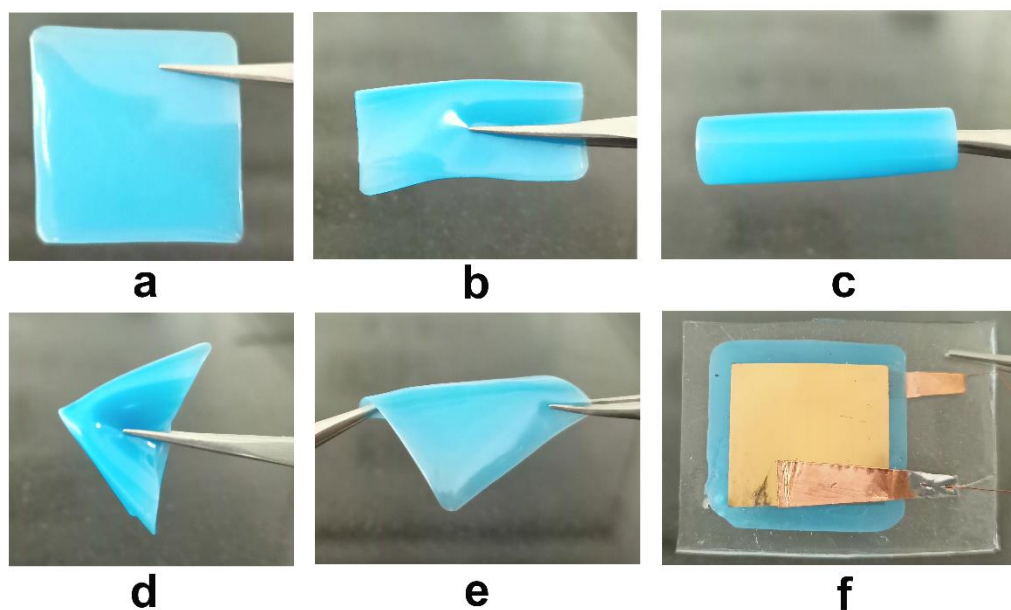


Figure 4A.6: Photographs of (a) the as-made 10 wt% 1-TPU composite film and its flexible nature for (b) folding (c) rolling (d) multi-fold bending (e) twisting operations. (f) Photograph of the as-fabricated 1-TPU composite device

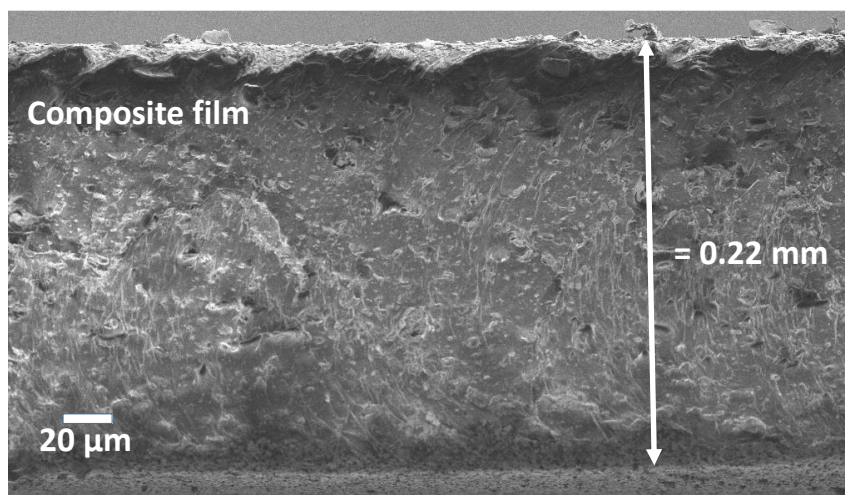


Figure 4A.7: The cross-sectional SEM image of the sandwiched structure of a representative 1-TPU composite film showing its thickness of around 0.22 mm.

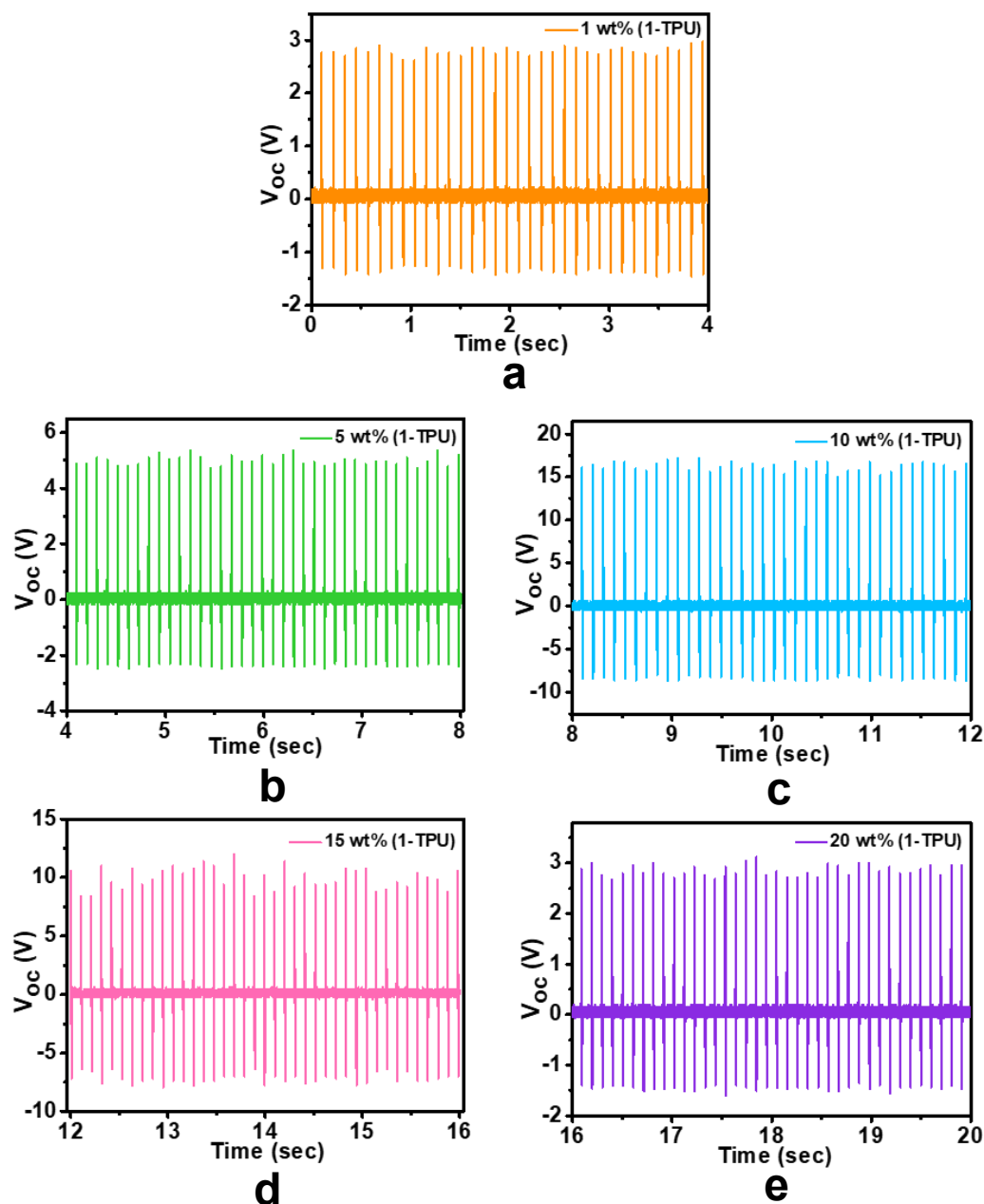


Figure 4A.8: Open-circuit output voltage measurements of various weight percentages (wt%) of poled 1-TPU composite devices

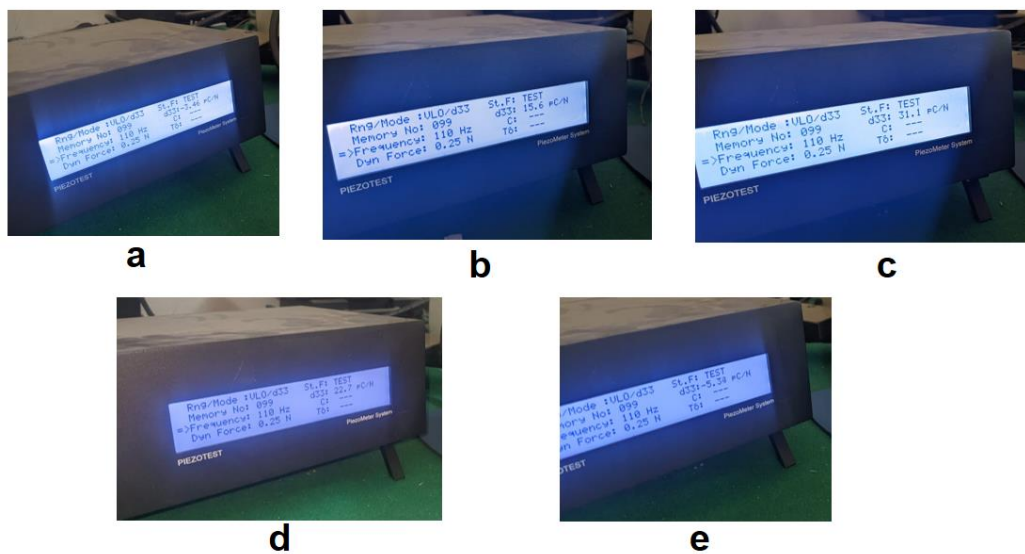


Figure 4A.9: Photographs of the d_{33} meter showing the direct Piezoelectric coefficients (d_{33}) of the poled 1, 5, 10, 15, 20 wt% of 1-TPU composite films

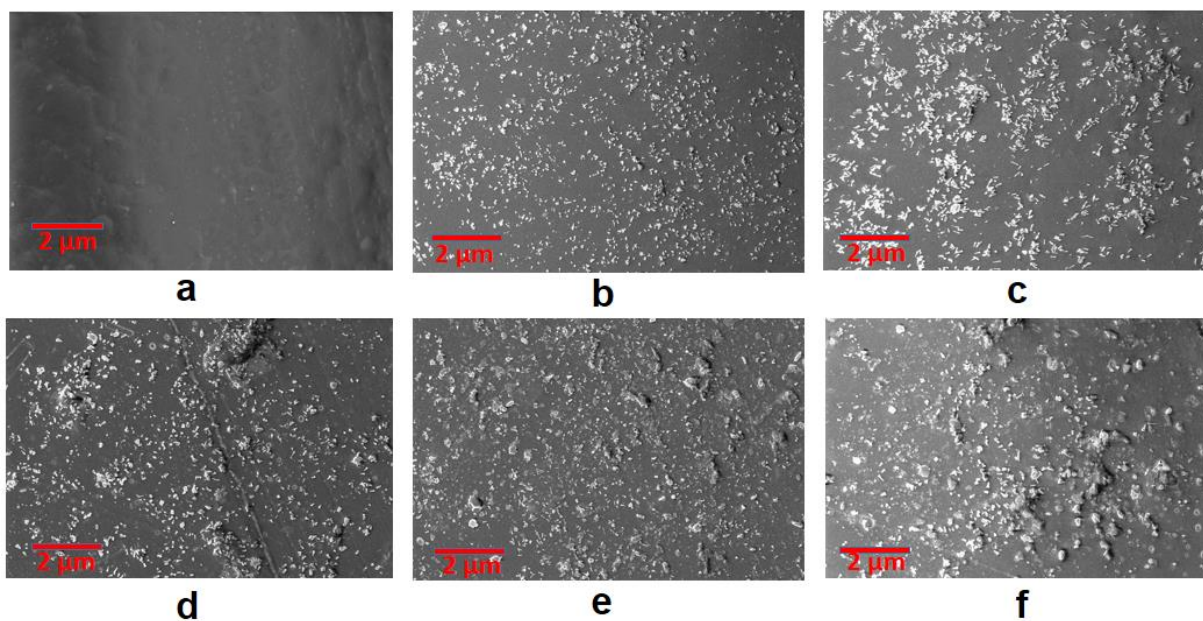


Figure 4A.10: SEM images of (a) neat TPU polymer and (b-f) the respective 1, 5, 10, 15, 20 wt% of 1-TPU composite films

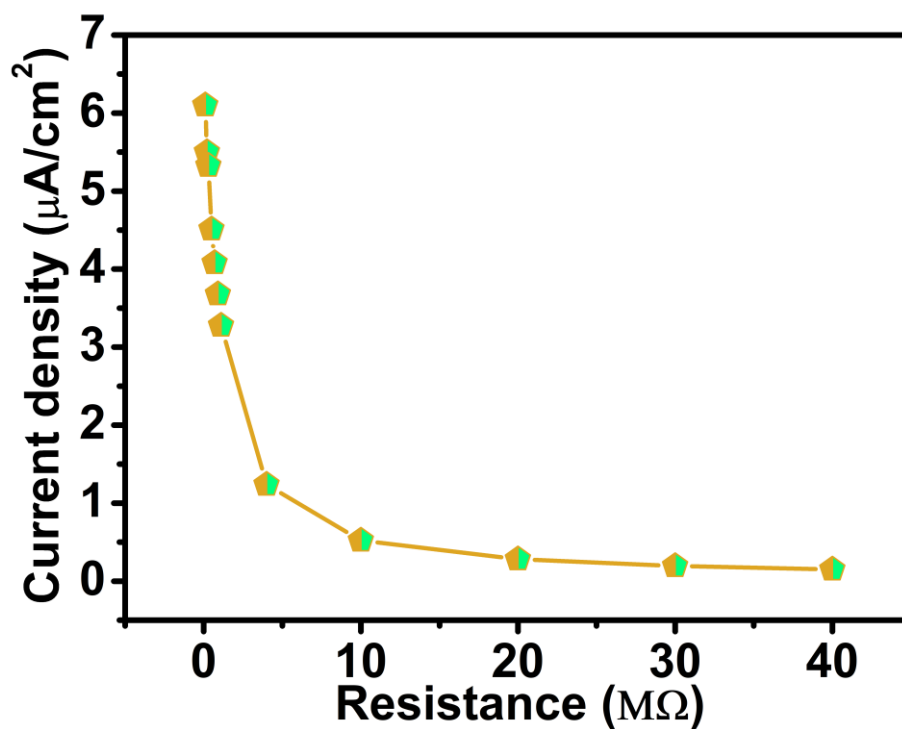


Figure 4A.11: Current density plot of 10 wt% 1-TPU device across various load resistance

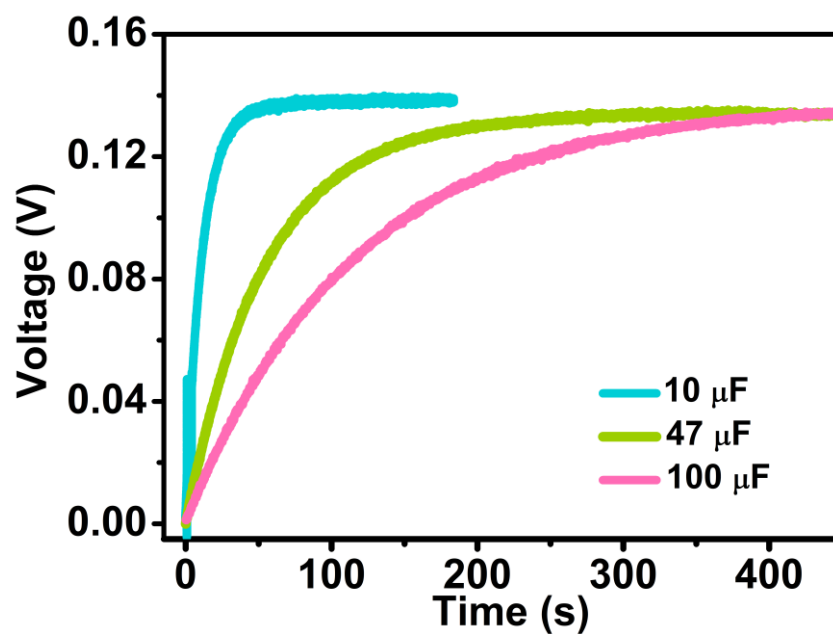
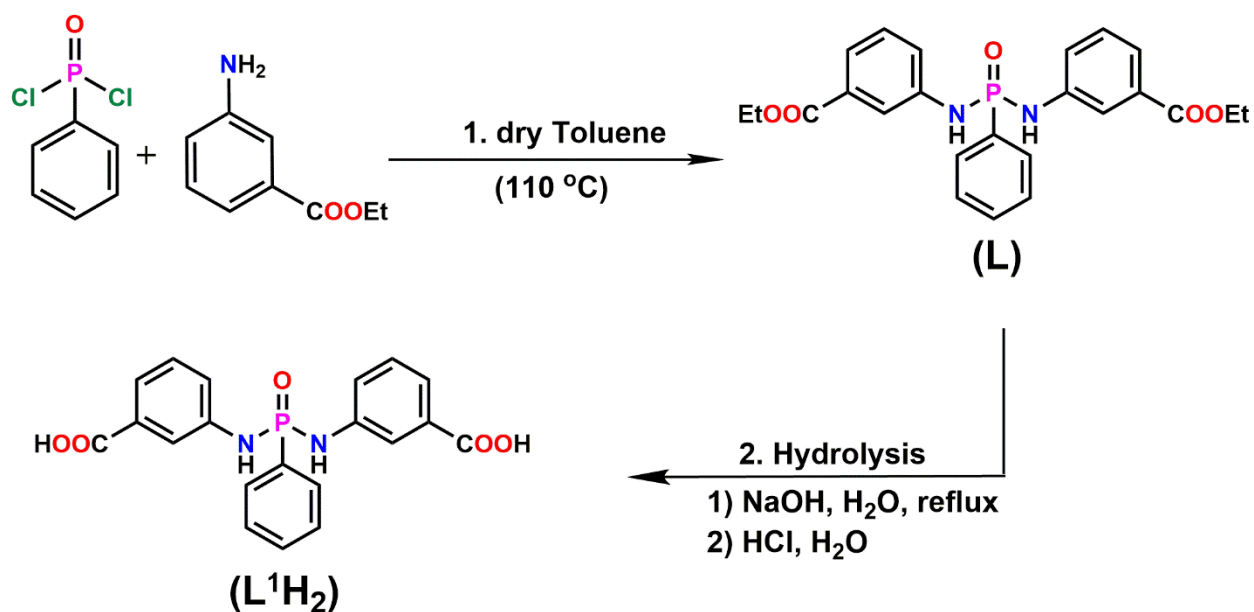
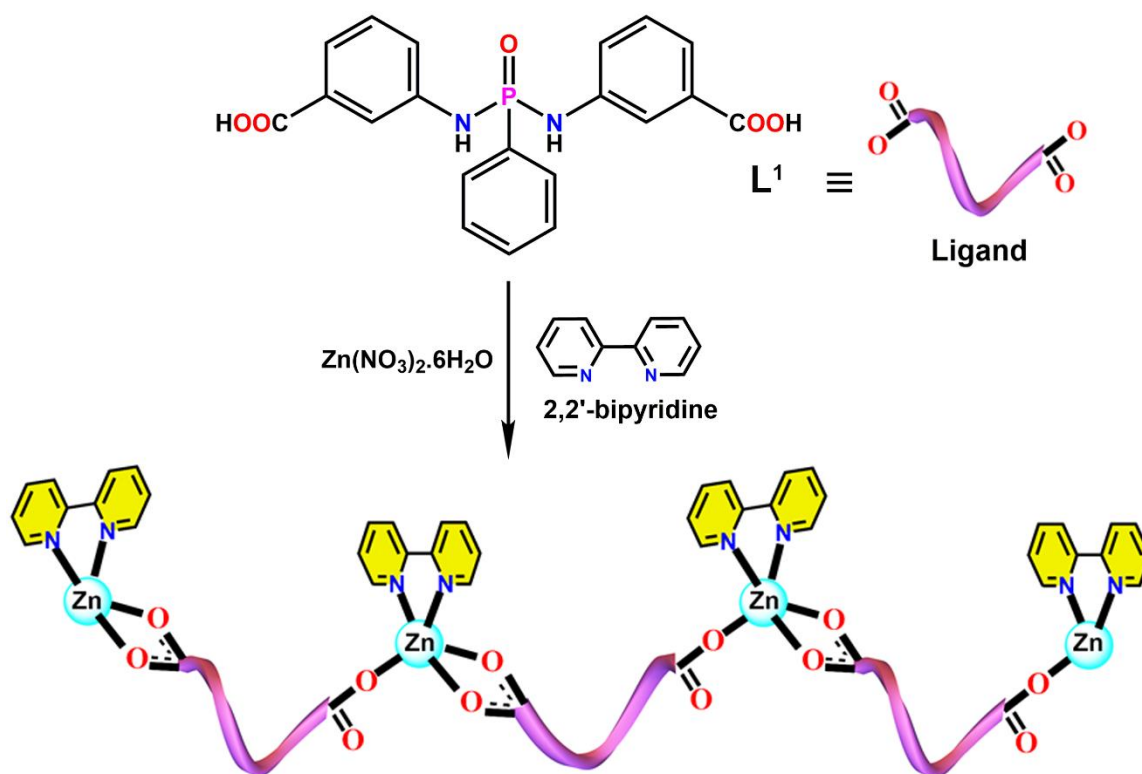


Figure 4A.12: Output saturation voltage of the 10 wt% 1-TPU device for different rated capacitances.

Scheme 5A.1: Synthesis of the ligand L¹H₂Scheme 5A.2: (a) Schematic diagram showing the formation of one-dimensional coordination network **1** of zinc with the dipodal ligand L¹ along with 2,2'-bipyridine chelating ligand.

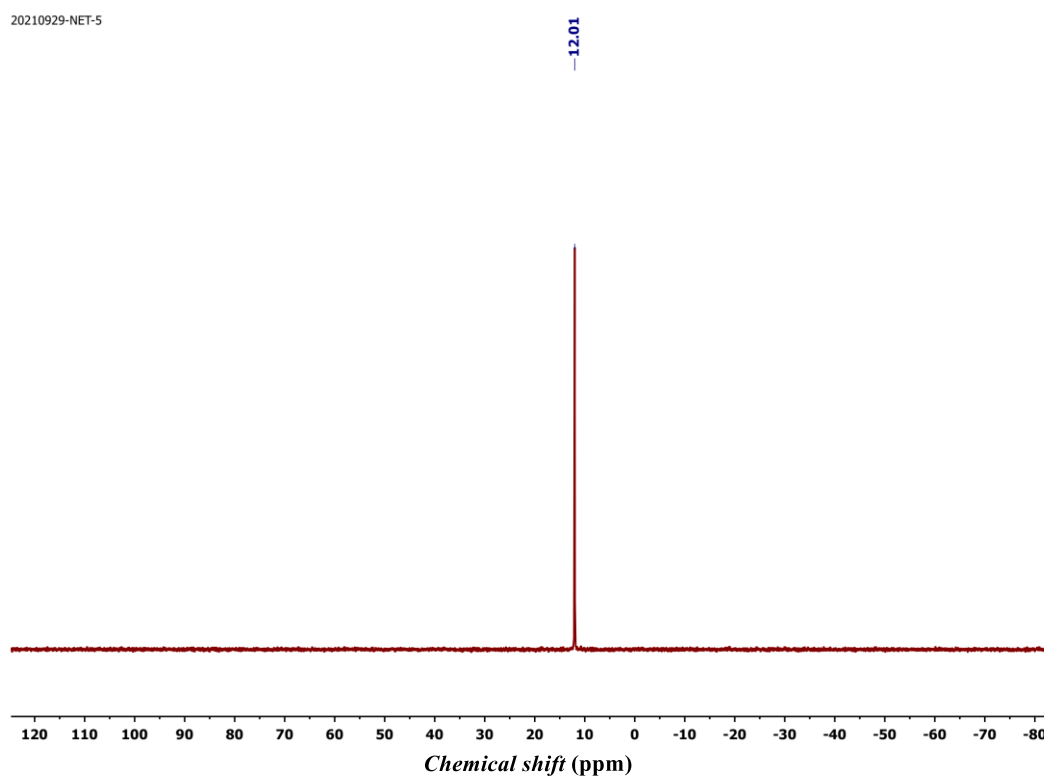


Figure 5A.1: The $^{31}\text{P}\{^1\text{H}\}$ spectrum of **L**

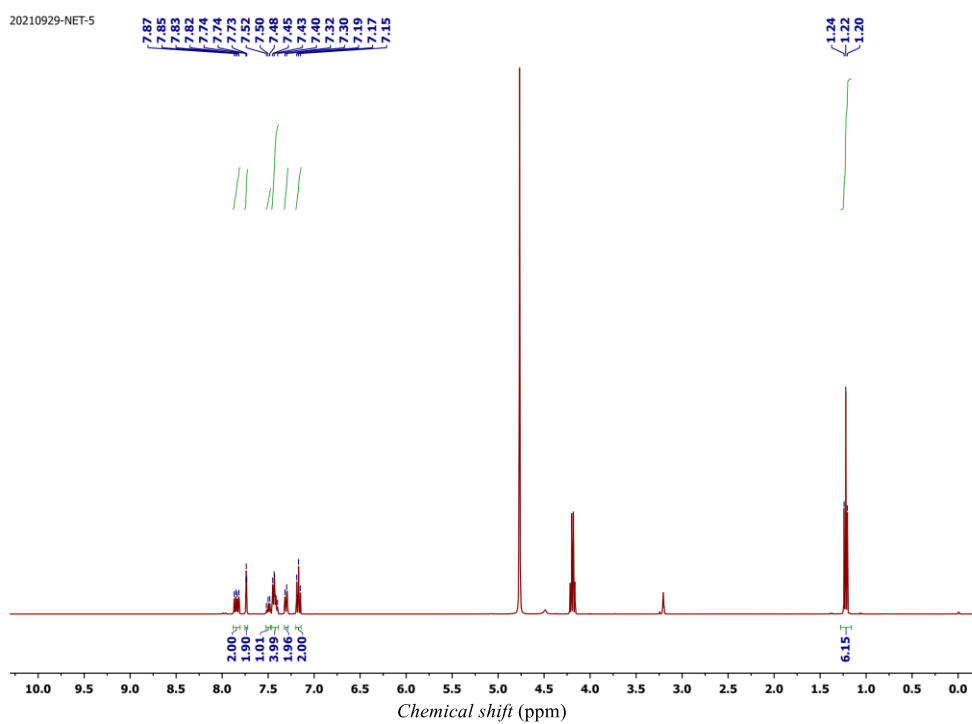


Figure 5A.2: The ^1H spectrum of **L**

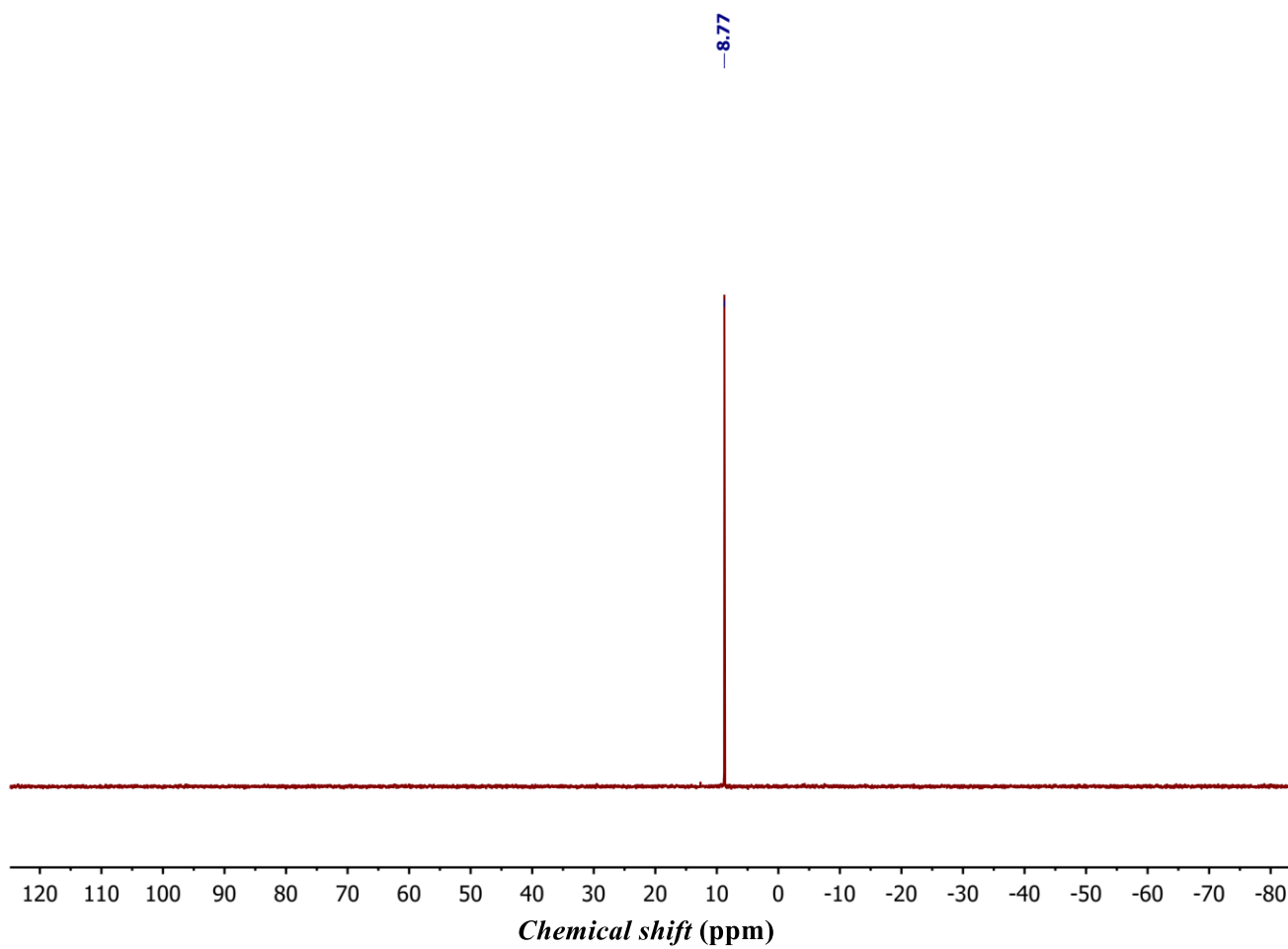
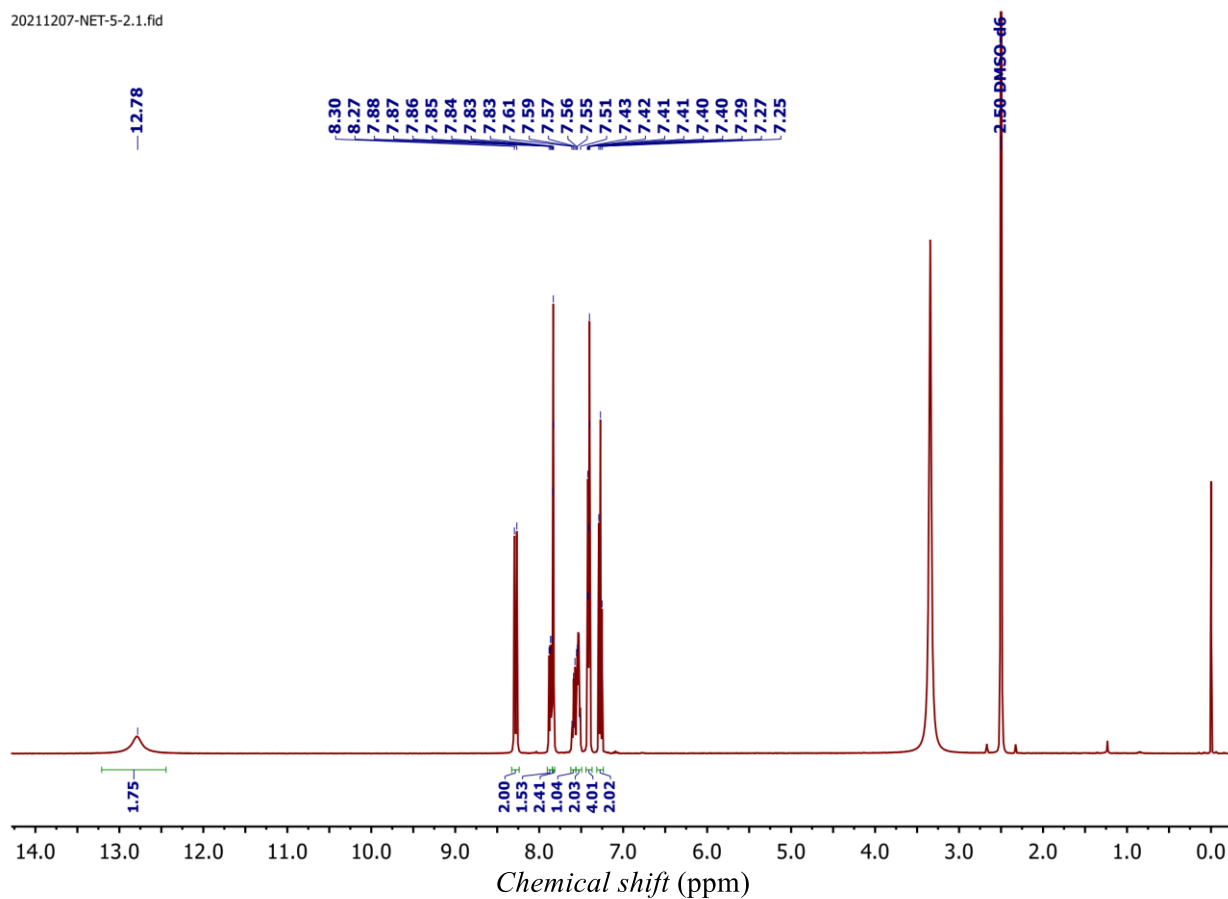


Figure 5A.3: The $^{31}\text{P}\{^1\text{H}\}$ spectrum of L^1H_2

20211207-NET-5-2.1.fid

**Figure 5A.4:** The ^1H spectrum of L^1H_2

The molecular structure of the ligand $\text{PhPO}(\text{NHC}_6\text{H}_4\text{COOEt})_2$ (**L**) was solved in the monoclinic space group $\text{P}2_1/c$. The asymmetric unit contains two molecules of the ligand. The P-N and P=O bond distances and N-P-N and N-P-C angles are consistent with the earlier reported amino-phosphoramidate ligands. It forms a 1D-*zigzag* H-bonded structure due to the N-H...O type H-bonding interaction between the proton of one of the amino group and the phosphoryl oxygen atom in one unit and the acetate O-atom in another unit (Figure 5A.5). The Ligand $[\text{PhPO}(\text{NH}(\text{C}_6\text{H}_4\text{COOH})_2)]$ (**L^{1H}₂**) was crystallized in the triclinic space group P-1. Again, the asymmetric unit contains two molecules of the ligand. The P-N and P=O bond distances and N-P-N and N-P-C angles in both **L** and **L^{1H}₂** are consistent with the earlier reported amino-phosphoramidate ligands. The protons attached the carboxylate groups were not located due to the poor quality of the X-ray data. It forms two types of type 8-membered (graph set $R_2^2(28)$) rings; one containing two carboxylate group and another one containing one carboxylate and one phosphoramidate group. The cumulative effect of these interactions leads to the formation of an intricate two dimensional H-bonded network (Figure 5A.7).

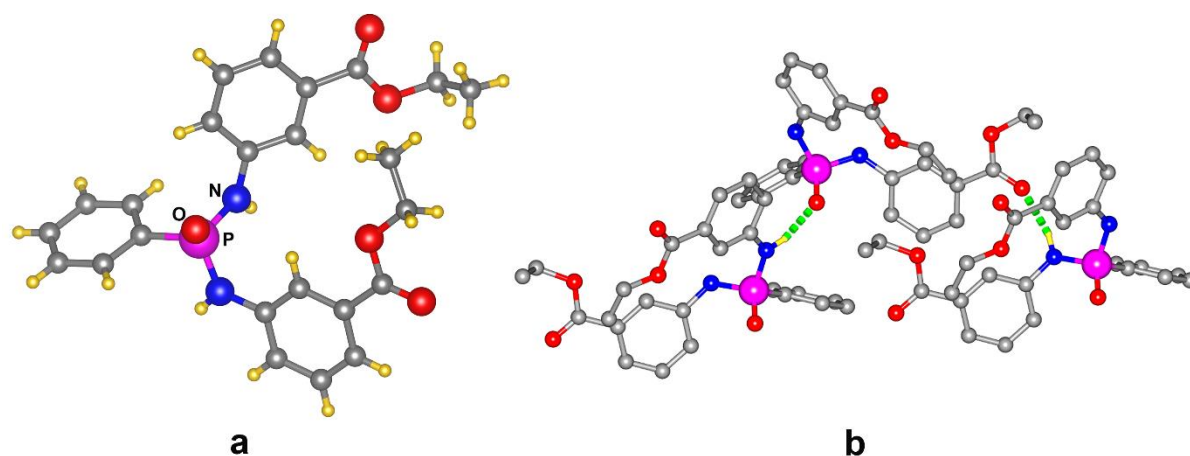


Figure 5A.5: Crystal structure of the ligand **L** (a) View of a monomeric unit of **L** (b) The hydrogen bonding interactions involving the N-H...O=P and N-H...O-C(acetate) motifs.

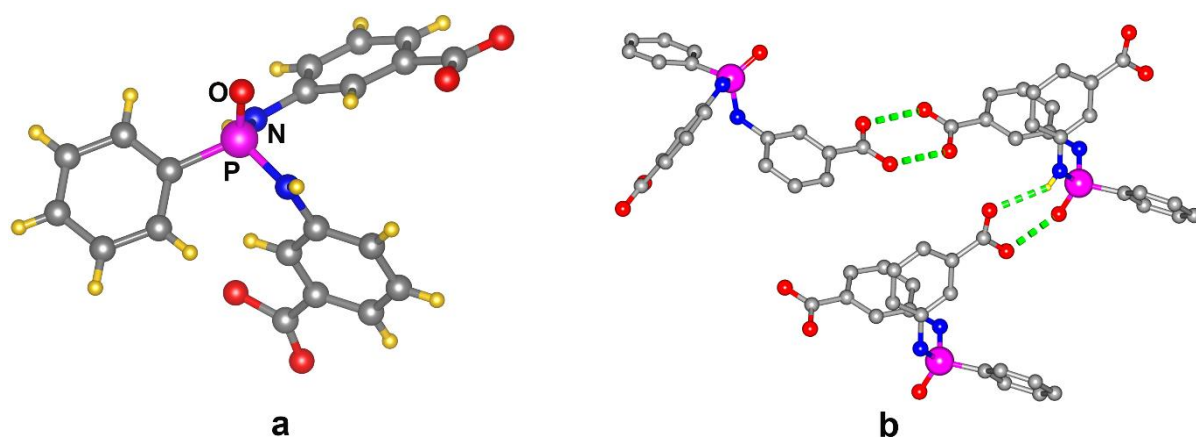


Figure 5A.6: Crystal structure of the ligand L^1 . (a) View of the monomeric unit (b) The hydrogen bonding interactions exhibited by the carboxylate groups.

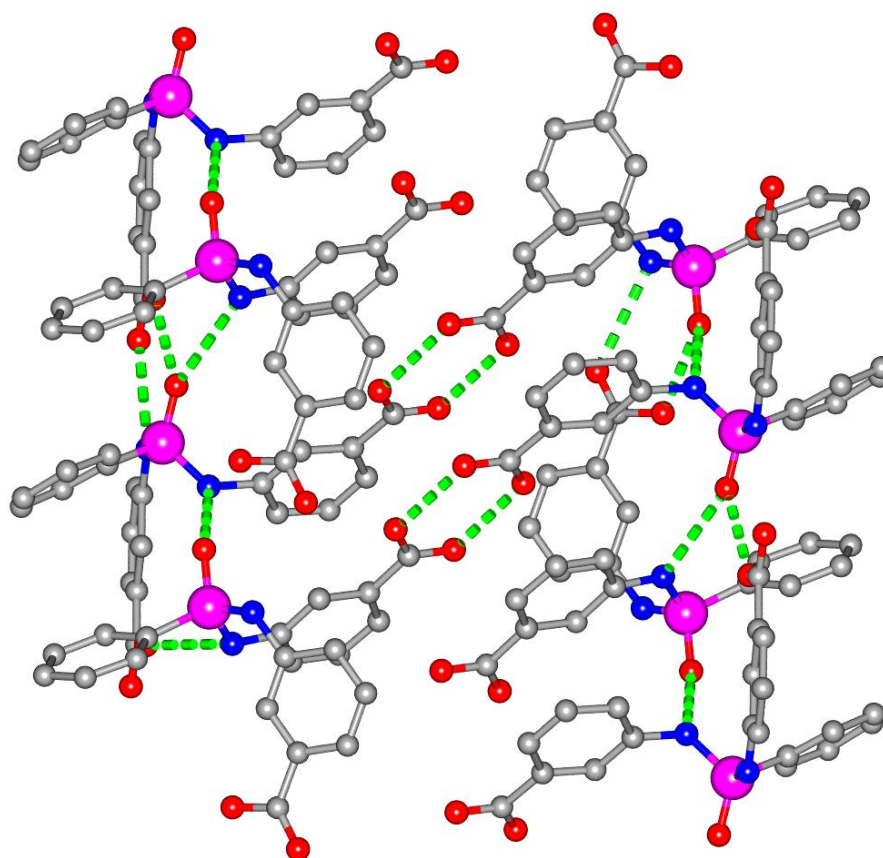


Figure 5A.7: The packing crystal structure of L^1H_2 showing the formation of the network structure mediated by H-bonding interactions. Hydrogen atoms are omitted for clarity of presentation.

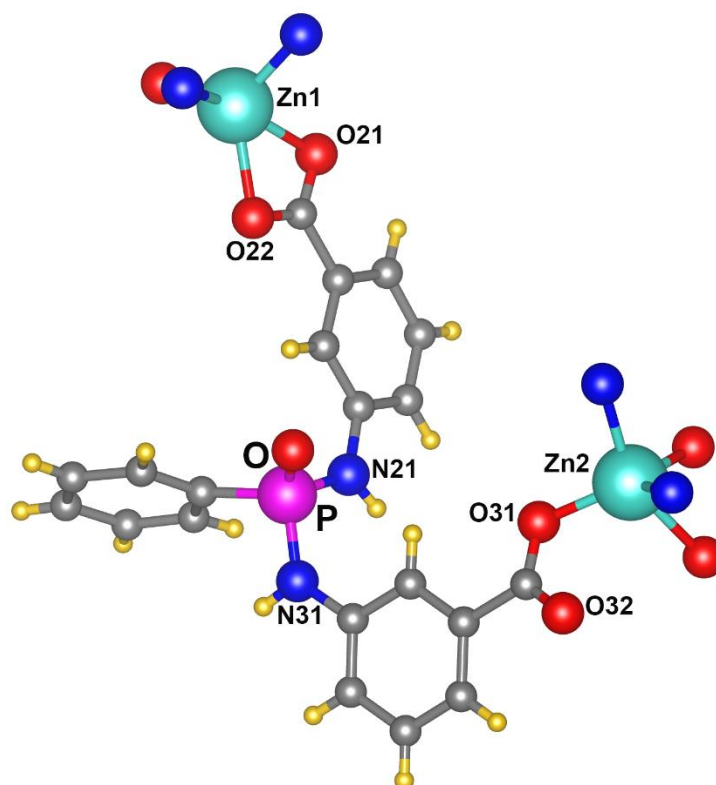


Figure 5A.8: Fragment of crystal structure of **1** showing the two distinct coordination modes of **L¹** with **Zn^{II}** ions

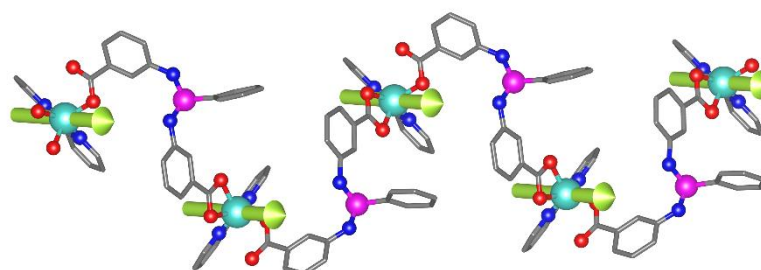


Figure 5A.9: The dipole moment vector around each polyhedra of zinc(II) ion in one-dimensional zig-zag chain showing the alignment of the vectors in one-direction.

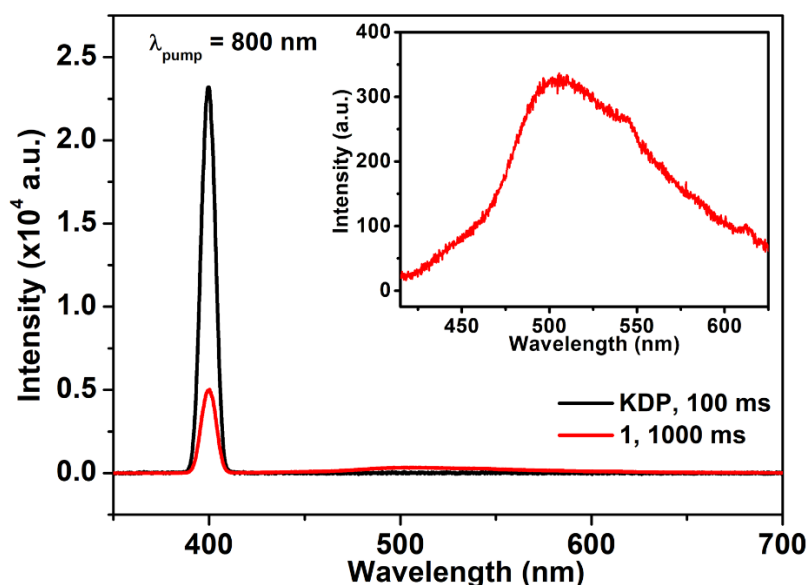


Figure 5A.10: SHG signal intensity of **1** with respect to standard KDP, the inset shows the zoomed-in view of the signal peaking at 490 nm due to 2PEL emission.

In addition to the SHG signal, it also exhibited a weak up-converted luminescence centered at 490 nm, most likely of two-photon excitation origin (Figure 5A.10). Temperature-dependent measurements indicate a steady decrease in the 2PEL intensity, which can be attributed to the thermal quenching of excited states. However, the SHG intensity remains almost unchanged, suggesting the absence of any structural phase transitions in the investigated temperature range (Figures 5A.11-5A.12). If one compares 2PEL results with linear optical steady-state luminescence data, it turns out that under ultraviolet excitation (365 nm) the emission maximum is shifted by 30 nm to the blue, i.e. peaks at 460 nm (Figure 5A.13-5A.14). As seen, the positions of luminescence maxima obtained under one- and two-photon excitation conditions do not match, pointing to the possibility that these emissions do not originate from exactly the same excited state.

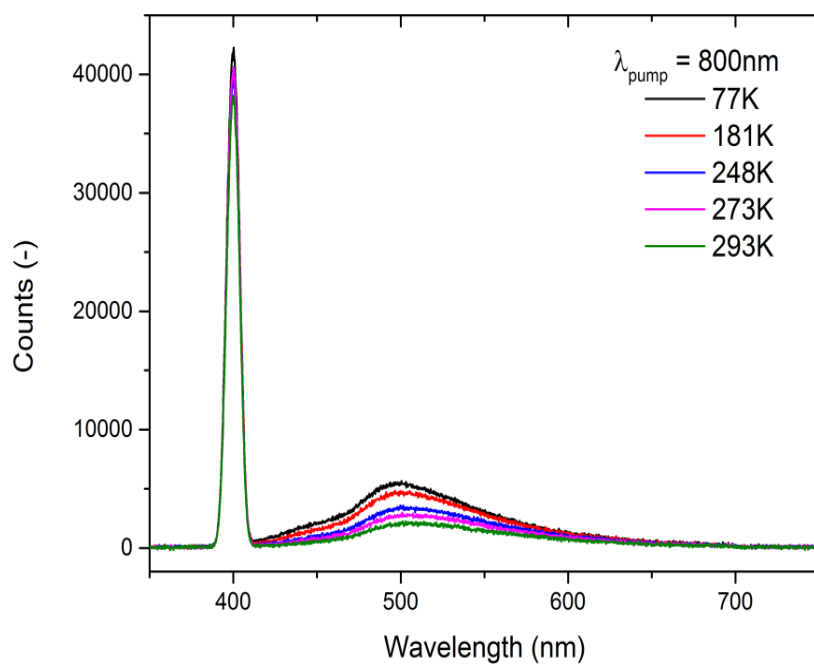


Figure 5A.11: The variable-temperature SHG and 2PEL spectra of **1**.

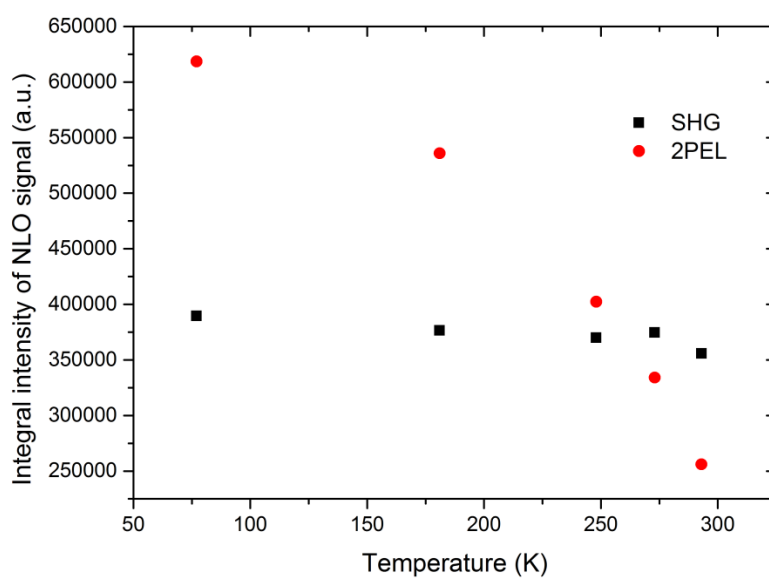


Figure 5A.12: Temperature dependence of integral intensities of SHG and 2PEL for **1**

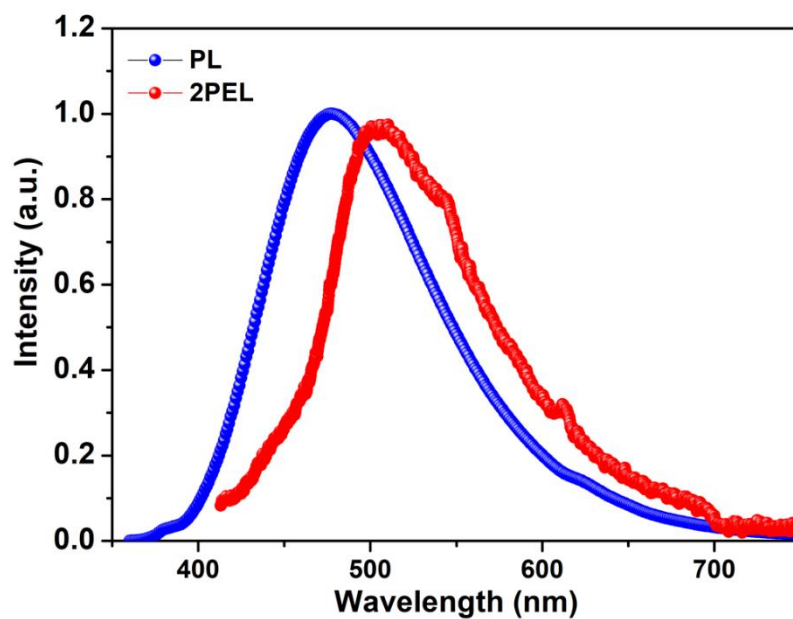


Figure 5A.13: The comparison of PL and 2PEL emission spectra for **1**

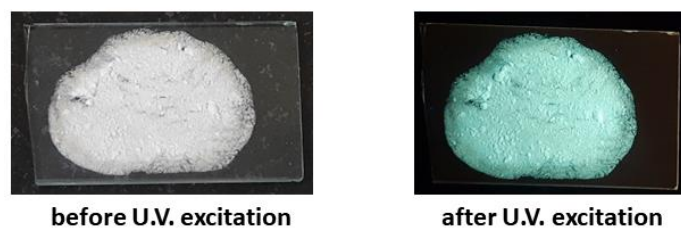


Figure 5A.14: Photographs of **1** under ambient and UV light (at 365 nm) on a pattern made up of its crushed crystals. A whitish cyan coloured emission was observed under irradiation with UV light

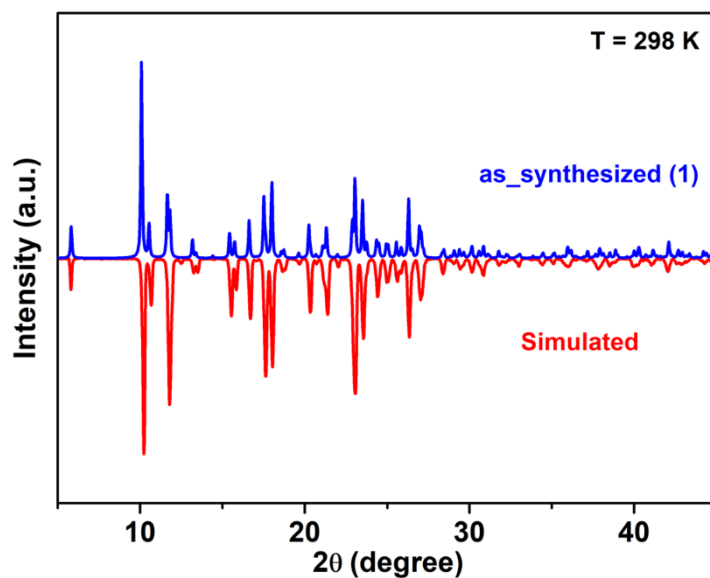


Figure 5A.15: Powder X-ray diffraction (PXRD) profile of as-synthesized (**1**) matching with simulated profile.

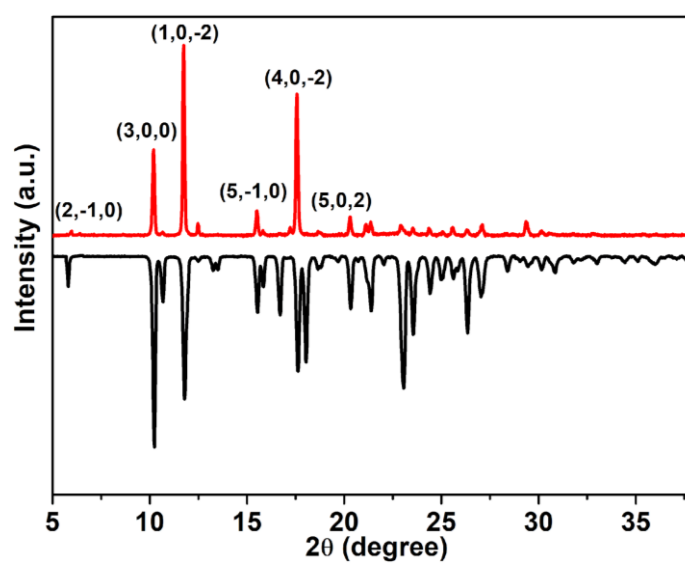


Figure 5A.16: Powder X-ray diffraction pattern for the thin film of **1** deposited on the Al substrate and its comparison with simulated patterns from X-ray derived structure.

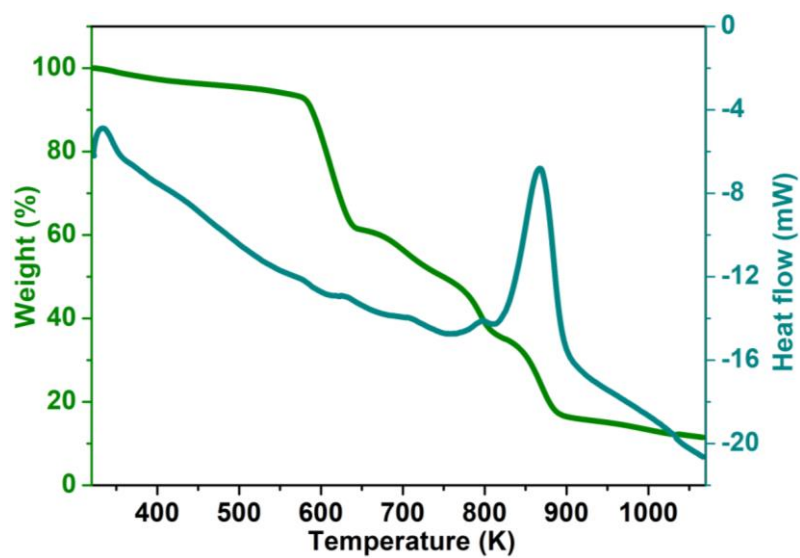


Figure 5A.17: Thermo-gravimetric analysis (TGA) plot of **1**

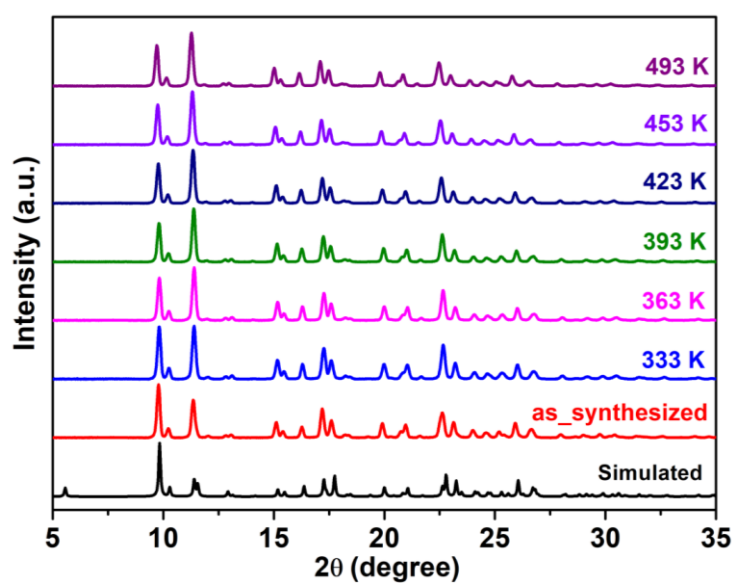


Figure 5A.18: Variable-Temperature Powder X-ray diffraction (VT-PXRD) pattern of **1**

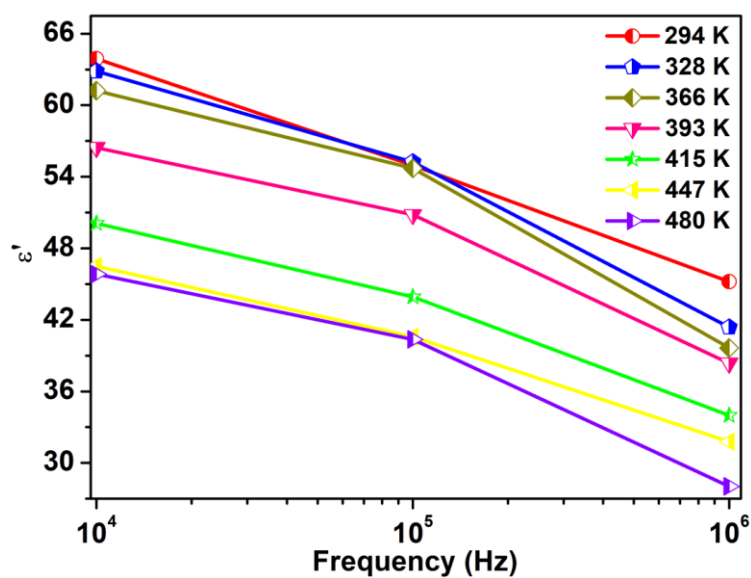


Figure 5A.19: Frequency-dependent real-part of dielectric Permittivity (ϵ') of **1** at various temperatures

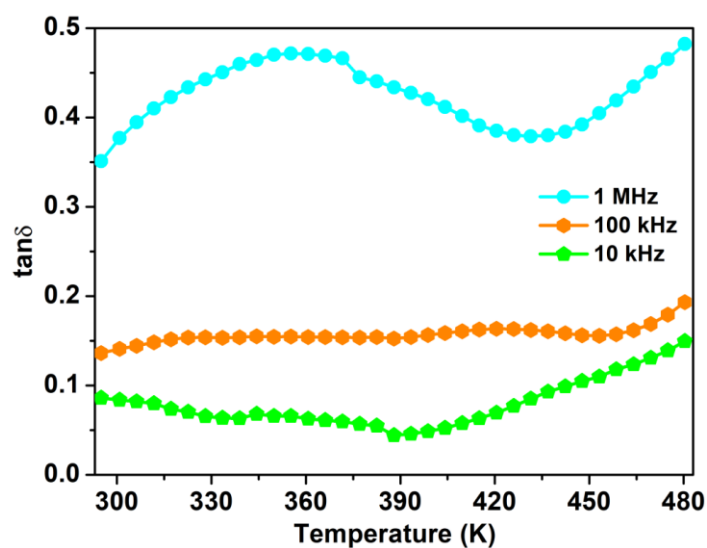


Figure 5A.20 Temperature-dependent dielectric loss ($\tan\delta$) of **1** at various frequencies

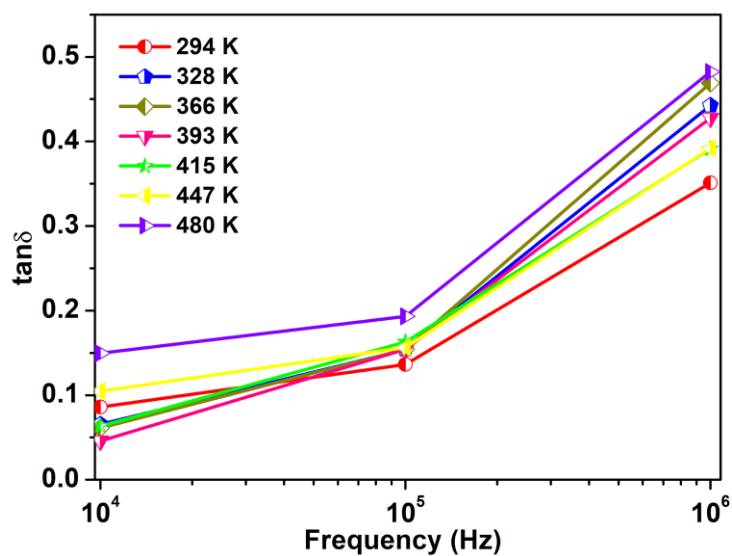


Figure 5A.21: Frequency-dependent dielectric loss ($\tan\delta$) at various temperatures

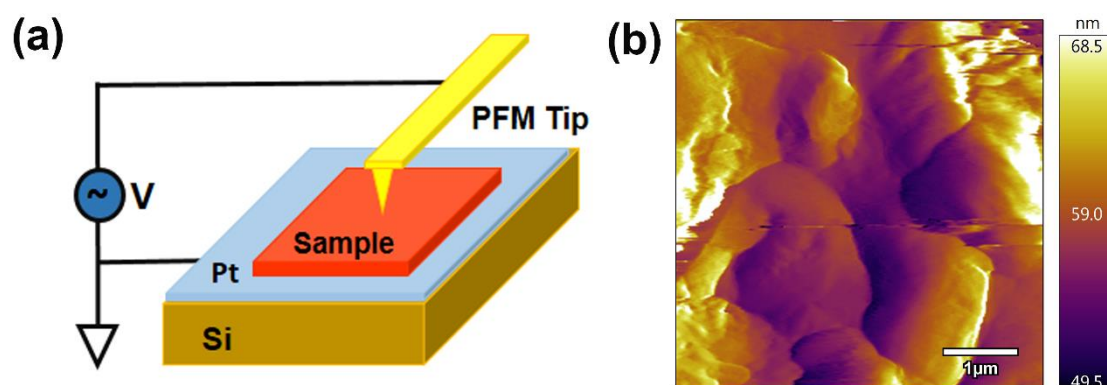


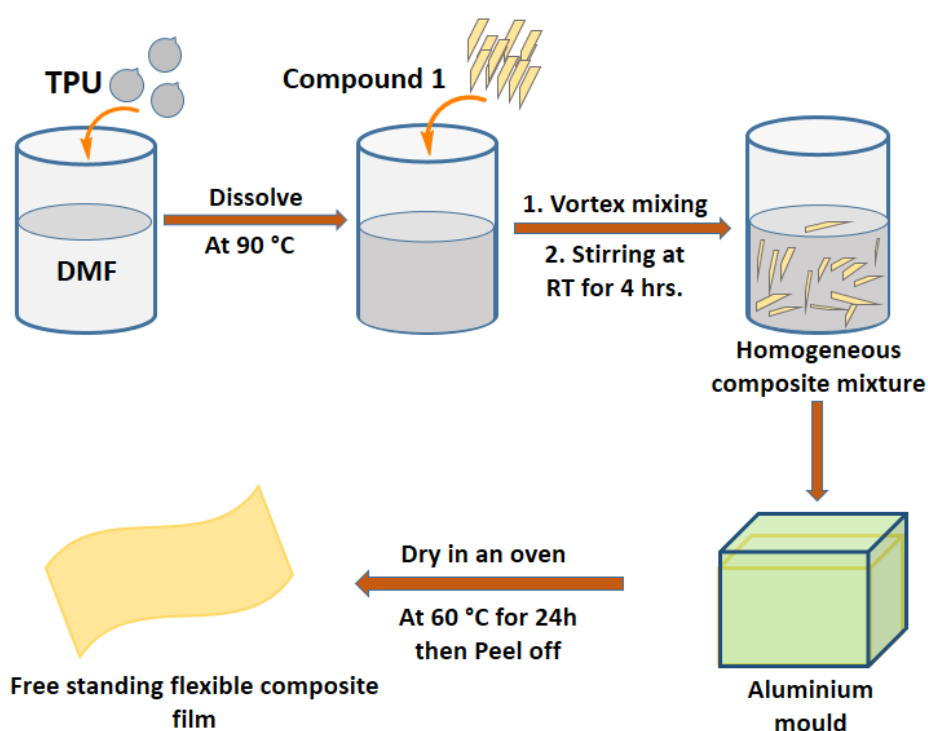
Figure 5A.22: (a) Schematic of a pellet of **1** mounted on the platinum electrode and scanned by the conductive AFM tip. (b) Topography image of the composite film

Table 5A.1: Comparison of saturated polarization (P_s), coercive field (E_c) and longitudinal piezoelectric coefficient (d_{33}) value for ferro- and piezo-active metal-ligand coordination polymers

Metal-organic inorganic coordination polymers	P_s ($\mu\text{C}/\text{cm}^2$)	E_c (kV/cm)	d_{33} / PFM amplitude	References
$\{[\text{Cu}_2\text{L}_4(\text{H}_2\text{O})_2] \cdot (\text{ClO}_4)_4 \cdot (\text{H}_2\text{O})_5 \cdot (\text{CH}_3\text{OH})\}_n$	1.8	16	-	1
$(\{[\text{CuL}^1_2(\text{H}_2\text{O})_2] \cdot (\text{NO}_3)_2 \cdot (\text{H}_2\text{O})_{1.5} \cdot (\text{CH}_3\text{OH})\}_\infty)$	21.79	5.9	-	2
$\{[\text{Zn}_6(\text{H}_2\text{O})_{12}][\text{TPTA}]_8\}(\text{NO}_3)_{12} \cdot 26\text{H}_2\text{O}$	0.95	0.86	-	3
$[\text{Cu}_6(\text{H}_2\text{O})_{12}(\text{TPPA})_8](\text{NO}_3)_{12} \cdot 45\text{H}_2\text{O}$, $[\{\text{Cu}_6\text{Cl}_4(\text{H}_2\text{O})_6(\text{TPPA})_8\}(\text{NO}_3)_8 \cdot 60\text{H}_2\text{O}]_n$	25.91, 26.79	0.22, 0.56	-	4
$\text{Cd}(\text{Imazethapyr})_2$	0.014	0.9	60.10 pC/N	5
MIL-53(Cr)	-	-	300-400 pm	6
Car_Zn.(MeCN)	-	-	4.7 pm/V	7
$\{[\text{Zn}(\text{L}^1)(\text{bpy})] \cdot (\text{H}_2\text{O})_{1.5}\}_\infty$ (1)	4.80	0.62	19.4 pm/V	This work

Table 5A.2: Details about the preparation of various mass fractions (wt%) and vol % of 1-TPU composite films

Composite (wt%)	Composite (vol%)	1 (in mg)	TPU (in mg)
1	8 %	10.22	1012
5	4.6 %	53.47	1016
10	9.8 %	113.77	1024
15	15.7 %	180.00	1020

**Figure 5A.23:** Schematic showing the procedure involved in preparation of 1-TPU composite films

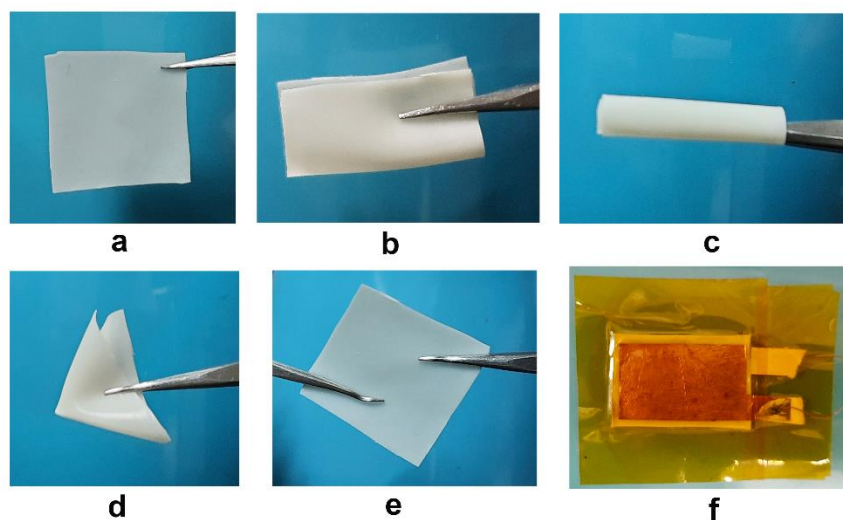


Figure 5A.24: Photographs of the 5 wt% **1**-TPU composite film showing (a) composite film and (b) folding (c) rolling (d) multi-fold bending (e) stretching operations (f) Photograph of the as-fabricated **1**-TPU composite device

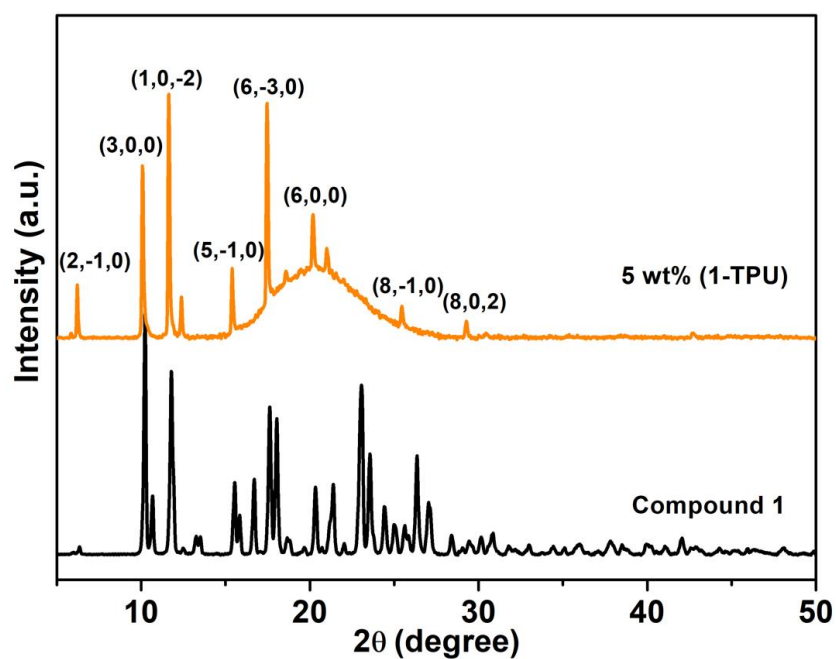


Figure 5A.25: PXRD of as synthesized compound **1** and its 5 wt% (**1**-TPU) composite film

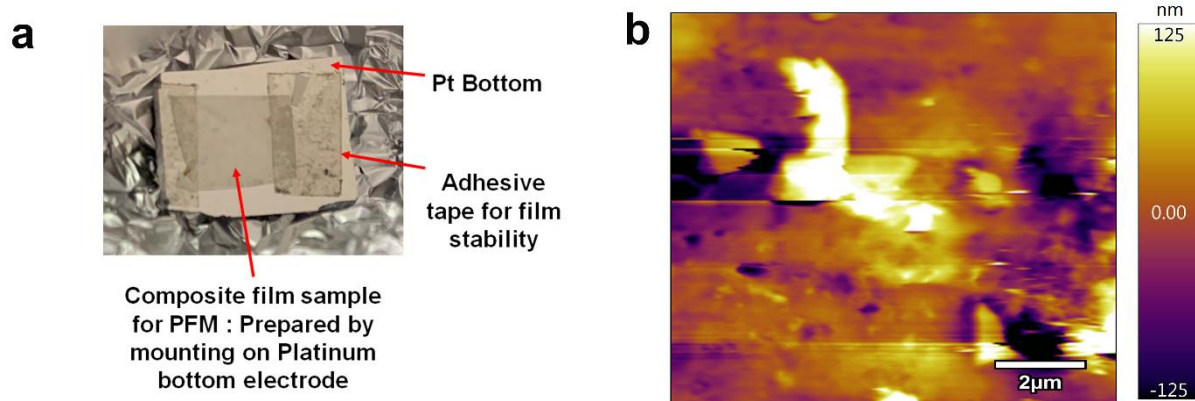


Figure 5A.26: Piezoresponse force microscopy (PFM) image based on the composite film (1-TPU) of $10 \times 10 \mu\text{m}^2$ area. (a) The composite film mounted on the platinum electrode. (b) Topography image of the composite film

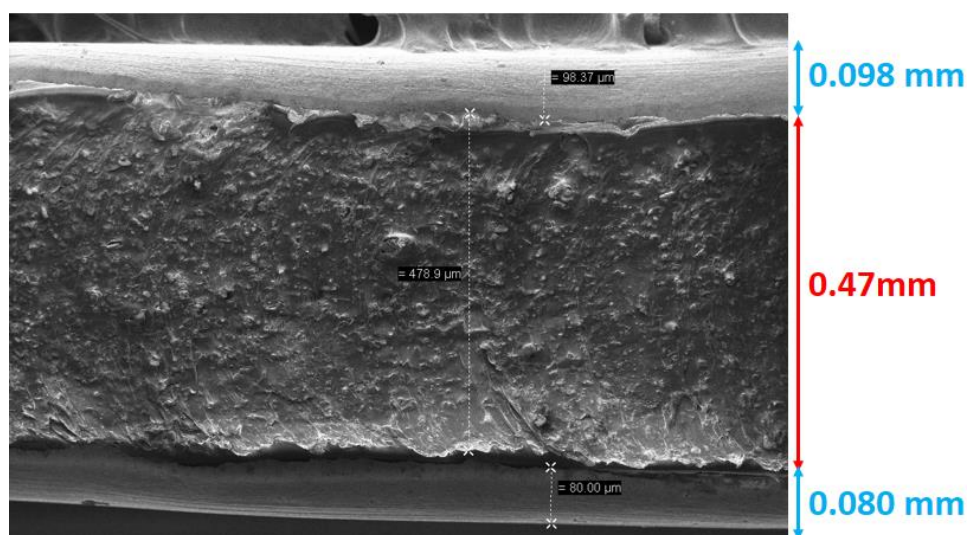


Figure 5A.27: Cross-sectional SEM image of 1-TPU composite film sandwiched between two copper electrodes

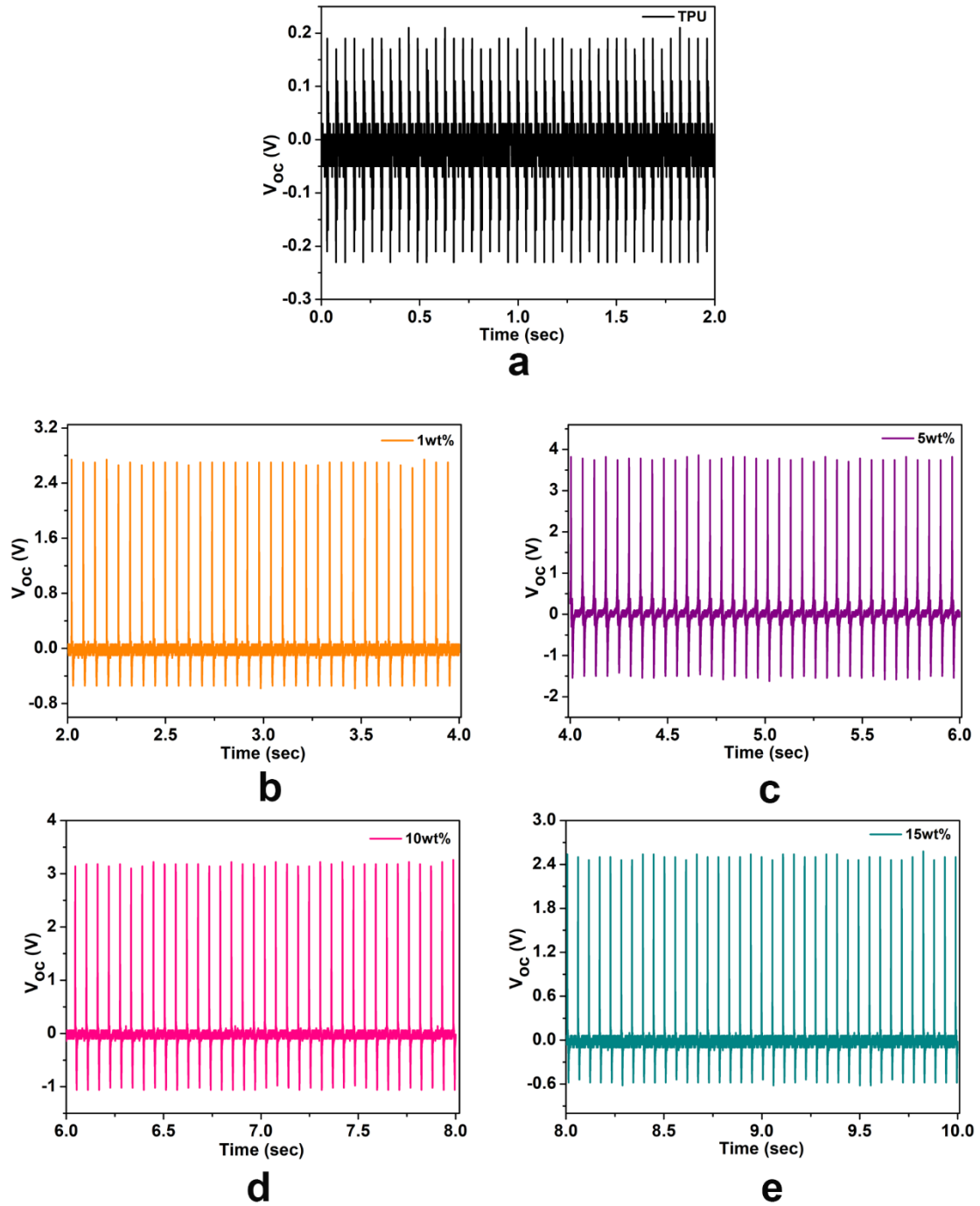


Figure 5A.28: Open-circuit output voltage measurements of various weight percentages (wt%) of poled 1-TPU composite devices

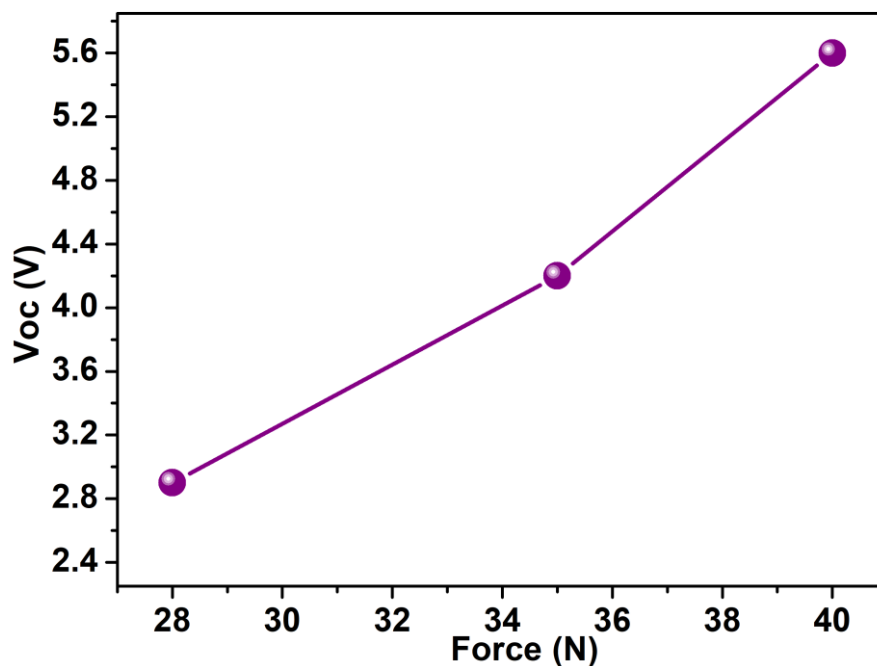


Figure 5A.29: Observed trends of voltage as a function of different force of the 5 wt% (1-TPU) composite device

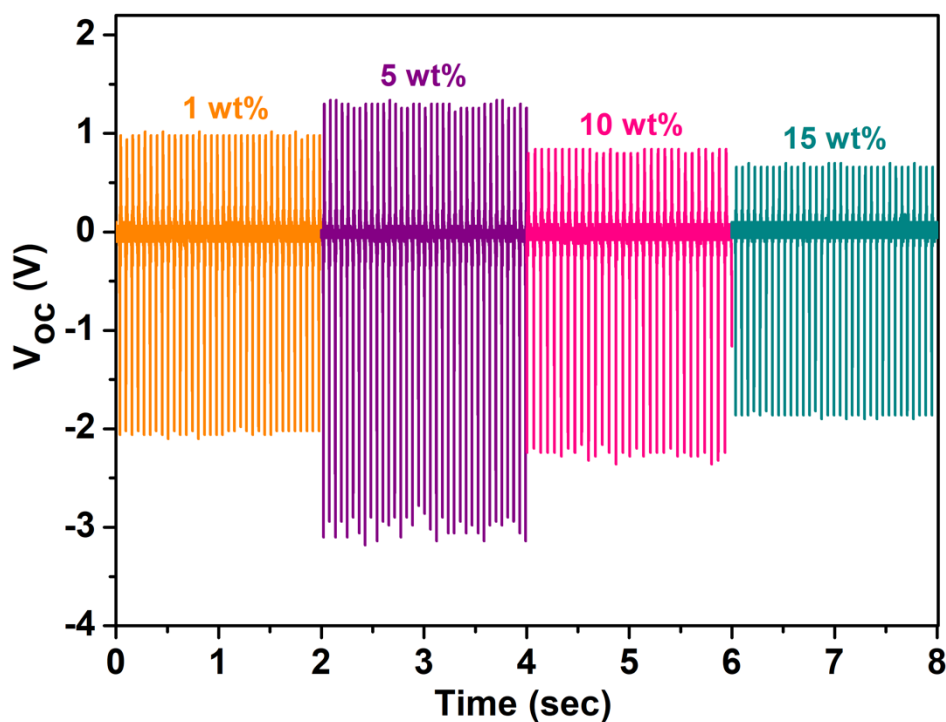


Figure 5A.30: Open-circuit output voltage measurements of all the (1, 5, 10, 15 wt%) 1-TPU device in reverse connection

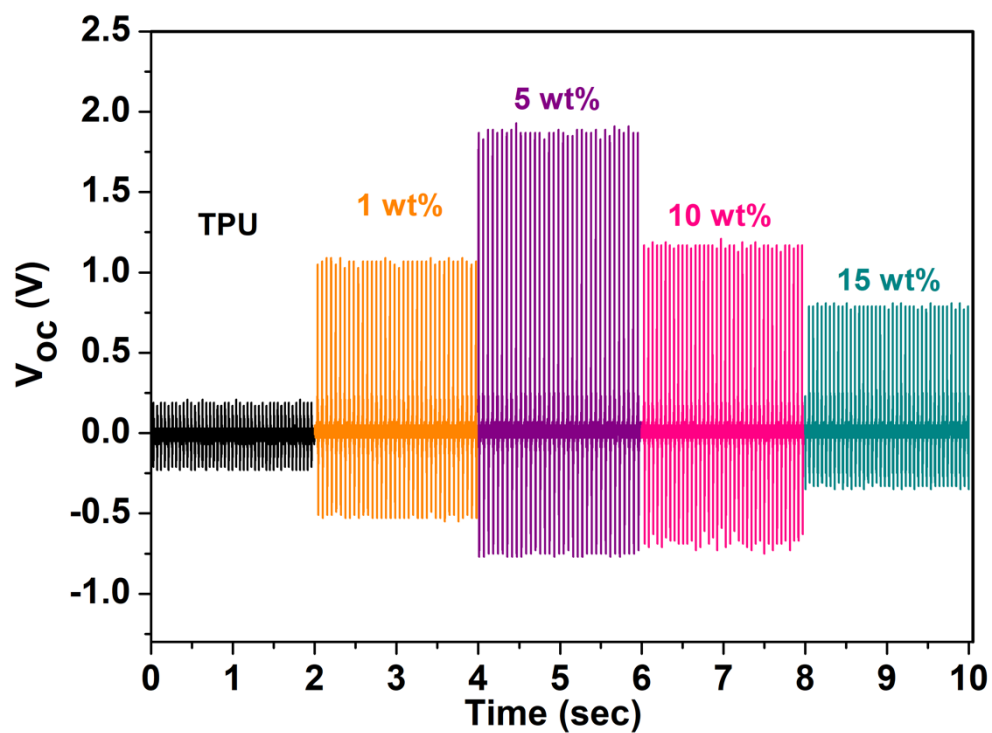


Figure 5A.31: Open-circuit output voltage measurements of various weight percentage (wt%) 1-TPU composite devices before poling

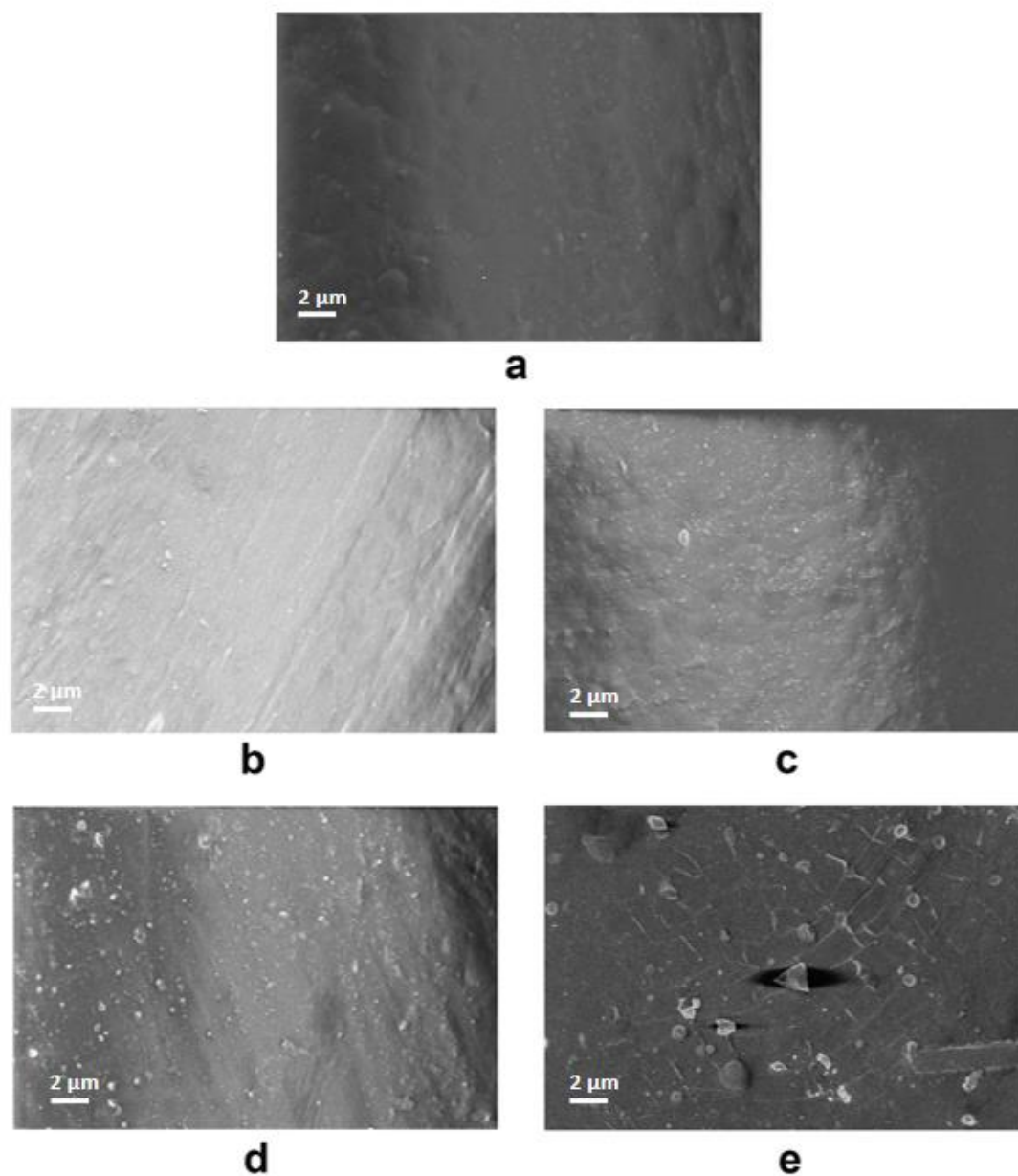


Figure 5A.32: SEM images of (a) TPU and (b-e) the respective 1, 5, 10, 15 wt% of 1-TPU composite films

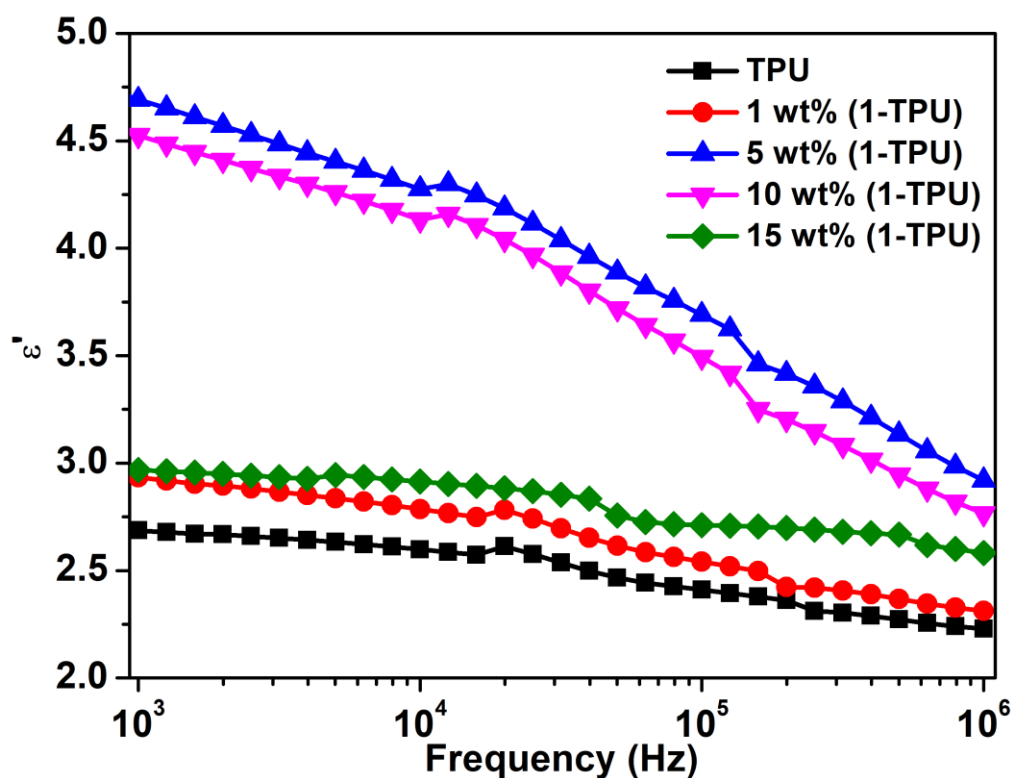


Figure 5A.33: Frequency-dependent measurements of real part of dielectric permittivity (ϵ') of various wt% of 1-TPU composite films.

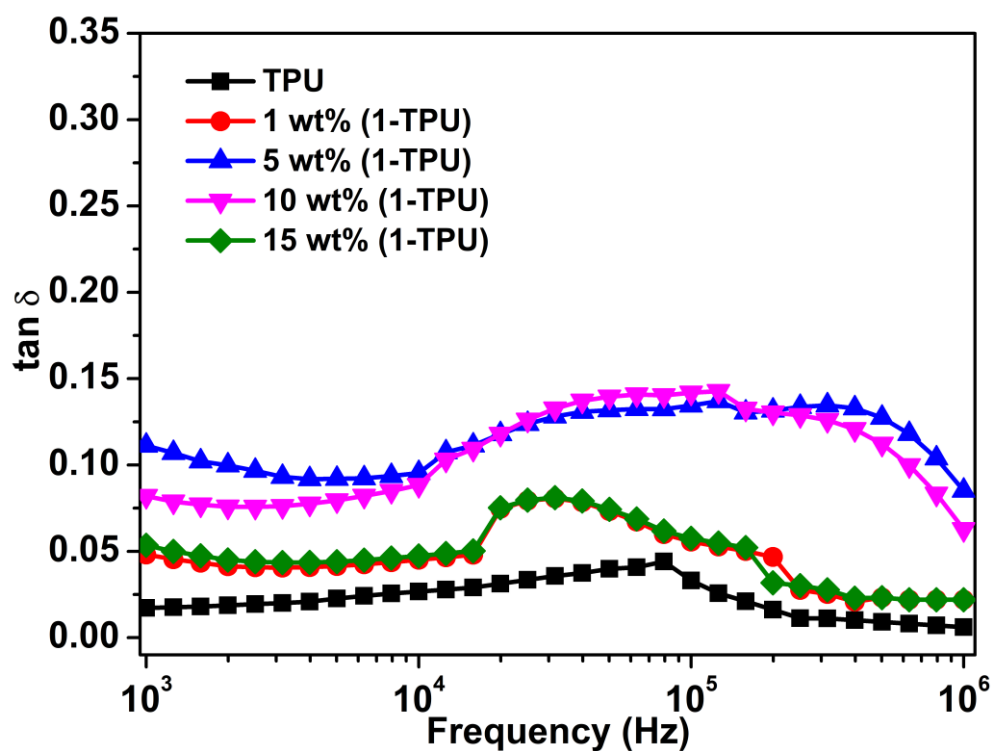


Figure 5A.34: Frequency-dependent measurements of dielectric loss ($\tan\delta$) of various wt% of 1-TPU composite films.

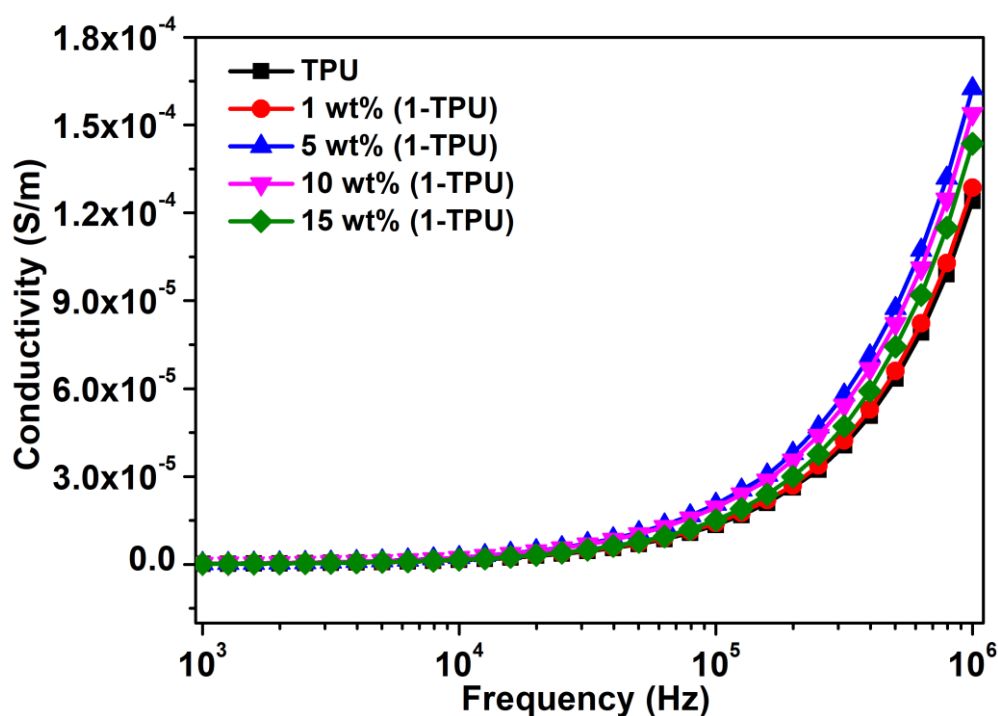


Figure 5A.35: Frequency-dependent conductivity measurements of various wt% of 1-TPU composite films.

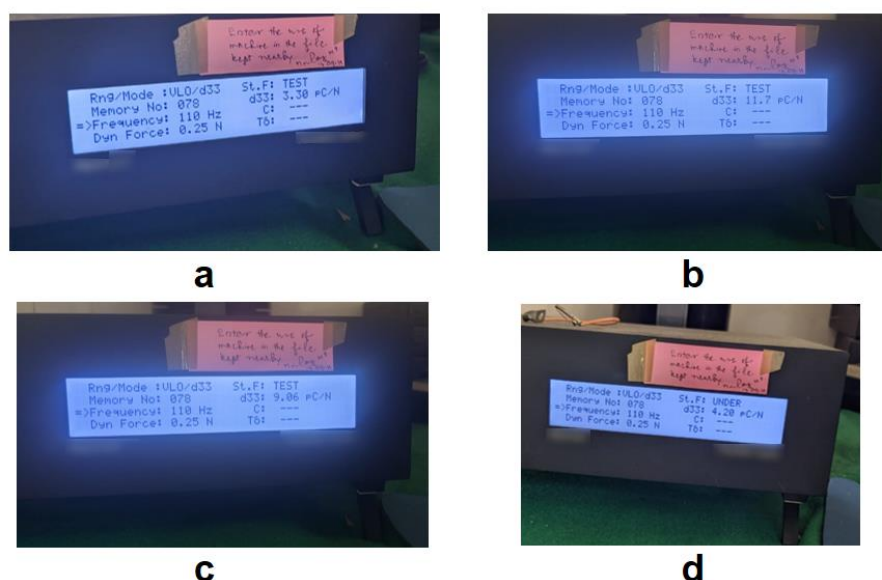


Figure 5A.36: Photographs of the d_{33} meter showing the direct Piezoelectric coefficients (d_{33}) of the poled 1, 5, 10, 15 wt% of 1-TPU composite films

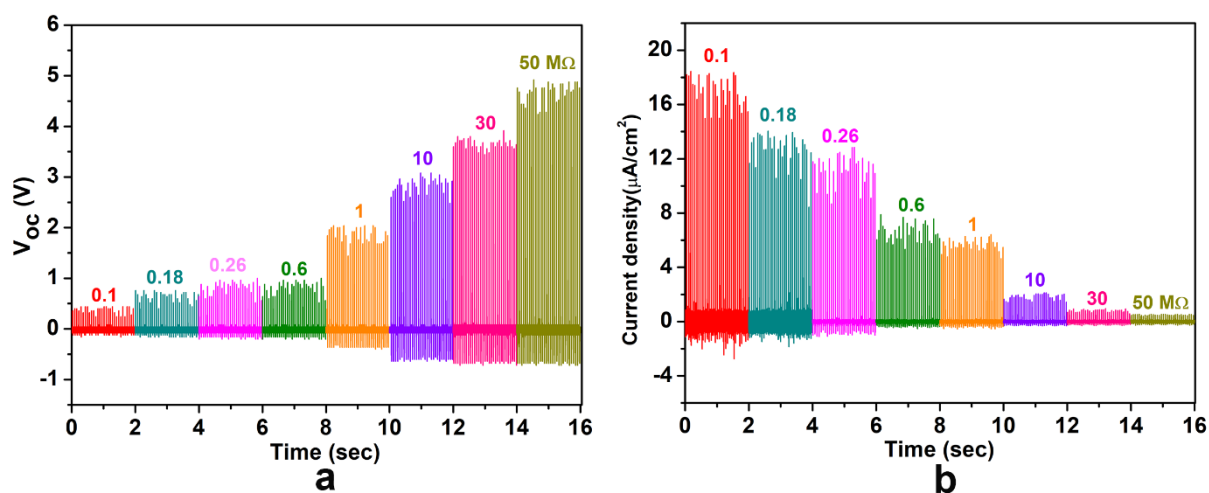


Figure 5A.37: (a) Voltage and (b) Current density across various load resistances of the best performing 5 wt% (1-TPU) device.

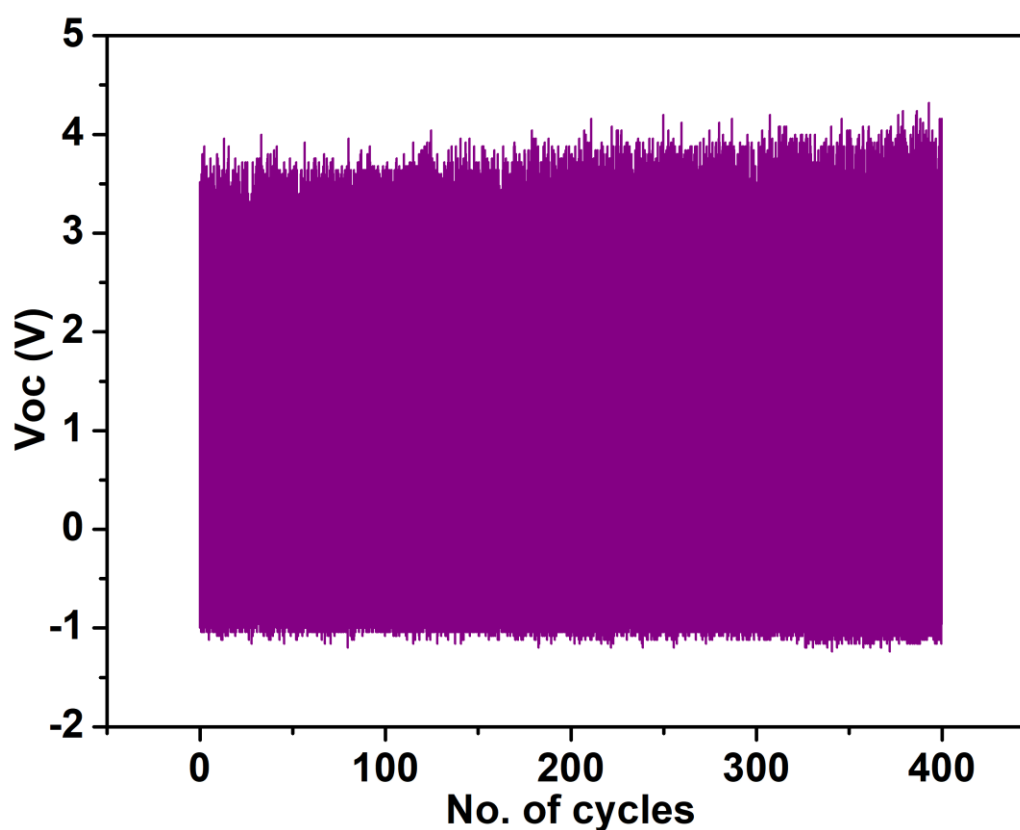


Figure 5A.38: Fatigue measurements of the 5 wt% 1-TPU device with a continuous applied force of 40 N force upto 400 cycles.

Table 5A.3: Comparison of output device performance of various hybrid piezoelectric energy harvesters.

Hybrid composite materials	Output voltage (V)	Current/Current density	Power/Power density	Active Area	References
Car_Zn.(MeCN)-PDMS	2.5 V	-	-	1 x 1 cm ²	7
Zr-MOF- PDMS	536 mV	-	-	2 x 1.5 cm ²	8
[Ph ₃ MeP] ₄ [Ni(NCS) ₆]-TPU	19.29	3.59 μ A/cm ³	50.26 μ W/cm ³	1.3 x 3 cm ²	9
(CdI ₂ -INH=CMe ₂)-PVDF	12 V	-	32 μ W/cm ²	2 x 1 cm ²	10
MAPI-PVDF	220 mV	-	-	2.9 x 1.5 cm ²	11
(CdI ₂ -NAP)-PVDF	22 V	-	24 μ W/cm ²	4 x 1.5 cm ²	12
PVDF-PLLA-SnO ₂ NF-MAPbI ₃	4.82 V	29.7 nA	-	0.25 X 0.25 cm ²	13
(TMFM)FeBr ₄	2.2 V	-	-	-	14
MASnI ₃ -PVDF	12 V	4 μ A/cm ²	21.6 μ W/cm ²	-	15
(BNT-ST)-PVDF	1.31 V	-	-	1 x 5 cm ²	16
(BZT-BCT)-PVDF	8.11 V	2.83 μ A	0.837 μ W	1.6 x 1.6 cm ²	17
BZT-BCT (nanofibres)- P(VDF-TrFE)	13.01 V	-	1.44 μ W	1 x 1 cm ²	18
PZT(nanofibres)-PDMS	1.63 V	-	0.03 μ W	-	19
ZnO-PVDF	2.23 V	-	-	-	20
(ZnO-NWs)-PVDF	0.1 V	10 nA/cm ²	16 μ W/cm ³	-	21
PVDF-nanofibre mats	114.2 mV/ μ m	-	-	-	22
PVDF-nanofibre membrane	12 V	-	-	-	23
5 wt% (1-TPU)	5.6 V	6.19 μA/cm²	14.6 μW/cm²	1.3 x 2 cm²	This work

*The overall effective electromechanical energy generating performance of the composite devices depends on multiple factors, such as the ratio of the piezoelectric particles and the polymer, materials dimensions (width, length and thickness), amount of piezoelectric particles in the film, phase purity of piezoelectric crystals, selection of supporting polymer, choice of electrode, active surface area between electrode and material, the magnitude of the mechanical force and applied frequency and the structural morphologies of the ferroelectric particles in the composite materials.

Note – PDMS = Polydimethylsiloxane; PVDF = Polyvinyl difluoride; MAPI = Methylammonium Lead Iodide; PLLA = poly(L-lactic acid); (TMFM)FeBr₄ = trimethylfluoromethylammonium iron(III)bromide; MASnI₃ = methylammonium tin iodide; BNT-ST = (0.78Bi_{0.5}Na_{0.5}TiO₃-0.22SrTiO₃), (BZT-BCT) = 0.5Ba(Zr_{0.2}Ti_{0.8})O₃-0.5(Ba_{0.7}Ca_{0.3})TiO₃, (BZT-BCT) = 0.5Ba(Zr_{0.2}Ti_{0.8})O₃-0.5(Ba_{0.7}Ca_{0.3})TiO₃, (ZnO-NWs) = Zinc oxide nanowires

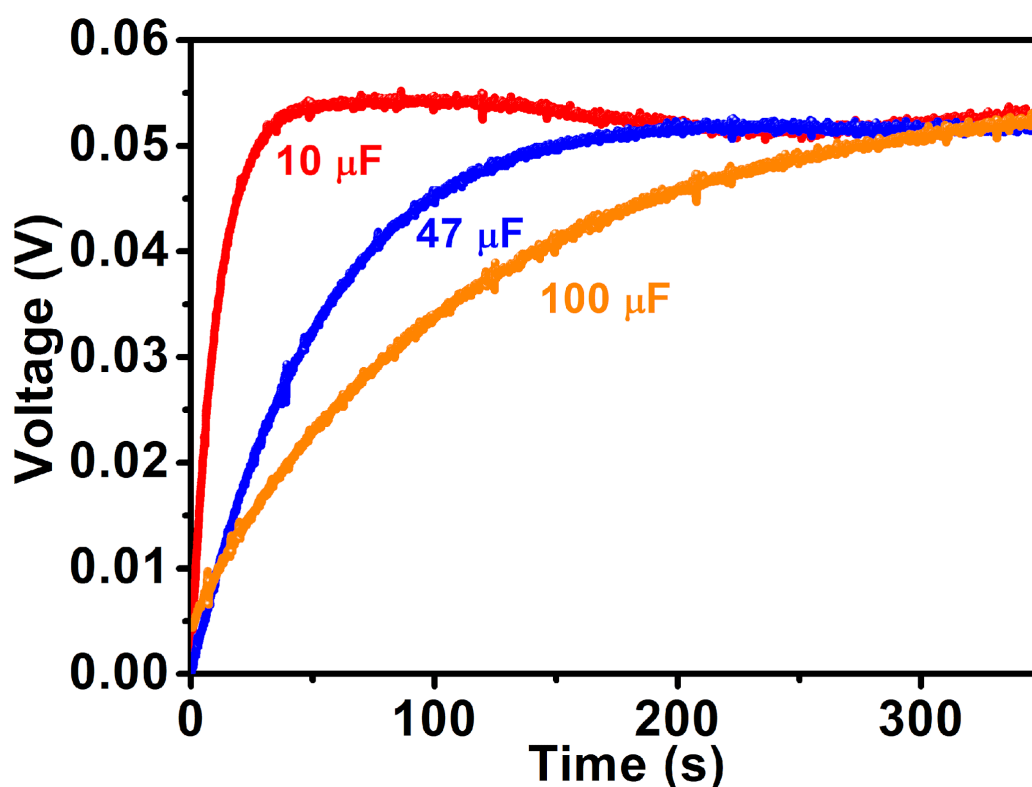


Figure 5A.39: Output saturation voltage of the 5 wt% 1-TPU device at different load capacitances.

A5.1 References

1. A. K. Srivastava, B. Praveenkumar, I. K. Mahawar, P. Divya, S. Shalini and R. Boomishankar, Chem. Mater., 2014, **26**, 3811-3817.
2. A. K. Srivastava, P. Divya, B. Praveenkumar and R. Boomishankar, Chem. Mater., 2015, **27**, 5222-5229.
3. A. Yadav, A. K. Srivastava, P. Kulkarni, P. Divya, A. Steiner, B. Praveenkumar and R. Boomishankar, J. Mater. Chem. C, 2017, **5**, 10624-10629.

4. N. Prajesh, A. Yadav, R. Gourkhede, B. Praveenkumar, A. Steiner and R. Boomishankar, *Chem. Asian J.*, 2020, **15**, 3275-3280.
5. D.-W. Fu, W. Zhang and R.-G. Xiong, *Dalton Trans.*, 2008, DOI: 10.1039/B806255B, 3946-3948.
6. F. Xue, J. Cao, X. Li, J. Feng, M. Tao and B. Xue, *J. Mater. Chem. C*, 2021, **9**, 7568-7574.
7. Y. Chen, S. Guerin, H. Yuan, J. O'Donnell, B. Xue, P.-A. Cazade, E. U. Haq, L. J. W. Shimon, S. Rencus-Lazar, S. A. M. Tofail, Y. Cao, D. Thompson, R. Yang and E. Gazit, *J. Am. Chem. Soc.*, 2022, **144**, 3468-3476.
8. B. H. Moghadam, M. Hasanzadeh and A. Simchi, *ACS Appl. Nano Mater.*, 2020, **3**, 8742-8752.
9. T. Vijayakanth, F. Ram, B. Praveenkumar, K. Shanmuganathan and R. Boomishankar, *Angew. Chem. Int. Ed.*, 2020, **59**, 10368-10373.
10. K. Roy, S. Jana, S. K. Ghosh, B. Mahanty, Z. Mallick, S. Sarkar, C. Sinha and D. Mandal, *Langmuir*, 2020, **36**, 11477-11489.
11. A. Sultana, S. K. Ghosh, M. M. Alam, P. Sadhukhan, K. Roy, M. Xie, C. R. Bowen, S. Sarkar, S. Das, T. R. Middy and D. Mandal, *ACS Appl. Mater. Interfaces*, 2019, **11**, 27279-27287.
12. K. Roy, S. Jana, Z. Mallick, S. K. Ghosh, B. Dutta, S. Sarkar, C. Sinha and D. Mandal, *Langmuir*, 2021, **37**, 7107-7117.
13. R. Tusiime, F. Zabihi, M. Tebyetekerwa, Y. M. Yousry, Y. Wu, M. Eslamian, S. Yang, S. Ramakrishna, M. Yu and H. Zhang, *J. Mater. Chem. C*, 2020, **8**, 2643-2658.
14. Y. Zhang, X.-J. Song, Z.-X. Zhang, D.-W. Fu and R.-G. Xiong, *Matter*, 2020, **2**, 697-710.
15. S. Ippili, V. Jella, J.-H. Eom, J. Kim, S. Hong, J.-S. Choi, V.-D. Tran, N. Van Hieu, Y.-J. Kim, H.-J. Kim and S.-G. Yoon, *Nano Energy*, 2019, **57**, 911-923.
16. S. H. Ji, J. H. Cho, Y. H. Jeong, J.-H. Paik, J. D. Yun and J. S. Yun, *Sens. Actuators, A*, 2016, **247**, 316-322.
17. J. Liu, B. Yang and J. Liu, *J Mater Sci: Mater Electron*, 2018, **29**, 17764-17770.
18. J. Liu, B. Yang, L. Lu, X. Wang, X. Li, X. Chen and J. Liu, *Sens. Actuators, A*, 2020, **303**, 111796.
19. X. Chen, S. Xu, N. Yao and Y. Shi, *Nano Lett.*, 2010, **10**, 2133-2137.

20. T. Yang, H. Pan, G. Tian, B. Zhang, D. Xiong, Y. Gao, C. Yan, X. Chu, N. Chen, S. Zhong, L. Zhang, W. Deng and W. Yang, *Nano Energy*, 2020, **72**, 104706.
21. M. Lee, C.-Y. Chen, S. Wang, S. N. Cha, Y. J. Park, J. M. Kim, L.-J. Chou and Z. L. Wang, *Adv. Mater.*, 2012, **24**, 1759-1764.
22. S.-H. Park, H. B. Lee, S. M. Yeon, J. Park and N. K. Lee, *ACS Appl. Mater. Interfaces*, 2016, **8**, 24773-24781.
23. M.-H. You, X.-X. Wang, X. Yan, J. Zhang, W.-Z. Song, M. Yu, Z.-Y. Fan, S. Ramakrishna and Y.-Z. Long, *J. Mater. Chem. A*, 2018, **6**, 3500-3509.